Active and Responsive Microparticle Systems for Biomolecule Detection

by

Cooper Paul Thome

B.S., University of Tennessee at Chattanooga, 2018

A dissertation submitted to the

Faculty of the Graduate School of the

University of Colorado in partial fulfillment

of the requirement for the degree of

Doctor of Philosophy

Department of Chemical and Biological Engineering

2024

Committee Members:

Dr. C. Wyatt Shields IV

Dr. Jennifer Cha

Dr. Xiaoyun Ding

Dr. Ankur Gupta

Dr. Daniel Schwartz

Abstract

Thome, Cooper Paul (Ph.D., Department of Chemical and Biological Engineering)

Active and Responsive Microparticle Systems for Biomolecule Detection

Dissertation directed by Assistant Professor C. Wyatt Shields IV

Detection of biomolecules from fluid samples using both qualitative and quantitative assays is essential for patient diagnosis, disease monitoring, and public health surveillance, among other applications. Numerous factors impact assay performance, workflow requirements, and potential end-use cases. These factors include the target biomolecule type, the type of matrix from which the biomolecule is to be detected, and the type of biorecognition elements that can interact with the target. Many qualitative assays benefit from user-friendliness, minimal points of error, and simple signal readouts that eliminate the need for complex instrumentation; however, they often fail to detect rare biomolecules. Moreover, while convenient for rapid testing, they typically cannot yield quantitative results, which lessens their usefulness in some areas. Quantitative assays, however, have the capacity to provide numerical readouts that offer a more comprehensive understanding of patient conditions. However, such assays commonly have multiple potential points of user-related error that can lead to false results; moreover, they often necessitate extensive user engagement and the use of complex, expensive, and bulky instrumentation, ultimately limiting their use to specialized laboratory settings.

This dissertation presents multiple projects that focus on the engineering of microparticle systems to drive advancements in quantitative biomolecule detection approaches by simplification of signal transduction methods and assay processing requirements. To simplify signal transduction

methods, we show proof-of-concept for a label-free, motion-based biomolecule detection system using active particles that propel via induced-charge electrophoresis (ICEP). We prepare induced-charge electrophoretic microsensors (ICEMs) for the capture of two model biomolecules and show that the specific capture of biomolecules leads to direct signal transduction through ICEM speed suppression at low concentrations. We further present dielectrophoretic polarizability measurement (DPM) as a method to study the effects of surface modifications on the polarizability of surfaces in systems that leverage induced-charge electroosmotic flows and study to the speed of surface-modified particles similar to ICEMs that propel by ICEP. Through use of this method, we show that ICEM speed suppression upon protein capture likely arises from both changes to the surface polarizability of the particle as well as interactions of the particle with solid surfaces.

To simplify assay processing requirements, we present a new a class of acoustic-responsive microparticles, termed functional negative acoustic contrast particles (fNACPs), and a handheld, ergonomic acoustic pipette for the rapid, sensitive, and user-friendly detection of biomolecules. The fNACPs are decorated with biorecognition motifs for the specific capture of target biomarkers from whole blood, and the acoustic pipette contains an acoustofluidic trapping channel in which fNACPs are robustly trapped and rapidly separated from whole blood. Using this system, we demonstrate the detection of an antibody biomarker from whole blood at picomolar levels. Finally, in a separate project, we present a multiplexed fNACP assay for the simultaneous detection of multiple biomolecules from single samples, as well as a high-throughput, siphon-based multichannel acoustic separator for the simultaneous separation of fNACPs from multiple samples. Overall, the findings presented in this dissertation provide numerous advancements in the fields of particle-based biomolecule detection, acoustofluidics, and electrokinetics, among others.

"What I want to talk about is the problem of manipulating and controlling things on a small scale"

–Richard P. Feynman, 1959

"So do I"

–Cooper P. Thome, 2024

Dedication

To my parents, Paul and Laurie Thome.

Acknowledgments

My progression to and through graduate school would not have been possible without the contributions of so many people. I am certain I cannot express my gratitude to the extent that I would like, but here's a (very informal and short) shot at it:

First, I would like to thank my Ph.D. advisor, Dr. C. Wyatt Shields IV. Your guidance, support, and expertise have been nothing short of transformative for me, and you have helped me to accomplish things that I never could have anticipated when I first started at CU. If nothing else, your impact on me is evidenced by my extensive use of "e.g." and "i.e." in my writing, which I got from you very early on in grad school. You have been excellent at motivating me to accomplish stellar work, but have always done so in a thoughtful, balanced manner. You are exceptionally bright and kind, and I greatly admire that you never fail to congratulate and celebrate the achievements of members of the lab. I am so proud to be a founding member of the lab, and I cannot wait to see what you accomplish in the future. I know that as I move forward in my career, you will continue to serve as one of my main role models.

Thank you to the members of my lab – I have been so fortunate to work alongside such smart, funny, and kind people. An especially big shoutout to Dr. Nicole Day – starting the lab and working through grad school together as been such a pleasure. I'm glad that my mere presence seemed to miraculously resolve so many of your issues in lab, because I certainly owe you for all that I have learned from you. To all the lab members, thank you for the laughs, support, and conversations over the years. I genuinely cannot imagine a better group of people to work with. While I'll be sad to leave the lab, I know its future is bright in your (and Wyatt's) hands.

I would also like to thank a great number of mentors, coworkers, and collaborators that have contributed to my growth and development as a researcher and person. First, thank you to Dr. Greg O'Dea and other members of the Honors College at UTC – becoming a member of the Brock Scholars Program was transformative for me and was one of the first things that initiated

my path toward graduate school. Thank you to the late Dr. Frank Jones, with whom I first began chemical engineering research and who motivated me to pursue research opportunities that, at the time, I thought were out of my reach. Thank you to Dr. Bradley Harris and Dr. Trevor Elliott, who both helped me to continue research in the face of difficulty and to honor Dr. Jones' legacy, even to a minor degree, through completing work he inspired. Thank you to my numerous mentors at Georgia Tech, including Dr. Elsa Reichmanis, Leslie O'Neill, and Nancy Healy. Thank you especially to Dr. Bailey Risteen – you showed me how exciting research can be. I was still uncertain whether I even wanted to do research when we met. After working with you, I was determined to pursue graduate school. Thank you to Dr. Lynn Rathbun and all of my mentors in Japan, including Dr. Guoping Chen and Yingjun Yang, as well as all of the other group members at NIMS. You were all part of one of the most memorable times of my life, and I will always cherish it. Thank you to Kathryn Mullins – working with you was so much fun, and I'll always look back on my experience at Chattem/Sanofi fondly. Thank you to my committee members, Dr. Ankur Gupta, Dr. Daniel Schwartz, Dr. Jennifer Cha, and Dr. Xiaoyun Ding, for helping me to progress as a researcher. Finally, thank you to all of my collaborators for your expertise and time. Together, we have invented and discovered some really fascinating, exciting things.

Thank you to all of the (at the time) undergraduate students I mentored over my time at CU. It was such an honor to teach each one of you, and none of the work in this dissertation would have been possible without your help. Thank you for your patience, dedication, and persistence as we navigated research problems together. I learned so much from each of you, and I consider working with you to be one of the most rewarding, enriching parts of my time at CU. I am genuinely SO proud to see each of you achieving such cool, impressive things now. As always, keep in touch and please reach out if there is any way I can help you in the future.

Thank you to my friends from all over. An especially big thanks to my friends from Boulder, including (in alphabetical order) Bryant Andres, Dan Bell, Grant Baumann, Jeremy Herman, Yuvee Fischler, Zach Baumer, Zack Blanchette, as well as their associated partners. Hanging out with you all provided much needed respite from the grind of graduate school, and I

am incredibly lucky to have you as friends. You're all awesome. The last 5 years of shredding, camping, Dark Horse, games, and general goofing around have been some of the best of my life.

A big thank you to Paula Pranda. My words will especially fail to adequately convey my thanks here. I feel lucky to even know you – you light up every room you're in. The last year of graduate school was especially challenging for me, and I would not have been able to navigate it without your continuous support, help, and company. I have so much more to say, but I'll do so elsewhere. In general, I just hope to always make you feel as loved and supported as you do me.

Finally, thank you to my family. To my father, Paul, and mother, Laurie, for their endless dedication to supporting our family members and their aspirations and interests. You two are, and will always be, my main role models. Dad, thank you for teaching me to be persistent and how to build things. Additionally, thank you for the bottomless supply of sandpaper. I used it for half of the projects in this dissertation. Mom, thank you for always being there for me, and, of course, thank you for being my first teacher. I don't know what your approach to homeschooling was, but it seems like it was pretty successful. To my siblings, Owen and Elise, thank you for supporting me and just being really cool people in general. I love you all so much!

Table of Contents

List of Tables

List of Figures

List of Appendix Figures

Chapter 1: Introduction

1.1 Biomolecule Detection

Detection of biomolecules, a process known as biosensing, is essential for a myriad of applications including patient diagnosis,[1] disease management,[2] and environmental monitoring.[3,4] While there exist a vast number of biomolecule detection approaches, all incorporate three main elements: a target biomolecule, or biomarker, being detected (e.g., small molecules, proteins, nucleic acids), a recognition element that specifically identifies the target biomolecule, and a transducer that converts biomolecule recognition into a measurable output signal.[4–6]

Design of biomolecule detection assays is a multifaceted challenge, and a great number of factors impact eventual assay performance, workflow requirements, and potential end-use cases. These factors include biomolecule target type (e.g., high molecular weight proteins >~60 kDa, small molecules < 1 kDA),[7–9] the type and content of the matrix from which the target is to be detected (e.g., blood, saliva, wastewater), and the type of biorecognition elements that can interact with the target (e.g., aptamers, antibodies),[10–12] among others. One of the predominant factors that influences both assay end use and workflow requirements is the signal that is transduced upon target recognition. Some of these signals (e.g., appearance of visible lines) are simple in nature and can be interpreted by the unaided eye, while others are too complex or subtle to be perceived without the use of additional equipment (e.g., minor changes in magnitude of fluorescence).[13]

While the utilized assay signal does not solely dictate the end-use applications of an assay, it does often influence the classification of the assay within two broad categories – qualitative or quantitative assays – that both hold distinct value for patient diagnosis and disease monitoring.[14,15]

Many qualitative assays benefit from user-friendliness, minimal points of error, and simple signal readouts that eliminate the need for complex instrumentation; however, they generally fail to enumerate biomarkers or detect rare (e.g., picomolar-level) analytes. For example, lateral flow assays (LFAs) are implemented widely for point-of-care (POC) testing due to their ease-of-use and simple signal readouts. LFAs often utilize gold colloid-conjugated recognition elements that can be immobilized in a defined region of a sample pad in the presence of target biomolecules, yielding a signal that can be easily analyzed by eye.[16,17] While convenient for rapid testing, LFAs typically cannot yield quantitative results, which lessens their usefulness in evaluating immune states on the individual and population-levels, among other applications.[18,19] Quantitative assays, however, have the capacity to provide numerical readouts that offer a more comprehensive understanding of patient conditions. Enzyme-linked immunosorbent assays (ELISAs) are considered the gold standard for quantitative biomarker detection due to their ability to provide high sensitivity and specificity; however, ELISAs entail numerous blocking, labeling, and washing steps that require significant user engagement for several hours.[20,21] As a result, this assay and others like it introduce multiple potential points of user-related error that can lead to false results; moreover, ELISAs necessitate the use of complex, expensive, and bulky instrumentation for both processing and measurement of the complex and subtle colorimetric signals generated during the assay, ultimately limiting the use of ELISAs to specialized laboratory settings.

1.2 Active and Responsive Particle-based Biomolecule Detection

Active and responsive colloidal particles convert energy in their surroundings to locomotion, either by locally dissipating energy to drive motion at small length scales, as is the case for active particles, or by responding to a global energy gradient, as is the case for responsive

particles.[22] Such active and responsive particles have found use in a multitude of applications, including drug delivery,[23–26] cell manipulation,[27–29] flexible electronics,[30–32] and cargo transport.[33–37] These particles can be propelled by various energy sources, including magnetic,[38–43] acoustic,[24,44–46] and electric fields,[33,47–50] as well as catalytic reactions.[51–55] In recent years, researchers have developed numerous approaches to detect biomolecules using both active, responsive, and inactive nano- and microparticle-based systems.[56–59] Compared to traditional, non-particle-based biomolecule detection assays, such as ELISAs, particle-based assays can enhance the detection of biomolecules by improving sample mixing, reducing required sample volumes, and imparting additional assay tunability.[21,60,61] These assays are generally classified by their output signal, with the most commonly demonstrated classes being electrochemical and optical; thus, signals generated by recognition events often manifest as changes in electrical signal,[62,63] solution color,[61,64] or fluorescence.[52,65] Because these signals require complex or nonstandard equipment for signal measurement (e.g., ultraviolet-visible spectrophotometers,[61] fluorimeters[65]), systems that generate easily measured signals are of great interest for both point-of-care and laboratory-based assays.

To simplify detection assay signals, relative to those of electrochemical or optical biosensing approaches, a handful of groups have demonstrated active-particle-based systems in which biomolecule concentration is correlated with particle motion using optical microscopy,[51,66,67] mobile phone imaging,[68,69] or direct visualization by colorimetric analysis.[70] Despite these advancements, in a majority of the motion-based detection approaches developed thus far, biomolecule concentration and motion are only indirectly linked, and the capture or presence of the target biomolecule does not innately lead to signal production. Instead, use of additional components such as enzymatic,[70] antibody-based,[67,68] or metallic labels[51,66] are required

to produce a change in motion. Introduction of these additional components inherently complicates systems by introducing new modes of failure and necessitating extra steps that increase assay time.

A number of particle-based technologies have also been developed to simplify workflows of quantitative assays that utilize complex signals. For example, magnetic bead-based separation is often employed to capture and isolate molecules and cells from complex samples for downstream analysis and detection.[71,72] However, this approach can involve long separation times (i.e., multiple minutes before wash steps), is not easily scalable, and is prone to particle loss during particle wash steps, ultimately resulting in the loss of target molecules.[73–75] Other bead-based technologies, which sometimes also utilize magnetic beads for sample separation, enable multiplexed assays in which a range of biomarkers can be detected simultaneously.[76,77] This simplifies biomolecule detection workflows by reducing the number of assays that must be run to characterize a given sample, but the assays typically still require extensive user engagement and complex processing involving specialized equipment.

1.3 Dissertation Overview and Aims

This dissertation focuses on engineering microparticle systems to drive advancements in biomolecule detection approaches by simplification of signal transduction and reduction of assay processing requirements. More specifically**, the overall objective of this dissertation was to leverage 1) electrokinetic active particle systems to explore novel forms of label-free, simplified signal transduction and 2) acoustic-responsive microparticles and acoustofluidic devices to simplify workflows associated with the processing of quantitative biomarker detection assays.** These goals were addressed through the following aims:

Aim 1. Investigate novel forms of signal transduction using active particles

Aim 1.1. Investigate induced-charge electrophoresis (ICEP) of functional particles for biosensing (Chapter 2)

Aim 1.2. Employ dielectrophoresis (DEP)-based techniques to study the effects of surface modifications on induced-charge electroosmotic (ICEO) flows and the ICEP of functional particles (Chapter 3)

Aim 2. Design of a particle-based, acoustofluidics-enabled assay for simplified biosensing processing (Chapter 4)

Aim 2.1. Design of functional negative acoustic contrast particles (fNACPs) for the capture of biomolecules

Aim 2.2. Design of a handheld acoustic pipette system for rapid fNACP assay processing

Aim 3. Design of a high-throughput acoustofluidic system for simple, multiplexed biosensing (Chapter 5)

Aim 3.1. Design of a multiplexed fNACP assay for the simultaneous detection of multiple biomolecules

Aim 3.2. Design of a high-throughput multichannel acoustic separator for the simultaneous processing of multiple samples

1.4 Chapter Summaries

The following chapters detail four projects that address Aims 1-3, presented above. Chapter 2 addresses Aim 1.1 and details the preparation and use of induced-charge electrophoretic microsensors (ICEMs) for the rapid, simple, and label-free detection of biomolecules. The ICEMs are composed of polystyrene and gold Janus particles functionalized with antifouling coatings and biomolecule-specific recognition elements. In an applied electric field, the ICEMs propel by ICEP. Upon capture of biomolecules, the speed of ICEM propulsion decreases, enabling microscopy-based biomolecule detection. In this chapter, we show that the specific capture of biomolecules leads to direct signal transduction through ICEM speed suppression at concentrations as low as 0.1 nM.

Chapter 3 addresses Aim 1.2 and details the development and use of dielectrophoretic polarizability measurement (DPM) as a method to determine the effects of surface modification on induced-charge electroosmotic (ICEO) flows. We propose the use of DPM in combination with theoretical models of complex ICEO-based systems as an approach to both predict and study the mechanisms of surface modification-induced changes to the behavior of these complex systems. By combining this method with a theoretical framework to model the speed of Janus particles travelling by ICEP, we investigate the mechanisms by which biomolecule-induced ICEM speed suppression, discussed first in Chapter 2, occurs.

Chapter 4 addresses Aim 2 and details the development of a novel class of acoustic-responsive particles, referred to as functional negative acoustic contrast particles (fNACPs), that are modularly modified with antifouling polymers terminated in biorecognition motifs for the specific capture of biomolecules. After capture, biomolecule targets can be labeled *in situ* by fluorescent secondary antibodies for detection by fluorescence measurement. Chapter 4

additionally details the development of a handheld acoustic pipette, which contains an acoustofluidic trapping channel for the rapid purification of fNACPs to enable their separation from complex biofluids like whole blood. We demonstrate use of the fNACP assay and acoustic pipette to achieve sensitive and streamlined biomolecule detection from whole blood in under 1 hour and 15 minutes. To demonstrate toward-point-of-care use of this system, we additionally show the development and use of a custom fluorimeter for benchtop analysis of the fNACP assay.

Chapter 5 addresses Aim 3 and shows further development of the fNACP assay, presented in Chapter 4, by fluorescently barcoding the fNACPs and creating a multiplexed fNACP assay for the simultaneous detection of multiple biomolecules from single samples. We additionally demonstrate the development of a high-throughput multichannel acoustic separator for the simultaneous separation of fNACPs from multiple samples. Like the acoustic pipette presented in Chapter 4, the multichannel acoustic separator in Chapter 5 utilizes acoustofluidic trapping for the rapid purification of fNACPs from complex fluid samples. However, unlike the acoustic pipette, the multichannel acoustic separator was designed for laboratory-based workflows, rather than point-of-care implementation. We show that all fluid flow through the separator is driven by a microfluidic siphon in order to eliminate the need for fluid pumps and characterize the use of the separator for the processing of multiple sample types. Finally, we show use of the fNACP assay and multichannel acoustic separator for the sensitive and high-throughput detection of biomolecules from whole blood.

In addition to the projects that address Aims 1-3, presented in Chapters 2-5, this dissertation includes discussion of fundamental research that was not directly motivated by the advancement of biomolecule detection techniques. This additional project focused on the fundamental

investigation of the motion of multiparticle Janus particle assemblies, which display a rich array of motion types when propelled by ICEP. This work is presented in Appendix A.

The projects presented in this dissertation generated numerous advancements in the fields of particle-based biosensing, acoustofluidics, and electrokinetics, among others. Beyond this, they serve as foundations for exciting future research and inventions. Chapter 6 details the major findings of the projects presented in Chapters 2-5, as well as the advancements they may enable.

Chapter 2: Electrokinetic active particles for motion-based biomolecule detection

Previously published as: Thome, C. P.; Hoertdoerfer, W. S.; Bendorf, J. R.; Lee, J. G.; Shields, C. W. I. Electrokinetic Active Particles for Motion-Based Biomolecule Detection. *Nano Lett*. **2023**, 23 (6), 2379–2387. https://doi.org/10.1021/acs.nanolett.3c00319. All supplementary media may be obtained at the source of publication.

2.1 Abstract

Detection of biomolecules is essential for patient diagnosis, disease management, and numerous other applications. Recently, nano- and microparticle-based detection has been explored for improving traditional assays by reducing required sample volumes and assay times as well as enhancing tunability. Among these approaches, active particle-based assays that couple particle motion to biomolecule concentration expand assay accessibility through simplified signal outputs. However, most of these approaches require secondary labeling, which complicates workflows and introduces additional points of error. Here, we show proof-of-concept for a label-free, motion-based biomolecule detection system using electrokinetic active particles. We prepare induced-charge electrophoretic microsensors (ICEMs) for the capture of two model biomarkers, streptavidin and ovalbumin, and show that the specific capture of biomarker leads to direct signal transduction through ICEM speed suppression at concentrations as low as 0.1 nM. This work lays the foundation for a new paradigm of rapid, simple, and label-free biomolecule detection using active particles.

2.2 Introduction, Results, and Discussion

Detection of biomolecules, a process known as biosensing, is essential for a myriad of applications including patient diagnosis,[1] disease management,[2] and environmental monitoring.[3,4] While there exist a vast number of biomolecule detection approaches, all incorporate three main elements: a target biomolecule, or biomarker, being detected (e.g., small molecules, proteins, nucleic acids), a recognition element that specifically identifies the target biomolecule, and a transducer that converts biomolecule recognition into a measurable output signal.[4–6]

In recent years, researchers have developed numerous approaches to detect biomolecules using both active and inactive nano- and microparticle-based systems.[56–59] Compared to traditional, non-particle-based biomolecule detection assays, such as enzyme-linked immunosorbent assays (ELISAs), particle-based assays can enhance the detection of biomolecules by improving sample mixing, reducing required sample volumes, and imparting additional assay tunability.[21,60,61] These assays are generally classified by their output signal, with the most commonly demonstrated classes being electrochemical and optical; thus, signals generated by recognition events often manifest as changes in electrical signal,[62,63] solution color,[61,64] or fluorescence.[52,65] Because these signals require complex or nonstandard equipment for signal measurement (e.g., ultraviolet-visible spectrophotometers,[61] fluorimeters[65]), systems that generate simplified and easily measured signals are of great interest. To this end, a handful of groups have demonstrated active-particle-based systems in which biomolecule concentration is correlated with particle motion using optical microscopy,[51,66,67] mobile phone imaging,[68,69] or direct visualization by colorimetric analysis.[70] Despite these advancements, in a majority of the motion-based detection approaches developed thus far, biomolecule concentration and motion are only indirectly linked, and the capture or presence of the target biomolecule does not innately lead to signal

production. Instead, use of additional components such as enzymatic,[70] antibody-based,[67,68] or metallic labels[51,66] are required to produce a change in motion. Introduction of these additional components inherently complicates systems by introducing new modes of failure and necessitating extra steps that increase assay time. To our knowledge, Zhang *et al.* are the only group to have developed a label-free, particle motion-based biosensing system.[78] However, their system was only shown to detect DNA and the assay required complex functionalization with five separate oligonucleotides and an enzyme to enable DNA capture and signal transduction.

Here, we present a simple, label-free, particle-based biomolecule detection system wherein the specific capture of target biomolecules directly influences particle speed. Specifically, we explore induced-charge electrophoresis (ICEP) of biomolecule-specific Janus particles, termed induced-charge electrophoretic microsensors (ICEMs), to directly link biomolecule concentration and particle motion. We functionalize gold-polystyrene (PS) Janus particles with biotin as a recognition element for the capture of a model target biomolecule, streptavidin (SA), and show that specific capture of SA by ICEMs leads to direct signal transduction in the form of ICEM speed suppression (Fig. 2.1A). Finally, by straightforward analysis of videos captured via optical microscopy, we show that ICEM speed decreases in a concentration-dependent manner (Fig. 2.1B). This work introduces a new paradigm for rapid, simple, and label-free active particle-based biomolecule detection. By tuning particle functionalization, we expect that this approach will provide a flexible platform to detect a broad range of biomarkers.

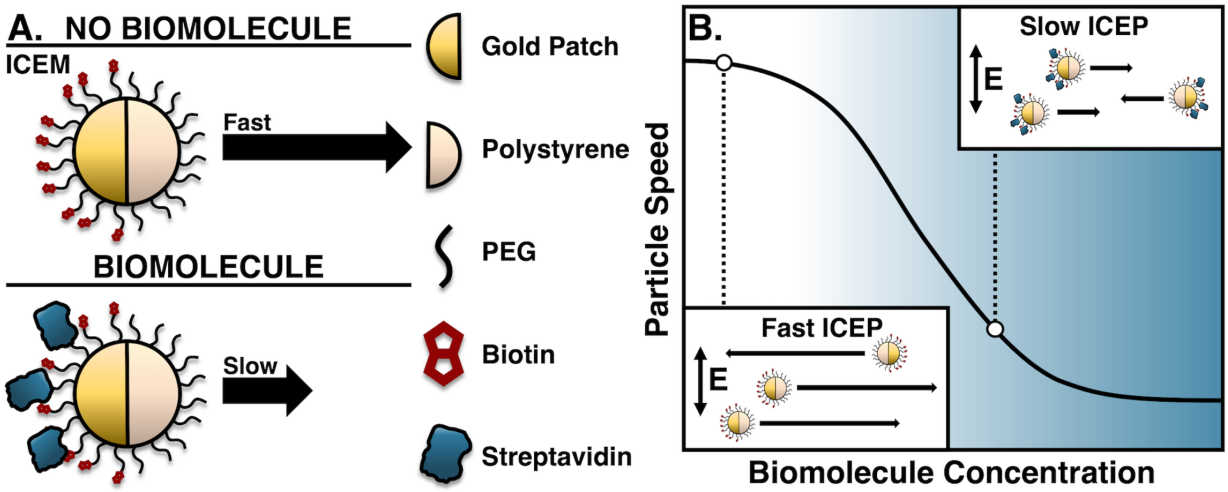

Figure 2.1. Overview of the ICEM-based biomolecule detection platform. A) Schematic representation of biomolecule detection by ICEMs. ICEMs are composed of polystyrene (PS) Janus particles with one gold-coated hemisphere. The PS side of particles is functionalized with polyethylene glycol (PEG) to reduce nonspecific adsorption of off-target matrix components and reduce particle-surface interactions. The gold hemisphere is functionalized with biotin recognition elements for capture of the model target biomolecule, streptavidin (SA). As more SA is captured by ICEMs, the electrophoretic speed of particles visually and quantifiably decreases. B) Schematic representation of the ICEM speed response with increasing biomolecule concentration.

ICEP refers to the process by which particles propel in an alternating current (AC) electric field due to asymmetric electroosmotic flows originating from a corresponding asymmetry in particle polarizability or geometry.[79] In the case of a spherical, metallodielectric Janus particle, ICEP stems from a disparity in the polarizability of each hemisphere of the particle: one metallic and highly polarizable, and one dielectric and weakly polarizable.[80,81] When a uniform AC field in the kHz frequency range is applied to a spherical Janus particle submerged within a liquid, the particle reorients by dielectrophoresis (DEP) such that the interface between the hemispheres aligns parallel with the field, yielding the largest possible induced dipole moment.[82] After reorientation by DEP, the applied field initially intersects perpendicular to the particle surface and ions in solution accumulate preferentially at the metallic hemisphere, yielding an induced charge cloud. At steady state, the induced charge cloud causes expulsion of the field lines parallel to the

surface, and fluid is drawn to the particle parallel to the field and ejected perpendicular to the field, away from the metallic hemisphere.[83] This asymmetric ejection of fluid leads to particle propulsion in the direction of the dielectric hemisphere.

Since the first experimental demonstration of ICEP of Janus particles,[82] numerous groups have performed fundamental studies on the ICEP of particles with different shapes[84–86] and patch geometries.[87–89] Beyond fundamental studies, Park and Yossifon demonstrated the ICEP of nonfunctional Janus particles for transportation of secondary functional cargo particles for biosensing applications,[90] yet no group has demonstrated the direct detection of biomolecules by ICEP to date. Interestingly, ICEP offers a unique approach for direct, label-free signal transduction. In earlier work, it has been shown that induced electroosmotic flows at a flat metal surface, analogous to those seen in ICEP of a Janus particle, can be affected by surface contaminants.[91] This arises from dielectric shielding of the polarizable surface as well as "buffering" of ions through surface reactions, both of which reduce the magnitude of the induced flows. This finding has been corroborated by others: Boymelgreen *et al*. showed that the speed of Janus particles coated with poly(L-lysine)-g-poly(ethylene glycol) was suppressed compared to that of uncoated particles due to shielding of surface charges.[92–94] Additionally, in a study of DEP of gold-PS Janus particles, Honegger and Peyrade showed that protein adsorbed on the gold hemisphere leads to dielectric shielding and a reduction in polarizability.[95] Thus, we hypothesized that specific capture of biomolecules of interest on the metallic surface of Janus particles may directly lead to measurable changes in their electrophoretic motion.

The most common type of Janus particle used in ICEP studies consists of a PS sphere and a gold hemispheric patch due to their large mismatch in polarizability.[82,87,92,96] Here, we used carboxylated PS as the base particle material to enable conjugation of aminated species. The

unfunctionalized Janus particles were prepared by a convective assembly-inspired approach.[97] In short, 5.1 μm carboxylated, red fluorescent PS particles were deposited in a submonolayer on glass slides to ensure that the particles did not overlap (Fig. 2.2A). Proper submonolayer deposition was confirmed via brightfield microscopy (Fig. B.1). The submonolayers of particles were then coated with 10 nm of chromium (Cr) and 30 nm of gold (Au) using electron beam evaporation. Particles were mechanically scraped from the slides and resuspended in pure milli-Q water (MQW), as high solution ion content has been shown to suppress ICEP.[82] We used both scanning electron microscopy (Fig. 2.2B and Fig. B.2) and fluorescence microscopy (Fig. B.3) to confirm that the metallic patch covered one hemisphere of the particles completely and that no irregularities in the patch shape were present. We noted that most particles (i.e., ≈ 95%) exhibited the expected patch shape.

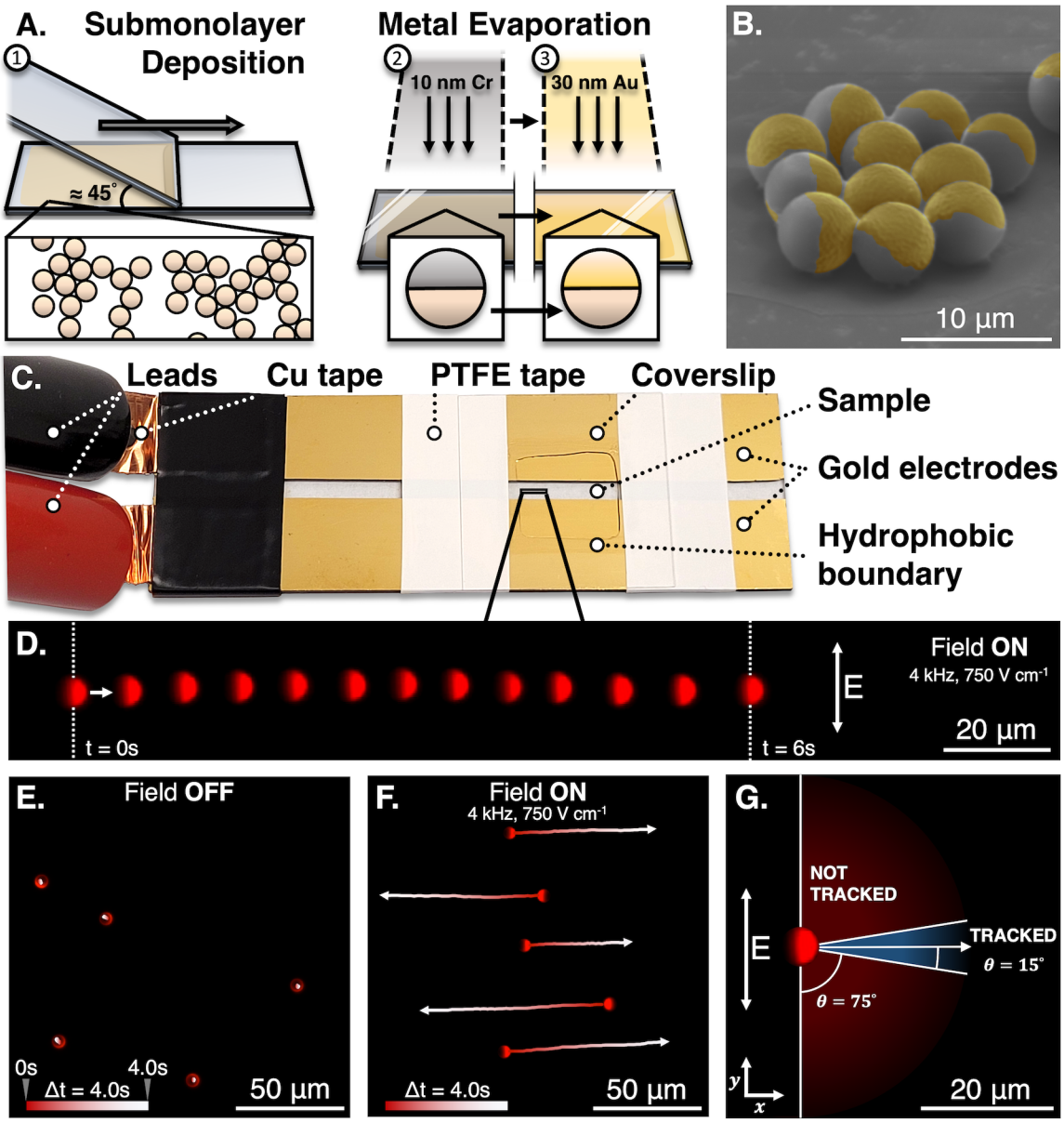

Figure 2.2. Electrokinetic Janus particle preparation, propulsion, and tracking. A) Schematic illustration of the Janus particle preparation process. PS particles are deposited on a glass slide in a submonolayer using a convective assembly method. Particles are then coated with chromium and gold using electron beam evaporation. Janus particles are then mechanically scraped off the glass slide and transferred to MQW. B) Representative scanning electron microscopy image of coated Janus particles. Yellow color was applied to highlight the location of gold patches on the particles, as indicated by visually rough surfaces. C) Image of a propulsion chamber. The sample of particles is placed between the two gold electrodes within a hydrophobic boundary and two PTFE spacers. After applying a coverslip, the aqueous particle sample spreads to the boarders of the hydrophobic boundary. An electric field is generated by applying an AC square wave from a function generator attached to the device by leads and copper tape. D) Superimposed images of a

single particle undergoing ICEP within a propulsion chamber over the course of 6.0 seconds. As is characteristic of ICEP, particles propel perpendicular to the applied electric field and in the direction of the PS hemisphere. The first frame of captured videos with the electric field E) off and F) on with superimposed particle paths over the course of 4.0 seconds. G) Schematic illustration of tracking criteria implemented in this study. Only particles that exhibited linear movement 0˚ ± 15˚ of normal to the applied field in either direction were tracked.

ICEP experiments are typically performed in chambers with either a sandwich electrode setup, in which planar electrodes (e.g., indium-tin oxide coated glass slides) are assembled on top of one another,[90,98] or in a coplanar electrode setup where two electrodes are positioned parallel on the same plane with a small gap separating them.[82,87] When metallodielectric particles undergo ICEP, they travel perpendicular to the applied field. As such, in the sandwich setup, particles undergoing ICEP can travel in any direction parallel to the electrode planes (i.e., in the x- and y-direction; coordinates shown in Fig. 2.2), whereas in the coplanar setup, particles only travel parallel to the edges of the electrodes (i.e., in the x-direction). Thus, coplanar devices can provide a more favorable environment for identifying particles propelling via ICEP rather than by other propulsion mechanisms, such as bulk fluid flow. Thus, we utilized coplanar electrode propulsion chambers for all experiments in this study. The chambers were fabricated by depositing 20–30 nm chromium and 100 nm gold on standard borosilicate glass slides masked with a thin strip of Kapton tape spanning the length of the slide; after metal deposition, the tape was removed to reveal the two electrodes (Fig. 2.2C). Leads were attached using conductive copper tape. During experiments, a hydrophobic pen was used to draw a small square outline overlapping the two electrodes, and two pieces of polytetrafluoroethylene (PTFE) tape were placed perpendicular to the electrodes at the boarder of the hydrophobic boundary. Finally, 10–20 μL of a particle sample (i.e., at ≈ 2.5×10^5 particles mL^{-1}) in MQW was pipetted onto the chamber within the boundary, and a coverslip was placed on top of the PTFE tape. A square wave (4 kHz for all experiments)

was applied to the chamber to generate the AC electric field (~500–1000 V cm^{-1}) within it. We evaluated chamber operation by loading a solution of unfunctionalized Janus particles into a chamber situated on a fluorescence microscope equipped with a camera. After applying a 4 kHz, 750 V cm^{-1} field, most Janus particles reoriented and exhibited linear propulsion parallel to the chamber electrodes. We used Fiji/ImageJ analysis software to determine mean particle speeds in the x-direction from captured videos. A representative time lapse image of a single particle undergoing ICEP is shown in Fig. 2.2D. This motion is clearly distinguishable from Brownian motion (Fig. 2.2E), and multiple particles can be tracked in a single video (Fig. 2.2F). During experiments, we observed that some particles did not travel parallel to the chamber electrodes, and instead were biased toward one electrode or exhibited helical trajectories. The presence of these modes of propulsion likely indicates that some particles had defects in their shape or in the shape of the gold patch.[99] To eliminate such cases from our analysis, we implemented tracking criteria and strictly tracked the speeds of particles travelling within 15˚ parallel to the edges of the electrodes at the water-coverslip interface (Fig. 2.2G). The tendency for particles to rise to this interface during reorientation arises at least partially due to DEP forces, but their linear motion once at the interface is strictly due to ICEP.[82]

When designing a biomolecule detection assay, it is crucial to minimize matrix effects, as they may interfere with the assay and lead to false results.[100] We speculated that nonspecific adsorption of proteins or other molecules to either hemisphere of the ICEMs could potentially influence their electrophoretic motion. To minimize nonspecific adsorption, we designed the ICEMs to include a polyethylene glycol (PEG)-based antifouling layer on the PS hemisphere as well as between the gold hemisphere and biotin recognition element.[101] To form the antifouling layer on the PS hemisphere, we conjugated 1 kDa PEG-amine to the particles using carbodiimide

coupling.[102] In short, Janus particles were mixed in a solution of 1-ethyl-3-(3-dimethylaminopropyl)carbodiimide (EDC) and 1 kDa mPEG amine in 2-(N-morpholino)ethanesulfonic acid (MES) buffer for 2 hours at room temperature (Fig. 2.3A). As other PEG-containing molecules have been shown to affect ICEP,[92] we assessed the impact of this layer on particle ICEP. To do so, we washed the PEG-modified particles with MQW and completed tracking experiments to measure particle speed as described earlier. Interestingly, we found that the addition of a PEG layer on the PS side of particles increased particle speed from 12.8 to 15.8 μm s^{-1} (Fig. 2.3B). This moderate increase in speed is unlikely to originate from changes in the asymmetric polarizability of the particles, as PEG and PS have similar polarizabilities as dielectric materials.[95,103] Instead, we speculate that this increase in speed is due to decreased interactions between the particles and glass substrate, as tracked particles were located along the water-coverslip interface.[104]

To functionalize ICEMs for biorecognition, we selected biotin as a model recognition element and streptavidin (SA) as a model biomarker. Biotin is a small molecule while SA is a large (~52.8 kDa) protein,[105] both of which have precedence as models in biosensing assays.[90,106] To impart antifouling properties to the gold hemisphere of the particles, we integrated an antifouling layer by binding the biotin recognition element to the gold through a PEG linker; notably, this PEG linker is also expected to allow more favorable biotin orientations to enhance SA capture, relative to surface-bound biotin.[107] However, we speculated that increasing distance between the captured biomolecule and gold hemisphere may reduce signal transduction. Thus, the length of this PEG linker was selected such that biomolecules would be captured and held, at most, ~6.3 nm from the gold hemisphere.[108] To functionalize the gold hemisphere of the particles, we mixed PEG-modified particles in a solution of 1 kDa biotin-PEG-thiol (BPT) and 3 mM

ethylenediaminetetraacetic acid (EDTA) in phosphate-buffered saline (PBS) overnight. As modification to the gold hemispheres of the particles may lead to changes in the electrophoretic motion of ICEMs, we functionalized particles using a range of BPT concentrations and assessed particle speed after washing into MQW. We found that increased concentrations of BPT did not lead to any significant change in propulsion speed (Fig. 2.3C). Because we observed no significant changes between binding conditions, we selected the 10 mg mL^{-1} BPT concentration as our standard functionalization condition to maximize the amount of BPT conjugated to the gold surface.

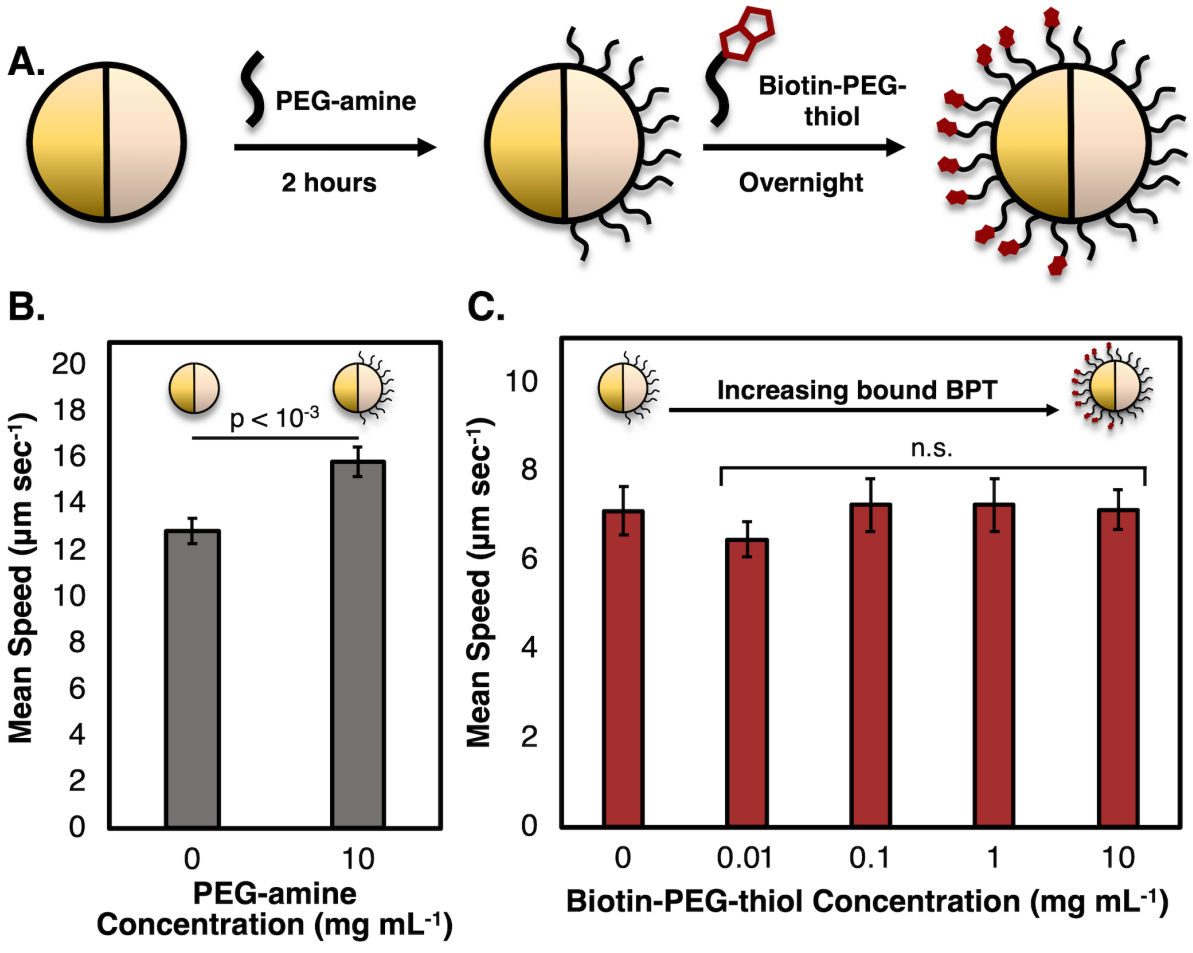

Figure 2.3. ICEM functionalization and speed characterization. A) Schematic representation of the ICEM functionalization protocol. Blank Janus particles are incubated in a solution of PEG-

amine and EDC in MES buffer for 2 hours, during which PEG-amine is covalently bound to carboxyl groups on the PS surface through carbodiimide coupling. Particles are washed 3–4 times, resuspended in a solution of biotin-PEG-thiol, and mixed overnight, enabling the coupling of biotin-PEG-thiol through thiol-gold bonding. B) Mean speed of ICEMs without and with bound PEG on the PS hemisphere. Particles with PEG displayed greater speeds, relative to those without ($N > 25$ for both conditions). C) Mean speed of ICEMs with PEG identically bound to the PS hemisphere and incubated with increasing concentrations of BPT. All particle samples, including the control, were incubated in PBS and washed into MQW four times, with only concentration of BPT in the PBS solution differing between groups. No condition led to significantly different speeds compared to that of the control ($N > 25$). Error bars in B) and C) indicate standard error of the mean.

To assess the detection performance of the ICEMs, we conducted SA capture assays over a range of SA concentrations. In short, we functionalized ICEMs with PEG on the PS hemisphere and PEG-biotin on the gold hemisphere as described earlier. After conjugation, the particles were washed four times into 1X PBS. Then, $2.5x10^5$ ICEMs were removed from the ICEM solution and resuspended in 100 μL of solutions of Alexa 594-conjugated SA in PBS over the range of 0 to $2x10^4$ nM SA and allowed to incubate while mixing at room temperature for 30 minutes. After incubation, the particles were washed into MWQ, placed in a propulsion chamber, and tracked as described earlier (Fig. 2.4A). ICEM movement was substantially suppressed for all SA conditions, and significantly differed ($P < 0.05$) from that of the control above 1 nM SA (Fig. 2.4B). Above 100 nM, additional increases in SA concentration did not further suppress particle movement below a ~46% maximum reduction in speed. Experimental data was fit to a 4 parameter logistic curve (4PL), commonly used to fit experimental data from biosensing assays such as ELISA.[109] Representative particle tracks from both the control (0 nM SA) and the maximum SA concentration ($2x10^4$ nM) demonstrate the clear visual difference between speed of particles incubated with or without SA (Fig. 2.4C). The modest variability in recorded speeds for a given SA condition may have originated from inhomogeneities in functionalization or differences in

particle size and patch morphology not observed during studies. Minimization of these sources of deviation should be a target for future implementation of ICEMs.

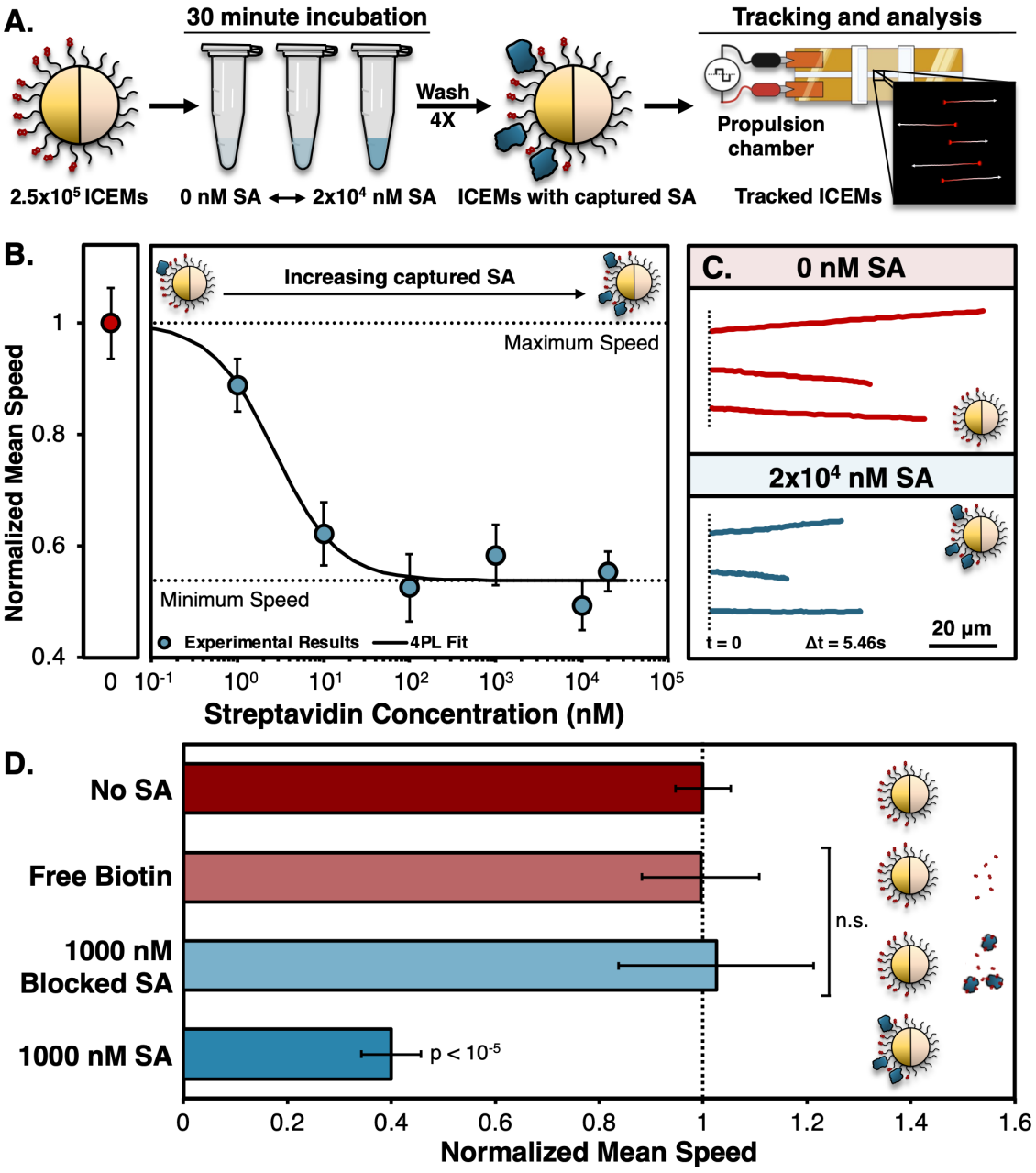

Figure 2.4. ICEM biomolecule detection studies. Schematic representation of the biomolecule detection protocol. ICEMs are incubated for 30 minutes in solutions spiked with SA and are subsequently washed four times. Particles are then placed in the propulsion chamber, positioned on a camera-equipped microscope, and the electric field is engaged. Captured videos are analyzed

to quantify mean particle speeds. B) Normalized mean ICEM speeds after incubation with SA-spiked solutions with concentrations ranging from 0–2x104 nM SA. A decrease in particle speed was observed at 1 nM SA, though this decrease was not significant ($P = 0.08$). All data points above 1 nM SA differed significantly from the control (0 nM SA). Particles reached their minimum speed at 100 nM. Experimental data was fit to a 4PL curve model to generate a curve fit ($N > 21$ for all conditions). C) Representative path tracks of three ICEMs each from both the control (no SA) and 2x104 nM SA conditions. Tracks indicate both x- and y-positions over 5.48 seconds. D) Normalized mean speed of particles incubated in 1000 nM SA ($N = 5$), as well as no SA ($N = 11$), 1000 nM blocked SA ($N = 5$), and free biotin ($N = 7$) as controls. The speed of particles incubated with 1000 nM SA was significantly lower than that of the control conditions ($p < 10\text{-}5$ relative to the 0 nM SA control). Error bars in B) and D) indicate standard error of the mean.

To confirm that the observed decrease in ICEM speed was due to specific capture of SA rather than nonspecific adsorption, we functionalized ICEMs as described earlier. We then blocked a solution of SA by incubation with a ~500-fold molar excess of free biotin. We diluted the blocked SA to 1000 nM in PBS. We then incubated $2.5x10^5$ ICEMs with PBS, 1000 nM SA in PBS, 1000 nM blocked SA in PBS, and an equimolar solution of free biotin in PBS, relative to that of the blocked SA solution. After incubation, particles were washed and tracked as described earlier. We found that neither ICEMs incubated in free biotin nor ICEMs incubated in blocked SA exhibited decreased speeds relative to the control, but that those incubated in 1000 nM SA exhibited a significant decrease in particle speed (Fig. 2.4D). These results indicate that decreases in ICEM speed are specifically due to the capture of SA rather than nonspecific adsorption.

To evaluate the potential of the ICEMs to detect alternative target biomolecules, we tested their ability to sense the protein ovalbumin (OVA) using antibody recognition. To facilitate this assay, we functionalized ICEMs with PEG on their PS hemispheres as described and anti-ovalbumin immunoglobulin G (anti-OVA IgG) on their Au hemispheres (Fig. 2.5A) as recognition elements for OVA. We incubated $2.5x10^5$ anti-OVA ICEMs with 0 and 1.1 μM OVA in PBS for 30 minutes while mixing at room temperature. After incubation, particles were washed and tracked

as described earlier. We found that the anti-OVA ICEMs incubated with OVA exhibited a significant decrease in propulsion speed relative to the control without OVA. This result is noteworthy, as the use of antibodies as ICEM recognition elements substantially increases the breadth of potential detectible targets and thus the potential diagnostic value of ICEMs.

In addition to detecting other biomolecules, we hypothesized that the sensitivity of the assay could be improved by reducing the number of ICEMs per sample, therefore increasing the ratio of target biomarkers to particles (Fig. 2.5C). To test this hypothesis, we compared the assay performance at a low SA concentration (i.e., 0.1 nM) using both the standard number (i.e., $2.5x10^5$) and a 25-fold-reduced number of ICEMs (i.e., $1x10^4$). In addition to evaluating the speed of ICEMs not incubated with SA, we determined the speed of ICEMs incubated with 0.1 nM bovine serum albumin (BSA) as a control for specificity. We found that the speed of ICEMs incubated in SA at the standard ICEM number did not differ significantly from that of the control, but that using the reduced ICEM amount yielded a significant decrease in ICEM speed (Fig. 2.5D). Thus, the sensitivity of the assay can be conveniently tuned by adjusting the number of ICEMs. Furthermore, no significant decrease in speed was observed for particles incubated with BSA. This provides further evidence that the antifouling PEG layers prevent nonspecific adsorption of proteins, a promising result for future use of ICEMs in more biologically relevant fluids.

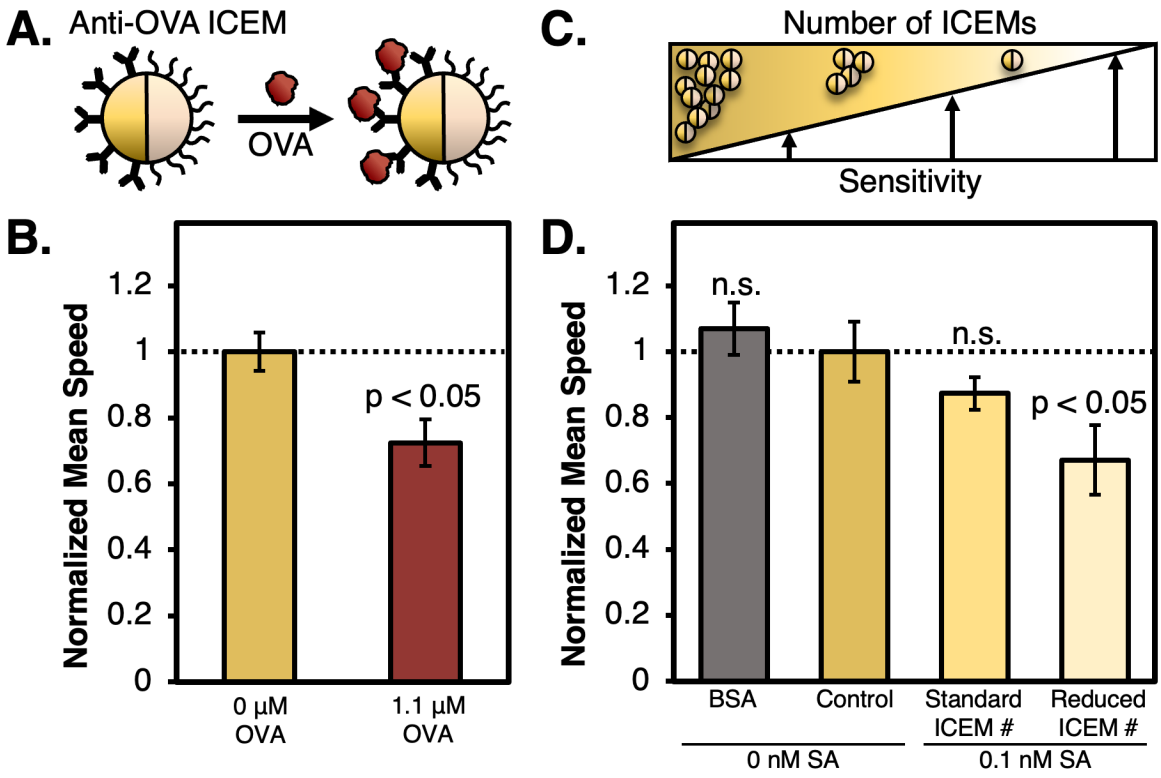

Figure 2.5. Programmability of the ICEM-based assay to capture alternative biomolecules through antibody recognition and enhance sensitivity through reduced particle concentration. A) Schematic representation of the capture of OVA by anti-OVA ICEMs. B) Normalized mean speed of ICEMs incubated in 1.1 µM OVA (N = 12) compared to a 0 µM OVA control (N = 10). The speed of anti-OVA ICEMs incubated with OVA was significantly lower than that of the 0 µM OVA control ($p < 0.05$). C) Schematic representation of assay tunability by varying ICEM number. As the number of ICEMs per sample decreases, sensitivity increases by increasing the concentration of SA on the surfaces of particles. D) Normalized mean speed of ICEMs incubated in 0.1 nM SA at standard ($2.5x10^5$) and reduced ($1x10^4$) ICEM numbers (N = 14 and N = 6, respectively) as well as no SA (N = 7) and 0.1 nM BSA (N = 15) as controls. The speed of ICEMs incubated in 0.1 nM SA at the reduced ICEM number was significantly lower than that of the 0 nM SA control ($p < 0.05$). Error bars in B) and D) indicate standard error of the mean.

In summary, we have demonstrated the use of ICEP of functional metallodielectric Janus particles, ICEMs, as a means of simple and label-free biosensing. In doing so, we have shown the first example of ICEP as a mechanism of signal transduction for specific biomolecule detection. We functionalized ICEMs with an antifouling PEG layer and biotin recognition elements for the

capture of SA and showed that decreased ICEM speed occurred only with specific capture of SA. Moreover, a continuous decrease in mean particle speed was observable from 1–100 nM SA when using $2.5x10^5$ ICEMs per sample, likely due to increased dielectric shielding of the gold patch. We also showed that ICEMs can be functionalized with antibody recognition elements for the capture of different protein biomolecule targets, which will be advantageous in future implementations of ICEM-based assays for detecting physiologically relevant biomolecules. Finally, we showed that sensitivity can be enhanced by reducing the number of ICEMs used in the assay by achieving a 10-fold lower detection (0.1 nM SA) by using $1x10^4$ ICEMs per sample.

Relative to traditional assays, such as ELISA, which can require several hours to complete, the ICEM-based assay requires only ~1 hour to yield results. Moreover, by coupling biomolecule concentration to particle motion detected from an optical microscope and eliminating the need for fluorimeters, ultraviolet-visible spectrophotometers, or other complex measurement systems, ICEMs enhance assay accessibility. The simple functionalization of, and direct signal transduction by, ICEMs also significantly reduces potential points of error that exist in the vast majority of particle and particle motion-based assays. Beyond current benefits, there are ample opportunities to further expand upon the performance and applications of the demonstrated ICEM-based assay. Thanks to the simple recognition element conjugation approach, the presented ICEMs could be easily tuned for recognition and capture of a range of biomolecules of interest by conjugating aptamers, antibodies, or other recognition elements to the gold hemisphere of the particles. Future investigation of the specific mechanisms by which signal transduction occurs would broaden possible applications of the ICEMs. In particular, this may enable expansion of the range over which signal transduction occurs or allow for transduction to occur at lower concentrations of biomolecules, further increasing the sensitivity of the ICEM-based assay. This future work will

explore the limit of detection and specificity of the ICEMs to more established biosensing methodologies. The assay could additionally be multiplexed for simultaneous detection of a panel of biomolecules by production of shape- or color-barcoded ICEMs, each with unique biomolecule specificities. Finally, by automating ICEM propulsion and tracking or integrating the assay into a mobile phone-based detection system, time to results could be decreased substantially, expanding accessibility and simplicity of the ICEM-based biomolecule detection system.

2.3 Methods and Materials

2.3.1 Janus particle preparation.

Janus particles were prepared by electron-beam evaporation of chromium (Cr) and gold (Au) onto a submonolayer of 5.1 μm red fluorescent carboxyl polystyrene (PS) particles (Magsphere). To prepare the submonolayer, two borosilicate glass slides were cleaned and dried with acetone (Millipore Sigma). The substrate slide was mounted horizontally on the immobile portion of a GenieTouch syringe pump (Kent Scientific), while the deposition slide was mounted on the moving portion of the pump connected to the driveshaft. The deposition slide was brought into contact with the stationary slide at a roughly 45˚ angle. The particles were washed four times into milli-Q water (MQW) to remove surfactants and concentrate the solution to 10 wt.%. After briefly sonicating and vortexing the particle solution, 10 μL was pipetted onto the substrate slide at the point of contact with the deposition slide, forming a thin, uniform line across the contact line between the slides. The syringe pump was set to the full position for a 30 mL Becton Dickinson syringe, and the deposition slide was pushed across the substrate slide at a rate of 2.5 mL min^{-1} until the deposited particle solution was exhausted approximately halfway across the deposition slide. This corresponded to an ejected volume of ~13 mL, as indicated by the syringe pump. The

deposition slide was then cleaned to prevent particle buildup after which the slides were once again brought into contact slightly past where the previous deposition ended. This procedure was repeated to fill the slide. Slides with submonolayers were then coated with a 10 nm layer of Cr for increased metal patch adhesion and a 30 nm layer of Au using an electron-beam evaporator (Edwards Auto 306 Cryo). Coated particles were then removed from their slides by gently scraping with a metal spatula, resuspended in MWQ, and transferred into a microcentrifuge tube. Finally, particles were sonicated for 30–60 seconds to separate particle aggregates.

2.3.2 Janus particle/ICEM washing.

To wash Janus particles/ICEMs, they were first resuspended in MQW or PBS with 0.02 vol.% polysorbate 20 (Tween 20, Sigma Aldrich) to aid in pelleting and subsequently centrifuged at 10,000xG for 6 minutes. The 0.02 vol.% Tween 20 was excluded only when washing particles into pure MQW immediately before i) submonolayer deposition or ii) propulsion experiments. Particles were typically washed 3–4 times between experimental steps.

2.3.3 Conjugation of mPEG-amine to Janus particles.

Janus particles were functionalized with PEG on their PS hemisphere using carbodiimide coupling. Typically, $5x10^6$ Janus particles were resuspended in 110 μL of 10 mg mL^{-1} methoxypolyethylene glycol amine (mPEG-amine, 1 kDa, Alfa Aesar) in 0.05 M 2-(N-morpholino)ethanesulfonic acid monohydrate (MES, MP Biomedicals) buffer (pH = 5.0) containing 100 mg mL^{-1} 1-ethyl-3-(3-dimethylaminopropyl)carbodiimide hydrochloride (EDC, Chem Impex). This solution was then incubated for 2 hours at ambient temperature in a VorTemp 56 shaking incubator (Labnet) at 900–1100 rpm. The particles were occasionally redispersed if

settling was noted. At the end of the incubation time, the solution was washed 3–4 times with 1X phosphate buffered saline (PBS, VWR Life Science) with 0.02 vol.% Tween 20.

2.3.4 Conjugation of biotin-PEG-thiol to Janus particles to prepare ICEMs.

To conjugate biotin-PEG-thiol (BPT, 1 kDa, Biopharma PEG) to the Au hemisphere of the Janus particles, $5x10^6$ Janus particles with PS-conjugated PEG were resuspended in 110 µL of a solution of 10 mg mL^{-1} BPT in PBS with 3 mM ethylenediaminetetraacetic acid (EDTA, Sigma) at pH = 8. This solution was incubated overnight at ambient temperature in a shaking incubator at 900–1100 rpm. At the end of the incubation time, the solution was typically washed three times in MWQ with 0.02 vol.% Tween 20. With this step, the ICEMs were fully functionalized.

2.3.5 Anti-ovalbumin thiolation.

A 1 mg mL^{-1} solution of thiolated anti-ovalbumin (anti-OVA, rabbit anti chicken OVA IgG, BioRad) in PBS with 3 mM EDTA (pH = 8.0) was prepared by first diluting 100 µL of a stock 5 mg mL^{-1} anti-OVA solution with 400 µL of 3 mM EDTA in PBS. Then, following recommendations from the manufacturer, the solution was passed through a 10 mL Zeba spin desalting column (7K molecular weight cut-off, Thermo) to transfer the antibody to a pure solution of 3 mM EDTA in PBS. Then, 23 µL of a 1.4 mM solution of Traut's reagent (2-iminothiolane, Thermo) was added to 500 µL of the 1 mg mL^{-1} antibody solution. The resultant solution was incubated at ambient temperature for 1 hour. After incubation, excess Traut's reagent was removed from the protein solution by means of an additional Zeba spin column, yielding a 1 mg mL^{-1} solution of thiolated anti-OVA in PBS with 3 mM EDTA.

2.3.6 Conjugation of anti-OVA to Janus particles to prepare anti-OVA ICEMs.

To conjugate thiolated anti-OVA to the Au hemispheres of the Janus particles, $5x10^5$ Janus particles with PS-conjugated PEG were resuspended in 10 μL of a solution of 0.1 mg mL^{-1} thiolated anti-OVA in PBS with 3 mM EDTA. This solution was incubated at ambient temperature for 2 hours in a shaking incubator at 760 rpm. After incubation, the solution was washed thrice with 0.02 vol.% Tween 20 in PBS. With this step, the ICEMs were fully functionalized for capture of OVA.

2.3.7 Capture by ICEMs.

Streptavidin (SA), Alexa Fluor 594-conjugated SA (Invitrogen), OVA, or free biotin (D-(+)-biotin, Research Products International Corporation) was diluted with PBS to 100 μL at the desired concentration, depending on experimental requirements. Then, $2.5x10^5$ ICEMs were resuspended in the SA solution and allowed to incubate at ambient temperature for 30 minutes in a shaking incubator at 900–1100 rpm. At the end of the incubation time, each condition was washed 3–4 times with MQW, after which each ICEM condition was resuspended in 200–500 μL MQW.

2.3.8 SA blocking.

To create a blocked SA control, free biotin was dissolved in DIW and added to a solution of SA in a roughly 500-fold molar excess. The solution was then allowed to incubate for 75 minutes.

2.3.9 Coplanar propulsion chamber fabrication.

To fabricate coplanar propulsion chambers, borosilicate glass slides were masked with a roughly 2 mm paper or adhesive tape mask that covered the length of the slides. Then, electron-beam evaporation was used to deposit 20–30 nm Cr and 100 nm Au on the masked slides. After removal of the mask, the roughly 2 mm uncoated gap in the center of the slide along its length remained, with two electrodes on either side. Two strips of copper tape were applied on top of the Au electrodes to form connection points for electrical leads.

2.3.10 ICEM propulsion experiments.

The coplanar devices were washed thoroughly with acetone before each experiment. A hydrophobic barrier pen (IHC World) was used to draw a roughly 1.25 cm x 1.25 cm square outline overlapping the two electrodes. Two pieces of polytetrafluorethylene (PTFE) tape (RS Crum & Company) were placed perpendicular to the electrodes at the boarder of the hydrophobic boundary, leaving a small rectangular space between them. 10–20 μL of Janus particles or ICEMs were pipetted onto the small space left between the PTFE tape spacers and the Au electrodes, and a coverslip was placed over the sample and spacers. Then, the entire apparatus was placed on a Zeiss AxioVert A1 TL/RL inverted fluorescence microscope equipped with a Axiocam 305 mono camera (Zeiss, Germany). An Agilent 33210A waveform generator (Agilent) was attached to a Tegam 2340 high voltage amplifier (Tegam), from which electrical leads were attached to the copper tape affixed to the propulsion chamber electrodes. A 4 kHz square wave alternating current (AC) signal was generated, amplified, and applied to the propulsion chamber, forming an electric field with magnitudes that ranged from 500–1000 V cm^{-1}. Resultant particle motion was observed

and recorded using the microscope camera, typically in fluorescence mode using a 120 W mercury lamp (Excelitas), 545/25 nm excitation filter, and 605/70 nm emission filter (Zeiss).

2.3.11 Particle speed analysis.

Videos of ICEMs undergoing ICEP captured during experiments were analyzed using ImageJ software. Videos were exported as AVI files while maintaining the native micron/pixel ratio and relative time information. Using ImageJ, each frame was converted to a binary image in a stack, and individual particle positions in each frame were extracted by use of either the "analyze particles" or "Trackmate" options in the software. The linear speed of each particle was then calculated using this extracted data. Only speeds of ICEMs that traveled linearly within 15˚ of normal to the Au electrodes were recorded and analyzed.

2.3.12 Four parameter logistic fitting.

ICEM speed data from 0–2x10^4 nM SA, shown in Figure 2.5B of the main text, was fit with a four-parameter logistic (4PL) curve to visualize ICEM responses and determine the maximum and minimum response values. To do so, we fit experimental data to the standard 4PL equation, given by:

$$y = b + \frac{a - b}{1 + \left(\frac{x}{c}\right)^d} \tag{2.1}$$

where y is ICEM speed, x is SA concentration, c is the mid-range concentration, d is the slope factor, and a and b are ICEM speed or response at the minimum and maximum SA concentrations, respectively. MATLAB was used for all fitting. Extracted parameter values were a = 11.51 μm

sec^{-1}, b = 6.20 μm sec^{-1}, c = 2.70, and d = 2.18. Using these values, we established a roughly 46% decrease in ICEM speed at the maximum SA concentration tested.

2.4 Author Contributions

The manuscript was written through contributions of all authors, and all authors have given approval to the final version of the manuscript.

2.5 Acknowledgements

The authors thank Dr. Ankur Gupta for helpful discussions.

Chapter 3: Dielectrophoretic polarizability measurement for the study of electrokinetic active particles

The contents of Chapter 3 will be submitted as a manuscript in Fall of 2024. Coauthors on this manuscript will include Alanna R. Duarte (co-first author), Wren S. Hoertdoerfer, Caroline R. Praetzel, Alec Pellicciotti, Dr. Ankur Gupta, Dr. Michael A. Bevan, and Dr. C. Wyatt Shields IV. C.P.T. led experimental sample preparation and modification, experimental setup, and analysis of ICEP data with the help of coauthors. A.R.D. led analysis of DEP data with the help of coauthors. Dr. Ankur Gupta devised the theoretical framework for prediction of ICEP speed. The contents of Chapter 3 were written from the joint effort of C.P.T. and A.R.D.

3.1 Abstract

Induced-charge electroosmosis (ICEO) is a robust approach to drive microfluidic flows by application of electric fields across polarizable surfaces and has been used extensively for object manipulation, microfluidic pumping, and active particle propulsion, among other applications. While ICEO in pristine systems is well characterized, surfaces in real systems are often modified or contaminated by complex molecules, and it is not well-understood how and to what extent these molecules impact ICEO flows. Here, we introduce dielectrophoretic (DEP) polarizability measurement, DPM, as a method to experimentally determine effects of surface modifications on the polarizability of surfaces in systems that leverage ICEO. The method utilizes DEP trapping of probe particles that replicate the surface modifications of complex physical systems. By analysis of the equilibrium motion of trapped probe particles and use of a core and shell model, individual

contributions to the effective polarizability of probe particles by surface modifications may be identified. This DPM-generated polarizability data can then be used to both predict theoretical effects of modifications on ICEO in various complex systems and reveal instances in which changes to system behavior are governed by mechanisms unrelated to modification-induced polarizability changes. Here, we validate this method by comparison with experimentally observed changes to the speed of Janus particles travelling by induced-charge electrophoresis (ICEP), which arises from asymmetric ICEO flows around micron-scale particles. We show that DPM enables prediction of a decrease in particle speed upon protein capture by silica-gold Janus particles modified with polyethylene glycol (PEG) and biotin-PEG-thiol. We additionally reveal that experimentally observed increases in the speed of polymer-modified Janus particles are likely governed by effects unrelated to changes to particle polarizability. Overall, this work lays the foundation for broader implementation of DPM, which could be key for future design of ICEO-based systems or for the study of complex ICEO-based phenomenon.

3.2 Introduction

Induced-charge electroosmosis (ICEO) is a commonly utilized approach for driving fluid flows via application of electric fields across polarizable surfaces. ICEO has been implemented in a number of microfluidic and colloidal systems for a range of applications, including microfluidic pumping and mixing,[110,111] object manipulation,[112–114] and active particle propulsion.[115–117] Though the general theory describing ICEO flows is well established, it fails to accurately describe the complexity of real systems;[117,118] in many applications of ICEO, surfaces are often modified to meet design criteria (e.g., for antifouling) or otherwise come into contact with contaminants (e.g., polymers, proteins, and small molecules) from complex fluids.[119–121] Many studies have examined how the ion concentration,[122,123] solution rheology,[119,124] or other properties of the surrounding fluid can impact ICEO,[117] but fewer have examined how surface-bound or surface-adjacent molecules influence ICEO. It is known that the presence of contaminants on polarizable surfaces can impact these induced flows,[125] though such effects have received little attention in literature and the mechanisms by which surface-adjacent molecules influence ICEO are not fully defined. Finally, while the theoretical effects of solid dielectric coatings on ICEO have been described,[118] it remains a challenge to predict the effect of complex surface modifications or contaminants on ICEO, and there exists no standardized approach to do so.

One increasingly prevalent implementation of ICEO flows, induced-charge electrophoresis (ICEP), leverages asymmetric ICEO flows around micron-scale particles to enable particle transport for cargo manipulation,[126,127] complex micromotor motion,[128–130] and biosensing.[90,131] These asymmetric ICEO flows stem from a corresponding asymmetry in the polarizability of the particle, as is characteristic of Janus particles composed of a spherical dielectric material with one hemisphere coated with a metal. In previous work, we modified the surfaces of such particles with

polymers for the purposes of biomolecule detection.[131] Upon capture of protein, the Janus particles exhibited decreased ICEP propulsion speeds, enabling microscopy-based biomolecule detection. We hypothesized this decrease in speed originated from dielectric shielding of the metallic hemisphere of the particles by captured proteins, resulting in diminished ICEO flows about the metallic hemisphere, which is supported by related findings in literature.[125,132,133] However, this hypothesis could not be explicitly tested due to lack of established methods for measuring such effects on complex microparticle systems.

In this work, we introduce dielectrophoretic (DEP) polarizability measurement, or DPM, as an approach to experimentally measure the polarizability of modified surfaces and subsequently theoretically predict effects of surface modifications on ICEO flows. While existing characterization techniques, such as zeta potential measurements, can inform linear electro-osmotic flows for the classical, or 'fixed charge', electrokinetic picture arising from innate material surface charge, this method aims to more directly probe and predict the effects of the induced dipole on a polarizable material that drive nonlinear ICEO flows in a applied external field.[118] This method makes use of positive and negative DEP (pDEP and nDEP) trapping[134] of surface-modified probe particles that replicate more complex physical systems to enable measurement of modification-induced changes to the effective polarizability of material surfaces. This information generated from DPM can then be used to theoretically predict the impact of changes to material polarizability on ICEO flows emanating from similarly modified surfaces in more complex systems, as well as to identify behaviors that are not predominantly mediated by changes to polarizability. While the DPM method could be applied to study a range of ICEO-based systems by simply adjusting the theoretical model employed post-DPM measurement, we elected to study the ICEP of differentially modified Janus particles to experimentally validate the DPM method.

Studying ICEP offers both i) the ability to modify particles using methods identical to those used during modification of probe particles and ii) a simple microscopy-based approach for the measurement of resultant particle motion and, indirectly, the underlying changes in ICEO flows. Thus, we produced six distinct types of Janus particles by modifying their surfaces with various combinations of polyethylene glycol (PEG), biotin-PEG-thiol (BPT), and the protein streptavidin (SA). We then propelled each of the differentially modified Janus particle types by ICEP and characterized their motion to observe effects of these surface modifications. To conduct DPM characterization, we produced five types of probe particles with surface modifications comparable to those of the Janus particles and determined resultant particle polarizability characteristics by DEP manipulation and analysis of DEP tracking data for each probe particle type. Compared to other methods used to assess particle DEP properties such as velocity-based measurements[133] or DEP force measurements using optical tweezers,[135] the method used to assess particle polarizability here achieves sensitive and specific measurement of the dipole-field interactions driving DEP. We then used a core and shell model to determine the individual contributions of each surface modification to the changes in probe particle polarizabilities. Finally, we devised a theoretical model that utilizes DPM-generated polarizability data to predict the speeds of surface-modified Janus particles travelling by ICEP (Fig. 3.1). We found that the DPM-based theoretical predictions agreed with experimentally observed decreases in ICEP motion upon capture of proteins by surface-modified particles. These results support the hypothesis that the presence of protein directly contributes to changes in ICEO flows by alteration of the effective polarizability of metallic surfaces. We additionally found that, while modifications to the metallic hemisphere by polymers were theoretically predicted to decrease ICEO flows and resultant motion, experiments instead revealed an increase in ICEP speed. This suggests that mechanisms unrelated

to changes in surface polarization are at play in the studied ICEP system, and we hypothesize that the increase in ICEP motion arises in part from decreased particle-surface interactions in experiments. Overall, we expect the DPM method to be impactful for predicting and studying the effects of complex surface modifications on the performance of a range of systems that utilize ICEO for microfluidic pumping, mixing, and particle propulsion.

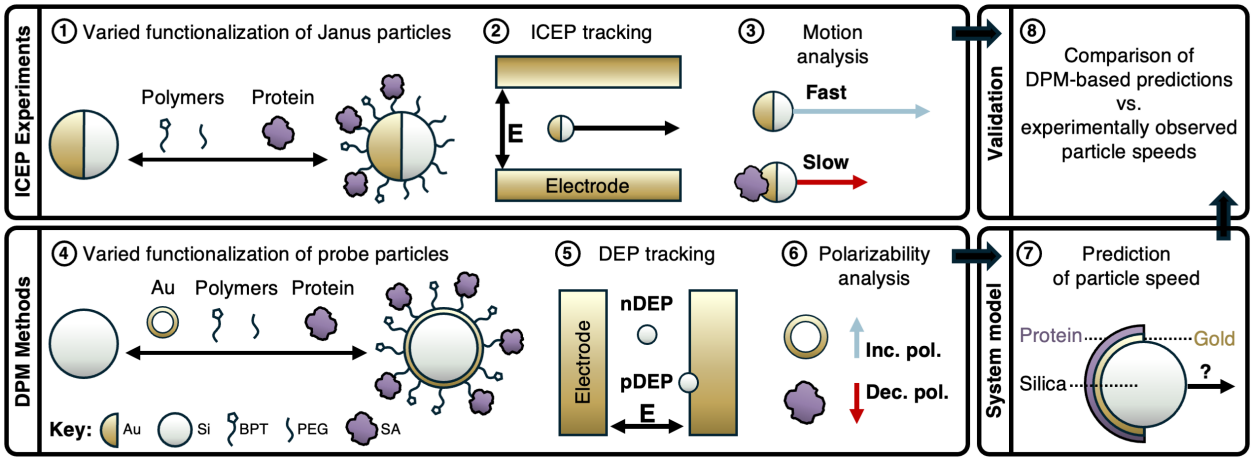

Figure 3.1 Study workflow. (1) Janus particle surfaces are modified with polymers (i.e., BPT or PEG) or protein (i.e., SA). (2) The modified Janus particles are propelled by ICEP and their resultant motion is recorded. (3) Recorded Janus particle motion is analyzed to determine effects of surface modification on particle motion. (4) The surfaces of probe particles are modified with Au, polymers, or protein. (5) The modified probe particles are trapped by DEP and their motion is recorded. (6) Recorded probe particle equilibrium motion is analyzed to determine surface modification-mediated changes to particle polarizability. (7) Information from 6 is used to predict flows and resultant motion of identically modified Janus particles using a theoretical framework. (8) Theoretical predictions from 7 are compared to experimental results from 3.

3.3 Experimental

3.3.1 Janus particle fabrication.

Janus particles were prepared as previously described.[128,131] Briefly, 2 μm commercial silica particles (Millipore Sigma) were washed 3X with milli-Q water (MQW) and concentrated to create a 10 wt.% solution of particles in MQW. The particles were then deposited in a

submonolayer on glass slides using a convective assembly approach. The submonolayers were then coated with 10 nm of chromium (Cr) and 30 nm of gold (Au) via electron-beam evaporation. The resultant Janus particles were removed from the substrate by gently scraping with a metal spatula, resuspended in MQW, and transferred to a microcentrifuge tube for storage. The particles were sonicated for ~30 s to separate aggregates before use.

3.3.2 Janus particle washing.

Particles were suspended in MQW or phosphate-buffered silane (PBS) (Research Products International) with 0.04 vol.% polysorbate 20 (Tween 20, Sigma-Aldrich) and centrifuged at 5,000xG for 1 minute. The supernatant was aspirated from the particle pellet, and the particles were again resuspended with wash solution. This process was typically repeated 2-3X.

3.3.3 Janus particle surface modification.

To modify the Au hemisphere of the Janus particles, the particles were incubated with a 10 mg/mL solution of 1 kDa BPT (Biopharma PEG) in 3 mM ethylenediaminetetraacetic acid (EDTA) (Sigma-Aldrich) in PBS (pH ~8) overnight at ambient temperature while mixing at 1200 rpm on a shaking incubator (VorTemp 56, Labnet). After incubation, the particles were washed into MQW. To modify the Si hemisphere of the Janus particles, the particles were incubated in a 10 mg/mL solution of 1 kDa mPEG-silane (Laysan Bio) in 10^{-4} M aqueous HCl (Sigma-Aldrich) overnight at ambient temperature while mixing at 1200 rpm. After incubation, the particles were washed into MQW. To functionalize Janus particles with both PEG and BPT, modification with BPT was performed first.

3.3.4 Incubation and capture of SA by Janus particles.

Approximately 10^6 particles were suspended in 400 μL of a 1000 nM solution of Alexa Flour 594-conjugated SA (Thermofisher Invitrogen) in PBS. The particles were incubated at 1200 rpm for 30 minutes at ambient temperature. After incubation, the particles were washed into MQW.

3.3.5 ICEP propulsion and recording.

To create a coplanar electrode chamber for ICEP propulsion, the center of a glass slide was masked with a 2 mm wide strip of Kapton tape along the long axis of the slide. Then, 10 nm Cr and 100 nm Au were deposited onto the slide via electron-beam evaporation. After metal deposition, the Kapton tape was removed to reveal two coplanar electrodes. Conductive copper tape was attached to each electrode to form a connection point for leads from a function generator. To prepare the propulsion chamber for each tracking experiment, a hydrophobic barrier pen (IHC World) was used to draw a small square between both electrodes, and two pieces of polytetrafluoroethylene (PTFE) tape (RS Crum & Company) were placed at the boarders of the hydrophobic barrier to act as coverslip spacers. The chamber was placed on a Zeiss Axiovert A1 TL/RL inverted fluorescence microscope equipped with a Axiocam 305 mono camera (Zeiss, Germany) and connected to an Agilent 33210A waveform generator (Agilent) and a Tegam 2340 high voltage amplifier (Tegam). 10 μL of solutions containing approximately $3x10^6$ particles mL^{-1} were pipetted into the hydrophobic square of the chamber, and a coverslip was placed on top of the PTFE spaces. Prior to use, coverslips were submerged and cleaned with 5% Decon90 in deionized water (DIW) overnight. The applied field frequency and strength for all experiments were 4 kHz and 750 V cm^{-1}, respectively. After application of the field, particle movement was

recorded for 60 s or more. The propulsion chamber was cleaned by wiping with an acetone-soaked tissue between experiments.

3.3.6 ICEP tracking analysis.

At least 30 individual Janus particles were tracked for each condition investigated, and particle position data was extracted from captured videos using the MTrack2 plugin found in standard Fiji/ImageJ software. MATLAB was used for all data processing. We used a custom code to plot position data and to calculate the total displacement of each particle within each particle condition, as well as the mean total displacement for each condition. All tracking data and plots can be found in Fig. C.1 and C.2 of the Supplementary Materials. Mean particle speed was determined by fitting all displacement data within a given condition by simple linear regression and subsequent extraction of the resultant slope. Significance between conditions was initially evaluated by analysis of covariance (ANCOVA) using the "aoctool" MATLAB function and significance between the speeds of paired conditions was evaluated via Tukey-Kramer tests using the "multcompare" MATLAB function.

3.3.7 Silica probe particle surface modification.

Silica probe particles were modified following a protocol identical to that used to modify the silica hemisphere of Janus particles. In short, 2 μm silica microparticles were washed into ethanol and subsequently pelleted. The particles were then resuspended in a 10 mg/mL solution of 1 kDa PEG-silane in 0.0001M aqueous HCl and allowed to mix overnight at ambient temperature and 1200 rpm. After incubation, the probe particles were washed into MQW.

3.3.8 Gold-shell silica probe particle surface modification.

Gold-shell silica probe particles were modified following a protocol identical to that used to modify the gold hemisphere of Janus particles. In short, 1 μm silica particles with a shell of 2-5 nm gold nanoparticles (Si-Au, NANOCS) were first washed into MQW. After pelleting, the particles were resuspended in a 10 mg/mL solution of 1 kDa BPT in 3 mM EDTA in PBS (pH ~8) and allowed to mix overnight at ambient temperature and 1200 rpm. After incubation, the probe particles were washed into MQW. Then, to ensure that the BPT-modified gold-shell particles best replicated the BPT and PEG functionalized Janus particles, the probe particles were resuspended in a 10 mg/mL solution of 1 kDa PEG-silane in 0.0001M aqueous HCl and allowed to mix overnight at ambient temperature and 1200 rpm. After incubation, the probe particles were washed into MQW.

3.3.9 Incubation and capture of SA by probe particles.

Approximately 10^7 particles were suspended in 1000 μL of a 1000 nM solution of Alexa Flour 594-conjugated SA in PBS to ensure the same SA area:particle surface area ratio as used in the incubation and capture of SA by Janus particles. The particles were incubated at 1200 rpm for 30 minutes at ambient temperature. After incubation, the particles were washed into MQW.

3.3.10 Flow cytometry for probe particle analysis.

Probe particle fluorescence was analyzed via flow cytometry (BD FACScelesta) after incubation with fluorescent SA. Particle solutions for each experimental condition were suspended

in PBS with 0.04 vol.% Tween 20. Data was analyzed by FlowJo (BD). Additional results and details can be found in Fig. C.3 and the Supplementary Materials.

3.3.11 Zeta potential measurements.

Each of the prepared probe particle types were resuspended in 1 mL of MQW. The samples were transferred to an Omega cuvette (Anton Parr) and zeta potential of each probe particle type was determined using a Litesizer 500 (Anton Parr).

3.3.12 DEP trapping and recording.

DEP trapping was performed using a coplanar interdigitated electrode (IDE) device (NanoSPR) comprised of electrodes 20 μm wide ($d_e = 20$ μm) separated by a gap of 20 μm ($d_g = 20$ μm). Electrical wires were soldered to the connection points at the ends of the electrodes to enable connection to a function generator. The trapping chamber was formed using a thin silicone rubber spacer (USA Sealing) with a ~4 mm hole in the center created by a biopsy punch to confine the liquid particle sample. Prior to each experiment, the electrode device and silicone spacer were washed with acetone and DIW, respectively. To prepare the chamber for a sample, the spacer was placed on the electrode device such that the IDEs were confined within the center spacer hole. The IDE device was then fastened to a custom 3D printed holder that enabled stabilized mounting of the device on the microscope stage (Fig. C.4). The same Zeiss Axiovert A1 TL/RL inverted fluorescence microscope equipped with a Axiocam 305 mono camera used for ICEP tracking was used for DEP tracking. The soldered wires were then attached to the function generator and 10 μL of a liquid particle sample with an approximate concentration of $5x10^5$ particles mL^{-1} suspended

in MQW was pipetted onto the electrodes within the silicon spacer and covered by a cover slip. The loaded sample was left to sit for at least 5 minutes to allow particles to settle to their approximate mechanical equilibrium height in the solution.[134,136]

After the initial 5-minute settling period, the function generator was used to produce a nonuniform electric field by application of a sinusoidal AC signal ($V_{pp} = 500$ mV, $E_0 = 250$ V cm^{-1}) at a set frequency within the range of 200 kHz – 5 MHz. Once the electric field was applied, the sample was left to sit for an additional 5 minutes to allow for particles to reach their approximate dielectrophoretic equilibrium position.[136,137] During this second waiting period, the electrode landscape was scanned using the microscope camera to find an area for optimal tracking. To determine an optimal tracking region, we considered the condition of the trapping electrodes and the number of trackable particles in view. Specifically, the trapping electrodes were inspected for any visible signs of damage, and we ensured at least 5 trackable particles were within the frame and within the viable electrode gaps. Particles that were visibly immobile at any point of the tracking were excluded as they were assumed to be adsorbed to the substrate and not exhibiting DEP motion.[138] Particles were also considered trackable if they were sufficiently far away from neighboring particles (i.e., >10 μm separation) for the duration of the tracking to avoid additional colloidal interactions that would affect DEP motion.[139] Following the second 5-minute waiting period, the DEP equilibrium motion of the set of particles in frame was recorded for 10 minutes. Device cleaning and preparation, sample loading, and DEP trapping including the settling periods were repeated at 10 frequencies (200, 315, 400, 630, 795, 1000, 1500, 2500, 4000, and 5500 kHz) for each probe particle type studied.

3.3.13 DEP tracking analysis.

2-12 particles were analyzed at each frequency for each probe particle condition investigated, based on the quality of the reported particle tracks. Similar to the tracking method used for ICEP, the MTrack2 Fiji/ImageJ plugin was used to extract electrode position and particle position data from the experimental videos. To improve contrast for precise particle localization for conditions producing low particle contrast (i.e., unmodified and modified Si-Au particles), a Difference of Gaussian (DoG) filter was applied to the videos prior to tracking. The Gaussian standard deviations used for filtering were $\sigma_1 = 5$ and $\sigma_2 = 5.1$.

3.3.14 Analysis of DEP data.

MATLAB was again used for all following data processing. First, particle tracks were normalized to their respective electrode gaps using position data from MTrack2. MATLAB's "histogram" function generated position-dependent sampling probability statistics from normalized particle trajectories. Using MATLAB's built-in binning algorithm, Scott's rule was used to determine histogram bin width and bin numbers for each data set.[140] For the cases in which the produced histogram displayed significant noise about the peak, bin widths were manually increased to effectively smooth the histogram and improve fitting. Boltzmann's equation was then used to transform this sampling probability histogram to a corresponding relative potential energy landscape within the electrode gap. Finally, the dielectrophoretic theoretical potential energy expression was calculated and fit to the experimental potentials to determine the Clausius-Mossotti factor, f_{CM}. After repeating this analysis at each frequency studied for a particular particle type and plotting f_{CM} as a function of applied field frequency, the effective particle permittivity was calculated by fitting the theoretical f_{CM} to the experimentally measured data points.

3.3.15 Estimation of individual contributions to permittivity.

To elucidate the individual permittivity contributions of each surface modification on a given probe particle (i.e., the last step of the DPM method), we followed a *smeared-out sphere* approach.[141] This is an iterative process in which the effective permittivity of any modified probe particle, which we measure through analysis of DEP data, can be decomposed into a sphere formed by concentric dielectric shells of permittivity ε_i. The equation for the effective complex permittivity of this multi-shell sphere with N shells is a function of the effective complex permittivity of a modeled homogenous *smeared-out* inner sphere (of $N-1$ shells) and the complex permittivity of the outer-most N^{th} shell. By deriving the real component of this complex expression, the permittivity contribution of each surface modification, ε_i, was determined by relating the measured real effective permittivity of a given probe particle to the measured real effective permittivity of the precursing probe particle and solving for the unknown permittivity contribution of the outermost shell.

3.3.16 Model for ICEP speed prediction.

Results from the DPM method described above were used to predict ICEO flows in our target model system and investigate predicted changes to these flows as a result of material polarizability changes. Established general nonlinear, first order electrokinetic theory was followed to derive expressions for the induced zeta potential and particle velocity,[118,142] with special consideration taken for the asymmetry in the azimuthal direction originating from Janus particle material asymmetry and additional contributions to the linearized potential drop across the

double layer as a result of surface modifications. This modelling approach is further described in the Results and Discussion section.

3.4 Results and Discussion

3.4.1 ICEP tracking and analysis.

To enable ICEP propulsion and Janus particle tracking, we prepared silica-based Janus particles by coating one hemisphere of 2 μm silica particles with Au. We additionally fabricated a coplanar electrode chamber on a standard glass slide to allow placement on an inverted microscope equipped with a camera (Fig. 3.2a). Janus particle samples were placed within a hydrophobic boundary drawn on the surface of the coplanar electrode chamber. The Au electrodes of the propulsion chamber were connected to a function generator and amplifier, which were used to apply a 4 kHz, 750 V cm^{-1} field to the particle samples in the chamber. After application of the field, Janus particle motion was captured by video recording. Upon analysis of particle position data, we noted that the silica-based Janus particles used in this study exhibited frequent tilting and reversals of direction (Fig. 3.2b). This frequent orientation change leads to complications in determining particle velocities, as particle orientation directly impacts particle speed in confined systems where particles undergo motion at solid-liquid interfaces.[143] To extract meaningful motion data, we therefore first determined the total displacement of recorded particles over time. Because we analyzed over 30 particles per condition, the mean displacement over time appeared linear for all conditions (Fig. 3.2c), as can be expected of a singular particle travelling in a straight line by ICEP. To determine the mean particle speed for each condition, we then fit all displacement data by simple linear regression and extracted the slope of the fit.

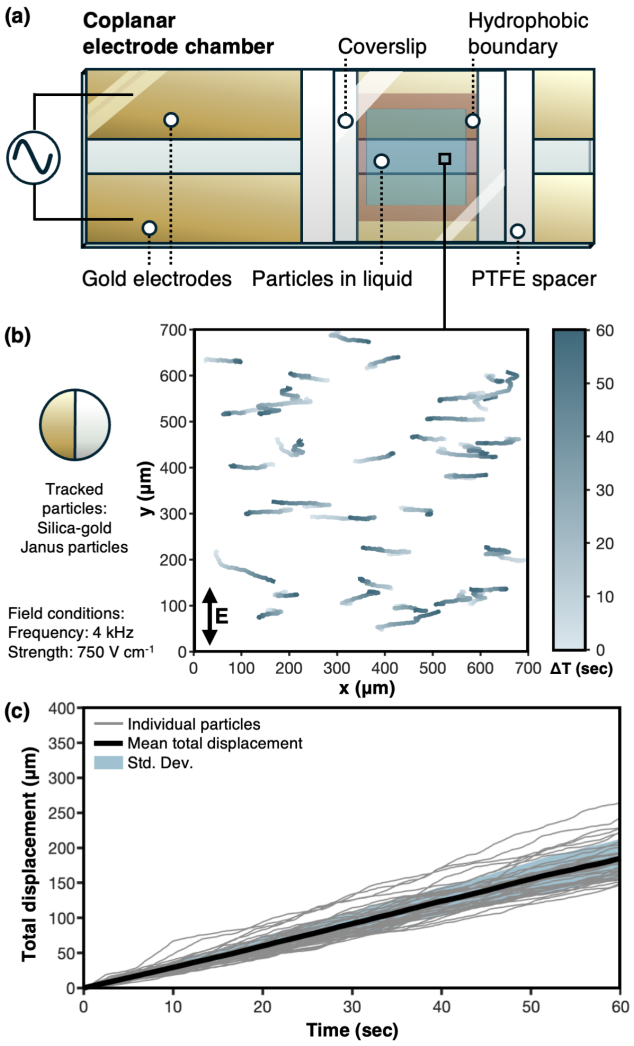

Figure 3.2. ICEP experimental methods and analysis. Schematic of the coplanar electrode propulsion chamber. **(b)** Exemplary particle tracks over the course of 60 s from propulsion of Janus particles modified with BPT on the Au hemisphere and PEG on the silica hemisphere. Particle tracks are compiled from multiple recordings. **(c)** Exemplary total displacement and average total displacement of tracked Janus particles from (b). Shaded region indicates standard deviation.

3.4.2 Surface modifications affect the ICEP of Janus particles.

In our previous work, we prepared induced-charge electrophoretic microsensors (ICEMs) which consisted of polystyrene-based Janus particles modified with PEG on the polystyrene hemisphere and biotin-PEG on the Au hemisphere; we found that, upon capture of SA, ICEM speed decreased.[131] To both validate the DPM method and further elucidate the origins of this

effect in this study, we prepared six surface-modified Janus particle sample types inspired by our previous work. Here, we elected to produce silica-based Janus particles. We selected PEG as the main silica surface modification, as it is commonly used as an antifouling agent in microfluidic and colloidal applications.[144] Finally, we chose to study the modification of Au surfaces by biotin-PEG and selected SA as a model protein; SA binds biotin with strong non-covalent interactions, which ensures attachment of protein to biotin-modified particle surfaces during experiments.[145] The six Janus particle sample types range from unmodified silica-Au Janus particles to silica-Au Janus particles modified with protein and multiple polymers (Fig. 3.3a). The specific particle types include: blank Janus particles (JPs), JPs with PEG on the Si hemisphere (JP-PEG), JPs with PEG-biotin on the Au hemisphere (JP-BPT), and JP-BPTs incubated with SA (JP-BPT-SA). We additionally produced JPs with PEG on the Si hemisphere and PEG-biotin on the Au hemisphere; these particles are functionally identical to ICEMs in previous work and are named as such here. Finally, we examined ICEMs incubated with SA (ICEM-SA).

Upon propelling the particles via ICEP (Fig. C.1, C.2) and subsequently extracting the mean particle speed for each condition (Table C.1), significance between conditions was determined by ANCOVA and post hoc Tukey-Kramer tests. Analysis of the speed of the various particles revealed trends similar to those previously observed. Relative to unmodified JPs, those with PEG on either or both hemispheres (JP-BPT, JP-PEG, and ICEM) displayed significantly greater speeds. This can likely be attributed to decreased interactions between the particles and the glass coverslip of the coplanar electrode chamber, the interface at which all particles were tracked.[132] This hypothesis is supported in part by the more substantial increase in particle motion when both hemispheres were modified with PEG (i.e., ICEMs); over the course of Janus particle tracking, both hemispheres regularly come into contact with the glass interface. Additionally, upon

incubation with SA, the particles demonstrated a significant decrease in particle motion, relative to their controls. This effect was most substantial between the ICEM and ICEM-SA conditions, which aligns with previous observations.

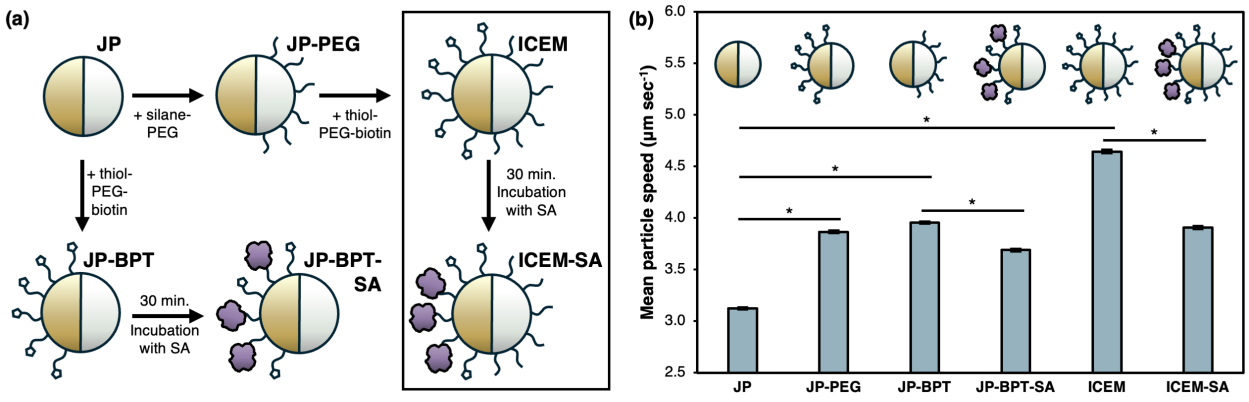

Figure 3.3. ICEP surface modification and motion results. (a) Schematic of the surface modification approach used to generate all six Janus particle types analyzed in the study. **(b)** Mean estimated speed of each Janus particle type. N > 30, *P<0.0005, error bars indicate STE of estimated slope from linear regression.

3.4.3 DEP tracking and analysis.

DEP refers to the electrokinetic phenomenon by which particles suspended in a nonuniform electric field undergo motion due to particle polarization and the resulting interaction of the dipole with the field gradient.[134,136] Changes to the degree of particle electric polarization can manifest as changes in the particle DEP response and equilibrium motion.[146] Here, we describe a method to assess modification-induced changes to the effective polarizability of surface materials by observation and analysis of the DEP equilibrium motion of probe particles with various surface modifications. By building upon a previously demonstrated method to sensitively measure the interaction between the induced dipole of a polarizable particle and the applied electric field,[134] we present DPM as a framework to leverage DEP to predict changes to ICEO flows in various

target systems. Tracking and analysis of DEP equilibrium behavior of particles allows direct and sensitive measurement of dipole-field interaction energies on the thermal energy scale whereas other methods, such as force measurements using optical tweezers, are limited by resolution.[135] Additionally, this method offers enhanced sensitivity to dipole-field interactions compared to dielectrophoretic velocity-based measurements as dissipative hydrodynamic forces present in such transport measurements increase complexity.[133]

When a nonuniform electric field is applied to a suspended particle, the particle moves by DEP in order to minimize the potential energy of the induced dipole.[134,136] The net potential energy for a single colloid suspended above a substrate in a nonuniform electric field can be expressed as the sum of the electrostatic interactions with the substrate, particle gravitational potential energy, and induced dipole-field interactions given by[134,147]

$$u^{net}(x,z) = u_e(z) + u_g(z) + u_{DEP}(x,z). \tag{3.1}$$

In the absence of an electric field, the particle will settle to a mechanical equilibrium height, h_m (Table C.2), by a balance between the electrostatic repulsion from the substrate, $u_e(z)$, and the gravitational potential energy, $u_g(z)$. Juarez et al. show that when the field is applied, the particles are confined within several hundred nanometers normal to the surface and excursions about the mechanical equilibrium height are minimal due to the strong forces acting in the z direction.[134] The induced dipole-field interactions described by,

$$u_{DEP}(x,z) = -2\pi a^3 \varepsilon_m f_{CM} E^*(x,z)^2 \tag{3.2}$$

solely contribute to measurable excursions in the x direction as a result of the dielectrophoretic force acting on the particle induced dipole, where a is the particle radius, ε_m is the permittivity of the medium, and $E^*(x,z)$ is the normalized electric field (Table C.2).[134,139] As such, the net 2D

potential energy can be projected onto the x dimension to obtain the effective potential in the x direction, where only the induced dipole-field potential energy is considered. Finally, as seen in Equation (3.2), the strength and direction of induced dipole-field interactions and the resulting DEP motion are dependent on the relative polarizable properties of the particle and the medium, embedded in the real component of the Clausius-Mossotti factor,

$$f_{CM} = Re\left[\left(\tilde{\varepsilon}_p - \tilde{\varepsilon}_m\right)/\left(\tilde{\varepsilon}_p + 2\tilde{\varepsilon}_m\right)\right] \tag{3.3}$$

where $\tilde{\varepsilon}_p$ and $\tilde{\varepsilon}_m$ are the complex permittivity values of the particle and the medium, respectively, expressed in the full form as

$$\tilde{\varepsilon} = \varepsilon - i\sigma/\omega\,, \tag{3.4}$$

and dependent on the conductivity, σ, and angular frequency of the applied field, ω.[136] In cases where $f_{CM} > 0$, the particle is more polarizable than the suspending medium and the potential energy of the induced dipole is minimized in the region of greatest field strength, located at the edge of the electrodes ($x = \pm d_g/2$). In cases where $f_{CM} < 0$, the suspending medium is more polarizable than the particle and the potential energy of the induced dipole is minimized at the electric field minimum, located at the center of the electrode gap ($x = 0$). Particle migration toward the location of the field maximum (i.e., when $f_{CM} > 0$) is known as positive dielectrophoresis (pDEP), whereas migration toward the location of the field minimum (i.e., when $f_{CM} < 0$) is known as negative DEP (nDEP). These locations are considered the lateral DEP equilibrium positions and the reference points, x_r, for the following analysis.

To experimentally assess the relative polarizable properties of probe particle types and the suspending medium, probe particles were manipulated by DEP and their equilibrium motion was analyzed. Particle samples suspended in MQW were pipetted into a rubber tracking chamber

fastened to confine the particle sample over an IDE array connected to a function generator (Fig. 3.4a). Once the probe particle sample had sufficient time to reach a mechanical equilibrium position,[134,136] an AC voltage of a fixed amplitude of 500 mV was applied to the electrodes oscillating at a single frequency between the range of 200 kHz – 5.5 MHz. Upon application of the field, particles moved via DEP to their respective equilibrium positions where potential energy is minimized, and sufficient time was allotted for particles to reach this position.[136,137] After this, we captured 10-minute videos of the equilibrium DEP motion of the probe particles. After analysis of these videos, individual particle position trajectories were normalized to their respective electrode gaps and plotted for all frames using individual particle tracking data and electrode positions (Fig. 3.4b). This position data was then used to generate histograms of particle position frequency. Experimentally, the precise theoretical lateral equilibrium position, x_r, indicated by the histogram peak location, may be impacted by distortions in the applied electric field caused by slight damage to or irregularities in the electrodes, which is commonly observed after repeated use and cleaning of the IDEs. To account for these slight experimental deviations and to maintain the integrity of the following analysis method, if needed, the particle positions were slightly shifted to align their peaks to the theoretical equilibrium position. The histogram was then converted to a relative sampling probability distribution by normalizing the histogram by the bin value at the reference point, x_r (Fig 3.4c).

The Boltzmann's equation, expressed as

$$\frac{u(x) - u(x_r)}{k_B T} = ln[p(x_r)/p(x)], \tag{3.5}$$

was used to transform the relative sampling probability distribution to a relative potential energy landscape between the electrodes (Fig. 3.4d), where k_B is Boltzmann's constant, T is absolute

temperature, and $x_r = 0$ for nDEP and $x_r = \pm d_g/2$ for pDEP.[134,147] The electric field in Equation (3.2) was evaluated at estimated reference heights of $z = h_m + a$ for nDEP and $z = a$ for pDEP[134] to obtain the theoretical effective potential in the x direction. From here, the relative theoretical potential energy (Equation (3.5)) was calculated and fit to the experimental values obtained from the transformation of relative sampling probability to relative potential energy to determine the f_{CM} for the studied particle at a single frequency. Nonlinear regression was used to fit the theoretical potential energy landscape to the transformed data, using f_{CM} as the only adjustable parameter (Fig. 3.4d). The above tracking and analysis was performed at 10 frequencies for each probe particle type to yield full experimental f_{CM} profiles over the frequency range of 200 kHz – 5.5 MHz. We did not explore the DEP motion of particles at frequencies lower than 200 kHz as to avoid interfering effects on the particle motion due to AC electroosmotic flows over the electrodes produced at lower frequencies.[136,148]

Finally, these individual f_{CM} profiles were used to determine the effective polarizability of each probe particle type by estimation of effective particle permittivity, ε_p. Using nonlinear regression and ε_p as the only adjustable parameter, Equation (3.3) was calculated and fit to the experimental profiles (Table C.2). The conductivity of the particle, σ_p, was calculated using an expression describing the conductivity of a dielectric sphere suspended in a dielectric medium considering the particle surface conductance (Table C.2).[149,150] The conductivity of the medium used for fitting, σ_m, was assumed to be 6.4 μS/cm which is on the order of what can be expected for water in the presence of ions from the conjugated materials or dissolved ions.[151] The effective particle permittivity for each probe particle type was determined and used to compare the effects

of each surface modification on particle polarizability, as described in the "Individual contributions of surface modifications to particle permittivity" section below.

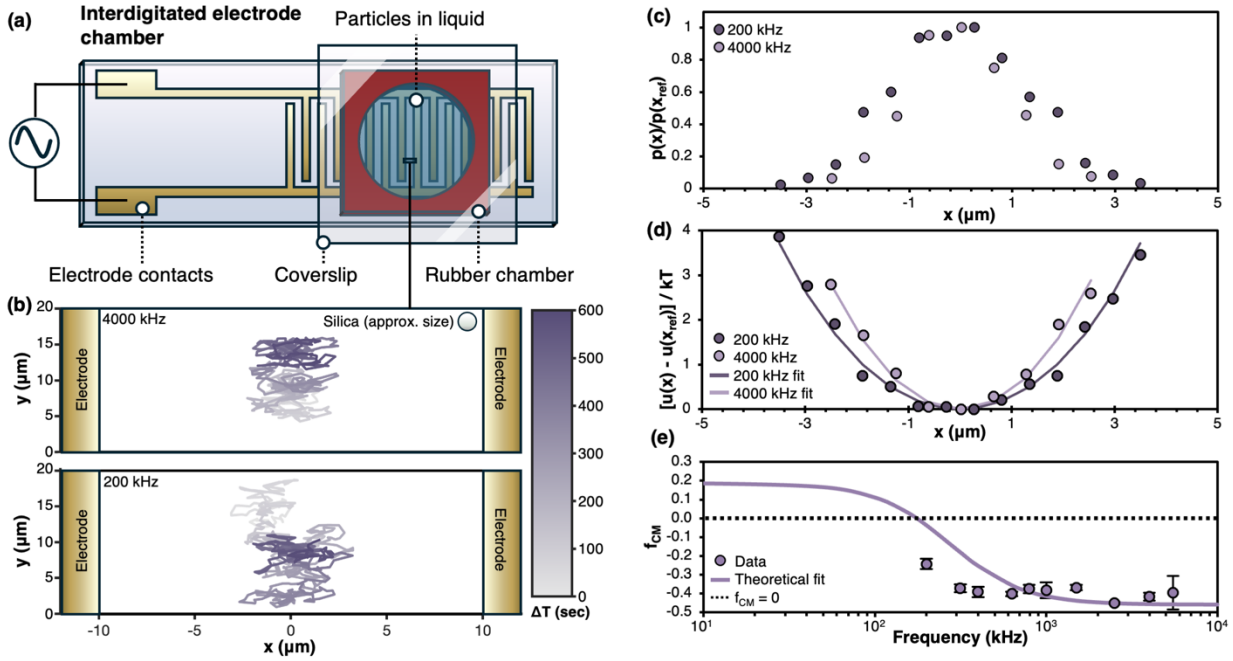

Figure 3.4. DEP experimental methods and analysis. (a) Schematic of the interdigitated electrode trapping chamber. **(b)** Exemplary particle tracks over the course of 600 s from trapping of blank Si probe particles at 4000 and 200 kHz. **(c)** Probability distribution of particles from (b). **(d)** Potential energy distributions of particles from b and c, obtained by Boltzmann inversion of data in (c). **(e)** f_{CM} of Si probe particles at each investigated frequency and theoretical fit over the range of 10^1-10^4 kHz. N = 2-12, error bars indicate standard error.

3.4.4 Probe particle surfaces can be modified for comparison with Janus particles.

To elucidate the individual effects of each surface modification on the polarizability – and resultant motion – of Janus particles, we evaluated five distinct probe particle types by DPM (Fig. 3.5a). These probe particles include blank silica particles (Si), Si particles with surface-bound PEG (Si-PEG), Si particles with a shell of Au nanoparticles (Si-Au), Si-Au particles with surface-bound biotin-PEG (Si-Au-BPT), and Si-Au-BPT particles incubated with SA (Si-Au-BPT-SA). All

surface modifications were completed with the same methods and conditions (e.g., reagent concentrations, incubation times) utilized for surface modification of the Janus particles. Because of this, we made the assumption that the modification characteristics, including grafting density of the polymers and surface coverage by SA, were identical for both the Janus particles and probe particles. However, it should be noted that, while the Au coating process forms a continuous Au layer on Janus particles, the Au-Si particles are coated with a shell of nanoparticles with diameters of 2-5 nm. Though the polarizability characteristics of these Au layers likely differ, we assume that their overall behavior in electric fields is similar enough to allow valid comparison between the probe particles and Janus particles. After modification of probe particle surfaces, we indirectly confirmed successful modification with PEG by flow cytometry (Fig. C.3). We further measured the zeta potential of all probe particle types for confirmation of surface modification and use in subsequent calculations. The zeta potential of Si-PEG (-40.6 ± 0.7 mV) particles differed substantially from that of Si particles (-51.7 ± 0.8 mV); as PEG is not a highly charged molecule, the decrease in magnitude of the zeta potential from Si to Si-PEG particles further indicates the presence of PEG on the particle surface. The zeta potentials of Si-Au-BPT and Si-Au-BPT-SA particles (-27.5 ± 0.6 mV and -27.0 ± 0.8 mV) were moderately more negative than that of the Si-Au particles (-23.7 ± 0.7 mV), again providing evidence of successful surface modification. Importantly, there was no significant difference between the zeta potential of probe particles with or without SA.

3.4.5 Surface modifications change polarizability properties of probe particles.

By measuring and fitting particle-field interaction potentials at 10 frequencies for each probe particle type, we were able to plot the frequency-dependent polarization behavior relative to

the suspending medium, f_{CM} vs ω (Fig. 3.5a, Fig. C.5, and Table C.3). We then estimated effective particle permittivity values as described earlier, allowing for direct comparison of the polarizability properties of the varied probe particle types (Fig. 3.5c).

Blank Si probe particles were measured to have the lowest effective particle permittivity of 1.94×10^{-11} F/m. The effective particle permittivity slightly increased upon the addition of PEG, and Si-PEG probe particles were measured to have an effective permittivity of 4.54×10^{-11} F/m. Si-Au probe particles exhibited the greatest measured effective particle permittivity of 4.12×10^{-10} F/m, as can be expected due to the highly polarizable gold shell around the particles. Measured effective particle permittivity further decreased with the addition of BPT and SA to the gold-shelled particles, where $\varepsilon_{Si\text{-}Au\text{-}BPT} = 2.00 \times 10^{-10}$ F/m and $\varepsilon_{Si\text{-}Au\text{-}BPT\text{-}SA} = 1.60 \times 10^{-10}$ F/m. These findings illustrate the sensitivity of this method to modification-induced changes in material polarizability.

3.4.6 Individual contributions of surface modifications to particle permittivity.

The final step in the DPM framework is to determine the effects of individual surface modifications on particle permittivity. To do so, we used a theoretical core and shell model to solve for the permittivity value of each surface modification using effective particle permittivity results from the previous step of the DPM framework.

Huang et al. present a multi-shell theoretical model for a cell in the form of concentric dielectric spheres of permittivity ε_i and radius R_i $(i = 1, 2, 3 \ldots N)$.[141] According to the model, for a particle with N-shells, the effective particle complex permittivity $\tilde{\varepsilon}_{p\,eff}$ can described by

$$\tilde{\varepsilon}_{p\,eff} = \tilde{\varepsilon}_N \frac{(R_N/R_{N-1})^3 + 2\dfrac{\left(\tilde{\varepsilon}_{N-1\,eff} - \tilde{\varepsilon}_N\right)}{\left(\tilde{\varepsilon}_{N-1\,eff} + 2\tilde{\varepsilon}_N\right)}}{(R_N/R_{N-1})^3 - \dfrac{\left(\tilde{\varepsilon}_{N-1\,eff} - \tilde{\varepsilon}_N\right)}{\left(\tilde{\varepsilon}_{N-1\,eff} + 2\tilde{\varepsilon}_N\right)}}, \tag{3.6}$$

where $\tilde{\varepsilon}_N$ is the effective complex permittivity of the outermost shell and $\tilde{\varepsilon}_{N-1\,eff}$ represents the effective complex permittivity of the inner sphere with $N-1$ shells. Following this formulation, the real component of this expression was derived and the effective particle permittivity results of probe particles from DPM experiments were used to systematically solve for the effective permittivity contributions of each surface modification ε_i, modeled as individual shells (Table C.2). For example, by substituting the DPM determined real effective particle permittivity values of the Si-PEG and Si probe particles for $Re\left[\tilde{\varepsilon}_{p\,eff}\right]$ and $Re\left[\tilde{\varepsilon}_{N-1\,eff}\right]$, respectively, the permittivity contribution of the PEG layer is determined by solving for $Re[\tilde{\varepsilon}_N]$ (Fig. 3.5c). The conductivity values of the effective inner particle, $\sigma_{N-1\,eff}$, and the outermost layer, σ_N, appearing in the expression were similarly calculated as in the previous step in analysis.[149,150] This process was repeated to extract the permittivity of each surface modification ε_i (Fig. 3.5d). In general, these individual permittivity contributions or permittivity values that are obtained as the final results from the DPM method can be incorporated into any desired system model to predict changes in ICEO flows due to surface modifications.

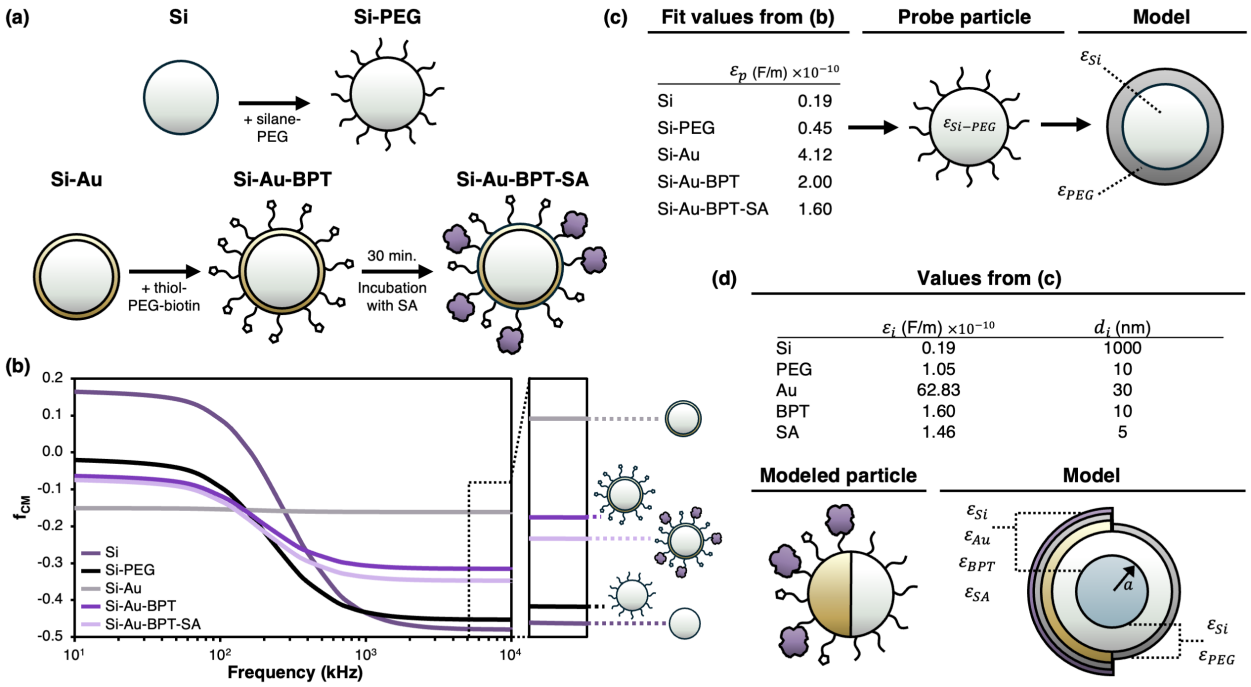

Figure 3.5. DEP surface modification, f_{CM} fit results, details for layer permittivity determination, and details for the theoretical model for motion prediction. (a) Schematic of the surface modification approach used to generate all five probe particle types analyzed in the study. (b) f_{CM} fits for all five probe particle types analyzed in the study. (c) Particle permittivity fit values from (b) and schematic representation of the core and shell model used to determine permittivity contributions from individual surface modifications. (d) Individual permittivity contributions from each surface modification generated in (c) and schematic representation of the theoretical model to predict motion of Janus particles with identical surface modifications

3.4.7 Modelling theoretical Janus particle motion.

In the present work, we elected to investigate the effects of surface modifications and resultant changes in surface polarizability on ICEO flows by studying the ICEP of surface-modified Janus particles. As such, we developed a corresponding theoretical model to predict Janus particle ICEP speed for comparison and validation with experiments.

To theoretically predict how measurable changes in surface polarizability due to modifications affect ICEO flows around Janus particles and thus ICEP speed, we solve the geometry-dependent nonlinear electrokinetic equations[142] and model the electrostatic potential

drop across the screening cloud, specifically accounting for contributions of the surface modifications. Here, we consider a spherical particle of radius a present in a binary electrolyte with a bulk concentration of ions such that the bulk is electroneutral ($c_+ = c_- = c_0$). The Debye length, defined for a symmetric *z*:*z* electrolyte by

$$\lambda = \sqrt{\frac{\varepsilon_m k_B T}{2(ze)^2 c_0}}, \tag{3.7}$$

where ε_m is the electrical permittivity of the solvent and e is the charge of an electron, is assumed to be thin ($\lambda/a \ll 1$). We note that a thin Debye length approximation was made for solution simplification although this assumption may not be entirely representative of experiments performed in water. To account for this, a Debye length of λ = 450 nm was used in calculations which is a reasonable order of magnitude for a Debye length present in MQW. Moreover, we anticipate the finite Debye length corrections to only change the resulting trends by a factor that will be cancelled out when comparing velocity ratios.

The particle is assumed to be coated with different material types with thicknesses d_i where $i =$ Si, PEG, Au, BPT, and SA with the assumption $d_i/a \ll 1$ (Fig. 3.5d). To incorporate the effect of different surface modifications, treated here as individual "coatings", we assume that these layers each posses an individual electrical permittivity of ε_i. Additionally, we assume that the surface charges are small enough that a linearized potential drop is possible and described by

$$\zeta_i = \frac{\zeta_0}{1 + \sum_i \frac{\varepsilon_m d_i}{\lambda \varepsilon_i}} = \frac{\zeta_0}{1 + K}, \tag{3.8}$$

where ζ_0 is the induced zeta potential over a conducting sphere.

To calculate ζ_0, we follow the approach by Squires and Bazant[118,142] beginning with defining that the electric field is applied in the $\mathbf{e}_z$ direction, parallel to the interface of the two

particle hemispheres, such that $\mathbf{E} = E_0\mathbf{e}_z$ far from the particle. It is experimentally observed that particles instantly reorient upon application of the electric field and align the line of asymmetry with the electric field. To represent this, particle asymmetry is assumed to be in the azimuthal direction, denoted by angle φ, where the polar angle is denoted by θ. ζ_0 is calculated by solving the Laplace equation with the conditions that there is no flux on the surface and the far-field electric field is described as

$$\zeta_0 = -\frac{3}{2}E_0 a\cos\theta\,. \tag{3.9}$$

Considering the asymmetry in the azimuthal, φ direction, we denote ζ_i as

$$\zeta_i = \frac{\zeta_0}{1+K_1}, 0 \le \varphi \le \pi, \tag{3.10}$$

corresponding to the Au Janus particle hemisphere and

$$\zeta_i = \frac{\zeta_0}{1+K_2}, \pi \le \varphi \le 2\pi \tag{3.11}$$

corresponding to the Si Janus particle hemisphere.

We note that Squires and Bazant require that the total charge on the particle be zero, which the above equations satisfy.[118,142] The velocity of the particle is calculated by using the standard formula based on slip velocity, i.e.,

$$\mathbf{U} = -\frac{1}{4\pi a^2}\int_S \mathbf{u}_s dS\,, \tag{3.12}$$

where S denotes the surface of the particle and $\mathbf{u}_s$ is the local slip velocity given by

$$\mathbf{u}_s = -\frac{\varepsilon_m}{\mu}\zeta_i \mathbf{E}_\parallel, \tag{3.13}$$

where $\mathbf{E}_\parallel = -\frac{3}{2}E_0\sin\theta\,\mathbf{e}_\theta$. Substituting the value of slip velocity described above, it is straightforward to calculate that

$$\mathbf{U} = c\left(\frac{1}{1+K_1} - \frac{1}{1+K_2}\right)\mathbf{e}_y, \tag{3.14}$$

where c is a constant.

There are various assumptions in the result that require discussion. First, the derivation assumes a conducting core whereas experiments were performed with Si. To handle this assumption, Si was incorporated as an individual "coating" in calculations. While this is an approximate method, we believe it is qualitatively representative of the real system. Second, the derivation assumes that the attachment of entities can be represented as a volumetric dielectric constant. In reality, there may be ionic exchanges in this region that depend on layer density and composition. These effects are currently not included in the model, but could be accounted for in future work.

3.4.8 DPM and modelling can inform effects of surface modifications on ICEO flow.

Using the individual surface modification permittivity results from the complete DPM analysis, JP, JP-PEG, JP-BPT, ICEM, and ICEM-SA particles were modeled to predict the particle velocities for each using eq 14 (Table S4). We evaluated particle speed at both λ = 1000 nm, which is near the upper limit of Debye length in pure water, and λ = 32 nm, which is the approximate value for Debye length for water with σ_m = 6.4 μS/cm (i.e., the assumed conductivity of water used in experiments). Modifications to the more polarizable Au hemisphere, over which ICEO flows are greatest, led to a predicted decrease in ICEP speed. Here, these theoretical calculations predicted a decrease in speed (i.e., ~4.2–55% for λ = 1000–32 nm) upon the addition of BPT on the Au side (Fig. 6a) and an even further decreased speed (i.e., ~6.4–66% for λ = 1000–32 nm) upon the specific capture of SA by BPT. The calculations did not predict a substantial change in

speed due to modification of the Si hemisphere by PEG (JP-PEG particles) relative to blank JPs at either Debye length. Because ICEP is driven by asymmetric ICEO flows that are dominated by the ICEO flow surrounding the more polarizable surface, it is reasonable that predicted speed suppression only occurs when the Au side is modified.[142]

Upon comparison with experimentally measured ICEP speeds, we found that the predicted relative decrease in ICEP speed upon capture of SA by ICEMs reflected the experimentally observed decrease in particle speed (Fig. 6b). While the magnitude of speed decrease predicted by our model varied with the assumed Debye length, the experimentally observed speed fell within the predicted speed range. This finding supports the hypothesis that the decrease in ICEP motion arises in part from changes to the polarizability of the Au hemisphere of the Janus particle, which results in decreased ICEO flows. It should be noted, however, that the presence of protein on the particle's Au hemisphere may also affect the particle-coverslip interactions and contribute to particle speed suppression via these interactions. Future work to eliminate assumptions for the Debye length, thickness of modification layers, or other model parameters may result in closer matching of experimentally observed and theoretically predicted speed values and changes.

We additionally found that theoretical predictions deviate from experimentally observed speeds of particles modified with PEG (i.e., JP-PEG, JP-BPT, and ICEMs) relative to unmodified JPs (Fig. 3.6a). While the presence of BPT on the Au hemisphere of the particles was predicted to suppress particle motion and the presence of PEG on the silica hemisphere of the particles was predicted to have limited effects on particle speed, both led to increases in particle speed during experiments (Fig. 3.3b, 3.6a). As discussed earlier, these discrepancies are likely explained, in part, by decreased interaction strengths between the Janus particles and the glass coverslip at which the particle were tracked.[132] Such effects are not present and cannot be measured via the DPM

method, nor were they taken into account in our theoretical speed predictions. Regardless, our DPM-based predictions indicate that the experimentally observed speed increases are not mechanistically explained by changes to particle polarizability. In reality, surface modification-induced changes to the motion of Janus particles undergoing ICEP likely arise from a combination of changes to polarizability, surface interactions, and potentially other factors not considered here.

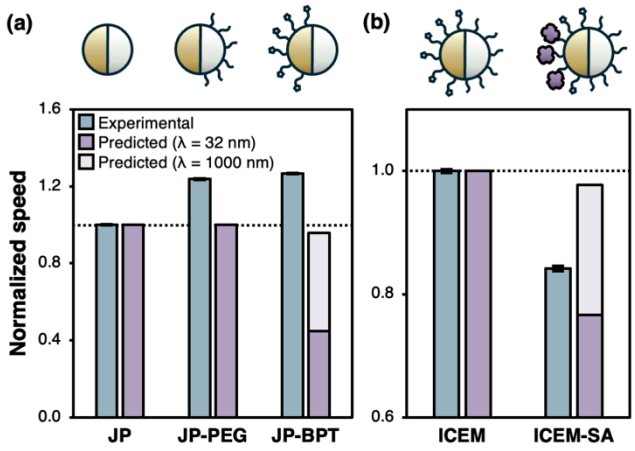

Figure 3.6. Comparison of experimentally measured ICEP speed and theoretically predicted speed. (a) Normalized speed of Janus particles modified by polymers relative to unmodified Janus particles **(b)** Normalized speed of ICEMs with captured SA relative to control ICEMs. Error bars indicated STE.

3.5 Conclusions

In this work, we have introduced dielectrophoretic polarizability measurement, DPM, as a method to measure the effects of complex surface modifications on the effective polarizability of probe particles. By use of a core and shell model, the DPM method enabled determination of the individual contributions of multiple surface modifications to the changes in probe particle polarizabilities. This information was combined with a theoretical model for ICEP propulsion, allowing us to predict changes to the speed of Janus particles traveling by ICEP, as well as investigate the mechanisms by which such changes occur. We additionally modified and experimentally observed the speed of six different Janus particle types to validate this approach. We found that the DPM-based theoretical predictions accurately predicted decreases in ICEP speed when protein is captured on surfaces, as observed experimentally in this and previous work. These findings support the hypothesis that decreases in ICEP speed upon capture of protein are mechanistically driven in part by direct changes to the polarizability of metallic surfaces of the Janus particles. The DPM-enabled predictions also revealed the presence of additional mechanisms by which ICEP motion is altered by surface modification; there are some discrepancies between predicted and experimental findings that are likely explained by the presence of particle-surface interactions in the experimental case, which are not accounted for in our predictions nor measured by DPM. Thus, the DPM method not only helps to predict influence of surface modifications on ICEO, but can also reveal situations in which experimentally observed changes in ICEO are driven by effects unrelated to surface polarizability. The predictive capabilities of the DPM-based method are thus likely strongest for induced electrophoretic or electroosmotic systems in which surface-surface interactions are not present (e.g., microfluidic pumps). However, this method can be greatly informative in systems in which surface-surface

interactions or other confounding variables are present. Future work toward enhancing the predictive capabilities of the method may benefit from inclusion of damping factors in theoretical calculations to account for surface effects. Additionally, future work focused on validating the DPM method against systems in which surface-surface or other confounding interactions are not present may provide key insights toward further development and implementation of this measurement method.

Chapter 4: Acoustic pipette and biofunctional, acoustic-responsive microparticle system for rapid picomolar-level biomolecule detection in whole blood

Previously published as: Thome, C. P.; Fowle, J. P.; McDonnell, P.; Zultak, J.; Jayaram, K.; Neumann, A. K.; López, G. P.; Shields, C. W. Acoustic Pipette and Biofunctional Elastomeric Microparticle System for Rapid Picomolar-Level Biomolecule Detection in Whole Blood. *Sci. Adv.* **2024**, *10* (42), eado9018. https://doi.org/10.1126/sciadv.ado9018. All supplementary media, including video and stereolithography files, may be obtained at the source of publication.

4.1 Abstract

Most biosensing techniques require complex processing steps that generate prolonged workflows and introduce potential points of error. Here, we report an acoustic pipette to purify and label biomarkers in 70 minutes. A key aspect of this technology is the use of functional negative acoustic contrast particles (fNACPs), which display biorecognition motifs for the specific capture of biomarkers from whole blood. Due to their large size and compressibility, the fNACPs robustly trap along the pressure antinodes of a standing wave and separate from blood components in under 60 seconds with >99% efficiency. fNACPs are subsequently fluorescently labeled in the pipette and are analyzed by both a custom, portable fluorimeter and flow cytometer. We demonstrate the detection of anti-OVA antibodies from blood at picomolar levels (35–60 pM) with integrated controls showing minimal non-specific adsorption. Overall, this system offers a simple and versatile approach for the rapid, sensitive, and specific capture of biomolecules.

4.2 Introduction

Detection of biomolecules from biofluids using both qualitative and quantitative assays is essential for patient diagnosis and disease monitoring.[14,15] Many qualitative assays benefit from user-friendliness, minimal points of error, and simple readouts that eliminate the need for complex instrumentation; however, they generally fail to enumerate biomarkers or detect rare (picomolar-level) analytes. For example, lateral flow assays (LFAs) are implemented widely for point-of-care (POC) testing due to their ease-of-use and simple readouts that can be analyzed by eye.[16,17] However, LFAs typically cannot yield quantitative results, which lessens their usefulness in evaluating immune states on the individual and population-levels.[18,19] Quantitative assays, however, have the capacity to provide numerical readouts that offer a more comprehensive understanding of patient conditions. Enzyme-linked immunosorbent assays (ELISAs) are considered the gold standard for quantitative biomarker detection due to their ability to provide high sensitivity and specificity; however, ELISAs entail numerous blocking, labeling, and washing steps that require substantial user engagement for several hours.[20,21] As a result, this assay and others like it introduce multiple potential points of user-related error that can lead to false results; moreover, they require the use of complex, expensive, and bulky instrumentation that limits their use in laboratory settings.

To merge the benefits of qualitative and quantitative biosensing assays, we have developed a class of acoustically responsive functionalized microparticles and a handheld, ergonomic acoustic pipette for the rapid, sensitive, and user-friendly detection of biomarkers by downstream fluorescence analysis (Fig. 4.1, upper row). The presented system offers multiple advantages over ELISA while maintaining the same effective sensitivity. To accomplish this, the pipette contains an acoustofluidic trapping channel wherein biospecific functional negative acoustic contrast

particles (fNACPs) are rapidly purified from whole blood via acoustofluidic trapping. Due to their negative acoustic contrast, fNACPs trap along the acoustofluidic channel walls while cells are pushed to the center of the channel due to their positive acoustic contrast. By relying on acoustic trapping, this technology i) eliminates the need for extensive sample preparation, ii) enables a simplified assay workflow with reduced points of potential user error, and iii) decreases overall assay time to only 70 minutes.

The fNACP functionalization approach we utilize allows for the simple tuning of fNACP biomarker specificity. To facilitate biomarker detection in this study, fNACPs were functionalized with antifouling polymer brushes terminated with antigen recognition elements to capture antibody biomarkers (Fig. 4.1, lower row). Using ovalbumin (OVA)-functionalized fNACPs, we show the sensitive detection of anti-OVA immunoglobulin G (IgG) antibodies (Ab) at picomolar levels (35 pM) when analyzed by flow cytometry. By integrating wash buffer and fluorescent secondary antibodies into the acoustic pipette, we demonstrate a simplified assay workflow in which, after capture of anti-OVA from whole blood, fNACPs can be rapidly purified from blood, washed, labeled with a fluorescent antibody, and ejected for fluorescence analysis with only approximately 10 minutes of user involvement. Enumeration of biomarker concentration can then be completed by comparison to fNACP-based assay calibration curves. Finally, we show toward-POC detection of anti-OVA IgG at 100 nM using a custom benchtop fluorimeter designed to house the acoustic pipette. The fluorimeter dramatically simplifies fluorescence analysis compared to that which is required by flow cytometry, which in turn substantially broadens the range of situations in which the presented NACP-based assay may be applied. This technology could thus be useful for monitoring the health of patients or informing diagnoses for a breadth of diseases and conditions,

such as viral infections, bacterial infections, cancer, and allergic reactions, which are detectible via measurement of biomarker levels in biofluids.

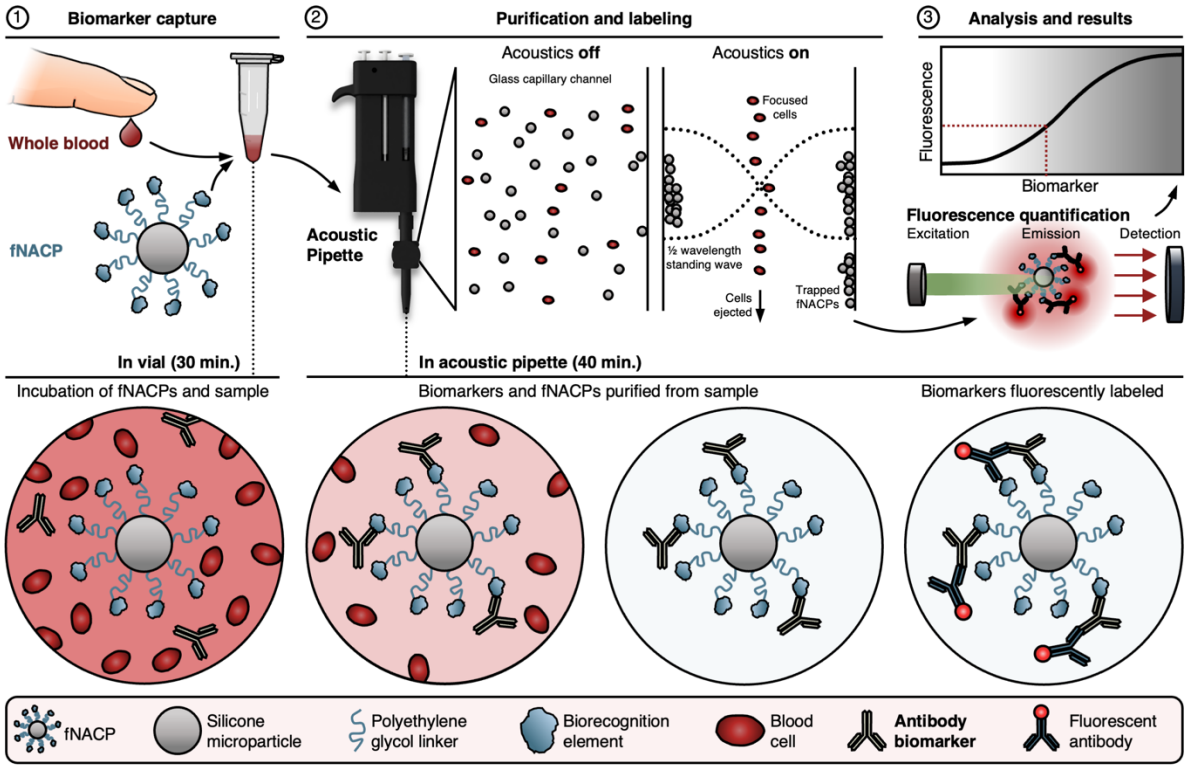

Figure 4.1. Schematic overview of the particle-based, acoustic pipette-enabled biosensing assay. fNACPs capture target biomarkers from whole blood samples. fNACPs are then purified from blood components by acoustic trapping, and captured biomarkers are labeled with a fluorescent antibody within the acoustic pipette. fNACP fluorescence is then measured to determine biomarker presence and concentration. Illustrations are not to scale.

4.3 Results

4.3.1 Production of trappable, low polydispersity microparticles

Acoustic standing wave-based acoustofluidic separation leverages acoustic radiation forces to direct particles, cells, or other objects towards different stable positions along the standing wave. The primary acoustic force acting axially (i.e., perpendicular to the channel walls) on particles in an acoustic standing wave is given by:

$$F_p = -\left(\frac{\pi p^2 V_p \beta_f}{2\lambda}\right)\varphi(\beta,\rho)\sin(2kx) \tag{4.1}$$

where p is the pressure amplitude, V_p is the particle volume, λ is the ultrasonic wavelength, x is distance from the pressure node, and k is defined as $\frac{2\pi}{\lambda}$. The acoustic contrast factor, $\varphi(\beta,\rho)$, is given by:

$$\varphi(\beta,\rho) = \frac{5\rho_p - 2\rho_f}{2\rho_p + \rho_f} - \frac{\beta_p}{\beta_f} \tag{4.2}$$

where variables ρ and β represent the density and compressibility, respectively, and the subscripts p and f denote the suspended object and the carrier fluid, respectively.[106,152,153] When a half-wavelength standing wave is established within a microfluidic channel, such as a glass capillary, positive acoustic contrast particles (PACPs) with diameters much smaller than the wavelength (e.g., cells) move towards the pressure node, which is located along the middle of the channel.[154] Alternatively, negative acoustic contrast particles (NACPs) undergo acoustophoresis to the antinodes along the walls of the channel. In addition to the primary radiation force, particles and cells in the channel also experience a secondary radiation force, which is attractive between particles at close distances.[153,155] Therefore, when NACPs undergo acoustophoresis, they are forced to the channel walls and subsequently aggregate. Finally, beyond the axial component of the acoustic radiation force, particles in an acoustofluidic channel experience a lateral acoustic radiation force that originates from gradients in the local acoustic potential along the channel and acts parallel to the channel, toward regions of local acoustic minima or maxima. In certain conditions, such as at high acoustic radiation forces, this can result in acoustic trapping, which we define as the immobilization of NACPs along the pressure antinodes in the presence of an applied flow, due to both the lateral component of the primary acoustic radiation force and the secondary

acoustic radiation force exceeding the force on NACPs from Stokes' drag.[155,156] Previous work has shown use of continuous acoustic separation of NACPs from cells or other PACPs by an acoustic standing wave within trifurcating microfluidic channels; however, to our knowledge, static trapping of NACPs under continuous flow has not been rigorously demonstrated.[106,157–159] This trapping approach eliminates the need for complex fluidic channels, relative to continuous separation, simplifying device manufacturing and reducing costs. Unlike trapping of NACPs, trapping of PACPs has been shown previously; however, because the fluid flow rate at the channel walls is much lower than that at the middle of the channel, trapping of NACPs can occur at throughputs much higher than trapping associated with PACPs.[156,160–162] Finally, due to the discriminant forces on cells and elastomeric particles in an acoustic standing wave, acoustofluidic technologies have the potential for higher separation purities than methods using optical, electrical, or magnetic fields.[163,164]

To leverage the multiple benefits of separation via trapping of NACPs, we developed a technique to produce highly trappable, microscale NACPs. Base NACPs were first produced by homogenization of a polymer precursor containing 0.1% v/w triethoxyvinylsilane (TEOVS) in Sylgard 184 polydimethylsiloxane (PDMS) submerged in a solution of Pluronic F108 surfactant. PDMS was selected as the primary NACP material due to its inherent negative acoustic contrast,[152] while TEOVS was included to yield functional silane groups on the surfaces of NACPs for later functionalization steps.[165] After homogenization and formation of precursor droplets in an emulsion, the solution was heated to cure the PDMS and form polydisperse NACPs. As the use of polydisperse NACPs in a fluorescence-based assay was expected to increase variability of measurements (Fig. D.1), we opted to isolate a low-polydispersity fraction of the NACPs by sequential vortexed filtration through 40, 30, and 20 μm filters, collecting the NACPs retained by

the 20 μm filter (Fig. 4.2A). This process yields NACPs with a low polydispersity (Fig. 4.2B) with a mean size of 24.3 μm (coefficient of variance (CV) = 12.4%, Fig. 4.2C). These particles are large relative to many particles used in diagnostic assays.[166] While the use of smaller particles in assays may offer the potential for faster particle-biomarker binding interactions due to increased diffusivity, we expected that the larger particle size also facilitates faster, more robust trapping of particles under flow, as the magnitude of acoustic radiation forces scales proportionally with the volume of particles (cubically with the radius), as seen in Equation (4.1).[153] As such, we anticipated that the use of larger, more trappable particles would enhance the isolation and recovery of captured biomarker. If desired, the NACP size could be easily tuned without modification of the production approach by simply selecting filters sized for the isolation of a smaller population of NACPs; however, a detailed investigation of the interplay between particle size and total recovered biomarker is reserved for future studies.

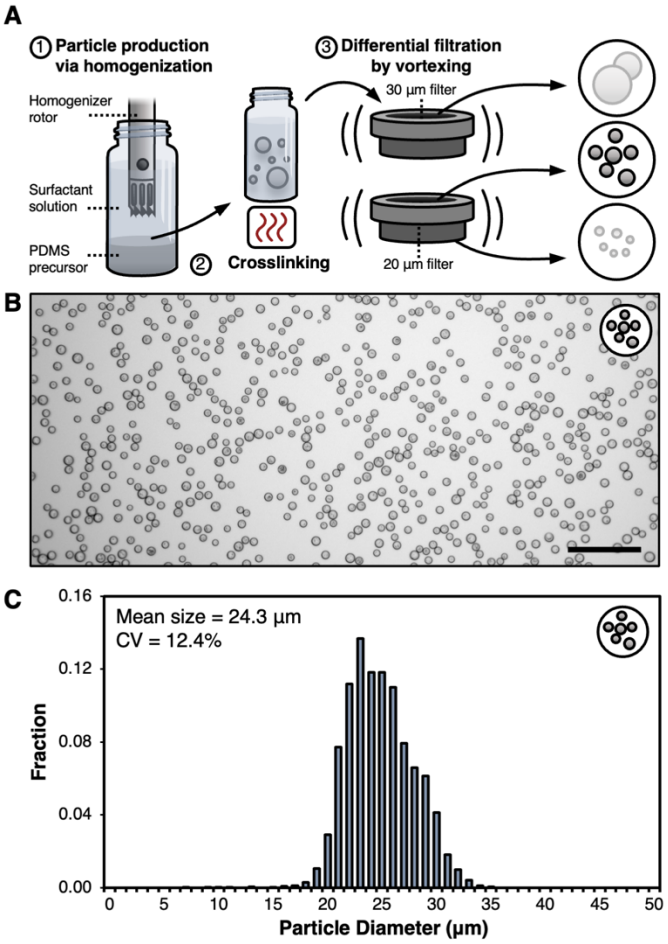

Figure 4.2. NACP production. (A) Schematic overview of NACP production. A PDMS precursor is homogenized to form droplets. The solution is heated to facilitate PDMS crosslinking. Cured particles are filtered while vortexing to isolate a low-polydispersity fraction of NACPs. (B) Brightfield microscopy image of isolated NACPs. Scale bar = 100 µm. (C) Histogram of isolated NACP sizes, as determined by image analysis (N = 3812).

To assess the acoustic trapping of NACPs, we fabricated an acoustofluidic trapping channel by affixing a square glass capillary with a 1 mm x 1 mm inner width and height to a piezoelectric transducer possessing a resonance frequency of 750 kHz (Fig. 4.3A). The transducer was actuated by applying an AC sine wave via leads connected to a function generator and amplifier. By operating the transducer at or near 750 kHz, a half-wavelength standing wave was established in the capillary channel. We monitored transducer heating by measurement of the transducer

temperature after prolonged (> 5 min) application of 750 kHz sine waves of increasing voltages (from 1 to 50 V_{pp}) and determined that application of a 30 V_{pp} sine wave did not cause heating above 37˚C; as such, transducers were operated at 30 V_{pp} for the remainder of the studies. We passed a solution of fluorescent streptavidin-coated NACPs in phosphate buffered saline (PBS) through the device at a flow rate of 0.5 mL min^{-1} and applied a 750 kHz sine wave to the transducer. We found that the NACPs were strongly trapped along channel walls (Fig. 4.3B, Supplementary Video). Trapping was readily achieved due to the large volume of the NACPs (>20 μm dia.) compared to past studies.[167]

4.3.2 Purification of NACPs from whole blood

Whole blood is replete with red blood cells (RBCs), white blood cells (WBCs), and platelets that have the potential to disrupt pressure waves by scattering, possibly reducing the ability to acoustically trap NACPs.[152,153,168] Previously, researchers have either removed or lysed RBCs when conducting acoustofluidic separations from whole blood.[169,170] However, use of RBC lysis buffer requires an additional processing step, complicating and elongating assays. To evaluate the necessity of an RBC lysis step in the acoustic pipette, we mixed $5x10^4$ NACPs with 100 μL whole porcine blood containing sodium heparin anticoagulant, whereby WBCs were stained with NucBlue Live Cell Stain, and diluted to 1 mL with either 1X RBC lysis buffer or wash buffer composed of 1% w/v bovine serum albumin (BSA) in PBS. We then passed the solutions through the acoustofluidic trapping channel at a flow rate of 0.5 mL min^{-1} with acoustics engaged and collected both the separated waste, rich in blood components, and the purified sample of NACPs (Fig. 4.3C). Using flow cytometry, we enumerated i) NACP retention, quantified by dividing the number of NACPs in the purified sample by the total number of NACPs in the purified sample and

waste, and ii) sample purity, quantified by comparing the number of WBCs in the purified sample to the total number in both the purified sample and waste (Fig. D.2). We found that use of RBC lysis buffer did not significantly improve NACP retention nor sample purity (Fig. 4.3D), indicating that RBC lysis is not necessary at the flow rate tested, simplifying assay workflows and increasing POC translatability.

Previous demonstrations of acoustofluidic separation of NACPs have been unable to achieve high flow rates, limiting their value in rapid diagnostics applications.[152,164,170] The main challenge in increasing flow rates through acoustofluidic devices is that such increases result in NACP channel residence times that are insufficient for full separation. Li *et al.* were able to achieve 97.5% NACP separation by continuous separation in a trifurcating channel, but the flow rate was limited to 50 μL min^{-1}.[106] We hypothesized that this limited throughput was a result of the smaller acoustic radiation forces on the NACPs due to their smaller sizes (i.e., 1.5 μm in the study by Li *et al.* compared to the 24.3 μm NACPs in this study). To evaluate the achievable throughput of our system, we again mixed $5x10^4$ NACPs with 100 μL stained whole porcine blood and diluted to 1 mL with wash buffer. We passed the mixtures through the device at 0.5–6.0 mL min^{-1} using a syringe pump and analyzed the resultant separated waste and purified samples as described earlier. We found that the retention of NACPs remained above 95% at flow rates up to 5 mL min^{-1}, 100-fold higher than that achieved by Li *et al.* (Fig. 4.3E). Moreover, sample purity remained above 95% for all evaluated flow rates (Fig. 4.3F). To ensure high (i.e., ~99%) NACP retention, all subsequent acoustofluidic purifications were performed at 3 mL min^{-1}.

Characterization of the trapping channel described thus far utilized a syringe pump to establish precise flow rates. To assess manual operation of the acoustofluidic trapping channel, which is expected to lead to less precise flow rates, five human operators manually pushed fluid

through the device by syringe while targeting a flow rate of 3 mL min^{-1}. We found that manual operation of the device did not significantly differ from operation by syringe pump, establishing that the trapping channel could be integrated into the handheld acoustic pipette without sacrificing separation performance (Fig. 4.3G, Fig. D.3).

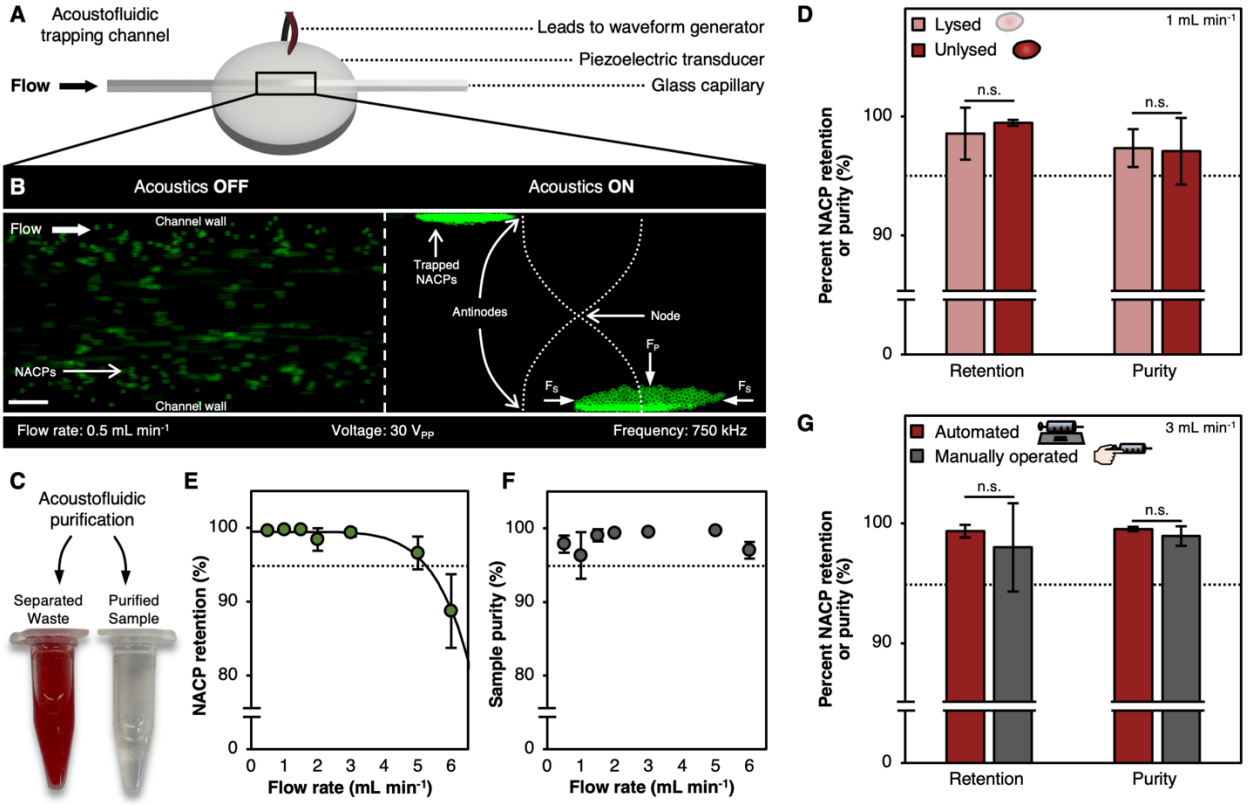

Figure 4.3. NACP trapping and purification from whole blood. (A) Schematic illustration of the acoustic trapping channel including the piezoelectric transducer, glass capillary, and electrical leads. **(B)** Acoustic trapping of NACPs within a glass capillary supporting a half-wavelength standing wave. NACPs, shown in green, were coated with fluorescent streptavidin. Scale bar = 200 µm. **(C)** Representative images of separated waste, rich in cells, and a purified sample, rich in NACPs, after processing 5x10^4 NACPs in 100 µL unlysed blood diluted to 1 mL with wash buffer in the acoustofluidic trapping channel at 0.5 mL min^{-1}. **(D)** Comparison of NACP retention and sample purity after separation from lysed and unlysed blood samples, N ≥ 4. **(E)** NACP retention over a range of flow rates through the acoustofluidic trapping channel, N ≥ 4. **(F)** Sample purity over a range of flow rates through the acoustofluidic trapping channel, N ≥ 4. **(G)** Comparison of NACP retention and sample purity after separation by automated syringe pump (red bars; N = 5) and manual operation (grey bars; N = 24). Data for manual operation is compiled from 5 individual

operators, each with 4 or 5 individual samples. All data is presented as mean ± standard deviation and significance between conditions was evaluated using one-tailed Student's t-tests.

4.3.3 fNACP functionalization

To create a functional assay that leverages the NACPs, we designed an on-particle sandwich assay resembling ELISA, wherein target biomarkers are specifically captured by recognition elements bound to the surfaces of functionalized NACPs (fNACPs) and subsequently labeled by fluorescent secondary antibodies for analysis (Fig. 4.1, Fig. 4.4A). When designing a biomolecule detection assay, it is crucial to minimize matrix effects, as they may interfere with the assay and lead to false results.[100] We speculated that nonspecific adsorption of proteins or other molecules to the fNACPs could result in improper labeling by the secondary antibody; as such, we designed the fNACPs to include a polyethylene glycol (PEG)-based antifouling layer.[47,101] Thus, to functionalize base-NACPs, we bound 2 kDa biotin-PEG-silane (BPS) to silane reactive groups from the incorporated TEOVS on NACP surfaces, yielding biotin-functionalized NACPs with an intrinsic antifouling coating. Biotin is a small molecule that binds strongly to streptavidin (SA), a moderate-sized (~52.8 kDa) protein with four biotin binding sites.[105] Because of its four binding sites, addition of SA to the fNACPs enables subsequent conjugation of a variety of biotinylated recognition elements (e.g. antibodies, aptamers). Here, we selected biotinylated OVA as a model biorecognition element and anti-OVA IgG as a model biomarker. While the model biorecognition element and antibody biomarker pair are not clinically relevant, the proteins are structurally and functionally similar to many proteins that are. Thus, functionalization of fNACPs with more clinically relevant biotinylated recognition elements (e.g., SARS-CoV-2 spike protein) would likely produce similar assay performances when detecting their respective clinically relevant biomarkers (e.g., anti-SARS-CoV-2 spike protein antibodies). Further, anti-OVA is not naturally

found in porcine blood, allowing us to spike in known concentrations. Notably, the inclusion of the PEG linker, in addition to providing antifouling properties, is expected to allow more favorable orientations of OVA to enhance anti-OVA capture, relative to OVA bound directly to the NACP surface.[107]

4.3.4 fNACP functionalization specificity

To investigate specificity of NACP functionalization, we produced low polydispersity NACPs and functionalized their surfaces with the BPS linker. We then incubated BPS-decorated NACPs with fluorescent SA (FSA), yielding FSA-functionalized NACPs (Fig. 4.4B). We assessed FSA fluorescence via flow cytometry; as controls, we analyzed the fluorescence of blank NACPs, NACPs incubated with FSA blocked by free biotin, and NACPs without the BPS linker and incubated in FSA (Fig. 4.4C). Compared to the control groups, BPS-decorated NACPs incubated with FSA had substantially greater fluorescence intensity, suggesting that SA binding to fNACPs is specific and enhanced by the BPS linker. Moreover, the decreased fluorescence of NACPs with BPS and incubated with blocked FSA, relative to NACPs without BPS and incubated with FSA, provides evidence that inclusion of BPS suppresses nonspecific adsorption of proteins.

4.3.5 fNACP functionalization durability

To assess if particles functionalized with SA are impacted by conditions that will be present in a typical acoustic pipette-enabled assay, we mixed $5x10^4$ FSA-functionalized NACPs in 1 mL wash buffer and subsequently separated the mixture in an acoustic trapping channel. We measured the median fluorescence of the purified NACPs by flow cytometry. As a control, we also measured fluorescence of FSA-functionalized particles from the same batch that did not undergo additional

manipulation after functionalization (Fig. 4.4D). There was no significant decrease in fluorescence of the separated particles, indicating that NACP functionalization to the point of SA was resilient against the assay conditions associated with acoustofluidic separation.

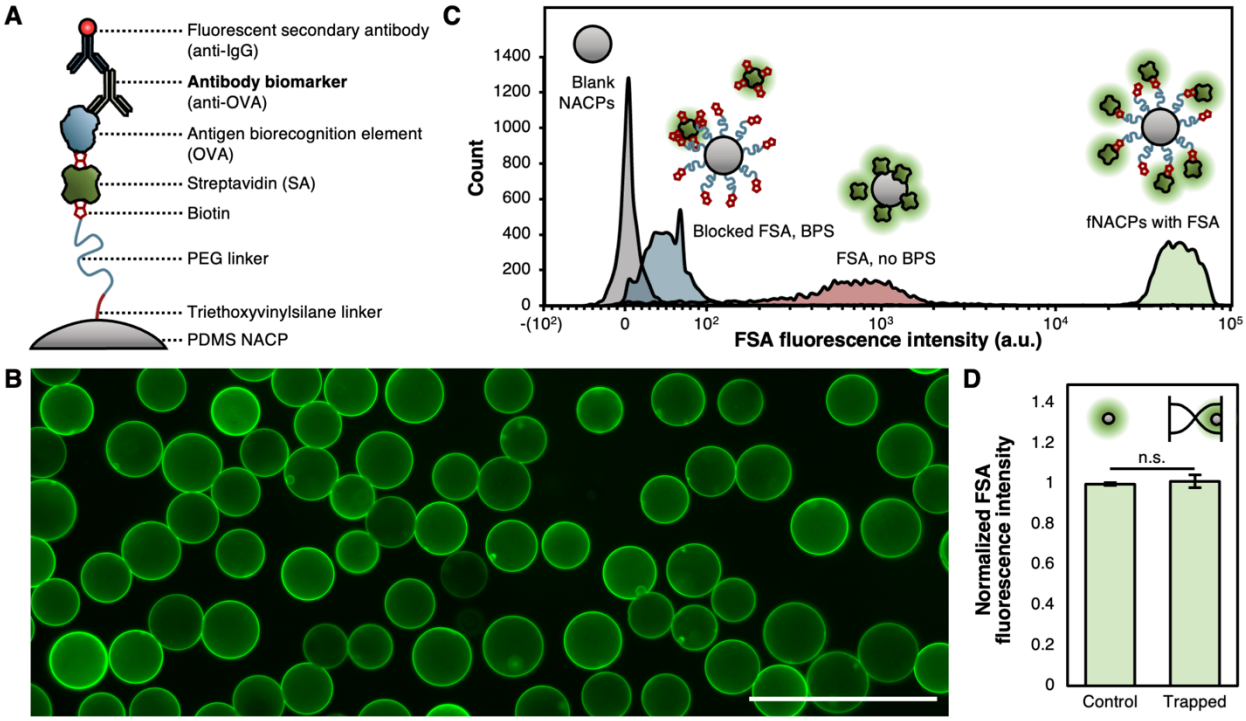

Figure 4.4. fNACP functionalization. (A) Schematic illustration of fNACP functionalization. (B) Fluorescence microscopy image of fNACPs functionalized with fluorescent SA (FSA). Scale bar = 100 µm. (C) Histograms of fluorescence intensity of fNACPs without FSA, incubated with blocked FSA, incubated with FSA and without BPS, and with FSA and BPS as normal. Data is presented on a biexponential x-axis. (D) Comparison of NACP FSA fluorescence intensity with and without acoustic separation. Data is presented as median ± standard deviation, N = 5. Significance between conditions was evaluated using a one-tailed Student's t-test.

4.3.6 fNACP-based assay

To create an fNACP-based assay with a built-in control, we generated nonfluorescent anti-OVA-specific fNACPs (capture fNACPs) and fluorescent NACPs lacking a recognition element (control NACPs) (Fig. 4.5A). To generate the control NACPs, we functionalized NACPs with green FSA as described earlier, and subsequently blocked remaining biotin-binding sites by

incubation with a >12-fold molar excess of free biotin. During coincubation of capture fNACPs and control NACPs with samples containing spiked anti-OVA, anti-OVA should only bind to capture fNACPs. Then, during the subsequent labeling step, red fluorescent secondary antibodies should only bind to anti-OVA on the nonfluorescent capture fNACPs. During subsequent fluorescence analysis, the green fluorescent control NACPs can be checked for red fluorescence as an indicator of nonspecific adsorption (Fig. D.4).

4.3.7 Standalone fNACP assay performance in buffer

We measured the performance of the fNACP-based assay by measuring the limit of detection (LOD), lower limit of quantification (LLOQ), upper limit of quantification (ULOQ), and dynamic range. We define the LOD in this study as the concentration of biomarker that yields an average median fluorescence intensity (MFI) three standard deviations above the median background fluorescence. The LLOQ and ULOQ are defined as the lowest and highest concentration of biomarker, respectively, that can be reliably quantified, which is generally accepted to be that which yields a CV < 20%; the dynamic range is the range between the LLOQ and ULOQ.[171,172] To quantify these metrics, we resuspended $1x10^4$ control NACPs and $1x10^4$ capture fNACPs in 100 μL wash buffer spiked with anti-OVA over the range of 10^{-4} – 10^4 nM anti-OVA and incubated at room temperature for 30 min under agitation. The number of each NACP type used per sample ($1x10^4$) was selected to ensure that sufficient numbers of NACPs were present for analysis by flow cytometry while also minimizing total particle number to avoid potential dilution of signal across particles. The total surface area of the particles used was approximately 58% of that of a single well on a 96-well plate, commonly used in ELISA. After anti-OVA capture, the particles were incubated with fluorescent anti-IgG for 30 min. The particles

were then washed and analyzed via flow cytometry (Fig. 4.5B, Fig. D.4, Fig. D.5). To enable enumeration of biomarkers and extract assay performance characteristics, experimental data was fit to a 5-parameter logistic curve (5PL), commonly used to fit experimental data from biosensing assays such as ELISA.[109,173] Using this curve fit, the LOD and LLOQ were determined to be 0.035 nM, a sensitivity on the order of that reported for a commercial ELISA for anti-OVA (0.013 nM).[174] We were unable to determine an ULOQ, as all investigated high anti-OVA concentrations yielded CVs < 20%. While the ULOQ could not be quantified, it is apparent that the dynamic range of the assay is much larger than that of commercial ELISAs (i.e., spanning at least 6 orders of magnitude, surpassing ELISA, which spans only ~2 orders of magnitude). The wide dynamic range of the assay relative to that of ELISA largely stems from the dissimilar signals and signal measurement approaches used in each assay. Fluorescence measurement systems typically allow measurement of fluorescence intensities at high cutoff values before signal saturation, whereas colorimetric measurements used for ELISA are limited by saturation of the optical density, restricting the dynamic range.[175–177] As expected, the fluorescence of the control NACPs did not significantly increase with increasing anti-OVA concentration, indicating that the labeling by the secondary antibody was specific, as shown in a representative image of the control NACPs and capture fNACPs after completion of the assay (Fig. 4.5C).

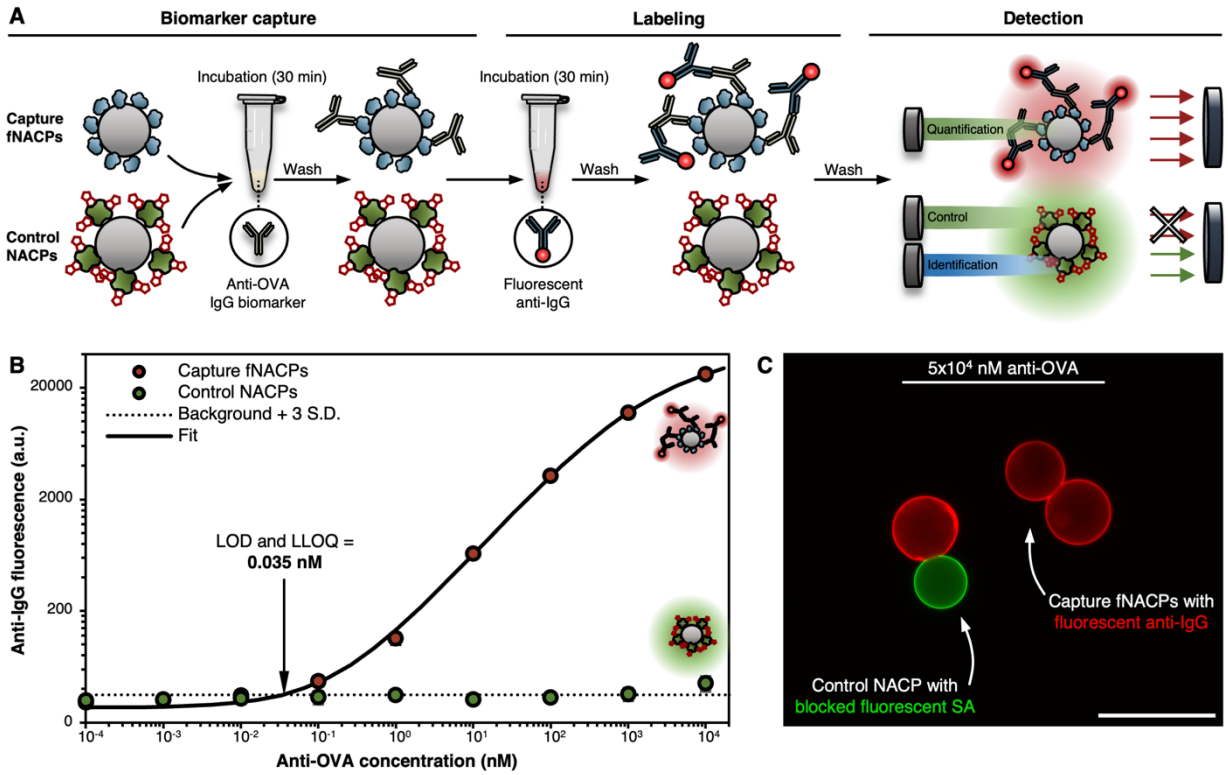

Figure 4.5. fNACP assay overview. (A) Schematic illustration of standalone NACP-based assay for anti-OVA detection. Capture fNACPs and control NACPs are incubated with anti-OVA, separated, and analyzed simultaneously by flow cytometry. **(B)** Capture fNACP and control NACP anti-IgG fluorescence over range of anti-OVA concentrations spiked in buffer. Data was fit to a 5PL curve to determine LOD and LLOQ. Data is presented as mean MFI ± standard deviation, N = 3. Dotted line indicates the baseline fluorescence of fNACPs without fluorescent anti-IgG. **(C)** Overlaid fluorescence microscopy images of control NACPs and capture fNACPs after incubation with fluorescent anti-IgG after incubation with $5x10^4$ nM anti-OVA. Images were captured using green and red fluorescence channels. Scale bar = 50 μm.

4.3.8 Acoustic pipette design and assay workflow

Using primarily CAD and 3D printing, we created the ergonomic, handheld acoustic pipette (Fig. 4.6A, Fig. D.6). To accommodate all necessary assay components, the pipette was designed with two main parts: i) the main pipette body, which contains three syringe chambers to store wash buffer and fluorescent secondary antibody, and ii) the trapping tip, which contains the acoustofluidic trapping channel and related components (Fig. 4.6B). The trapping tip is detachable

from the main body of the pipette, and switching between chambers is facilitated by a facile twist-and-lock mechanism (Fig. 4.6 inset). The trapping channel is accessed by piercing an elastomeric injection port with needles attached to each of the three chambers in the main body of the pipette. Notably, the injection port prevents contamination between chambers and additionally prevents air from entering the channel when switching between chambers, which could cause disruption of the acoustic standing wave in the trapping channel. Pipette components are sized to process 100 μL of whole blood, which is a standard volume for many blood-based detection assays that utilize finger-prick sampling.[178–180]

The pipette design enables a simple workflow that eliminates the many cumbersome steps associated with traditional immunoassays (Fig. 4.6C). Capture fNACPs and control NACPs are first resuspended in 100 μL whole blood containing the target biomarker and are incubated outside of the pipette in a tube for 30 min. Then, the sample is diluted in wash buffer from Chamber 3 of the pipette. The sample is then withdrawn from the sample tube with acoustics engaged, trapping the NACPs and fNACPs in the trapping tip, while the waste blood is pulled into Chamber 3 for containment. The particles are then further washed by pulling fresh wash buffer through the channel and into Chamber 3. The trapping tip is then switched to Chamber 1, acoustics are disengaged, and the particles are pulled into Chamber 1 for incubation with fluorescent secondary antibodies for 30 min. After incubation, the particles are ejected back into the trapping tip with acoustics engaged. The particles are further washed by switching back to Chamber 3 and withdrawing wash buffer past the particles. Finally, the acoustics are disengaged and wash buffer from Chamber 2 is used to eject the particles into tubes for analysis. Notably, user engagement is only required for approximately 10 minutes of the assay, and the entirety of the assay takes only approximately 70 minutes. Most of the assay time is consumed by the two 30-minute incubation

steps. Notably, this incubation time can vary based on the binding affinity between the recognition elements and the targets being detected as well as the concentrations of the various components. Optimization of these factors could potentially lead to even shorter assay times.

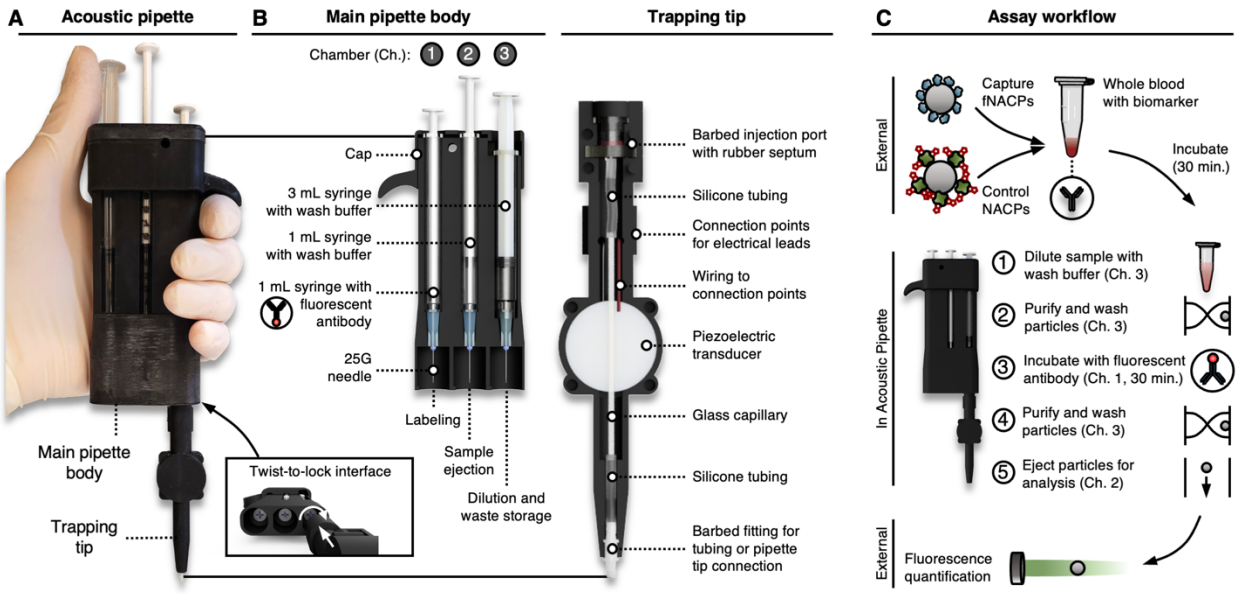

Figure 4.6. Acoustic pipette overview. (A) Image of acoustic pipette. Inset shows mechanism for movement and locking of trapping tip. **(B)** Schematic illustration of acoustic pipette internals, including the main pipette body and trapping tip. **(C)** Schematic illustration of general pipette-facilitated fNACP assay.

4.3.9 Performance of acoustic pipette-assisted, fNACP-based assay in whole blood

To evaluate the fNACP-based assay after integration into the acoustic pipette, we incubated $1x10^4$ control NACPs and $1x10^4$ capture fNACPs in 100 µL of whole blood spiked with anti-OVA over the range of 10^{-3} – 10^3 nM. After incubation, we used the acoustic pipette to purify, wash, and label the particles as described earlier (Fig. 4.7A). Upon analysis by flow cytometry, we found that the performance of the assay was similar to that of the standalone assay performed outside of the pipette in buffer, in terms of dynamic range, LOD, and general signal response. The measured

LOD and LLOQ were both 0.06 nM; this value is minimally elevated relative to the standalone assay conducted in buffer, as can be expected when conducting an assay in a complex biofluid like whole blood (Fig. 4.7B). Again, the dynamic range was not fully defined, but no apparent saturation point was reached, indicating a dynamic range spanning at least 5 orders of magnitude. The control NACPs exhibited slightly elevated anti-IgG fluorescence at high anti-OVA concentrations, relative to the assay conducted outside the pipette. We speculate this elevated fluorescence originated from nonspecific adsorption of proteins from blood, considering such elevation was not observed in the assay conducted in buffer alone. This suggests that detection of anti-OVA at high concentrations from whole blood may be inconclusive, necessitating retesting such samples after dilution. The control NACPs thus enable simple evaluation of assay performance and reliability, as designed. Future work dedicated to engineering the length, packing density, and composition of the antifouling polymer could further enhance the antifouling properties of the capture fNACPs and control NACPs to ultimately enhance assay performance in complex biofluids. Overall, the NACP-based assay performance remained predominantly unchanged when integrated with the acoustofluidic pipette and detecting biomarkers from whole blood samples.

4.3.10 Design and performance of custom fluorimeter for NACP-based assay analysis

While analysis of NACP fluorescence by flow cytometry helps to provide high sensitivity and a broad dynamic range owing to its use of narrow band laser excitation sources and highly sensitive photomultiplier tubes for emission detection, restricting analysis to flow cytometry is prohibitive to many POC testing situations due to bulkiness of – and lack of widespread access to – such instrumentation. To demonstrate integration of the NACP-based, acoustic-pipette enabled

assay into a POC-compatible system, we designed a custom benchtop fluorimeter that can dock with the acoustic pipette and analyze fNACP fluorescence. By integrating the NACP-based assay, pipette, and fluorimeter, the resultant system is portable and capable of simplified completion of the entire assay, including capture, isolation, and detection of biomarkers. The main components of the fluorimeter include an LED light source, a shortpass (SP) filter, a 100 μL cuvette, a longpass (LP) filter, and a photodiode (PD). During assays, fluorescent labels on the NACPs in the cuvette are excited by the filtered LED light, and light emission is detected by the photodiode (Fig. 4.7C, Fig. D.9). Notably, the 600 nm SP and 590 nm LP filters were selected specifically for analysis of the Alexa Fluor 594 fluorophore conjugated to the secondary antibody; by simply switching out these filters, other fluorophores can be detected by the system. Moreover, the cuvette size can be tuned depending on the volume of samples being tested, making the fluorimeter and its overall sensitivity customizable to application needs. The bulk of the setup, including a photodiode amplifier, mini oscilloscope, and the main fluorimeter body, easily fits on a benchtop. We designed and 3D printed a fluorimeter pipette docking cap to interface with the acoustic pipette; after all pipette-based assay processing has been completed, the pipette can be inserted directly into the fluorimeter to eject NACPs into the cuvette for analysis (Fig. 4.7D, E). A more detailed description of the fluorimeter setup can be found in the Supplementary Materials.

While flow cytometry analyzes fluorescence of individual particles, the custom fluorimeter excites and detects light emission from a large cluster of particles simultaneously. This decreases measurement time and post-measurement analysis substantially, increasing ease-of-use as a result. To maximize fluorescence signal from groups of particles, we modified the NACP-based assay by increasing the number of NACPs, as well as the sample volume, 10-fold. As the fluorimeter was designed for measurement of a single fluorophore, control NACPs were excluded from this study.

Thus, the workflow for using this instrument is identical to that shown in Fig. 4.7A, with the only difference being the exclusion of control particles. To test performance of the fluorimeter, we incubated 10^5 OVA-functionalized fNACPs in 1 mL of wash buffer spiked with 0, 10^1, 10^2, and 10^3 nM anti-OVA, subsequently labeled the fNACPs with fluorescent secondary antibody, and measured fluorescence using the fluorimeter. We measured significant detection at both 10^2 and 10^3 nM anti-OVA, as indicated both by statistical significance and by fluorescence signals at least 3 standard deviations above that of NACPs incubated with the secondary antibody and without anti-OVA (i.e., the background). While the signal at 10^1 nM anti-OVA was not significantly different from that of the background sample, the calculated P value of 0.07 suggests that this concentration is near the detection limit of the described system and assay. Because the fluorimeter prototype uses a broadband LED excitation source and silicon photodiode for emission detection, rather than a laser excitation source and photomultiplier tube that are used in flow cytometers, this sensitivity is lower than that associated with flow cytometry; however, the modular design of the fluorimeter could be exploited to enhance sensitivity in future work. For example, the photodiode can be replaced with a more sensitive detector (e.g., avalanche photodiode) or a smaller cuvette could be used to further concentrate the NACPs. Overall, we have created the first prototype POC measurement instrument that can be integrated with the handheld acoustic pipette and fNACP-based assay to enable the rapid and simple isolation and detection of proteins without bulky, expensive instrumentation. These results highlight the flexibility and potential of the NACP-based assay to capture various different biomarkers from whole blood in a rapid and sensitive manner.

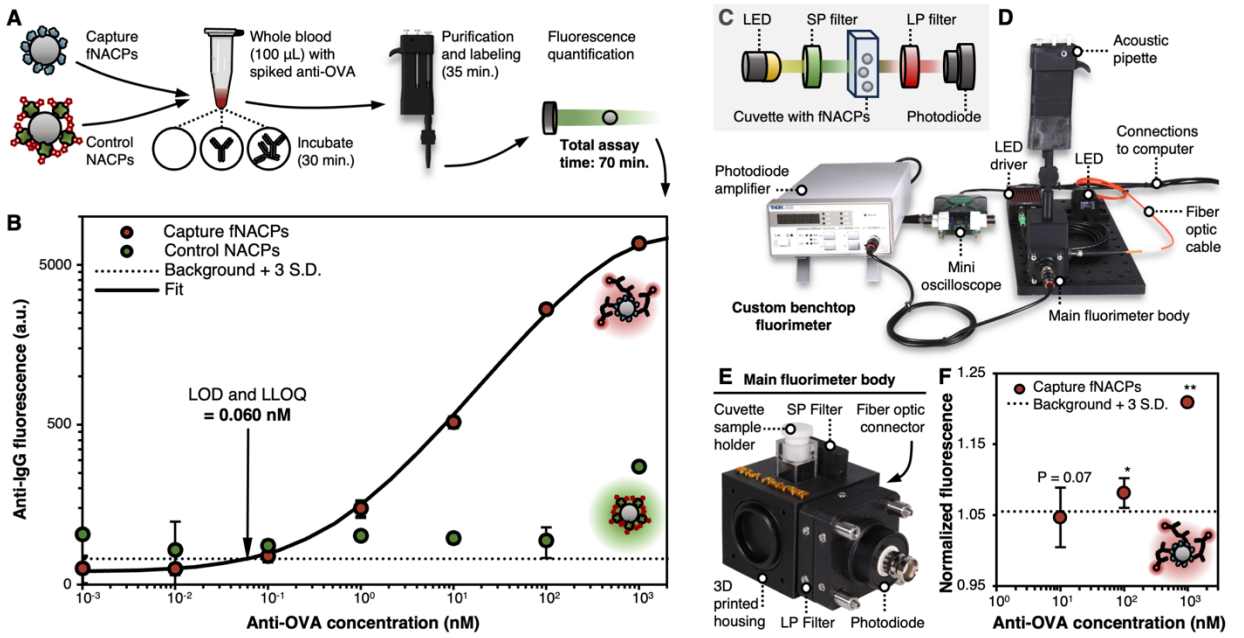

Figure 4.7. Detection of anti-OVA from whole blood in the acoustic pipette. (A) Schematic illustration of the workflow for detecting anti-OVA from whole blood in the acoustic pipette. **(B)** Fluorescence of anti-IgG on capture fNACPs and control NACPs over range of anti-OVA concentrations spiked in whole blood. Data was fit to a 5PL curve to determine the assay LOD and LLOQ. Dotted line indicates baseline fluorescence of fNACPs without fluorescent anti-IgG. Data is presented as mean MFI ± standard deviation. N = 3. **(C)** Schematic illustration of the primary components of the custom fluorimeter, including the LED source, a SP filter, a cuvette for containing the fNACP samples, a LP filter, and a photodiode detector. **(D)** Image of the custom benchtop fluorimeter and associated electronics. **(E)** Image of the main fluorimeter body, which houses all components from (c). **(F)** Capture fNACP anti-IgG fluorescence over range of anti-OVA concentrations spiked in buffer, as measured by the custom fluorimeter. Data is presented as normalized signal ± standard deviation. Significance between conditions was evaluated using a one-tailed Student's t-test. N = 3, *P<5x10^{-3}, **P<5x10^{-5}, relative to background.

4.4 Discussion

We demonstrate an NACP-based, acoustic pipette-enabled assay that isolates biomarkers from whole blood for rapid and sensitive detection in a simple, ergonomic handheld device. This work integrates two key innovations: i) fNACPs that specifically capture target biomolecules while suppressing nonspecific adsorption and ii) an acoustic pipette that enables the rapid purification, washing, and labeling of biomarkers. We describe methods to synthesize large NACPs with a low-

polydispersity (i.e., <15% CV) that can be acoustically trapped and purified from whole blood with high efficiency at rates up to 5 mL min^{-1}. We functionalized the NACPs to form fNACPs using a flexible conjugation approach that enables simple tuning of the fNACP specificity. We also designed a handheld acoustic pipette that contains all necessary components to conduct the fNACP-based assay, including wash buffer, a fluorescent secondary antibody, and a trapping channel supporting a half-wavelength acoustic standing wave. Using the acoustic pipette in combination with flow cytometry, we developed a serological assay to enumerate captured anti-OVA in small volumes of whole blood by comparison with calibration curves. Importantly, since we use fluorescent labels and not enzymatic labels, such as those as used in traditional ELISA, the most comparable clinical technology for biomarker quantification, the calibration curves can be prepared ahead of sample analysis when using particles from the same batch and fluorescent antibodies from the same lot (i.e., with the same number of fluorophores per antibody). This results in rapid analysis of single samples. Using this assay, we detected anti-OVA from whole blood with an LOD of 0.06 nM, a sensitivity competitive with commercial ELISA kits. Beyond this, we developed a portable, custom benchtop fluorimeter for analysis of samples processed in the acoustic pipette. Using a modified fNACP-based assay, we rapidly detected anti-OVA at 100 nM. By integrating the pipette and fluorimeter, thereby eliminating the need for flow cytometry, we show the ability for the NACP-based, acoustics-enabled assay to be simplified for biomarker detection in areas with limited resources. Such measurements may be especially useful in situations where test results must be obtained in timeframes much shorter than that required for shipment to and analysis by external laboratories.

This platform technology has the potential to dramatically shorten the time required to isolate and detect biomarkers (i.e., requiring only 70 minutes with less user engagement than

commercial ELISA methods of 4–6 hours). By integrating the system with a low-cost benchtop fluorimeter, this technology could be of great use for POC testing where timely analysis of single samples is necessary. Furthermore, it enables facile adaptation for detecting a range of antibodies, antigens, toxins, nucleic acids, or other types of biomarkers through its simple and modular method of functionalizing fNACPs. While the presented fNACP-based assay only allows for detection of a single biomarker, by barcoding fNACPs displaying different biorecognition elements with varied amounts of fluorophore, this technology could enable simple, rapid, fNACP-based multiplexing to enhance diagnostic capabilities. Furthermore, while not currently suited for POC detection, with the addition of an on-board power supply or modification of the signal transduction approach, the integrated acoustic pipette and fluorimeter system holds potential to enable deployment of POC diagnostic testing in remote areas, while maintaining – and potentially increasing – assay sensitivity compared to mainstay detection techniques. The acoustic pipette and fNACPs can also be of use independent of one another; the acoustic pipette could be a powerful tool for the simple and rapid separation of a host of other particle or cell types in laboratories or elsewhere, while the NACPs may help to expand the capabilities of other acoustofluidic systems that currently primarily utilize PACPs for sensing, object manipulation, or other applications.

4.5 Materials and Methods

4.5.1 NACP production.

NACPs were produced by mixing Sylgard 184 base (Dow Chemical) with Sylgard 184 crosslinker (Dow Chemical) at a 10:1 ratio by weight to form PDMS precursor. Triethoxyvinylsilane (TEOVS, Sigma-Aldrich) was added to the precursor at 0.1% v/w and the modified precursor was mixed thoroughly. Then, a surfactant solution composed of 1% w/w

Pluronic F108 (Sigma-Aldrich) in deionized water (DIW) was added to the precursor at a 10:1 ratio of surfactant solution to precursor. The mixture was homogenized using a T10 basic homogenizer (IKA), producing an emulsion of PDMS precursor droplets in surfactant solution. The mixture was cured for 2 hours at 80ºC, yielding a polydisperse population of NACPs. To isolate a population of particles between 20–30 μm, these particles were then filtered through cell strainers (PluriStrainer) while vortexing at speeds sufficient to agitate liquid in the cell strainer. Specifically, the NACPs particles were first filtered with a 40 μm filter while vortexing to agitate the particles in the filter. Particles that passed through the filter were collected. The filter was washed with the Pluronic F108 solution occasionally to remove trapped particles. This process was then repeated with a 30 μm filter. The particles were then filtered with a 20 μm filter. Particles retained by the 20 μm filter were washed into a tube and collected. The last step was repeated once more to further reduce polydispersity.

4.5.2 NACP sizing.

Filtered NACPs were pipetted onto a glass slide. Images of the microparticles were captured by a Zeiss AxioVert A1 TL/RL inverted fluorescence microscope equipped with a Axiocam 305 mono camera (Zeiss, Germany). NACP sizes were determined by analyzing captured images via Fiji/ImageJ software.

4.5.3 Functionalization of OVA-decorated fNACPs.

Low polydispersity NACPs were functionalized by conjugating the NACPs with a biotin-PEG-silane (BPS) linker and subsequently incubating BPS-decorated NACPs with streptavidin (SA). Typically, $5x10^6$ base NACPs were washed thrice with 0.004% v/v Tween 20 (Sigma-

Aldrich) in DIW and resuspended in 50 µL of a 30 mg mL^{-1} solution of 2 kDa silane-PEG-biotin (Laysan Bio) in phosphate buffered saline (PBS). Particles were allowed to incubate for 2 hours at room temperature while mixing on a VorTemp 56 shaking incubator (Labnet) at ~600 rpm with regular agitation by hand when particle settling was noted. NACPs were washed thrice with 0.004% v/v Tween 20 in PBS (Sigma-Aldrich). NACPs were resuspended in 100 µL of 1.7 mg mL^{-1} SA or Alexa Fluor 488-conjugated SA (FSA, Thermo) in PBS and incubated for 90 min at room temperature while mixing. After incubation, NACPs were washed thrice with 0.004% v/v Tween 20 in PBS (Sigma-Aldrich) and resuspended in 200 µL of 2.5 mg mL^{-1} biotin-OVA (Nanocs) in PBS. NACPs incubated for 90 min at room temperature while mixing. Finally, the fully functionalized fNACPs were washed thrice in wash buffer composed of 1% w/v BSA (Sigma-Aldrich) in PBS. After washing, the fNACPs were resuspended in wash buffer and stored at ~4˚C until use. All wash steps in this protocol and subsequent procedures involved centrifuging the solution at 3,000xg for 3 min, aspirating the supernatant, and resuspending the pellet in the same volume of fluid. All mixing and incubation steps described in this procedure and subsequent procedures were performed in 1.5 mL low protein binding microcentrifuge tubes (Thermo).

4.5.4 Functionalization of control NACPs.

NACPs were functionalized with FSA as described earlier. Then, ~$2.5x10^6$ FSA-conjugated particles were incubated in 100 µL of 13.3 mg mL^{-1} free biotin (VWR), representing >12-fold molar excess to FSA, in PBS for 90 min while mixing at room temperature. Then, control NACPs were washed thrice in wash buffer. After washing, fNACPs were resuspended in wash buffer and stored at ~4˚C until use.

4.5.5 Evaluation of fNACP functionalization specificity.

For these studies, FSA in solution was pre-blocked with free biotin prior to incubating with fNACPs to evaluate capture specificity. Blocked FSA was produced by adding a ~12.7-fold molar excess of free biotin and incubating for 1 hour to yield a 1.7 mg mL^{-1} solution of biotin-blocked, Alexa Fluor 488-conjugated SA. NACPs were incubated with or without BPS as described earlier and subsequently incubated with FSA. MFI of particles i) without BPS or FSA, ii) without BPS but with FSA, iii) with BPS and blocked FSA, and iv) with BPS and FSA were measured using a BD FACSCelesta flow cytometer (BD).

4.5.6 Evaluation of fNACP functionalization durability.

NACPs were functionalized with FSA as described earlier and $5x10^4$ particles were diluted to 1 mL in wash buffer. Fluorescent NACPs were then trapped in a trapping channel in the dark at a flow rate of 1 mL min^{-1} with an applied signal of 30 Vpp and 741 kHz. While NACPs were trapped, an additional 1 mL of wash buffer was pulled through the channel to remove any unbound FSA. After trapping, the acoustics were disengaged, NACPs were ejected from the channel, and their fluorescence was analyzed by flow cytometry. NACPs from the same functionalization batch that were not passed through the trapping channel were used as a control.

4.5.7 Standalone fNACP assay.

$1x10^4$ control NACPs and $1x10^4$ capture fNACPs were resuspended in 100 µL wash buffer spiked with rabbit anti-chicken OVA (Biorad) over the range of 10^{-4} – 10^4 nM anti-OVA. Particles were incubated for 30 min at room temperature while mixing. After incubation, particles were washed thrice in wash buffer and resuspended in a 10 µg mL^{-1} solution of Alexa Fluor Plus 594-

conjugated donkey anti-rabbit IgG (Thermo) in PBS. Particles were again incubated at room temperature while shaking for 30 min. After incubation, we washed the particles and analyzed median fluorescence intensity of the anti-IgG on single NACPs via flow cytometry. Control NACPs were identified by FSA fluorescence.

4.5.8 Trapping channel fabrication and operation.

The trapping channel was fabricated by attaching a ~50 mm long, 1 mm x 1 mm inner width and height square glass capillary (VitroCom) to a thickness mode piezoelectric transducer with a resonance frequency of 750 kHz (STEMINC MD20T27F750S, t = 2.7 mm, d = 20 mm) using cyanoacrylate glue (Gorilla Glue Company). 24 AWG wires (Digikey), used as transducer leads, were soldered to either side of the transducer. Silicone tubing (Freudenberg Medical) was then attached to either end of the capillary and sealed with cyanoacrylate glue and Parafilm (VWR). For experiments with the acoustic pipette, a barbed Luer adapter (Fisher Scientific) was then attached to one side of the tubing. A rubber septum was cut to size from a 0.8 mm thick silicone rubber sheet (Grainger) and inserted into the Luer adapter. A 3D printed needle guide was then inserted into the adapter to compress the septum, forming a sealed injection port. The final device was then placed into a 3D-printed trapping channel. The transducer leads were coupled with leads from a waveform generator (33210A, Agilent) and amplifier (75A250AM2, Amplifier Research) connected in series. The applied frequency and voltage were measured using an oscilloscope (InfiniiVision, Keysight). Trapping channels were operated by applying a sinusoidal wave at ~750 kHz and 30 V_{pp} based on a series of optimization studies (see Supplementary Materials for details).

4.5.9 Evaluation of NACP trapping.

$5x10^4$ NACPs were resuspended in 100 µL blood (whole porcine blood with sodium-heparin, Lampire Biological Laboratories). Lysed blood samples were produced by adding 100 µL of 10x red blood cell lysis buffer (eBiosense RBC lysis buffer, Invitrogen) and 800 µL wash buffer in PBS. Unlysed blood samples were produced by adding 900 µL wash buffer. Two drops of NucBlue Live Cell Stain (ThermoFisher) were added to each sample to stain WBCs for subsequent analysis by flow cytometry. To prepare the trapping channel, 4 mL of DIW were passed through the device to clean it and to remove air. Then a 3 mL syringe (BD) was attached to a GenieTouch syringe pump (Kent Scientific). The leads of the trapping channel were attached to the waveform generator and oscilloscope, and the channel was attached to the 3 mL syringe by silicone tubing. Samples were mixed on a vortexer and then withdrawn through the device at a fixed flow rate (i.e., 0.5–6.0 mL min^{-1}) with the acoustics engaged. After the 1 mL sample had been withdrawn, 0.5 mL wash buffer was withdrawn at the same flow rate with acoustics on to wash the trapped particles and remove any residual blood components. The syringe containing the 1.5 mL of waste was removed, ejected into a 1.5 mL microcentrifuge tube, and replaced with a 1 mL syringe (BD) containing 800 µL of wash buffer. The acoustics were deactivated, and the new wash buffer was injected into the device at 2 mL/min, washing out trapped particles into an empty 1.5 mL microcentrifuge tube. The device was rinsed with DIW or wash buffer between each sample. Manual device operation experiments were performed identically, but the syringes were operated by hand rather than a syringe pump. Operators targeted a flow rate of 3 mL min^{-1} by ejecting a known volume of fluid in a set amount of time while attempting to maintain a steady flow. For experiments involving video or image captures during NACP trapping, the trapping channel was placed on an inverted microscope stage with the transducer oriented along top of the channel.

4.5.10 Flow cytometry for trapping evaluation.

All samples were analyzed for purity and retention using flow cytometry. The cytometer was operated for 90 seconds per sample. Waste samples were analyzed at a flow rate of 60 μL min^{-1}, and purified samples were analyzed at 12 μL min^{-1}. Gating involved isolation of NACPs based on forward and side scatter (see Supplementary Materials for details), while gating of WBCs involved measurement of the fluorescence of the nuclear stain. NACP retention was defined as:

$$NACP\ retention = \frac{NACP_S}{NACP_S + NACP_W} \times 100\% \tag{4.3}$$

where $NACP_S$ denotes the number of NACPs remaining in the purified sample and $NACP_W$ denotes the number of NACPs in the waste fraction. Sample purity was defined as:

$$Sample\ purity = \left(1 - \frac{WBC_S}{WBC_S + WBC_W}\right) \times 100\% \tag{4.4}$$

where WBC_S denotes the number of WBCs found in the purified sample and WBC_W denotes the number of WBCs found in the waste.

4.5.11 Acoustic pipette design and fabrication.

Most acoustic pipette components, including the main body and trapping tip, were designed in AutoCAD Fusion 360 and 3D printed on a masked stereolithography 3D printer (SL1S, Prusa Research) using Tough Black resin (Prusa Research). STL files of the main acoustic pipette components are available and described in Supplementary Materials. Printed parts were washed in isopropyl alcohol (ThermoFisher Scientific) and underwent post-print drying and curing within a curing chamber (CW1S, Prusa Research) before device assembly. Parts were designed to be

assembled through pressure fitting. Chambers in the main body consisted of a single 3 mL syringe and two 1 mL syringes (BD), and 25 G needles (BD) were used to pierce the injection port of the trapping tip. Pipette assembly schematics are available in Supplementary Materials (Fig. D.7 and D.8).

4.5.12 Acoustic pipette-enabled assay.

The acoustic pipette was typically prepared by filling Chamber 1 with 100 µL of a 40 µg mL^{-1} solution of Alexa Fluor Plus 594-conjugated donkey anti-rabbit IgG, Chamber 2 with 400 µL wash buffer, and Chamber 3 with 1 mL wash buffer. Capture fNACPs and control NACPs were resuspended in 100 µL of whole porcine blood with spiked anti-OVA spanning 10^{-3} – 10^{3} nM. Samples incubated outside of the pipette in 1.5 mL microcentrifuge tubes for 30 min while mixing at 1020 rpm on a VorTemp mixer. Samples were then diluted to 1 mL with wash buffer from Chamber 3 of the pipette. Samples were then withdrawn from the sample tube with acoustics engaged, trapping the particles in the channel, while the waste blood was pulled into Chamber 3 for containment. The particles were then further washed by pulling 500 µL fresh wash buffer through the channel and into Chamber 3. The trapping tip was then switched to Chamber 1, the acoustics were disengaged, and the particles were withdrawn into Chamber 1 to be labeled by the fluorescent secondary antibody. Particles were then incubated for 30 min in Chamber 1. After incubation, the particles were passed back into the trapping tip with acoustics engaged. Particles were further washed by switching back to Chamber 3 and withdrawing 500 µL fresh wash buffer past the trapped particles. Finally, the trapping tip was switched to Chamber 2, the acoustics were disengaged, and the particles were ejected into sample tubes for analysis by flow cytometry. To generate a concentration response curve, this procedure was repeated for each concentration of

anti-OVA in spiked in whole blood. After each sample was processed, NACPs were removed from the device and placed on a rotator during incubation for 36 min to allow time for the concurrent processing of multiple samples. After all samples were processed, samples were inspected by flow cytometry as described earlier.

4.5.13 Custom fluorimeter design, assembly, and use.

The custom fluorimeter consisted of the main fluorimeter housing, filtering optics, photodetector, photodiode amplifier, LED driver, LED, data acquisition unit, and computer. The main housing blocked external light and held the cuvette sample, aligning it to the incoming LED light. A pipette docking cap sat on top of the housing and allowed the pipette to mate with the fluorometer housing and inject a sample into the cuvette below. The main fluorimeter housing, pipette docking cap, SP and LP filter holders, and photodiode holder were designed using AutoCAD Fusion 360 and 3D printed in matte black PLA using a Bambu Labs P1S 3D printer. STL files of the main housing and associated components are available and described in more detail in the Supplementary Materials. A commercially available LED driver (Thorlabs) set to 700 mA drove a high-power 9.9 mW, 565 nm fiber-coupled LED. Emitted LED light traveled through a 1 m long and 400 μm diameter multimode SMA-SMA fiber patch cable (Thorlabs) to a threaded SMA to SM1 fiber adapter (Thorlabs) with a 20 mm focal length collimating lens, mounted in one of the four 25.4 mm housing side ports. Light was filtered through a 600 nm SP filter (Thorlabs) before entering the cuvette chamber. Collimated light striking the Alexa Fluor Plus 594 fluorophore on fNACPs inside the cuvette caused fluorescence emission with a peak at 617 nm. Photons emitted 90 degrees relative to the incident light passed through a 590 nm LP filter with a 610 nm pass wavelength (Edmund Optics) before being received by a silicon photodiode with

350–1100 nm sensitivity (Thorlabs). Photocurrent produced by the silicon photodiode was measured by a benchtop photodiode amplifier (Thorlabs), producing a ±10 V analog output with a gain A_{PD} of 10^8 ± 5%. Notably, this photodiode amplifier can be replaced by a custom credit card-sized electronics board to further enhance portability of the fluorimeter in future iterations. Analog output was acquired with a portable USB oscilloscope (Digilent) and the waveform was recorded on a laptop to a CSV file using Waveforms (Digilent) at a rate of 100 Hz. Resulting signal characteristics and statistics were processed using Microsoft Excel. Additional details regarding specific components, part numbers and function of the custom fluorimeter can be found in the Supplementary Materials.

4.5.14 Custom fluorimeter-enabled assay.

$1x10^5$ capture fNACPs functionalized with OVA were resuspended in 1000 µL wash buffer spiked with rabbit anti-chicken OVA (Biorad) over the range of 10^1 – 10^3 nM anti-OVA. Particles were incubated for 30 min at room temperature while mixing. After incubation, particles were washed thrice in wash buffer and resuspended in a 10 µg mL^{-1} solution of Alexa Fluor Plus 594-conjugated donkey anti-rabbit IgG (Thermo) in PBS. Particles were again incubated at room temperature while shaking for 30 min. After incubation, particles were washed, resuspended in 100 µL wash buffer, transferred to the fluorimeter cuvette, and finally analyzed using the custom fluorimeter. Fluorescence measurements were taken immediately after transferring the fNACPs to the cuvette to ensure particles were suspended during measurements.

4.5.15 5PL Fitting.

Concentration response curves, shown in Figs. 4.5B and 4.7B, were fit with a five-parameter logistic (5PL) curve to determine the LOD. To do so, we fit experimental data to the standard 5PL equation, given by:

$$y = b + \frac{a - b}{\left(1 + \left(\frac{x}{c}\right)^{d}\right)^{g}} \tag{4.5}$$

where y is the fluorescence intensity, x is the anti-OVA concentration, c is the mid-range concentration, d is the slope factor, a and b are the fluorescence intensities at the minimum and maximum anti-OVA concentrations, respectively, and g is the asymmetry factor. MATLAB was used for all fitting. LOD was determined by identifying the concentration at which the response was 3 standard deviations above the background response (i.e., NACPs without any fluorescent labels), as predicted by the curve fit. To confirm the fits were acceptable, we calculated percent relative error of experimentally measured values relative to those predicted by the fits and ensured that average relative error at each concentration fell below 25%. This data, along with fitted parameters for both standard curves shown in Figs. 4.5B and 4.7B, can be found in Fig. D.10 and Table D.l of the Supplementary Materials.

4.5.16 Statistical analysis.

Statistical analyses were performed using Microsoft Excel. Differences between groups were compared by one-tailed Student's t-tests, and $P < 0.05$ was considered significant in the analyses. All quantitative data is expressed as the mean ± standard deviation.

4.6 Acknowledgments

The authors would like to thank the Packard Foundation for their support of this project. The authors additionally thank Alexandra Dalton for help in performing acoustic pipette-based assay experiments.

4.7 Author Contributions

Conceptualization: CPT, JPF, PM, KJ, AKN, GPL, CWS

Data curation: CPT, JPF

Formal analysis: CPT, JPF, CWS

Funding acquisition: AKN, GPL, CWS

Investigation: CPT, JPF, PM

Methodology: CPT, JPF, PM, JZ, KJ, AKN, GPL, CWS

Project administration: PM, KJ, CWS

Resources: PM, KJ, CWS

Supervision: CPT, PM, JZ, KJ, AKN, GPL, CWS

Validation: CPT, JPF, PM, KJ, CWS

Visualization: CPT, JPF, PM, KJ

Writing—original draft: CPT, JPF, PM, CWS

Writing—review & editing: CPT, JPF, PM, JZ, KJ, AKN, GPL

Chapter 5: Siphon-based multichannel acoustic separator and biospecific, acoustic-responsive microparticles for high-throughput, tunable biomolecule detection

The contents of Chapter 5 will be submitted as a manuscript in Fall of 2024. Coauthors on this manuscript will include Creighton T. Tisdale and Dr. C. Wyatt Shields IV.

5.1 Abstract

Quantitative detection of biomolecules is essential in personal healthcare, public health surveillance, and environmental monitoring. However, purification of biomolecules from complex fluids can be challenging and often necessitates extensive sample pretreatment and involved workflows. Here, we present a multichannel acoustic separator and complementary biospecific, acoustic-responsive particles to simplify workflows and shorten the time needed to isolate and detect biomarkers from complex fluids. The multichannel acoustic separator is predominantly 3D printed and supports 12 acoustofluidic trapping channels that rapidly and effectively trap and isolate the biospecific particles from off-target contaminants in the fluid. Fluid flow through the channels is mediated by a semi-continuous siphon, which eliminates the need for fluid pumps and enhances the accessibility of the technology. Using this system, we show the sensitive detection of three disparate biomolecules in individual and multiplexed formats, as well as the detection of IgA from whole blood in approximately 70 minutes.

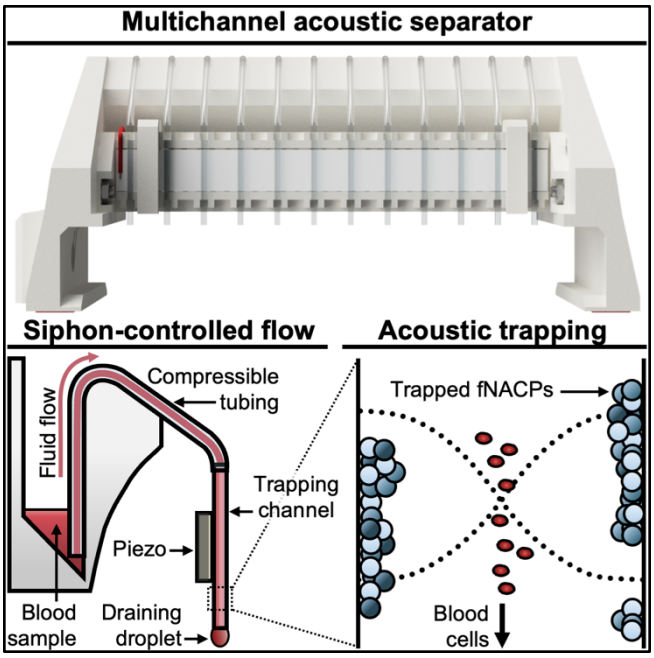

Figure 5.1. Graphical abstract. Overview of siphon-controlled flow and acoustic trapping within the multichannel acoustic separator.

5.2 Introduction

Quantitative detection of biomolecules is essential for a myriad of laboratory-based techniques including clinical diagnosis,[181–183] wastewater analysis for public health surveillance,[184,185] environmental monitoring,[186,187] and more. However, purification of target biomolecules can be challenging, especially when isolating molecules from complex samples like whole blood or other fluids that are crowded with off-target molecules, cells, or contaminants that can interfere with the specific isolation and detection of target molecules. Because of this, many biomolecule detection approaches require extensive sample preprocessing.[188] Moreover, many of the mainstay approaches for quantitative biomolecule detection, such as ELISA, involve substantial user engagement, long processing times, and complex workflows.[21,189] A number of technologies have been developed to simplify molecule isolation workflows. For example, magnetic bead-based separation is often employed to capture and isolate molecules and cells from

complex samples.[71,72] However, this approach can involve long separation times (i.e., multiple minutes before wash steps), is not easily scalable, and is prone to particle loss during particle wash steps, ultimately resulting in the loss of target molecules.[73–75]

In recent years, numerous acoustofluidic systems, which utilize ultrasound waves to manipulate particles and molecules in small fluid samples, have emerged as a promising technology for the isolation of a host of target molecules and objects.[190,191] Such systems have been demonstrated to be effective for the isolation of circulating tumor cells,[170,192] proteins,[193,194] and the and exosomes,[195] among other targets. Notably, acoustofluidic separation has been shown to be sufficiently gentle for the handling of fragile samples, such as cells, proteins, and extracellular vesicles. However, the majority of the acoustofluidic separation systems demonstrated to date cannot achieve separation at high flowrates and are thus unable to process samples at speeds necessary for widespread adaptation. Moreover, the vast majority of acoustofluidic separation approaches require the use of automated pumps for fluid actuation, which increases the barrier to implementation of such systems in laboratory settings. In our previous work, we developed a pump-free, handheld acoustic pipette for the rapid isolation and detection of biomolecules in under 70 minutes.[196] The acoustic pipette was designed for toward-point-of-care use and was only capable of processing one sample at a time, which limits its practicality in laboratory workflows that require high-throughput sample processing.

Here, we present a siphon-driven multichannel acoustic separator and a class of biospecific, acoustic-responsive particles for the simple, rapid, and high-throughput purification and detection of biomolecules in laboratory settings. The siphon-driven multichannel acoustic separator consists of 12 acoustic trapping channels for the concurrent processing of 12 samples within minutes. All fluid actuation through the 12 channels is mediated by a simple siphon, eliminating the need for

automated pumps or manual fluid manipulation. Each of the 12 channels supports a half-wavelength bulk acoustic standing wave which yields pressure nodes at the center of each channel and antinodes along the walls of each channel. The particles, termed functional negative acoustic contrast particles (fNACPs), are designed to specifically capture biomolecule targets from complex fluid samples, like whole blood. After capture of biomarkers, the fNACP samples are passed through the trapping channels of the device. Due to their negative acoustic contrast, the fNACPs are trapped strongly along the walls of the channel whereas other objects, such as red and white blood cells, are focused to the center of the channels and leave the channels as waste. The separation of NACPs by acoustic trapping occurs in seconds, and washing the particles requires only 1-3 minutes, depending on the fluid type. After washing the trapped fNACPs, the acoustics can be disengaged to collect the purified fNACPs in a 96-well plate (Fig. 5.2A, 5.2B). The biomolecules on the surfaces of fNACPs are then fluorescently labeled for downstream biomolecule quantification by fluorescence measurement.

We demonstrate use of the acoustic separator for the rapid and efficient purification of fNACPs from water and whole blood samples (Fig. 5.2C, 5.2D). We additionally show the simultaneous (i.e., multiplexed) isolation and detection of three biomolecules (i.e., anti-ovalbumin immunoglobulin G (IgG), immunoglobulin A (IgA), and immunoglobulin M (IgM)) by fluorescently barcoded fNACPs and show rapid isolation and detection (i.e., in < 70 min) of IgA from whole blood using the multichannel acoustic separator (Fig. 5.2E). While we demonstrate serological protein biomolecule detection here, the fNACPs and multichannel separator are not limited to this application; by modifying fNACP chemistry, the system could be beneficial for the rapid isolation and detection of a myriad of molecules or objects from various fluid samples for a wide range of applications (e.g., cell isolation, wastewater analysis, immunoprecipitation and

elution, or sample cleanup by negative selection). By eliminating the need for fluid pumps and enabling the rapid and simultaneous separation of 12 samples, the multichannel acoustic separator represents one of the fastest, simplest, and most accessible implementations of acoustofluidic separation technologies to date.

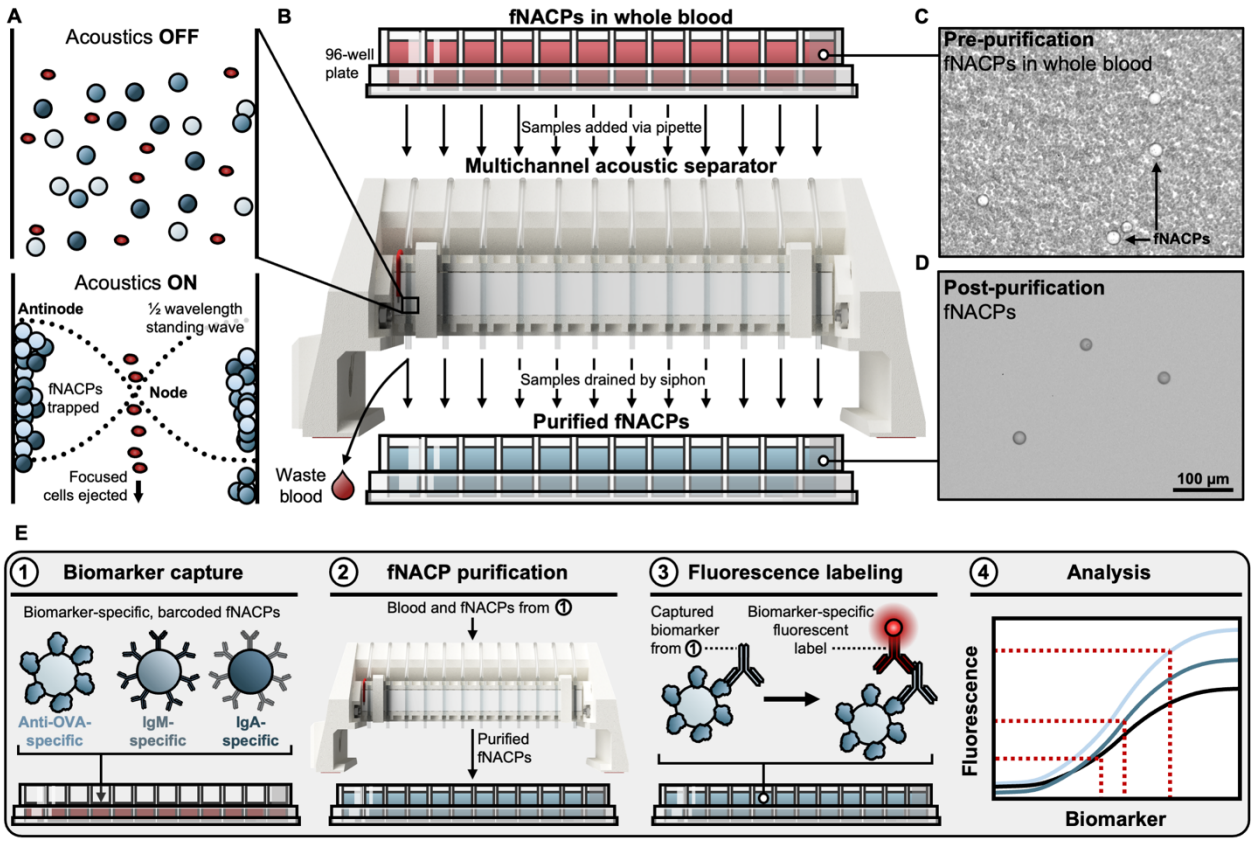

Figure 5.2. Multichannel separator and fNACP-based assay overview. A) Schematic representation of fNACPs being trapped along the walls of a channel at the antinodes of a standing wave for purification from blood samples. B) Schematic overview of the multichannel acoustic separator and the purification of fNACPs from whole blood in a 96-well plate format. C) Brightfield microscopy image of fNACPs mixed with whole blood prior to purification using the multichannel acoustic separator. D) Brightfield microscopy image of fNACPs after purification from whole blood using the multichannel acoustic separator. E) Schematic representation of the workflow for fNACP-based biomarker detection.

5.3 Results

5.3.1 The multichannel acoustic separator is 3D printed and holds a trapping channel array

To develop a multichannel acoustic separator that is easily integrated into existing laboratory workflows, we designed the device to interface with 96-well plates and 12-channel multichannel pipettes for the simultaneous processing of 12 samples. The separator consists of 5 main printed parts: the upper siphon chamber array, a trapping channel array holder, a left and right side, and an electrical port cover (Fig. 5.3A, 5.3B, E.1). The trapping array consists of 12 1x1 mm inner width and height glass capillaries that are approximately 25 mm in length, all affixed to a piezoelectric transducer possessing a resonance frequency of ~750 kHz. Two 3D printed transducer clips keep the transducer in position during use. Each capillary is connected to one chamber of the upper siphon chamber by compressible silicone tubing. Electrical leads for transducer operation are routed through the device to the electrical ports, which interface with common banana plugs.

When liquid samples are present in the channels of the separator, actuation of the piezoelectric transducer by application of a ~750 kHz alternating current sine wave results in establishment of half-wavelength standing acoustic waves within each channel. Because of this, acoustic radiation forces are exerted on objects smaller than the acoustic wavelength within each channel. The axial component of the primary acoustic radiation force (i.e., acting perpendicularly to the length of the channel) pushes objects toward either the node of the standing wave, located along the centerline of the channel, or the antinodes of the standing wave, located at the walls of the channel (Fig. 5.2A). The direction of this force is dependent on the acoustic contrast factor of the objects or particles, which can be positive or negative and describes the density and compressibility of the objects relative to that of the liquid in which they are suspended. Positive

acoustic contrast particles (PACPs) are forced to the nodes of the standing wave, whereas negative acoustic contrast particles (NACPs) are forced to the antinodes. Most cells and polymeric particles, including red and white blood cells, exhibit positive acoustic contrast when suspended in water or blood.[196,197] Here, to enable rapid separation from whole blood samples, we designed the fNACPs to have strong negative acoustic contrast. Importantly, the standing waves also exert primary acoustic radiation forces in the lateral direction (i.e., parallel to the length of the channel), as well as secondary acoustic radiation forces, which are attractive between particles at close distances. Because the fNACPs are forced to the channel walls where flow rate is low, relative to the center of the channel, and because of the secondary and lateral primary acoustic radiation forces, fNACPs can be strongly trapped against the channel walls at high flow rates while blood components are washed from the channels.[155,196,198] Such trapping of NACPs results in the ability to conduct acoustofluidic separation and purification at flow rates much higher than that traditionally achieved by systems that utilize only PACPs.[160–162]

5.3.2 Fluid actuation in the device is driven by siphon, allowing for repeated sample washing

To eliminate the need for pumps for actuation of fluid through the 12 trapping channels, we designed the multichannel acoustic separator such that fluid flow through each channel is driven by a siphon. To do so, we created an upper siphon chamber array that has 12 3D printed chambers that can accommodate ~1200 μL of liquid. The silicone tubing attached to the top of each capillary extends up and over the lip of the siphon array and down into the bottom of a singular siphon chamber where it is locked in place by pressure fitting (Fig. 5.3C). To prime the siphon for each channel, approximately 600 μL of liquid, typically wash buffer composed of 0.05% Tween20 in phosphate buffered saline (PBS), is added to the siphon chamber. The silicone tubing is

depressed by manual manipulation, drawing fluid from the chamber over the highest point of the tubing and down into the glass capillary. The fluid then drains by a siphon effect, and draining fluid exits from the tip of the capillary in discrete droplets. The droplet formation at the end of the capillary is driven primarily by hydrostatic pressure generated by liquid in the upper siphon chamber, and droplet breakoff occurs when the magnitude of the force of gravity on the droplet exceeds that of the surface tension forces holding the droplet to the capillary.[199,200]

In general, ideal large-scale siphons with a non-submerged outlet at a height below the inlet will drain fluid in the upper chamber until it reaches the height of the inlet, resulting in introduction of air to the siphon tubing and inability to restart the siphon without repriming.[201] However, the miniaturization of this siphon allows for the siphon stopping point to occur above the inlet before complete draining of the chamber. Because the liquid in each channel exits the channels as discrete droplets, the pressure driving the fluid flow must overcome the Laplace pressure associated with droplet formation at the liquid-air interface, which is proportional to the surface tension of the liquid.[202–205] By carefully tuning the height of the channel outlet relative to the channel inlet (ΔH in Fig. 5.3C), the Laplace pressure can be balanced with the hydrostatic pressure in the upper siphon chamber to arrest fluid flow before the height of the fluid in the upper siphon chamber reaches that of the inlet. This effect is similar to that utilized in capillary pressure control valves that utilize Laplace pressure to mediate flow in microfluidic devices.[206] To minimize the volume of fluid retained at the siphon stopping point, which is essential for effective washing and fluid exchange, we designed the upper siphon chambers to taper toward the tubing inlet at the bottom of the chamber. Upon addition of fluid to the upper chamber, typically 300 μL of wash buffer or diluted blood, the siphon effect is recovered, and the fluid again drains until reaching the liquid equilibrium height. An exact description of the fundamental physics governing the siphon

operation, which may involve frictional losses in the channels, differential capillary forces in varied sections of the channels, inertial effects, and perturbations of forming droplets by the piezoelectric transducer, is reserved for future work.[199,200,207] However, to confirm that the Laplace pressure at the outlet is the primary mechanism responsible for arresting the siphon function prior to complete draining, we tuned the ΔH of the separator such that the siphon stopping point was above the inlet when water was added to the upper siphon chambers and confirmed through repeated addition of 300 μL of water that the siphon repeatably stopped prior to full draining. We then submerged the end of the capillary in water to remove the liquid-air interface and, as a result, the Laplace pressure associated with droplet formation. We experimentally confirmed that the removal of this interface both after and prior to siphoning from the upper chambers resulted in full draining of the upper chamber and introduction of air to the channel.

Because the siphon effect in this device is semi-continuous (i.e., does not require more than one priming step), washing samples or transferring them to new fluids is extremely simple (Fig. 5.3D). For example, after priming a channel, an initial sample of fNACPs in whole blood can be added to the upper siphon chamber. As the sample is drawn through the channel via siphon, fNACPs are trapped over the trapping array. Upon cessation of flow at the siphon stopping point, wash buffer or other fluids can be added to the upper siphon chamber to wash away blood components into a waste container positioned below the device. This process can be repeated until the fNACP samples are sufficiently clean. The acoustics can then be disengaged, and fluid can again be added to the upper siphon chamber to release the fNACPs, which are collected in a 96-well plate positioned on the device. While this trapping and fluid transfer process was used to wash fNACPs in this work, it could also be used to transfer particles into labelling solutions, to functionalize particles in protocols similar to layer-by-layer coating, or to accomplish other tasks.

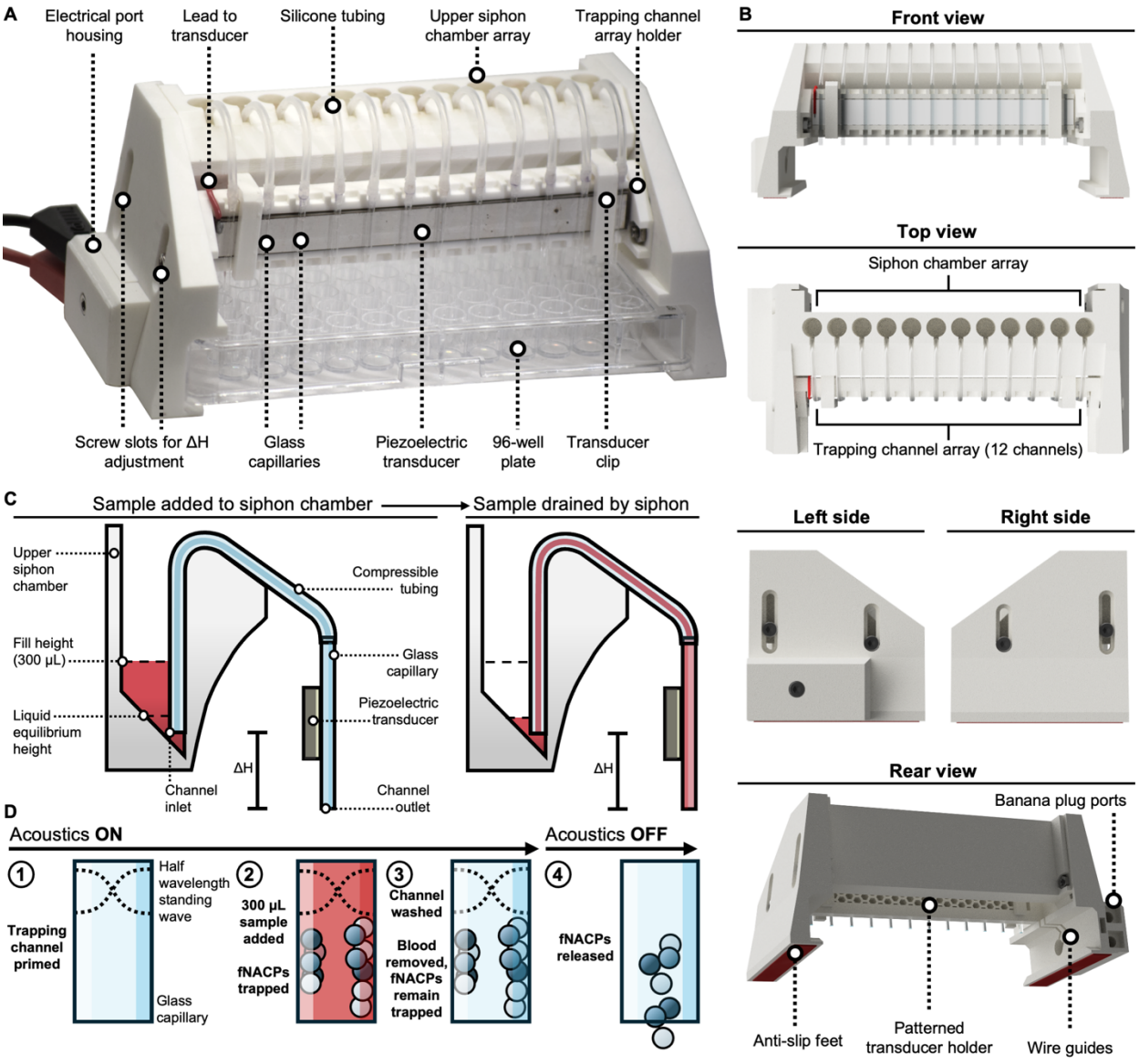

Figure 5.3. Overview of the multichannel acoustic separator design and use. A) Image and details of the assembled multichannel acoustic separator. B) Rendered images and details of the multichannel acoustic separator. C) Schematic representation of the upper siphon chamber upon addition of sample and after draining. D) Schematic representation of the fNACP purification process within a glass capillary mounted on the trapping channel array.

5.3.3 Siphon-based flow enables washing of blood from channels

To assess the ability to wash blood, which is replete with red blood cells, white blood cells, platelets, and other components, from the siphon chambers and channels of the acoustic separator, we adjusted ΔH such that the equilibrium liquid level was minimized (i.e., below the sloped section of the chamber but above the channel inlet) when blood was present in the device and then primed the channels with wash buffer. We then added 300 μL of 3X diluted porcine blood to the upper siphon chambers and allowed all channels to reach equilibrium (Fig. 5.4A). We then washed the channels by repeated addition of wash buffer to the siphon chambers and collected the fluid leaving the channel outlet. We diluted the collected samples by 13.3X in order to measure absorbance of the samples at 542 nm, an absorbance peak characteristic of whole blood (Fig. 5.4B, E.2). Because the samples collected from the first wash were primarily whole blood, absorbance by the samples was substantial and measurement of absorbance was not possible. However, we found that after 4 washes, the fluid remaining in the channels of the separator was sufficiently devoid of blood components. The absorbance of the collected was only 3.2 ± 0.3% of that collected after the second wash, whereas buffer alone had an absorbance that was 2.1 ± 0.3% of that collected after the second wash. Therefore, in remaining studies that required isolation of fNACPs from whole blood, the channel was washed 4X before collecting fNACPs. We repeated this general process for the washing of water-based samples and found that 2 washes were sufficient to clear the channels (Fig. E.3).

5.3.4 Siphon-based flow allows for processing of disparate fluid types

The fNACP assay involves flow of both blood and buffer through the device channels. Blood and buffer differ in their surface tensions, viscosities, and other fluid characteristics, which

ultimately results in different behavior when actuated by the siphon.[208,209] To explore these differences and to confirm the ability to process the disparate fluid types in the separator, the ΔH was manually adjusted until the fluid equilibrium height in all siphon chambers was minimized for water, buffer, and blood. Because the surface tension of water is greater than that of blood (i.e., ~71 mN m^{-1} for water versus ~51 mN $m^{-1}$for blood), the Laplace pressure at the outlet is more substantial for water samples, resulting in minimization of the fluid equilibrium height at larger ΔH values (~14 mm for water and buffer versus ~11 mm for blood). We captured videos of all three fluids draining by siphon after the addition of 300 μL of each fluid to the upper siphon chambers with the acoustics engaged. The chambers were considered fully drained when dripping of fluid in all channels had ceased for at least 10 s. Upon analysis of the videos, we plotted average volume drained from each channel over time (Fig. 5.4C). It should be noted that the flow is not continuous but rather pulsatile in nature, with the periods between droplets increasing as the fluid level in the upper chamber, and therefore hydrostatic pressure, drops. We found that water was drained by the siphons (t = ~17 s) more quickly than buffer (t = ~26 s) and blood (t = ~79 s).

One concern in acoustofluidic systems is that high flow rates may result in inability to trap NACPs, which would ultimately lead to loss of captured biomolecules in this system. Previously, we showed that in a similar system, NACPs of comparable size were trapped and retained at high percentages up to approximately 5 mL min^{-1}.[196] The maximum flow rates in the multichannel acoustic separator presented in this work were estimated by finding the slope of linearly fits to the first 10 s of the recorded volume per time plots for water, buffer, and blood. The maximum estimated flow rate was found to be 1.6 mL min^{-1} for water, and we speculated that these flow rates would be low enough to allow effective trapping of NACPs in the device.

5.3.5 Production of NACPs yields low-polydispersity particles

To produce non-functionalized NACPs, we followed a previously described protocol to produce low-polydispersity NACPs.[196] In short, NACPs were produced by homogenization of polydimethylsiloxane (PDMS) precursor with 0.1% v/w triethoxyvinylsilane (TEOVS) submerged in water with 1% Pluronic F108 surfactant. After curing the homogenized precursor droplets, we filtered the mixture to isolate a low-polydispersity fraction of NACPs. The resultant NACP population had a mean diameter of 23.0 μm and a coefficient of variance of 11.8%.

5.3.6 NACP trapping within the multichannel acoustic separator is efficient and rapid

To evaluate trapping of NACPs withing the separator, we first mixed NACPs coated with fluorescent protein in wash buffer at ~$1.7x10^5$ particles mL^{-1}. To this mixture, we added ~5 μL of a 5 wt% solution of 5.1 μm fluorescent polystyrene (PS) particles as a PACP model. We passed the particle solution through a trapping channel situated on a fluorescent microscope at 1 mL min^{-1} via syringe pump. Upon engaging the acoustics, the NACPs trapped rapidly against the walls of the channel while the PS PACPs continued through the middle of the channel without being trapped (Fig. 5.4D).

To more rigorously evaluate the trapping of the NACPs, we evaluated the trapping efficiency of NACPs from both water and blood (Fig. 5.4E, 5.4F). In biomolecule detection experiments, fNACPs are collected in a single step upon the addition of 300 μL of wash buffer after acoustics are disengaged. To assess what percent of the total NACPs are collected during this step and determine what percent is lost during the wash steps, we added $5x10^4$ NACPs to 300 μL samples of water and blood. We used the multichannel acoustic separator to trap the NACPs, wash the NACPs, and collect the NACPs. For samples in water, we washed twice; for samples in blood,

we washed four times. After NACP collection, we also washed the channels twice to flush any residual NACPs from the channels. We collected the fluid leaving the channels during each step (i.e., the initial addition of sample, the individual washes, the collection, and the residual washes). We enumerated the NACPs via flow cytometry and found that the effective NACP recovery was over 90% for purification from both water and blood samples. We further determined steps at which particle loss was occurring and found that the most substantial, though minor, loss occurred during the initial addition of sample (Fig. 5.4G). We speculated that this loss was due in part to the absence of already trapped NACPs in the trapping channels as the first NACPs in the sample passed through the channel. Because these initial particles would not be attracted to already trapped particles by secondary acoustic radiation forces, they are more prone to passing through the device without being trapped. This loss could be mitigated by used of trapping channels pre-seeded with NACPs along the channel walls, though implementation of this trapping channel feature is left to future work. Some loss also occurred during the collection step, as evidenced by the presence of some NACPs in the residual samples. This minor loss of particles could be avoided by future redesign of the acoustic separator to achieve higher flowrates during the collection step. Upon analysis of samples prior to and after purification via microscopy, we found that the purification method was successful in removing the vast majority of contaminants (i.e., red and white blood cells) from samples (Fig. 5.4H), which agrees with findings in previous work.[196]

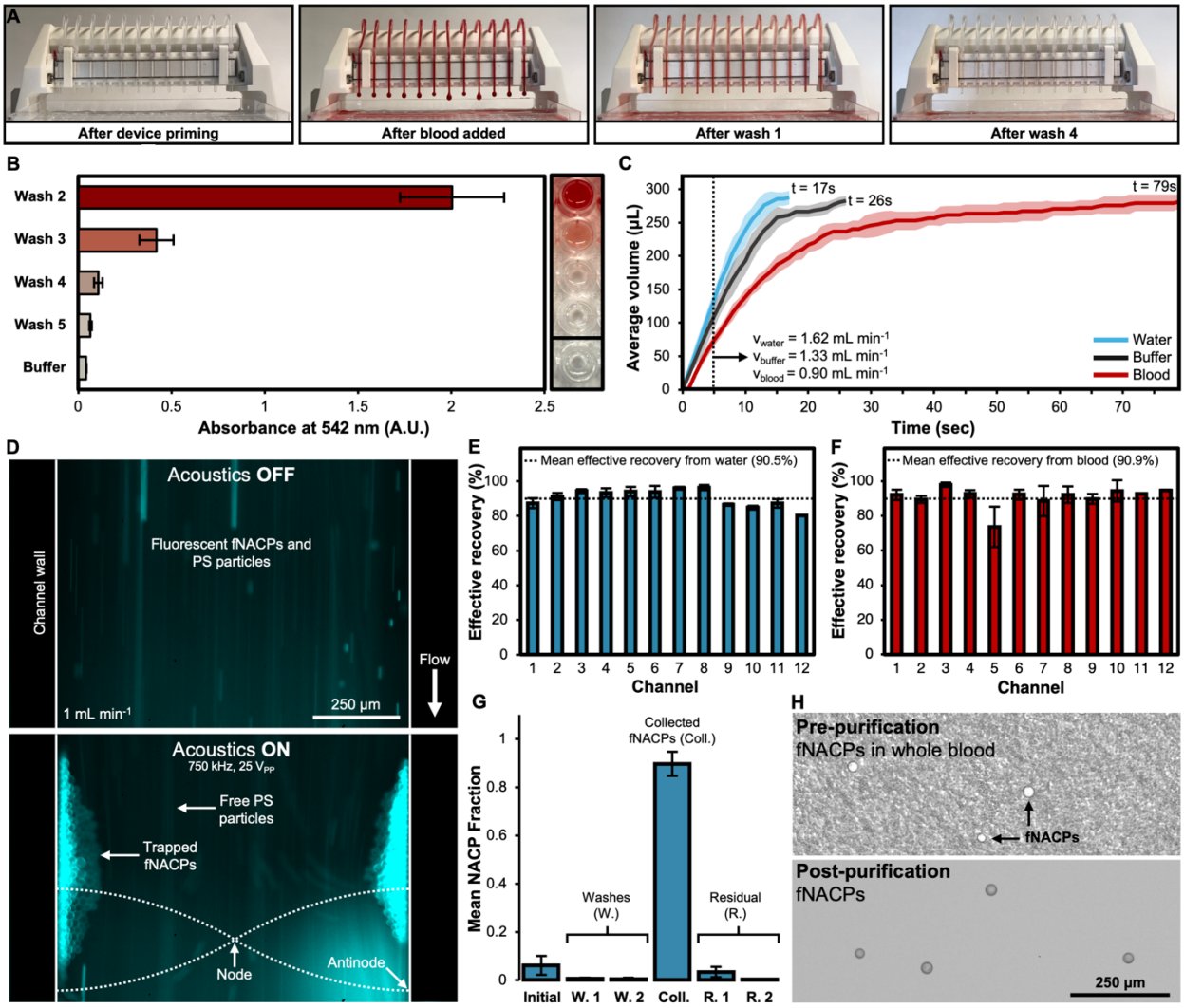

Figure 5.4. Characterization and performance of washing and trapping in the multichannel acoustic separator. A) Images of the multichannel acoustic separator at various stages of processing a blood sample. B) Absorbance of drained samples upon consecutive washes with buffer after an initial addition of whole blood to the multichannel acoustic separator. N=12, error bars indicate s.d. C) Estimated flow rate and volume per channel over time after the addition of water, buffer, and blood samples to the multichannel acoustic separator. Flow rate was estimated by linear fits of the first 5 s of each plot. D) Fluorescence microscopy images of fluorescent fNACPs and PS particles before and after engaging acoustics under an applied flow of 1 mL min^{-1}. E) Effective recovery of fNACPs from water in each of the 12 channels of the separator. All channels were washed twice. N=3, error bars indicate s.d. F) Effective recovery of fNACPs from blood in each of the 12 channels of the separator. All channels were washed four times. N=3, error bars indicate s.d. G) Mean NACP fraction recovered during the initial addition of sample, first and second washes, collection of fNACPs, and first and second residual washes. N = 12, error bars

indicate s.d. H) Brightfield microscopy images of fNACPs before and after purification from whole blood using the multichannel acoustic separator.

5.3.7 fNACP functionalization enables versatile biomarker specificity

The detection and enumeration of multiple antibodies and antibody isotypes in a clinical setting can be especially informative in assessing the state of, and immunological response to, infectious diseases in patients.[210] Multiplexed assays, which simultaneously detect multiple biomarkers in a single assay, can significantly enhance diagnostic confidence in such situations. However, conventional detection assays, such as ELISA, are generally not suitable for rapid multiplexed detection. Here, in addition to demonstrating isolation of a target biomarker from whole blood samples using the multichannel acoustic separator, we additionally aimed to create fNACPs with varied specificities to demonstrate the ability to create a multiplexed fNACP assay that can be easily analyzed by common laboratory-based fluorescence detection methods (i.e., flow cytometry).

To produce fNACPs we incubated NACPs with biotin-polyethylene glycol (PEG)-silane (BPS), followed by streptavidin (SA), followed by varied biotinylated biorecognition elements (BREs). The PEG chains of the BPS provide antifouling properties and additionally allow greater flexibility of the BRE to enhance biomolecule capture, relative to BREs immobilized on a solid surface.[101,107] As SA contains 4 biotin-binding sites, its use during the functionalization allows facile tuning of fNACP specificity by attachment of assorted biotinylated BREs (Fig. 5.5A).[105] In this study, we functionalized fNACPs for the capture of three distinct biomolecules: anti-OVA IgG, IgM, IgA. To enable detection of anti-OVA, IgM, and IgA, we functionalized fNACPs with OVA, anti-IgM, and anti-IgA BREs, respectively. To label and detect captured biomarkers by flow cytometry, we utilized red fluorescent anti-IgG, anti-IgM, and anti-IgA secondary labels (Fig.

5.5B). The target biomolecules in this work were selected to serve as diverse model biomarkers and vary in species type (i.e., mouse and rabbit), structure (i.e., monomeric anti-OVA, pentameric IgM, dimeric IgA) and size (i.e., ~150 kDa for anti-OVA, ~900 kDa for IgM, and ~500 kDa for IgA).[211] We additionally created control NACPs that can be included in each fNACP assay to reveal assay errors, such as increased fNACP fluorescence arising from nonspecific adsorption of biomolecules onto fNACPs. Instead of being modified with biotinylated BREs, the control NACPs are instead modified with biotinylated bovine serum albumin (BSA), which is a commonly utilized blocking protein. As specific binding of target biomolecules or secondary labels to BSA is not anticipated, the use of control NACPs alongside fNACP assays allows users to easily identify assay inaccuracies during fluorescence analysis. If control NACPs exhibit red fluorescence on the order of that recorded for fNACPs, the assay would be considered invalid and would require retesting.

Finally, to easily distinguish the control NACPs and three fNACP types, we functionalized the different groups with varied ratios of blue fluorescent SA to nonfluorescent SA during the SA incubation step. This yields particle groups that are fluorescently barcoded for simple distinction using flow cytometry. By gating the particles based on fluorescence and a size parameter (e.g. forward side scatter), each of the four NACP types can be easily distinguished and individually assessed for secondary label fluorescence (Fig. 5.5C).

5.3.8 fNACP assays enable sensitive biomolecule detection over a large dynamic range

To evaluate the performance of the three fNACP assays, we mixed 10^4 anti-OVA-, IgM-, or IgA-specific fNACPs and 10^4 control NACPs with 100 μL of PBS spiked with anti-OVA, IgM, or IgA, respectively, over multiple orders of magnitude (i.e., yielding sub-picomolar to micromolar

biomolecule concentrations). After a 30-minute incubation in a 96-well plate, we washed the particles and resuspended them in their respective labelling solutions, all at 10 μg mL^{-1}. After an additional 30-minute incubation, we again washed the particles and then analyzed particle fluorescence via flow cytometry. For all three assays, the generated standard curves exhibited an expected logarithmic increase in fluorescence as biomolecule concentration increased (Fig. 5.5D, 5.5E, and 5.5F). While the control NACPs displayed some elevation in fluorescence as biomolecule concentration increased, their fluorescence intensities were multiple orders of magnitude below that of the fNACPs, indicating acceptable assay function. This minor increase in fluorescence of the control particles could be mitigated by future optimization of the particle antifouling layer. To determine assay sensitivity, we fit the standard curves with 5 parameter logistic (5PL) curves and determined the sensitivity by calculation of the limit-of-detection (LOD), defined as the biomolecule concentration that yields fNACP fluorescence intensities 3 standard deviations above that of the background, based on the fit curves. The LOD of the anti-OVA, IgM, and IgA assays were 0.02 nM, 3.0 pM, and ~0.25 pM, respectively. These sensitivities are competitive with and on the same order as that of commercial ELISA assays, a finding that highlights the potential for implementation of the fNACPs assays in laboratory workflows.[212–214] In the case of IgA detection, the sensitivity was found to in fact be an order of magnitude lower than that of the commercial ELISA kit. Through these results, we additionally demonstrated the ability to capture a range of biomarker types through simple modifications to the fNACP functionalization. By tuning the specificity of the fNACPs, the assay could be adapted for the detection and evaluation of a range of clinically relevant biomarkers, rather than the model biomarkers evaluated here.

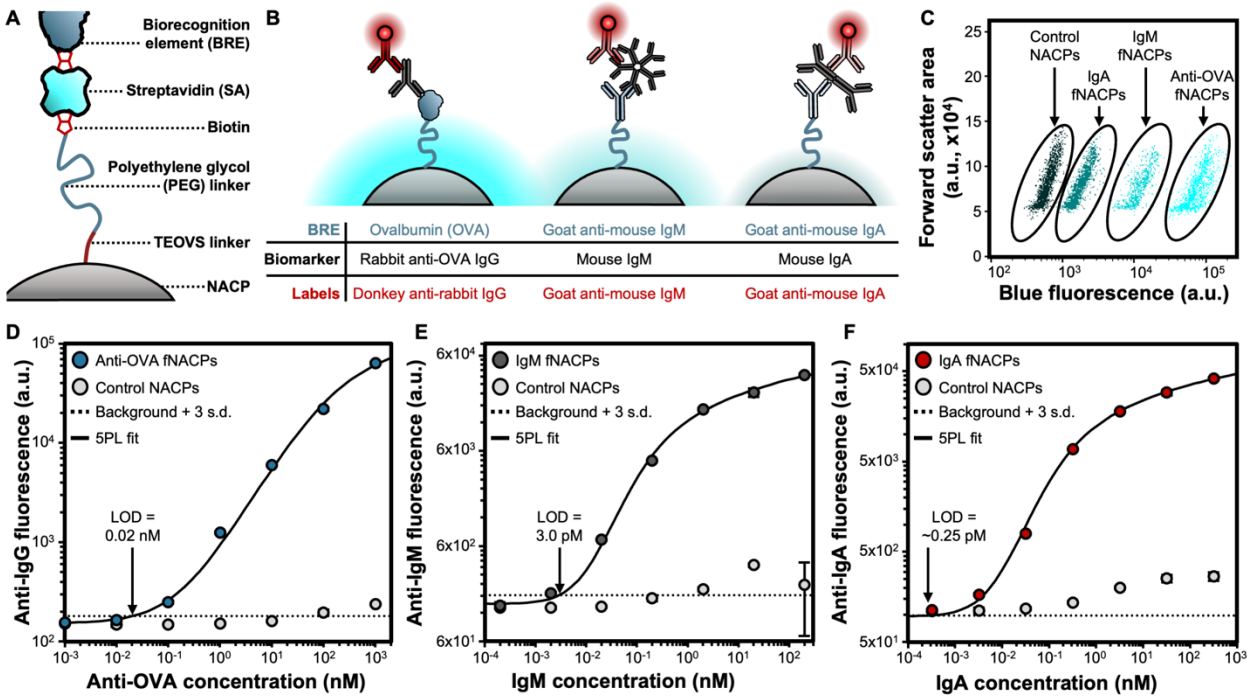

Figure 5.5. Details for and performance of the fNACP-based assay. A) Schematic representation of the functionalization approach employed to produce biomarker-specific fNACPs. B) Schematic representation of the BREs, biomarkers, and labels used to produce the three fNACP types in this study. C) Exemplary flow cytometry gating for the identification of fSA-barcoded fNACPs. D-F) fNACP assay calibration curves for the detection of anti-OVA, IgM, and IgA, respectively. N=3, error bars indicate s.d.

5.3.9 Barcoded fNACPs enable multiplexed biomarker detection

To evaluate the ability to multiplex the fNACP assays to achieve simultaneous detection of anti-OVA, IgM, and IgA, we mixed 10^4 of each fNACP type with 10^4 control NACPs and incubated all four particle types with PBS spiked with all possible combinations of 0 or 10 nM anti-OVA, 0 or 0.2 nM IgM, and 0 or 3.2 nM IgA. Notably, the control NACPs in this experiment were functionalized with fluorescent green SA to enable simpler visualization during later fluorescence analyses. We selected these concentrations as they fell within the middle of the detectible concentrations as discovered during individual standard curve experiments. We followed the same general steps of the individual assay experiments, including incubating the

particles for 30 min for biomolecule capture, washing the particles, and incubating once more in labelling solution. Here, the labelling solution consisted of 10 μg mL^{-1} of each of the secondary labels (i.e., fluorescent anti-IgG, anti-IgM, and anti-IgA). Upon fluorescence analysis, we found that none of the particle types exhibited increased fluorescence when no biomolecules were present, but all exhibited an expected increased fluorescence when all biomolecules were present (Fig. 5.6A). In all cases, the different fNACPs types only displayed increased fluorescence when the corresponding biomolecule was present in the sample, indicating the capture and detection of the biomolecules was specific and that the assay components do not non-specifically interact at levels that would impact simultaneous biomarker detection (Fig. 5.6B). We analyzed the samples by fluorescence microscopy and confirmed that, for the samples with all biomarkers present, the control particles did not exhibit red fluorescence from the secondary labels but that each of the three fNACPs types did (Fig. 5.6C). These experiments confirm the ability to create multiplexed fNACP-based assays, which could substantially decrease assay timescales in a myriad of laboratory-based biomolecule detection protocols.

5.3.10 The multichannel acoustic separator enables simplified detection from complex biofluids

Finally, to evaluate integration of the fNACP assay with the multichannel acoustic separator for detection of biomolecules from complex fluids, we conducted a model assay for the detection of IgA from whole blood. To do so, we incubated 10^4 IgA-specific fNACPs and 10^4 control NACPs with 100 μL of porcine blood spiked with IgA over the range of 0–32 nM in a 96-well plate. After a 30-minute incubation, we used the multichannel acoustic separator to trap and purify the fNACPs and control NACPs. We then incubated the particles in a labeling solution for 30 minutes, washed the particles, and analyzed particle fluorescence. The entire assay required

only approximately 70 minutes, and most of this time was consumed by the two 30-minute incubation steps. In the future, these incubations could be shortened through optimization of the protocol or use of higher affinity BREs and labels (Fig. 5.6D). We found that the IgA detection assay performed similarly to that conducted in buffer, and the LOD of the assay was found to be ~1.6 pM (Fig. 5.6E). While this LOD is an order of magnitude greater than that calculated for detection of IgA from buffer, this modest increase in LOD is reasonable for detection from complex fluids and is still competitive with commercially available ELISA kits.[214] These results demonstrate the ability of both the fNACP assay and the multichannel acoustic separator to be utilized for the detection of rare or low-concentration biomolecules from complex samples containing large amounts of off-target molecules and particulate.

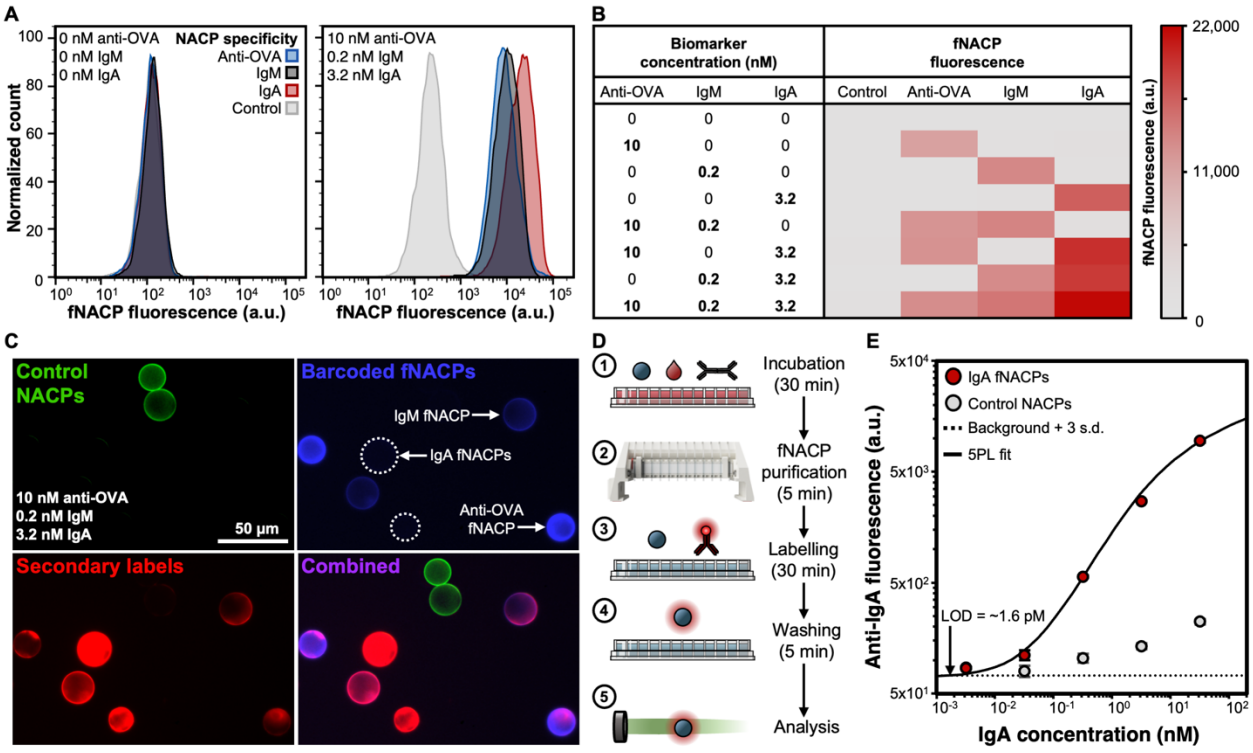

Figure 5.6. Multiplexed detection of anti-OVA, IgM, and IgA and detection of IgA from whole blood. A) Exemplary fluorescence distributions of fNACPs incubated without or with all

biomarkers present. B) Heat-map representation of particle fluorescence for all 8 evaluated multiplexing conditions. C) Individual and combined fluorescnce microscopy images of fNACPs after assaying a sample containing anti-OVA, IgM, and IgA. D) Schematic representation of the workflow utilized to process a whole blood-based fNACP assay using the multichannel acoustic separator. E) fNACP assay calibration curve for the detection of IgA from whole blood. N=3, error bars indicate s.d.

5.4 Discussion

In this work, we have presented a multichannel acoustic separator for the rapid, simplified, and high-throughput purification and detection of biomolecules from complex samples using fNACPs. The multichannel acoustic separator is capable of strongly trapping fNACPs via acoustic radiation forces within 12 parallel trapping channels. Flow through each of the channels is mediated by a semi-continuous siphon that eliminates the need for external pumps or manual fluid actuation, substantially simplifying workflows and increasing the accessibility of the technology.

We additionally demonstrated the ability to tune fNACP functionalization for the sensitive and specific capture and detection of a range of biomarkers through the detection of anti-OVA, IgM, and IgA. We further exhibited the capability of multiplexing the fNACP assay for the simultaneous detection of multiple biomarkers. Finally, we showed the use of IgA-specific fNACPs and the multichannel acoustic separator to enable high-throughput detection of biomolecules from fluids replete in off-target molecules and cells.

The presented multichannel acoustic separator is the first demonstrated acoustofluidic device that utilizes siphon-based flow and is therefore one of the simplest implementations of acoustofluidic technology to date. The device is designed to be easily integrated into existing detection workflows and interfaces with common laboratory supplies and equipment (i.e., 96-well plates, multichannel pipettes). By the future integration of a power source to drive the piezoelectric transducer of the trapping array, the device could be made to be completely portable for field-

based purification of biomolecules. Furthermore, by tuning and expanding on the fNACP functionalization, the system could be used for a myriad of purposes, including capture and purification of cells, small molecules, or other targets of interest. The barcoding approach could additionally be expanded upon to create multiplexed assays for greater numbers of targets in a single assay. Further tuning of the multichannel acoustic separator design could also enable a wider range of achievable flow rates, reductions in purification times, or separations by multiple field types (e.g., through the addition of a magnetic separator attachment). Overall, this 3D-printable device forms the foundation for widespread development and implementation of simplified, high-throughput acoustofluidic separators for laboratory-based workflows.

5.5 Experimental Procedures

5.5.1 Multichannel acoustic separator body design and fabrication

The multichannel acoustic separator was designed in Autodesk Fusion and 3D printed on a masked stereolithography 3D printer (SL1S, Prusa Research) using Fast Mecha White resin (Siraya Tech). Printed device parts include the upper siphon chamber, left side, right side, trapping array, electrical port cover, and two transducer clips (more details may be found in the Supplementary Materials). Printed parts were washed in ethanol (VWR), dried, and subsequently cured for 1 minute using a curing chamber (CW1S, Prusa Research) before device assembly. Imperfections in the printed parts, such as lipped edges originating from placement of parts on the print platform, were removed with sandpaper (Norton Abrasives).

5.5.2 Trapping array fabrication

To assemble the trapping array, ~65 mm sections of 1.02 ID x 2.16 OD silicone tubing (Freudenberg Medical) were attached to one end of 12, ~25 mm long, 1 mm x 1 mm inner width and height square glass capillaries (VitroCom) and the junctions were sealed with cyanoacrylate glue (Gorilla Glue Company) and Parafilm (VWR). The capillaries were then glued to a custom thickness mode piezoelectric transducer with a resonance frequency of 750 kHz (Chengdu Chengyao Technology Co., Ltd., PST4, t = 2.7 mm, w = 10 mm, l = 105 mm) using cyanoacrylate glue. During attachment of the capillaries to the transducer, care was taken to ensure that the capillaries were evenly distributed along the length transducer, were attached to the transducer at the middle of the capillaries, and that the open ends of each capillary were aligned. 24 AWG wires (Digikey), used as transducer leads, were soldered to either side of the transducer. The terminal end of the wires were then soldered to 4 mm female banana jack ports (Bei Qian).

5.5.3 Device fabrication

The assembled trapping array was placed on the trapping array holder, and the lead from the underside of the trapping array was passed through the lead hole. The two transducer clips were placed over the trapping array to keep the trapping array assembly in one piece during subsequent assembly steps. The trapping array was fastened to the left and right sides socket screws (Grainger, M3-0.5, l = 10 mm) and thin hex nuts (M3-0.50, w = 5.5 mm, h = 1.8 mm). Both banana ports were then passed through the lead through-holes of the left side and were seated in the banana port holder. Both wires were seated in the wire guides of the left side to avoid interference with well plates. The electrical port cover was then attached to the left side to contain both banana ports using a screw and nut. The upper siphon chamber was then attached to the device with two screws

and two nuts. The ends of the silicone tubes extending from each of the capillaries were then positioned at the bottom of the siphon chamber wells and the length of the tubes in the chambers were pushed into the tubing guides to be held in place. The external tip of the outlet of each glass capillary were coated with hydrophobic silicone solution (Rain-X glass water repellent) to ensure clean droplet separation during siphoning.

5.5.4 Multichannel acoustic separator operation

The device was connected to a function generator and amplifier via banana port and an oscilloscope was attached to each lead via banana port to alligator clip wiring. To engage acoustics, a ~750 kHz AC sine wave was applied at ~25 V_{pp}. To prime the siphon, 600 µL of water or buffer was added to each of the 12 siphon chambers via multichannel pipette. To complete priming, the compressible tubing of each channel was depressed and manipulated with a rolling motion to draw liquid from the siphon chambers through the entirety of each channel. Flow through each channel was then controlled strictly by the gravity-based siphon effect. Liquids in the siphon chambers were siphoned out of the chamber until equilibrium in pressure between the inlet and outlet of each channel was reached. The height, and therefore volume, of the fluid remaining in the siphon chambers after reaching equilibrium was tuned by adjusting relative siphon chamber and outlet height. When fluid remained in the chambers after equilibrium was reached, flow through each of the channels was reinitiated by addition of other liquids to the siphon chambers, typically 300 µL of water, buffer, or 3X diluted whole blood (porcine with sodium heparin, Lampire). While the siphon was active, liquid constantly drained through the channels and dripped from the trapping channel outlets into a waste container or 96-well plate for sample collection. Prior to use, water

and wash buffer were degassed for at least 1 hour to avoid generation of air bubbles in the device channels.

5.5.5 Evaluation of channel washing

To analyze effectiveness of device washing when samples suspended in water were present in the device, all 12 channels of the multichannel acoustic separator were primed with a solution of blue food color in water and acoustics were engaged. The channels were then washed 5 times. For every wash, the liquid leaving each channel was collected in a 96-well plate. After this, 200 µL of each sample was transferred to clear, flat bottom 96-well plate (Grenier). Finally, each sample was analyzed by recording absorbance at 630 nm using a plate reader (Infinite 200Pro, Tecan). To analyze effectiveness of device washing when samples suspended in diluted whole blood were present in the device, the same process was repeated after priming the channels with 3X diluted whole blood. Because the optical density of diluted whole blood is substantial, 15 µL of each collected sample was diluted to 200 µL with PBS prior to measurement of absorbance at 542 nm.

5.5.6 Evaluation of flow rate

To evaluate drained volume over time and, subsequently, flow rate when different fluids pass through the device, the device was primed with either water, buffer, or 3X diluted whole blood. Then, the acoustics were engaged and 300 µL of the respective liquid was added to the upper siphon chamber while recording a video. The video was recorded until all channels had stopped dripping for 10 s. These videos were analyzed to determine number of drops per channel as well as the timepoints for each droplet. Then, the drained volume from each channel was

determined by pipette. This volume was divided by the total number of drops per channel to yield an average drop volume per channel. The volume drained over time was then plotted assuming a constant volume per droplet.

5.5.7 NACP production

NACPs were produced as previously described.[196] Briefly, 0.1% v/w triethoxyvinylsilane (Sigma Aldrich) was thoroughly mixed with a 10:1 weight ratio mixture of Sylgard 184 base (Dow Chemical) and Sylgard 184 crosslinker (Dow Chemical). This mixture was submerged in a solution of 1% w/w Pluronic F108 (Sigma-Aldrich) in deionized water (DIW) and all components were homogenized for 1 min, producing polydisperse, uncured NACPs. The mixture was cured for 2 hours at 80ºC. The cured NACPs were then filtered through a series of cell strainers (PluriStrainer) while vortexing at speeds sufficient to agitate liquid in the cell strainer in order to isolate a low-polydispersity population of NACPs between 20-30 μm.

5.5.8 NACP sizing

NACPs were pipetted onto a glass slide and images were captured by a Zeiss AxioVert A1 TL/RL inverted fluorescence microscope equipped with a Axiocam 305 mono camera (Zeiss, Germany). NACP sizes were determined by analyzing images with Fiji/ImageJ software.

5.5.9 NACP washing

NACP washing during production and functionalization was completed by centrifugation at 3000xG for 3 minutes, followed by aspiration and resuspension. NACP washing in 96-well

plates was completed by centrifugation of the well plate at 1500xG for 1 minute, also followed by aspiration and resuspension.

5.5.10 Functionalization of control NACPs and anti-OVA-, IgM-, and IgA-specific fNACPs

NACPs were functionalized by conjugating the NACPs with a biotin-PEG-silane, followed by conjugation with SA, followed by conjugation with a biotinylated BRE. Typically, $5x10^6$ NACPs were washed thrice with 0.05% v/v Tween 20 (Sigma-Aldrich) in DIW and resuspended in 50 µL of a 30 mg mL^{-1} solution of 2 kDa silane-PEG-biotin (Laysan Bio) in DIW. Particles were incubated for 2 hours at room temperature while mixing on a VorTemp 56 shaking incubator (Labnet) at ~1200 rpm. NACPs were washed thrice with 0.05% v/v Tween 20 in PBS (Sigma-Aldrich). The NACPs were then resuspended in 100 µL of 1.7 mg mL^{-1} SA (ThermoFisher) and incubated for 90 min at room temperature while mixing. After incubation, NACPs were washed thrice with 0.05% v/v Tween 20 in PBS and resuspended in solutions containing biotinylated-BREs. For anti-OVA-specific fNACPs, the NACPs were resuspended in 200 µL of 2.5 mg mL^{-1} biotin-conjugated OVA (Nanocs) in PBS. For IgM-specific fNACPs, the NACPs were resuspended in 1000 µL of 0.5 mg mL^{-1} biotin-conjugated goat anti-Mouse IgM (ThermoFisher) in PBS. For IgA-specific fNACPs, the NACPs were resuspended in 1000 µL of 0.5 mg mL^{-1} biotin-conjugated goat anti-mouse IgA (Southern Biotech) in PBS. For all cases, particles were incubated for 90 min at room temperature while mixing. Finally, the fully functionalized fNACPs were washed thrice in storage buffer composed of 1% w/v BSA (Sigma-Aldrich) in PBS. After washing, the fNACPs were resuspended in storage buffer and stored at ~4˚C until use. Control NACPs were functionalized identically to fNACPs through conjugation of SA. After conjugation with SA,

control particles were incubated with 450 μL of a 2 mg mL^{-1} solution of biotin-conjugated BSA (ThermoFisher) in PBS.

5.5.11 Fluorescently barcoding fNACPs and control NACPs

To fluorescently barcode the fNACPs and control NACPs, the particles were incubated with varied ratios of nonfluorescent SA to fluorescent Alexa Fluor 405-conjugated SA (ThermoFisher) during the SA functionalization step. The ratios utilized include 1:0, 99:1, 9:1, and 0:1. During some experiments, control particles were instead functionalized with fluorescent Alexa Fluor 488 SA (ThermoFisher) alone.

5.5.12 fNACP trapping and purification

Before fNACP purification, the multichannel acoustic separator was primed with wash buffer and acoustics were engaged. Then, 300 μL samples containing 4-5x10^4 particles were added to the upper siphon chambers via multichannel pipette. After draining, the channels were washed 2-4 times by adding 300 μL of wash buffer to the upper siphon chambers and allowing the chambers to drain into a waste container until reaching equilibrium. Then, the acoustics were disengaged. After waiting 1-2 minutes, 300 μL of wash buffer was added to the upper siphon chambers and the fNACP-rich purified samples were collected on a 96-well plate.

5.5.13 Visual characterization of NACP trapping

To visually assess NACP trapping, ~5 μL of a 5 wt% solution of 5.1 μm red fluorescent carboxylated PS particles (Magsphere) was added to a ~1.7x10^5 particle mL^{-1} solution of NACPs coated with green fluorescent SA in wash buffer. The particle mixture was passed through a

trapping channel situated on the fluorescent microscope at 1 mL min^{-1} via syringe pump. Images of the trapping channels were captured before and after engaging the acoustics.

5.5.14 Evaluation of NACP trapping

To evaluate NACP trapping, samples of $5x10^4$ NACPs were added to 300 μL of either wash buffer or 3X diluted whole blood. The multichannel acoustic separator was primed with wash buffer and the acoustics were engaged. The NACP samples were added to the upper siphon chambers and the draining fluid was collected for analysis. The channels were then washed two (i.e., for separation from buffer) to four (i.e., for separation from blood) times and the drained fluid was collected in a 96-well plate. The acoustics were then disengaged and the NACPs were collected. To determine the extent of residual NACPs in the channels after NACP collection, the channels were then washed twice more and the draining fluid was collected. The volume of each collected sample was adjusted to the same approximate volume by pipette. Finally, all samples were analyzed by flow cytometry (BDFACSCelesta with a high-throughput sampler) and the number of NACPs in each sample were recorded. Notably, the samples from the initial addition of particles in blood, as well as the corresponding first two washes, had to be diluted 200, 100, and 10X, respectively, to properly evaluate NACP numbers with flow cytometry. These dilution factors were taken into account when completing data analysis. We then calculated trapping efficiency by the following:

$$Trapping\ efficicency = \frac{(NACPs_{collected})}{(NACPs_{initial} + NACPs_{washes} + NACPs_{collected} + NACPs_{residual})} \quad (5.1)$$

5.5.15 Individual fNACP assays

For anti-OVA, IgM, and IgA assays, 10^4 fNACPs specific to either anti-OVA, IgM, or IgA were mixed with 10^4 control NACPs. The particle mixtures with then resuspended in 100 μL PBS spiked with either anti-OVA spanning 0.001-1000 nM, IgM spanning 0.0002–200 nM, or IgA spanning 0.00032–320 nM in a 96-well plate. The samples were incubated for 30 min while mixing at 1200 rpm at room temperature. After incubation, samples were washed thrice in the well plate and were resuspended in labeling solutions. The labelling solutions for anti-OVA, IgM, and IgA detection were 10 μg mL^{-1} Alexa Fluor Plus 594-conjugated donkey anti-rabbit IgG IgG (ThermoFisher) in PBS, 10 μg mL^{-1} Alexa Fluor 594-conjugated goat anti-mouse IgM IgG (Southern Biotech) in PBS, or 10 μg mL^{-1} Alexa Fluor Plus 555-conjugated goat anti-mouse IgA IgG (Southern Biotech) in PBS, respectively. After incubating for 30 min while mixing at 1200 rpm at room temperature, the particles were washed thrice in the well plate. Finally, the particles were resuspended in 200 μL wash buffer and analyzed by flow cytometry.

5.5.16 Multiplexed fNACP assays

To test multiplexing of the fNACP assay, 10^4 of each of the 3 fNACP types and 10^4 control fNACPs were mixed and then resuspended in 100 μL PBS spiked with all 8 possible combinations of 0 or 10 nM anti-OVA, 0 or 0.2 nM IgM, and 0 or 3.2 nM IgA. The samples were incubated for 30 min while mixing at 1200 rpm at room temperature. After incubation, samples were washed thrice in the well plate and were resuspended in a labelling solution containing 10 μg mL^{-1} of each of the 3 fluorescent labels used for the individual fNACP assays. After incubating for 30 min while mixing at 1200 rpm at room temperature, the particles were washed thrice in the well plate. Finally, the particles were resuspended in 200 μL wash buffer and analyzed by flow cytometry.

5.5.17 fNACP assay in whole blood using the multichannel acoustic separator

For each sample, 10^4 IgA-specific fNACPs and 10^4 control NACPs were suspended in 100 µL of whole porcine blood with spiked IgA spanning 0.0032–32 nM in a 96-well plate. The samples were incubated for 30 min while mixing at 1200 rpm at room temperature. Samples were then diluted to 300 µL with wash buffer and were purified using the multichannel acoustic separator. The purified sample were collected in a round bottom 96-well plate and were pelleted, aspirated, and resuspended in 100 µL of a labelling solution containing 10 µg mL^{-1} Alexa Fluor Plus 555-conjugated goat anti-mouse IgA IgG (Southern Biotech) in PBS. After incubating for 30 min while mixing at 1200 rpm at room temperature, the particles were washed thrice in the well plate. Finally, the particles were resuspended in 200 µL wash buffer and analyzed by flow cytometry.

5.5.18 Assay curve fitting

Assay standard curves, shown in Figs. 5.5D-F and 5.6E, were fit with a five-parameter logistic (5PL) curve to determine the assay LOD. To do so, experimental data was fit to the standard 5PL equation, given by:

$$y = b + \frac{a - b}{\left(1 + \left(\frac{x}{c}\right)^d\right)^g} \tag{5.2}$$

where y is the fluorescence intensity, a and b are the fluorescence intensities at the minimum and maximum biomarker concentrations, respectively, x is the biomarker concentration, c is the mid-

range concentration, d is the slope factor, and g is the asymmetry factor. a was constrained to be the mean background fluorescence measured during experiments. MATLAB was used for all fitting. LOD was determined by identifying the concentration at which the response was 3 standard deviations above the background response (i.e., NACPs without any fluorescent labels), as predicted by the curve fit. Fit parameters may be found in Table E.1.

5.5.19 Statistical analysis

Differences between groups were compared by one-tailed Student's t-tests, and $P < 0.05$ was considered significant in the analyses. All quantitative data is expressed as the mean ± standard deviation.

Chapter 6: Concluding remarks

6.1 Summary of Key Findings

6.1.1 Key findings in Chapter 2

In Chapter 2, we demonstrated the use of ICEP of functional metallodielectric Janus particles, ICEMs, as a means of simple and label-free biosensing. We functionalized ICEMs with an antifouling PEG layer and biotin recognition elements for the capture of SA and showed that decreased ICEM speed occurred only with specific capture of SA. Moreover, a continuous decrease in mean particle speed was observable from 1–100 nM SA when using $2.5x10^5$ ICEMs per sample. We additionally showed the ability to functionalize ICEMs with recognition elements for the detection of antigens. Lastly, we showed that the ICEM assay sensitivity can be enhanced by reducing the number of ICEMs used and achieved a 10-fold lower detection (0.1 nM SA) by using $1x10^4$ ICEMs per sample. Through these findings, we demonstrated the first example of ICEP as a mechanism of signal transduction for specific biomolecule detection.

6.1.2 Key findings in Chapter 3

In Chapter 3, we presented DPM as a method to experimentally determine effects of surface modifications on the polarizability of surfaces in systems that leverage ICEO. We applied this method for the study of surface-modified Janus particles, inspired by the ICEMs presented in Chapter 2, travelling by ICEP. We showed that DPM enables prediction of a decrease in particle speed upon SA capture by silica-gold Janus particles modified with PEG and biotin-PEG-thiol due, in part, to a decrease in the polarizability of the gold hemisphere over which SA is captured. We additionally revealed that experimentally observed increases in the speed of polymer-modified

Janus particles are likely governed by effects unrelated to changes to particle polarizability, including changes to particle-surface interactions in the system. Overall, this work both 1) revealed potential fundamental mechanisms through which ICEM-based biomolecule detection, discussed in Chapter 2, is made possible and 2) laid the foundation for broader implementation of DPM, which could be key for future design of ICEO-based systems or for the study of complex ICEO-based phenomenon

6.1.3 Key findings in Chapter 4

In Chapter 4, we presented an acoustic pipette and fNACPs for the rapid, sensitive, and simple capture, purification, and detection of biomolecules. We described methods to synthesize large fNACPs with a low-polydispersity (i.e., <15% CV) that can be acoustically trapped and purified from whole blood with high efficiency at rates up to 5 mL min^{-1}. We functionalized the fNACPs using a flexible conjugation approach that enables simple tuning of the fNACP specificity. The presented acoustic pipette contains all necessary components to conduct fNACP-based assays, including wash buffer, a fluorescent secondary antibody, and a trapping channel supporting a half-wavelength acoustic standing wave. Using this system, we demonstrated the detection of anti-OVA antibodies from blood at picomolar levels (60 pM), a sensitivity competitive with commercial ELISA kits. Beyond this, we developed a portable, custom benchtop fluorimeter for analysis of samples processed in the acoustic pipette. Using a modified fNACP-based assay, we rapidly detected anti-OVA at 100 nM.

6.1.4 Key findings in Chapter 5

In Chapter 5, we presented a multichannel acoustic separator for the rapid, simplified, and high-throughput purification and detection of biomolecules from complex samples using fNACPs. The multichannel acoustic separator is capable of strongly trapping within 12 parallel trapping channels, and flow through each of the channels is mediated by a semi-continuous siphon that eliminates the need for external pumps or manual fluid actuation, substantially simplifying workflows and increasing the accessibility of the technology. We further demonstrated the capability of multiplexing the fNACP assay for the simultaneous detection of multiple biomarkers. Finally, we showed the use of IgA-specific fNACPs and the multichannel acoustic separator to enable high-throughput detection of biomolecules from fluids replete in off-target molecules and cells.

6.2 Outlook

6.2.1 Future directions for ICEP-based biomolecule detection

There are ample opportunities to further expand upon the performance and applications of the ICEM-based assay presented in Chapter 2. Thanks to the simple recognition element conjugation approach, the presented ICEMs could be easily tuned for recognition and capture of a range of biomolecules of interest by conjugating aptamers, antibodies, or other recognition elements to the gold hemisphere of the particles. The assay could additionally be multiplexed for simultaneous detection of a panel of biomolecules by production of shape- or color-barcoded ICEMs, each with unique biomolecule specificities. Finally, by automating ICEM propulsion and tracking or integrating the assay into a mobile phone-based detection system, time to results could

be decreased substantially, expanding accessibility and simplicity of the ICEM-based biomolecule detection system.

6.2.2 Future directions for the study of ICEP-based biomolecule detection

The findings presented in Chapter 3 support the hypothesis that decreases in the speed of Janus particles travelling by ICEP upon capture of protein are mechanistically driven in part by direct changes to the effective polarizability of metallic surfaces of the Janus particles, but also revealed the presence of additional mechanisms by which ICEP motion is altered by surface modification. This work thus provided key insights related to the ICEM-based signal transduction method presented in Chapter 2. However, future work to isolate and confirm the predominant mechanisms by which signal transduction occurs in the ICEM assay would substantially enhance future design and implementation of ICEM assays. This may be made possible through experiments that employ particle tracking around immobilized ICEMs to study associated ICEO flows or through removal of confounding effects, potentially made possible by tracking ICEMs in bulk liquid or at a liquid-liquid interface, rather than at a liquid-solid interface. These efforts may simplify the design of ICEM assays, enable expansion of the range over which ICEM-based signal transduction can occur, or allow for transduction to occur at lower concentrations of biomolecules, further increasing the sensitivity of the ICEM assays.

6.2.3 Future directions for DPM development

The findings presented in Chapter 3 additionally laid the foundation for the probe particle-based DPM method as a means of studying the effects of various modifications on the polarizability of surfaces in systems that leverage ICEO, and there are a great number of

opportunities for the advancement of this method. For instance, the predictive capabilities of the DPM method may benefit from future work to ensure probe particles accurately mimic the system of study or from inclusion of damping factors in theoretical calculations to account for surface effects. Efforts to automate parts of the measurement approach (e.g., automated frequency sweeps and recording) could also decrease barriers to use of the method. Perhaps most importantly, future work focused on validating the DPM method against systems in which surface-surface or other confounding interactions are not present may provide key insights toward further development and implementation of this measurement method.

6.2.4 Future directions for fNACP-based biomolecule detection

The fNACP and acoustic pipette technology presented in Chapter 4 has the potential to dramatically shorten the time required to isolate and detect biomarkers (i.e., requiring only 70 minutes with less user engagement than commercial ELISA methods of 4–6 hours). By adding an on-board power supply and integrating the system with a low-cost benchtop fluorimeter, the acoustic pipette and fluorimeter system holds the potential to enable deployment of POC diagnostic testing in remote areas, while maintaining – and potentially increasing – assay sensitivity compared to mainstay detection techniques. Through modification of the signal transduction approach, the fNACP assay output could be tuned to meet the requirements of a broader range of detection applications. The acoustic pipette and fNACPs can additionally be of use independent of one another; the acoustic pipette could be a powerful tool for the simple and rapid separation of a host of other particle or cell types in laboratories or elsewhere, while the NACPs may help to expand the capabilities of other acoustofluidic systems that currently primarily utilize PACPs for sensing, object manipulation, or other applications. Furthermore, by tuning and

expanding on the fNACP functionalization, the system could be used for a myriad of purposes, including capture and purification of cells, small molecules, or other targets of interest. The fNACP barcoding approach, presented in Chapter 5, could additionally be expanded upon to create multiplexed assays for greater numbers of targets in a single assay.

The multichannel acoustic separator presented in Chapter 5 was designed to be easily integrated into existing detection workflows and interface with common laboratory supplies and equipment (i.e., 96-well plates, multichannel pipettes). By the integration of a power source to drive the piezoelectric transducer of the trapping array, the device could be made to be completely portable for field-based purification of biomolecules. Further tuning of the multichannel acoustic separator design could also enable a wider range of achievable flow rates, reductions in purification times, or separations by multiple field types (e.g., through the addition of a magnetic separator attachment). The future redesign of the multichannel acoustic separator would benefit from a rigorous analysis of the parameters that dictate siphon function. While our work investigated some of these parameters at a surface level, in-depth study of the physical phenomenon governing the siphon function would be helpful in selecting materials, dimensioning components, or implementing new features for future versions of the device.

6.3 Final remarks

The projects presented in this dissertation are the culmination of over 5 years of research and the contributions of numerous talented researchers. Moreover, each project built off of, was made possible through, and was inspired by the past developments, inventions, and discoveries of an even greater number of scientists and engineers. In a similar fashion, I hope the unique

advancements presented in this work will inspire and facilitate future research, innovation, and discovery.

Chapter 7: Bibliography

(1) Ranjan, P.; Parihar, A.; Jain, S.; Kumar, N.; Dhand, C.; Murali, S.; Mishra, D.; Sanghi, S. K.; Chaurasia, J. P.; Srivastava, A. K.; Khan, R. Biosensor-Based Diagnostic Approaches for Various Cellular Biomarkers of Breast Cancer: A Comprehensive Review. *Anal. Biochem.* **2020**, *610*, 113996. https://doi.org/10.1016/j.ab.2020.113996.

(2) Wolkowicz, K. L.; Aiello, E. M.; Vargas, E.; Teymourian, H.; Tehrani, F.; Wang, J.; Pinsker, J. E.; Doyle, F. J.; Patti, M.; Laffel, L. M.; Dassau, E. A Review of Biomarkers in the Context of Type 1 Diabetes: Biological Sensing for Enhanced Glucose Control. *Bioeng. Transl. Med.* **2020**, *6* (2), e10201. https://doi.org/10.1002/btm2.10201.

(3) Justino, C. I. L.; Duarte, A. C.; Rocha-Santos, T. A. P. Recent Progress in Biosensors for Environmental Monitoring: A Review. *Sensors* **2017**, *17* (12), 2918. https://doi.org/10.3390/s17122918.

(4) Naresh, V.; Lee, N. A Review on Biosensors and Recent Development of Nanostructured Materials-Enabled Biosensors. *Sensors* **2021**, *21* (4), 1109. https://doi.org/10.3390/s21041109.

(5) Saylan, Y.; Erdem, Ö.; Ünal, S.; Denizli, A. An Alternative Medical Diagnosis Method: Biosensors for Virus Detection. *Biosensors* **2019**, *9* (2), 65. https://doi.org/10.3390/bios9020065.

(6) Polat, E. O.; Cetin, M. M.; Tabak, A. F.; Bilget Güven, E.; Uysal, B. Ö.; Arsan, T.; Kabbani, A.; Hamed, H.; Gül, S. B. Transducer Technologies for Biosensors and Their Wearable Applications. *Biosensors* **2022**, *12* (6), 385. https://doi.org/10.3390/bios12060385.

(7) Chieng, A.; Wan, Z.; Wang, S. Recent Advances in Real-Time Label-Free Detection of Small Molecules. *Biosensors* **2024**, *14* (2), 80. https://doi.org/10.3390/bios14020080.

(8) Makhammajanov, Z.; Kabayeva, A.; Auganova, D.; Tarlykov, P.; Bukasov, R.; Turebekov, D.; Kanbay, M.; Molnar, M. Z.; Kovesdy, C. P.; Abidi, S. H.; Gaipov, A. Candidate Protein Biomarkers in Chronic Kidney Disease: A Proteomics Study. *Sci. Rep.* **2024**, *14* (1), 14014. https://doi.org/10.1038/s41598-024-64833-8.

(9) Bodaghi, A.; Fattahi, N.; Ramazani, A. Biomarkers: Promising and Valuable Tools towards Diagnosis, Prognosis and Treatment of Covid-19 and Other Diseases. *Heliyon* **2023**, *9* (2), e13323. https://doi.org/10.1016/j.heliyon.2023.e13323.

(10) Morales, M. A.; Halpern, J. M. Guide to Selecting a Biorecognition Element for Biosensors. *Bioconjug. Chem.* **2018**, *29* (10), 3231. https://doi.org/10.1021/acs.bioconjchem.8b00592.

(11) Thomas, S. N.; Karger, A. B.; Altawallbeh, G.; Nelson, K. M.; Jacobs, D. R.; Gorlin, J.; Barcelo, H.; Thyagarajan, B. Ultrasensitive Detection of Salivary SARS-CoV-2 IgG

Antibodies in Individuals with Natural and COVID-19 Vaccine-Induced Immunity. *Sci. Rep.* **2022**, *12* (1), 8890. https://doi.org/10.1038/s41598-022-12869-z.

(12) Kallem, P.; Hegab, H. M.; Alsafar, H.; Hasan, S. W.; Banat, F. SARS-CoV-2 Detection and Inactivation in Water and Wastewater: Review on Analytical Methods, Limitations and Future Research Recommendations. *Emerg. Microbes Infect.* **2023**, *12* (2), 2222850. https://doi.org/10.1080/22221751.2023.2222850.

(13) Clarke, W.; Sokoll, L. J.; Rai, A. J. Chapter 12 - Immunoassays. In *Contemporary Practice in Clinical Chemistry (Fourth Edition)*; Clarke, W., Marzinke, M. A., Eds.; Academic Press, 2020; pp 201–214. https://doi.org/10.1016/B978-0-12-815499-1.00012-0.

(14) Chadwick, F. J.; Clark, J.; Chowdhury, S.; Chowdhury, T.; Pascall, D. J.; Haddou, Y.; Andrecka, J.; Kundegorski, M.; Wilkie, C.; Brum, E.; Shirin, T.; Alamgir, A. S. M.; Rahman, M.; Alam, A. N.; Khan, F.; Swallow, B.; Mair, F. S.; Illian, J.; Trotter, C. L.; Hill, D. L.; Husmeier, D.; Matthiopoulos, J.; Hampson, K.; Sania, A. Combining Rapid Antigen Testing and Syndromic Surveillance Improves Community-Based COVID-19 Detection in a Low-Income Country. *Nat. Commun.* **2022**, *13* (1), 2877. https://doi.org/10.1038/s41467-022-30640-w.

(15) Jeong, S.; Park, M.-J.; Song, W.; Kim, H.-S. Current Immunoassay Methods and Their Applications to Clinically Used Biomarkers of Breast Cancer. *Clin. Biochem.* **2020**, *78*, 43–57. https://doi.org/10.1016/j.clinbiochem.2020.01.009.

(16) Boehringer, H. R.; O'Farrell, B. J. Lateral Flow Assays in Infectious Disease Diagnosis. *Clin. Chem.* **2022**, *68* (1), 52–58. https://doi.org/10.1093/clinchem/hvab194.

(17) Gupta, R.; Gupta, P.; Wang, S.; Melnykov, A.; Jiang, Q.; Seth, A.; Wang, Z.; Morrissey, J. J.; George, I.; Gandra, S.; Sinha, P.; Storch, G. A.; Parikh, B. A.; Genin, G. M.; Singamaneni, S. Ultrasensitive Lateral-Flow Assays via Plasmonically Active Antibody-Conjugated Fluorescent Nanoparticles. *Nat. Biomed. Eng.* **2023**, *7* (7), 1556–1570. https://doi.org/10.1038/s41551-022-01001-1.

(18) Budd, J.; Miller, B. S.; Weckman, N. E.; Cherkaoui, D.; Huang, D.; Decruz, A. T.; Fongwen, N.; Han, G.-R.; Broto, M.; Estcourt, C. S.; Gibbs, J.; Pillay, D.; Sonnenberg, P.; Meurant, R.; Thomas, M. R.; Keegan, N.; Stevens, M. M.; Nastouli, E.; Topol, E. J.; Johnson, A. M.; Shahmanesh, M.; Ozcan, A.; Collins, J. J.; Fernandez Suarez, M.; Rodriguez, B.; Peeling, R. W.; McKendry, R. A. Lateral Flow Test Engineering and Lessons Learned from COVID-19. *Nat. Rev. Bioeng.* **2023**, *1* (1), 13–31. https://doi.org/10.1038/s44222-022-00007-3.

(19) Klumpp-Thomas, C.; Kalish, H.; Drew, M.; Hunsberger, S.; Snead, K.; Fay, M. P.; Mehalko, J.; Shunmugavel, A.; Wall, V.; Frank, P.; Denson, J.-P.; Hong, M.; Gulten, G.; Messing, S.; Hicks, J.; Michael, S.; Gillette, W.; Hall, M. D.; Memoli, M. J.; Esposito, D.; Sadtler, K. Standardization of ELISA Protocols for Serosurveys of the SARS-CoV-2 Pandemic Using Clinical and at-Home Blood Sampling. *Nat. Commun.* **2021**, *12* (1), 113. https://doi.org/10.1038/s41467-020-20383-x.

(20) Kontou, P. I.; Braliou, G. G.; Dimou, N. L.; Nikolopoulos, G.; Bagos, P. G. Antibody Tests in Detecting SARS-CoV-2 Infection: A Meta-Analysis. *Diagnostics* **2020**, *10* (5), 319. https://doi.org/10.3390/diagnostics10050319.

(21) Hosseini, S.; Vázquez-Villegas, P.; Rito-Palomares, M.; Martinez-Chapa, S. O. Advantages, Disadvantages and Modifications of Conventional ELISA. In *Enzyme-linked Immunosorbent Assay (ELISA): From A to Z*; Hosseini, S., Vázquez-Villegas, P., Rito-Palomares, M., Martinez-Chapa, S. O., Eds.; SpringerBriefs in Applied Sciences and Technology; Springer: Singapore, 2018; pp 67–115. https://doi.org/10.1007/978-981-10-6766-2_5.

(22) Harraq, A. A.; Choudhury, B. D.; Bharti, B. Field-Induced Assembly and Propulsion of Colloids. *Langmuir* **2022**, *38* (10), 3001–3016. https://doi.org/10.1021/acs.langmuir.1c02581.

(23) Lee, H.; Kim, D.; Kwon, S.; Park, S. Magnetically Actuated Drug Delivery Helical Microrobot with Magnetic Nanoparticle Retrieval Ability. *ACS Appl. Mater. Interfaces* **2021**, *13* (17), 19633–19647. https://doi.org/10.1021/acsami.1c01742.

(24) Lee, J. G.; Raj, R. R.; Thome, C. P.; Day, N. B.; Martinez, P.; Bottenus, N.; Gupta, A.; Wyatt Shields, C. Bubble-Based Microrobots with Rapid Circular Motions for Epithelial Pinning and Drug Delivery. *Small* **2023**, *19* (32), 2300409. https://doi.org/10.1002/smll.202300409.

(25) Gao, Y.; Sprinkle, B.; Springer, E.; Marr, D. W. M.; Wu, N. Rolling of Soft Microbots with Tunable Traction. *Sci. Adv.* **2023**, *9* (16), eadg0919. https://doi.org/10.1126/sciadv.adg0919.

(26) Lee, J. G.; Raj, R. R.; Day, N. B.; Shields, C. W. Microrobots for Biomedicine: Unsolved Challenges and Opportunities for Translation. *ACS Nano* **2023**, *17* (15), 14196–14204. https://doi.org/10.1021/acsnano.3c03723.

(27) Medina-Sánchez, M.; Schwarz, L.; Meyer, A. K.; Hebenstreit, F.; Schmidt, O. G. Cellular Cargo Delivery: Toward Assisted Fertilization by Sperm-Carrying Micromotors. *Nano Lett.* **2016**, *16* (1), 555–561. https://doi.org/10.1021/acs.nanolett.5b04221.

(28) Lin, Z.; Fan, X.; Sun, M.; Gao, C.; He, Q.; Xie, H. Magnetically Actuated Peanut Colloid Motors for Cell Manipulation and Patterning. *ACS Nano* **2018**, *12* (3), 2539–2545. https://doi.org/10.1021/acsnano.7b08344.

(29) Shields, C. W. Biohybrid Microrobots for Enhancing Adoptive Cell Transfers. *Acc. Mater. Res.* **2023**, *4* (7), 566–569. https://doi.org/10.1021/accountsmr.3c00061.

(30) Yin, S.-N.; Wang, C.-F.; Yu, Z.-Y.; Wang, J.; Liu, S.-S.; Chen, S. Versatile Bifunctional Magnetic-Fluorescent Responsive Janus Supraballs Towards the Flexible Bead Display. *Adv. Mater.* **2011**, *23* (26), 2915–2919. https://doi.org/10.1002/adma.201100203.

(31) Shi, Y.; Zhou, X.; Yu, G. Material and Structural Design of Novel Binder Systems for High-Energy, High-Power Lithium-Ion Batteries. *Acc. Chem. Res.* **2017**, *50* (11), 2642–2652. https://doi.org/10.1021/acs.accounts.7b00402.

(32) Sun, Y.; Yang, M.; Guo, Y.; Cheng, M.; Dong, B.; Shi, F. A Photowelding Strategy for Conductivity Restoration in Flexible Circuits. *Angew. Chem. Int. Ed.* **2020**, *59* (3), 1098–1102. https://doi.org/10.1002/anie.201909965.

(33) Boymelgreen, A. M.; Balli, T.; Miloh, T.; Yossifon, G. Active Colloids as Mobile Microelectrodes for Unified Label-Free Selective Cargo Transport. *Nat. Commun.* **2018**, *9* (1), 760. https://doi.org/10.1038/s41467-018-03086-2.

(34) Ghosh, S.; Ghosh, A. All Optical Dynamic Nanomanipulation with Active Colloidal Tweezers. *Nat. Commun.* **2019**, *10* (1), 4191. https://doi.org/10.1038/s41467-019-12217-2.

(35) Lyu, D.; Xu, W.; Zhou, N.; Duan, W.; Wang, Z.; Mu, Y.; Zhou, R.; Wang, Y. Biomimetic Thermoresponsive Superstructures by Colloidal Soft-and-Hard Co-Assembly. *Sci. Adv.* **2023**, *9* (26), eadh2250. https://doi.org/10.1126/sciadv.adh2250.

(36) Jin, D.; Wang, Q.; Chan, K. F.; Xia, N.; Yang, H.; Wang, Q.; Yu, S. C. H.; Zhang, L. Swarming Self-Adhesive Microgels Enabled Aneurysm on-Demand Embolization in Physiological Blood Flow. *Sci. Adv.* **2023**, *9* (19), eadf9278. https://doi.org/10.1126/sciadv.adf9278.

(37) Yang, Y.; Bevan, M. A. Cargo Capture and Transport by Colloidal Swarms. *Sci. Adv.* **2020**, *6* (4), eaay7679. https://doi.org/10.1126/sciadv.aay7679.

(38) Akolpoglu, M. B.; Alapan, Y.; Dogan, N. O.; Baltaci, S. F.; Yasa, O.; Aybar Tural, G.; Sitti, M. Magnetically Steerable Bacterial Microrobots Moving in 3D Biological Matrices for Stimuli-Responsive Cargo Delivery. *Sci. Adv.* **2022**, *8* (28), eabo6163. https://doi.org/10.1126/sciadv.abo6163.

(39) Alcântara, C. C. J.; Kim, S.; Lee, S.; Jang, B.; Thakolkaran, P.; Kim, J.-Y.; Choi, H.; Nelson, B. J.; Pané, S. 3D Fabrication of Fully Iron Magnetic Microrobots. *Small* **2019**, *15* (16), 1805006. https://doi.org/10.1002/smll.201805006.

(40) Maria-Hormigos, R.; Mayorga-Martinez, C. C.; Pumera, M. Magnetic Hydrogel Microrobots as Insecticide Carriers for In Vivo Insect Pest Control in Plants. *Small n/a* (n/a), 2204887. https://doi.org/10.1002/smll.202204887.

(41) Hou, Y.; Wang, H.; Fu, R.; Wang, X.; Yu, J.; Zhang, S.; Huang, Q.; Sun, Y.; Fukuda, T. A Review on Microrobots Driven by Optical and Magnetic Fields. *Lab. Chip* **2023**, *23* (5), 848–868. https://doi.org/10.1039/D2LC00573E.

(42) Mair, L. O.; Evans, B. A.; Nacev, A.; Stepanov, P. Y.; Hilaman, R.; Chowdhury, S.; Jafari, S.; Wang, W.; Shapiro, B.; Weinberg, I. N. Magnetic Microkayaks: Propulsion of Microrods Precessing near a Surface by Kilohertz Frequency, Rotating Magnetic Fields. *Nanoscale* **2017**, *9* (10), 3375–3381. https://doi.org/10.1039/C6NR09459G.

(43) Ye, H.; Wang, Y.; Liu, X.; Xu, D.; Yuan, H.; Sun, H.; Wang, S.; Ma, X. Magnetically Steerable Iron Oxides-Manganese Dioxide Core–Shell Micromotors for Organic and

Microplastic Removals. *J. Colloid Interface Sci.* **2021**, *588*, 510–521. https://doi.org/10.1016/j.jcis.2020.12.097.

(44) Louf, J.-F.; Bertin, N.; Dollet, B.; Stephan, O.; Marmottant, P. Hovering Microswimmers Exhibit Ultrafast Motion to Navigate under Acoustic Forces. *Adv. Mater. Interfaces* **2018**, *5* (16), 1800425. https://doi.org/10.1002/admi.201800425.

(45) Aghakhani, A.; Yasa, O.; Wrede, P.; Sitti, M. Acoustically Powered Surface-Slipping Mobile Microrobots. *Proc. Natl. Acad. Sci.* **2020**, *117* (7), 3469–3477. https://doi.org/10.1073/pnas.1920099117.

(46) Alina, T. B.; Kirkpatrick, H. B.; Bower, N. M.; Curry, S. D.; Ausec, T. R.; Saemundsson, S. A.; Mueller, E. N.; Shields, C. W.; Cha, J. N.; Goodwin, A. P. Effects of Phospholipid Structure on the Acoustic Cavitation of Functionalized Mesoporous Silica Nanoparticles: Implications for Image-Guided Drug Delivery. *ACS Appl. Nano Mater.* **2023**, *6* (14), 13720–13729. https://doi.org/10.1021/acsanm.3c02747.

(47) Thome, C. P.; Hoertdoerfer, W. S.; Bendorf, J. R.; Lee, J. G.; Shields, C. W. I. Electrokinetic Active Particles for Motion-Based Biomolecule Detection. *Nano Lett.* **2023**, *23* (6), 2379–2387. https://doi.org/10.1021/acs.nanolett.3c00319.

(48) Dou, Y.; Cartier, C. A.; Fei, W.; Pandey, S.; Razavi, S.; Kretzschmar, I.; Bishop, K. J. M. Directed Motion of Metallodielectric Particles by Contact Charge Electrophoresis. *Langmuir* **2016**, *32* (49), 13167–13173. https://doi.org/10.1021/acs.langmuir.6b03361.

(49) Kokot, G.; Faizi, H. A.; Pradillo, G. E.; Snezhko, A.; Vlahovska, P. M. Spontaneous Self-Propulsion and Nonequilibrium Shape Fluctuations of a Droplet Enclosing Active Particles. *Commun. Phys.* **2022**, *5* (1), 91. https://doi.org/10.1038/s42005-022-00872-9.

(50) Zhu, X.; Gao, Y.; Mhana, R.; Yang, T.; Hanson, B. L.; Yang, X.; Gong, J.; Wu, N. Synthesis and Propulsion of Magnetic Dimers under Orthogonally Applied Electric and Magnetic Fields. *Langmuir* **2021**, *37* (30), 9151–9161. https://doi.org/10.1021/acs.langmuir.1c01329.

(51) Wu, J.; Balasubramanian, S.; Kagan, D.; Manesh, K. M.; Campuzano, S.; Wang, J. Motion-Based DNA Detection Using Catalytic Nanomotors. *Nat. Commun.* **2010**, *1*, 36. https://doi.org/10.1038/ncomms1035.

(52) Jurado-Sánchez, B.; Pacheco, M.; Rojo, J.; Escarpa, A. Magnetocatalytic Graphene Quantum Dots Janus Micromotors for Bacterial Endotoxin Detection. *Angew. Chem. Int. Ed.* **2017**, *56* (24), 6957–6961. https://doi.org/10.1002/anie.201701396.

(53) Landry, B.; Girgis, V.; Gibbs, J. G. Controlling the Speed of Light-Activated Colloids with a Constant, Uniform Magnetic Field. *Small* **2020**, *16* (35), 2003375. https://doi.org/10.1002/smll.202003375.

(54) Soler, L.; Sánchez, S. Catalytic Nanomotors for Environmental Monitoring and Water Remediation. *Nanoscale* **2014**, *6* (13), 7175–7182. https://doi.org/10.1039/C4NR01321B.

(55) Li, D.; Liu, Y.; Yang, Y.; Shen, Y. A Fast and Powerful Swimming Microrobot with a Serrated Tail Enhanced Propulsion Interface. *Nanoscale* **2018**, *10* (42), 19673–19677. https://doi.org/10.1039/C8NR04907F.

(56) Pacheco, M.; López, M. Á.; Jurado-Sánchez, B.; Escarpa, A. Self-Propelled Micromachines for Analytical Sensing: A Critical Review. *Anal. Bioanal. Chem.* **2019**, *411* (25), 6561–6573. https://doi.org/10.1007/s00216-019-02070-z.

(57) Maria-Hormigos, R.; Jurado-Sánchez, B.; Escarpa, A. Biocompatible Micromotors for Biosensing. *Anal. Bioanal. Chem.* **2022**, *414* (24), 7035–7049. https://doi.org/10.1007/s00216-022-04287-x.

(58) Jurado-Sánchez, B.; Campuzano, S.; Pingarrón, J. M.; Escarpa, A. Janus Particles and Motors: Unrivaled Devices for Mastering (Bio)Sensing. *Microchim. Acta* **2021**, *188* (12), 416. https://doi.org/10.1007/s00604-021-05053-z.

(59) Yánez-Sedeño, P.; Campuzano, S.; Pingarrón, J. M. Janus Particles for (Bio)Sensing. *Appl. Mater. Today* **2017**, *9*, 276–288. https://doi.org/10.1016/j.apmt.2017.08.004.

(60) Molinero-Fernández, Á.; Arruza, L.; López, M. Á.; Escarpa, A. On-the-Fly Rapid Immunoassay for Neonatal Sepsis Diagnosis: C-Reactive Protein Accurate Determination Using Magnetic Graphene-Based Micromotors. *Biosens. Bioelectron.* **2020**, *158*, 112156. https://doi.org/10.1016/j.bios.2020.112156.

(61) Lu, C.; Liu, X.; Li, Y.; Yu, F.; Tang, L.; Hu, Y.; Ying, Y. Multifunctional Janus Hematite–Silica Nanoparticles: Mimicking Peroxidase-Like Activity and Sensitive Colorimetric Detection of Glucose. *ACS Appl. Mater. Interfaces* **2015**, *7* (28), 15395–15402. https://doi.org/10.1021/acsami.5b03423.

(62) Paniagua, G.; Villalonga, A.; Eguílaz, M.; Vegas, B.; Parrado, C.; Rivas, G.; Díez, P.; Villalonga, R. Amperometric Aptasensor for Carcinoembryonic Antigen Based on the Use of Bifunctionalized Janus Nanoparticles as Biorecognition-Signaling Element. *Anal. Chim. Acta* **2019**, *1061*, 84–91. https://doi.org/10.1016/j.aca.2019.02.015.

(63) Yang, Y.-J.; Zhou, Y.; Xing, Y.; Zhang, G.-M.; Zhang, Y.; Zhang, C.-H.; Lei, P.; Dong, C.; Deng, X.; He, Y.; Shuang, S. A Label-Free Aptasensor Based on Aptamer/NH2 Janus Particles for Ultrasensitive Electrochemical Detection of Ochratoxin A. *Talanta* **2019**, *199*, 310–316. https://doi.org/10.1016/j.talanta.2019.02.015.

(64) María-Hormigos, R.; Molinero-Fernández, Á.; López, M. Á.; Jurado-Sánchez, B.; Escarpa, A. Prussian Blue/Chitosan Micromotors with Intrinsic Enzyme-like Activity for (Bio)-Sensing Assays. *Anal. Chem.* **2022**, *94* (14), 5575–5582. https://doi.org/10.1021/acs.analchem.1c05173.

(65) Li, J.; Concellón, A.; Yoshinaga, K.; Nelson, Z.; He, Q.; Swager, T. M. Janus Emulsion Biosensors for Anti-SARS-CoV-2 Spike Antibody. *ACS Cent. Sci.* **2021**, *7* (7), 1166–1175. https://doi.org/10.1021/acscentsci.1c00173.

(66) Nguyen, K. V.; Minteer, S. D. DNA-Functionalized Pt Nanoparticles as Catalysts for Chemically Powered Micromotors: Toward Signal-on Motion-Based DNA Biosensor. *Chem. Commun.* **2015**, *51* (23), 4782–4784. https://doi.org/10.1039/C4CC10250A.

(67) Yu, X.; Li, Y.; Wu, J.; Ju, H. Motor-Based Autonomous Microsensor for Motion and Counting Immunoassay of Cancer Biomarker. *Anal. Chem.* **2014**, *86* (9), 4501–4507. https://doi.org/10.1021/ac500912c.

(68) Draz, M. S.; Lakshminaraasimulu, N. K.; Krishnakumar, S.; Battalapalli, D.; Vasan, A.; Kanakasabapathy, M. K.; Sreeram, A.; Kallakuri, S.; Thirumalaraju, P.; Li, Y.; Hua, S.; Yu, X. G.; Kuritzkes, D. R.; Shafiee, H. Motion-Based Immunological Detection of Zika Virus Using Pt-Nanomotors and a Cellphone. *ACS Nano* **2018**, *12* (6), 5709–5718. https://doi.org/10.1021/acsnano.8b01515.

(69) Yuan, K.; Cuntín-Abal, C.; Jurado-Sánchez, B.; Escarpa, A. Smartphone-Based Janus Micromotors Strategy for Motion-Based Detection of Glutathione. *Anal. Chem.* **2021**, *93* (49), 16385–16392. https://doi.org/10.1021/acs.analchem.1c02947.

(70) Russell, S. M.; Alba-Patiño, A.; Borges, M.; de la Rica, R. Multifunctional Motion-to-Color Janus Transducers for the Rapid Detection of Sepsis Biomarkers in Whole Blood. *Biosens. Bioelectron.* **2019**, *140*, 111346. https://doi.org/10.1016/j.bios.2019.111346.

(71) Frenea-Robin, M.; Marchalot, J. Basic Principles and Recent Advances in Magnetic Cell Separation. *Magnetochemistry* **2022**, *8* (1), 11. https://doi.org/10.3390/magnetochemistry8010011.

(72) He, J.; Huang, M.; Wang, D.; Zhang, Z.; Li, G. Magnetic Separation Techniques in Sample Preparation for Biological Analysis: A Review. *J. Pharm. Biomed. Anal.* **2014**, *101*, 84–101. https://doi.org/10.1016/j.jpba.2014.04.017.

(73) Arona, J. C.; Hall, T. J.; Mckinnirey, F.; Deng, F. Comparison of Four Commercial Immunomagnetic Separation Kits for the Detection of Cryptosporidium. *J. Water Health* **2023**, *21* (10), 1580–1590. https://doi.org/10.2166/wh.2023.217.

(74) Gómez-Pastora, J.; Xue, X.; Karampelas, I. H.; Bringas, E.; Furlani, E. P.; Ortiz, I. Analysis of Separators for Magnetic Beads Recovery: From Large Systems to Multifunctional Microdevices. *Sep. Purif. Technol.* **2017**, *172*, 16–31. https://doi.org/10.1016/j.seppur.2016.07.050.

(75) Johnston, H. E.; Yadav, K.; Kirkpatrick, J. M.; Biggs, G. S.; Oxley, D.; Kramer, H. B.; Samant, R. S. Solvent Precipitation SP3 (SP4) Enhances Recovery for Proteomics Sample

Preparation without Magnetic Beads. *Anal. Chem.* **2022**, *94* (29), 10320–10328. https://doi.org/10.1021/acs.analchem.1c04200.

(76) Cox, C. Bead-Based Multiplex Immunoassays: Procedures, Tips, and Tricks. In *Proteomic Profiling: Methods and Protocols*; Posch, A., Ed.; Springer US: New York, NY, 2021; pp 263–276. https://doi.org/10.1007/978-1-0716-1186-9_16.

(77) Liu, J.; Allo, B.; Winnik, M. A. Development of Multiplexed Bead-Based Immunoassays for Profiling Soluble Cytokines and CD163 Using Mass Cytometry. *ACS Meas. Sci. Au* **2022**, *2* (6), 629–640. https://doi.org/10.1021/acsmeasuresciau.2c00038.

(78) Zhang, X.; Chen, C.; Wu, J.; Ju, H. Bubble-Propelled Jellyfish-like Micromotors for DNA Sensing. *ACS Appl. Mater. Interfaces* **2019**, *11* (14), 13581–13588. https://doi.org/10.1021/acsami.9b00605.

(79) Boymelgreen, A.; Yossifon, G. Observing Electrokinetic Janus Particle–Channel Wall Interaction Using Microparticle Image Velocimetry. *Langmuir* **2015**, *31* (30), 8243–8250. https://doi.org/10.1021/acs.langmuir.5b01199.

(80) Harraq, A. A.; Choudhury, B. D.; Bharti, B. Field-Induced Assembly and Propulsion of Colloids. *Langmuir* **2022**, *38* (10), 3001–3016. https://doi.org/10.1021/acs.langmuir.1c02581.

(81) Peng, C.; Lazo, I.; Shiyanovskii, S. V.; Lavrentovich, O. D. Induced-Charge Electro-Osmosis around Metal and Janus Spheres in Water: Patterns of Flow and Breaking Symmetries. *Phys. Rev. E* **2014**, *90* (5), 051002. https://doi.org/10.1103/PhysRevE.90.051002.

(82) Gangwal, S.; Cayre, O. J.; Bazant, M. Z.; Velev, O. D. Induced-Charge Electrophoresis of Metallodielectric Particles. *Phys. Rev. Lett.* **2008**, *100* (5), 058302. https://doi.org/10.1103/PhysRevLett.100.058302.

(83) Bazant, M. Z.; Squires, T. M. Induced-Charge Electrokinetic Phenomena: Theory and Microfluidic Applications. *Phys. Rev. Lett.* **2004**, *92* (6), 066101. https://doi.org/10.1103/PhysRevLett.92.066101.

(84) Brooks, A. M.; Sabrina, S.; Bishop, K. J. M. Shape-Directed Dynamics of Active Colloids Powered by Induced-Charge Electrophoresis. *Proc. Natl. Acad. Sci.* **2018**, *115* (6), E1090–E1099. https://doi.org/10.1073/pnas.1711610115.

(85) Katuri, J.; Poehnl, R.; Sokolov, A.; Uspal, W.; Snezhko, A. Arrested-Motility States in Populations of Shape-Anisotropic Active Janus Particles. *Sci. Adv.* **2022**, *8* (26), eabo3604. https://doi.org/10.1126/sciadv.abo3604.

(86) Wang, Z.; Wang, Z.; Li, J.; Cheung, S. T. H.; Tian, C.; Kim, S.-H.; Yi, G.-R.; Ducrot, E.; Wang, Y. Active Patchy Colloids with Shape-Tunable Dynamics. *J. Am. Chem. Soc.* **2019**, *141* (37), 14853–14863. https://doi.org/10.1021/jacs.9b07785.

(87) Lee, J. G.; Brooks, A. M.; Shelton, W. A.; Bishop, K. J. M.; Bharti, B. Directed Propulsion of Spherical Particles along Three Dimensional Helical Trajectories. *Nat. Commun.* **2019**, *10* (1), 2575. https://doi.org/10.1038/s41467-019-10579-1.

(88) Lee, J. G.; Al Harraq, A.; Bishop, K. J. M.; Bharti, B. Fabrication and Electric Field-Driven Active Propulsion of Patchy Microellipsoids. *J. Phys. Chem. B* **2021**, *125* (16), 4232–4240. https://doi.org/10.1021/acs.jpcb.1c01644.

(89) Wang, Z.; Mu, Y.; Lyu, D.; Wu, M.; Li, J.; Wang, Z.; Wang, Y. Engineering Shapes of Active Colloids for Tunable Dynamics. *Curr. Opin. Colloid Interface Sci.* **2022**, *61*, 101608. https://doi.org/10.1016/j.cocis.2022.101608.

(90) Park, S.; Yossifon, G. Micromotor-Based Biosensing Using Directed Transport of Functionalized Beads. *ACS Sens.* **2020**, *5* (4), 936–942. https://doi.org/10.1021/acssensors.9b02041.

(91) Pascall, A. J.; Squires, T. M. Induced Charge Electro-Osmosis over Controllably Contaminated Electrodes. *Phys. Rev. Lett.* **2010**, *104* (8), 088301. https://doi.org/10.1103/PhysRevLett.104.088301.

(92) M.Boymelgreen, A.; Kunti, G.; Garcia-Sanchez, P.; Ramos, A.; Yossifon, G.; Miloh, T. The Role of Particle-Electrode Wall Interactions in Mobility of Active Janus Particles Driven by Electric Fields. *J. Colloid Interface Sci.* **2022**, *616*, 465–475. https://doi.org/10.1016/j.jcis.2022.02.017.

(93) Viefhues, M.; Manchanda, S.; Chao, T.-C.; Anselmetti, D.; Regtmeier, J.; Ros, A. Physisorbed Surface Coatings for Poly(Dimethylsiloxane) and Quartz Microfluidic Devices. *Anal. Bioanal. Chem.* **2011**, *401* (7), 2113. https://doi.org/10.1007/s00216-011-5301-z.

(94) Paratore, F.; Boyko, E.; Kaigala, G. V.; Bercovici, M. Electroosmotic Flow Dipole: Experimental Observation and Flow Field Patterning. *Phys. Rev. Lett.* **2019**, *122* (22), 224502. https://doi.org/10.1103/PhysRevLett.122.224502.

(95) Honegger, T.; Peyrade, D. Dielectrophoretic Properties of Engineered Protein Patterned Colloidal Particles. *Biomicrofluidics* **2012**, *6* (4), 044115. https://doi.org/10.1063/1.4771544.

(96) Pawar, A. B.; Kretzschmar, I. Fabrication, Assembly, and Application of Patchy Particles. *Macromol. Rapid Commun.* **2010**, *31* (2), 150–168. https://doi.org/10.1002/marc.200900614.

(97) Prevo, B. G.; Kuncicky, D. M.; Velev, O. D. Engineered Deposition of Coatings from Nano- and Micro-Particles: A Brief Review of Convective Assembly at High Volume Fraction. *Colloids Surf. Physicochem. Eng. Asp.* **2007**, *311* (1), 2–10. https://doi.org/10.1016/j.colsurfa.2007.08.030.

(98) Shields IV, C. W.; Han, K.; Ma, F.; Miloh, T.; Yossifon, G.; Velev, O. D. Supercolloidal Spinners: Complex Active Particles for Electrically Powered and Switchable Rotation. *Adv. Funct. Mater.* **2018**, *28* (35), 1803465. https://doi.org/10.1002/adfm.201803465.

(99) Al Harraq, A.; Bello, M.; Bharti, B. A Guide to Design the Trajectory of Active Particles: From Fundamentals to Applications. *Curr. Opin. Colloid Interface Sci.* **2022**, *61*, 101612. https://doi.org/10.1016/j.cocis.2022.101612.

(100) Dai, Y.; Liu, C. C. Recent Advances on Electrochemical Biosensing Strategies toward Universal Point-of-Care Systems. *Angew. Chem. Int. Ed.* **2019**, *58* (36), 12355–12368. https://doi.org/10.1002/anie.201901879.

(101) Zhuang, Y.; Zhu, Q.; Tu, C.; Wang, D.; Wu, J.; Xia, Y.; Tong, G.; He, L.; Zhu, B.; Yan, D.; Zhu, X. Protein Resistant Properties of Polymers with Different Branched Architecture on a Gold Surface. *J. Mater. Chem.* **2012**, *22* (45), 23852–23860. https://doi.org/10.1039/C2JM34306A.

(102) Thorek, D. L. J.; Elias, D. R.; Tsourkas, A. Comparative Analysis of Nanoparticle-Antibody Conjugations: Carbodiimide versus Click Chemistry. *Mol. Imaging* **2009**, *8* (4), 221–229.

(103) Sarode, A. V.; Kumbharkhane, A. C. Dielectric Relaxation Study of Poly(Ethylene Glycols) Using TDR Technique. *J. Mol. Liq.* **2011**, *164* (3), 226–232. https://doi.org/10.1016/j.molliq.2011.09.020.

(104) Upadhyayula, S.; Quinata, T.; Bishop, S.; Gupta, S.; Johnson, N. R.; Bahmani, B.; Bozhilov, K.; Stubbs, J.; Jreij, P.; Nallagatla, P.; Vullev, V. I. Coatings of Polyethylene Glycol for Suppressing Adhesion between Solid Microspheres and Flat Surfaces. *Langmuir* **2012**, *28* (11), 5059–5069. https://doi.org/10.1021/la300545v.

(105) Haugland, R. P.; You, W. W. Coupling of Antibodies With Biotin. In *Avidin-Biotin Interactions: Methods and Applications*; McMahon, R. J., Ed.; Methods In Molecular Biology™; Humana Press: Totowa, NJ, 2008; pp 13–23. https://doi.org/10.1007/978-1-59745-579-4_2.

(106) Li, L.; Shields, C. W.; Huang, J.; Zhang, Y.; Ohiri, K. A.; Yellen, B. B.; Chilkoti, A.; López, G. P. Rapid Capture of Biomolecules from Blood via Stimuli-Responsive Elastomeric Particles for Acoustofluidic Separation. *Analyst* **2021**, *145* (24), 8087–8096. https://doi.org/10.1039/D0AN01164A.

(107) Weimer, B. C.; Walsh, M. K.; Wang, X. Influence of a Poly-Ethylene Glycol Spacer on Antigen Capture by Immobilized Antibodies. *J. Biochem. Biophys. Methods* **2000**, *45* (2), 211–219. https://doi.org/10.1016/S0165-022X(00)00114-7.

(108) Ma, Z.; LeBard, D. N.; Loverde, S. M.; Sharp, K. A.; Klein, M. L.; Discher, D. E.; Finkel, T. H. TCR Triggering by pMHC Ligands Tethered on Surfaces via Poly(Ethylene Glycol) Depends on Polymer Length. *PLOS ONE* **2014**, *9* (11), e112292. https://doi.org/10.1371/journal.pone.0112292.

(109) O'Connell, M. A.; Belanger, B. A.; Haaland, P. D. Calibration and Assay Development Using the Four-Parameter Logistic Model. *Chemom. Intell. Lab. Syst.* **1993**, *20* (2), 97–114. https://doi.org/10.1016/0169-7439(93)80008-6.

(110) Paustian, J. S.; Pascall, A. J.; Wilson, N. M.; Squires, T. M. Induced Charge Electroosmosis Micropumps Using Arrays of Janus Micropillars. *Lab. Chip* **2014**, *14* (17), 3300–3312. https://doi.org/10.1039/C4LC00141A.

(111) Manshadi, M. K. D.; Mohammadi, M.; Zarei, M.; Saadat, M.; Sanati-Nezhad, A. Induced-Charge Electrokinetics in Microfluidics: A Review on Recent Advancements. *J. Micromechanics Microengineering* **2020**, *30* (11), 113001. https://doi.org/10.1088/1361-6439/abaf34.

(112) Chen, X.; Shen, M.; Liu, S.; Liu, T.; Chen, D.; Zhao, Y. A Simple Device for Protein Detection Actuated by Induced-Charge Electro-Osmotic Streaming. *Microsyst. Technol.* **2024**, *30* (2), 243–251. https://doi.org/10.1007/s00542-023-05603-w.

(113) Chen, X.; Liu, S.; Hu, X.; Liu, T.; Shen, M.; Peng, Y.; Hu, S.; Zhao, Y. Enrichment and Selection of Particles through Parallel Induced-Charge Electro-Osmotic Streaming for Detection of Low-Abundance Nanoparticles and Targeted Microalgae. *Anal. Chem.* **2023**, *95* (31), 11714–11722. https://doi.org/10.1021/acs.analchem.3c01729.

(114) Wang, S.; Zhang, Z.; Ma, X.; Yue, Y.; Li, K.; Meng, Y.; Wu, Y. Bidirectional and Stepwise Rotation of Cells and Particles Using Induced Charge Electroosmosis Vortexes. *Biosensors* **2024**, *14* (3), 112. https://doi.org/10.3390/bios14030112.

(115) Brooks, A. M.; Sabrina, S.; Bishop, K. J. M. Shape-Directed Dynamics of Active Colloids Powered by Induced-Charge Electrophoresis. *Proc. Natl. Acad. Sci.* **2018**, *115* (6), E1090–E1099. https://doi.org/10.1073/pnas.1711610115.

(116) Lin, C.-H.; Chen, Y.-L.; Jiang, H.-R. Orientation-Dependent Induced-Charge Electrophoresis of Magnetic Metal-Coated Janus Particles with Different Coating Thicknesses. *RSC Adv.* **2017**, *7* (73), 46118–46123. https://doi.org/10.1039/C7RA08527C.

(117) Feng, H.; Chang, H.; Zhong, X.; Wong, T. N. Recent Advancement in Induced-Charge Electrokinetic Phenomena and Their Micro- and Nano-Fluidic Applications. *Adv. Colloid Interface Sci.* **2020**, *280*, 102159. https://doi.org/10.1016/j.cis.2020.102159.

(118) Squires, T. M.; Bazant, M. Z. Induced-Charge Electro-Osmosis. *J. Fluid Mech.* **2004**, *509*, 217–252. https://doi.org/10.1017/S0022112004009309.

(119) Canpolat, C.; Qian, S.; Beskok, A. Induced-Charge Electro-Osmosis of Polymer-Containing Fluid around a Metallic Rod. *Microfluid. Nanofluidics* **2014**, *16* (1), 247–255. https://doi.org/10.1007/s10404-013-1204-y.

(120) Ren, Y.; Liu, W.; Jia, Y.; Tao, Y.; Shao, J.; Ding, Y.; Jiang, H. Induced-Charge Electroosmotic Trapping of Particles. *Lab. Chip* **2015**, *15* (10), 2181–2191. https://doi.org/10.1039/C5LC00058K.

(121) Wu, Z.; Li, D. Micromixing Using Induced-Charge Electrokinetic Flow. *Electrochimica Acta* **2008**, *53* (19), 5827–5835. https://doi.org/10.1016/j.electacta.2008.03.039.

(122) Boymelgreen, A.; Yossifon, G.; Miloh, T. Propulsion of Active Colloids by Self-Induced Field Gradients. *Langmuir* **2016**, *32* (37), 9540–9547. https://doi.org/10.1021/acs.langmuir.6b01758.

(123) Feng, H.; Zhao, L.; Zhong, X.; Lei, X.; Wong, T. N. Non-Monotonic Dependence of Induced-Charge Electro-Osmosis on Ion Concentration. *Colloids Surf. Physicochem. Eng. Asp.* **2021**, *622*, 126604. https://doi.org/10.1016/j.colsurfa.2021.126604.

(124) Feng, H.; Wong, T. N. Net Fluid Flow and Non-Newtonian Effect in Induced-Charge Electro-Osmosis of Polyelectrolyte Solutions. *Phys. Rev. E* **2019**, *100* (1), 013105. https://doi.org/10.1103/PhysRevE.100.013105.

(125) Pascall, A. J.; Squires, T. M. Induced Charge Electro-Osmosis over Controllably Contaminated Electrodes. *Phys. Rev. Lett.* **2010**, *104* (8), 088301. https://doi.org/10.1103/PhysRevLett.104.088301.

(126) Erez, S.; Karshalev, E.; Wu, Y.; Wang, J.; Yossifon, G. Electrical Propulsion and Cargo Transport of Microbowl Shaped Janus Particles. *Small* **2022**, *18* (3), 2101809. https://doi.org/10.1002/smll.202101809.

(127) Huo, X.; Wu, Y.; Boymelgreen, A.; Yossifon, G. Analysis of Cargo Loading Modes and Capacity of an Electrically-Powered Active Carrier. *Langmuir* **2020**, *36* (25). https://doi.org/10.1021/acs.langmuir.9b03036.

(128) Gyun Lee, J.; P. Thome, C.; A. Cruse, Z.; Ganguly, A.; Gupta, A.; Wyatt Shields, C. Magnetically Locked Janus Particle Clusters with Orientation-Dependent Motion in AC Electric Fields. *Nanoscale* **2023**, *15* (40), 16268–16276. https://doi.org/10.1039/D3NR03744D.

(129) Lee, J. G.; Al Harraq, A.; Bishop, K. J. M.; Bharti, B. Fabrication and Electric Field-Driven Active Propulsion of Patchy Microellipsoids. *J. Phys. Chem. B* **2021**, *125* (16), 4232–4240. https://doi.org/10.1021/acs.jpcb.1c01644.

(130) Boymelgreen, A.; Yossifon, G.; Park, S.; Miloh, T. Spinning Janus Doublets Driven in Uniform Ac Electric Fields. *Phys. Rev. E Stat. Nonlin. Soft Matter Phys.* **2014**, *89* (1), 011003. https://doi.org/10.1103/PhysRevE.89.011003.

(131) Thome, C. P.; Hoertdoerfer, W. S.; Bendorf, J. R.; Lee, J. G.; Shields, C. W. I. Electrokinetic Active Particles for Motion-Based Biomolecule Detection. *Nano Lett.* **2023**, *23* (6), 2379–2387. https://doi.org/10.1021/acs.nanolett.3c00319.

(132) Upadhyayula, S.; Quinata, T.; Bishop, S.; Gupta, S.; Johnson, N. R.; Bahmani, B.; Bozhilov, K.; Stubbs, J.; Jreij, P.; Nallagatla, P.; Vullev, V. I. Coatings of Polyethylene Glycol for Suppressing Adhesion between Solid Microspheres and Flat Surfaces. *Langmuir* **2012**, *28* (11), 5059–5069. https://doi.org/10.1021/la300545v.

(133) Honegger, T.; Peyrade, D. Dielectrophoretic Properties of Engineered Protein Patterned Colloidal Particles. *Biomicrofluidics* **2012**, *6* (4), 044115. https://doi.org/10.1063/1.4771544.

(134) Juárez, J. J.; Cui, J.-Q.; Liu, B. G.; Bevan, M. A. kT-Scale Colloidal Interactions in High Frequency Inhomogeneous AC Electric Fields. I. Single Particles. *Langmuir* **2011**, *27* (15), 9211–9218. https://doi.org/10.1021/la201478y.

(135) Wei, M.-T.; Junio, J.; Ou-Yang, H. D. Direct Measurements of the Frequency-Dependent Dielectrophoresis Force. *Biomicrofluidics* **2009**, *3* (1), 012003. https://doi.org/10.1063/1.3058569.

(136) Morgan, H.; Green, N. AC Electrokinetics: Colloids and Nanoparticles; Research Studies Press, 2003.

(137) Crews, N.; Darabi, J.; Voglewede, P.; Guo, F.; Bayoumi, A. An Analysis of Interdigitated Electrode Geometry for Dielectrophoretic Particle Transport in Micro-Fluidics. *Sens. Actuators B Chem.* **2007**, *125* (2), 672–679. https://doi.org/10.1016/j.snb.2007.02.047.

(138) Dokou, E.; Barteau, M. A.; Wagner, N. J.; Lenhoff, A. M. Effect of Gravity on Colloidal Deposition Studied by Atomic Force Microscopy. *J. Colloid Interface Sci.* **2001**, *240* (1), 9–16. https://doi.org/10.1006/jcis.2001.7626.

(139) Juárez, J. J.; Bevan, M. A. Interactions and Microstructures in Electric Field Mediated Colloidal Assembly. *J. Chem. Phys.* **2009**, *131* (13), 134704. https://doi.org/10.1063/1.3241081.

(140) Scott, D. W. Scott's Rule. *WIREs Comput. Stat.* **2010**, *2* (4), 497–502. https://doi.org/10.1002/wics.103.

(141) Huang, Y.; Holzel, R.; Pethig, R.; Wang, X.-B. Differences in the AC Electrodynamics of Viable and Non-Viable Yeast Cells Determined through Combined Dielectrophoresis and Electrorotation Studies. *Phys. Med. Biol.* **1992**, *37* (7), 1499–1517. https://doi.org/10.1088/0031-9155/37/7/003.

(142) Squires, T. M.; Bazant, M. Z. Breaking Symmetries in Induced-Charge Electro-Osmosis and Electrophoresis. *J. Fluid Mech.* **2006**, *560*, 65–101. https://doi.org/10.1017/S0022112006000371.

(143) Xiao, Z.; Duan, S.; Xu, P.; Cui, J.; Zhang, H.; Wang, W. Synergistic Speed Enhancement of an Electric-Photochemical Hybrid Micromotor by Tilt Rectification. *ACS Nano* **2020**, *14* (7), 8658–8667. https://doi.org/10.1021/acsnano.0c03022.

(144) Eng, Y. J.; Nguyen, T. M.; Luo, H.-K.; Chan, J. M. W. Antifouling Polymers for Nanomedicine and Surfaces: Recent Advances. *Nanoscale* **2023**, *15* (38), 15472–15512. https://doi.org/10.1039/D3NR03164K.

(145) Stayton, P. S.; Freitag, S.; Klumb, L. A.; Chilkoti, A.; Chu, V.; Penzotti, J. E.; To, R.; Hyre, D.; Le Trong, I.; Lybrand, T. P.; Stenkamp, R. E. Streptavidin–Biotin Binding Energetics. *Biomol. Eng.* **1999**, *16* (1), 39–44. https://doi.org/10.1016/S1050-3862(99)00042-X.

(146) Pethig, R. Review Article—Dielectrophoresis: Status of the Theory, Technology, and Applications. *Biomicrofluidics* **2010**, *4* (2), 022811. https://doi.org/10.1063/1.3456626.

(147) Wu, H.-J.; Everett, W. N.; Anekal, S. G.; Bevan, M. A. Mapping Patterned Potential Energy Landscapes with Diffusing Colloidal Probes. *Langmuir* **2006**, *22* (16), 6826–6836. https://doi.org/10.1021/la060501j.

(148) Bahukudumbi, P.; Everett, W. N.; Beskok, A.; Bevan, M. A.; Huff, G. H.; Lagoudas, D.; Ounaies, Z. Colloidal Microstructures, Transport, and Impedance Properties within Interfacial Microelectrodes. *Appl. Phys. Lett.* **2007**, *90* (22), 224102. https://doi.org/10.1063/1.2744480.

(149) O'Konski, C. T. ELECTRIC PROPERTIES OF MACROMOLECULES. V. THEORY OF IONIC POLARIZATION IN POLYELECTROLYTES. *J. Phys. Chem.* **1960**, *64* (5), 605–619. https://doi.org/10.1021/j100834a023.

(150) Khair, A. S.; Squires, T. M. The Influence of Hydrodynamic Slip on the Electrophoretic Mobility of a Spherical Colloidal Particle. *Phys. Fluids* **2009**, *21* (4), 042001. https://doi.org/10.1063/1.3116664.

(151) Shields IV, C. W.; Han, K.; Ma, F.; Miloh, T.; Yossifon, G.; Velev, O. D. Supercolloidal Spinners: Complex Active Particles for Electrically Powered and Switchable Rotation. *Adv. Funct. Mater.* **2018**, *28* (35), 1803465. https://doi.org/10.1002/adfm.201803465.

(152) Cushing, K. W.; Piyasena, M. E.; Carroll, N. J.; Maestas, G. C.; López, B. A.; Edwards, B. S.; Graves, S. W.; López, G. P. Elastomeric Negative Acoustic Contrast Particles for Affinity Capture Assays. *Anal. Chem.* **2013**, *85* (4), 2208–2215. https://doi.org/10.1021/ac3029344.

(153) Laurell, T.; Petersson, F.; Nilsson, A. Chip Integrated Strategies for Acoustic Separation and Manipulation of Cells and Particles. *Chem. Soc. Rev.* **2007**, *36* (3), 492–506. https://doi.org/10.1039/b601326k.

(154) Gao, L.; Wyatt Shields, C.; Johnson, L. M.; Graves, S. W.; Yellen, B. B.; López, G. P. Two-Dimensional Spatial Manipulation of Microparticles in Continuous Flows in Acoustofluidic Systems. *Biomicrofluidics* **2015**, *9* (1), 014105. https://doi.org/10.1063/1.4905875.

(155) Evander, M.; Nilsson, J. Acoustofluidics 20: Applications in Acoustic Trapping. *Lab. Chip* **2012**, *12* (22), 4667–4676. https://doi.org/10.1039/C2LC40999B.

(156) Hammarström, B.; Laurell, T.; Nilsson, J. Seed Particle-Enabled Acoustic Trapping of Bacteria and Nanoparticles in Continuous Flow Systems. *Lab. Chip* **2012**, *12* (21), 4296–4304. https://doi.org/10.1039/C2LC40697G.

(157) Johnson, L. M.; Gao, L.; Shields IV, C. W.; Smith, M.; Efimenko, K.; Cushing, K.; Genzer, J.; López, G. P. Elastomeric Microparticles for Acoustic Mediated Bioseparations. *J. Nanobiotechnology* **2013**, *11* (1), 22. https://doi.org/10.1186/1477-3155-11-22.

(158) Shields, C. W. I.; Johnson, L. M.; Gao, L.; López, G. P. Elastomeric Negative Acoustic Contrast Particles for Capture, Acoustophoretic Transport, and Confinement of Cells in Microfluidic Systems. *Langmuir* **2014**, *30* (14), 3923–3927. https://doi.org/10.1021/la404677w.

(159) Ohiri, K. A.; Evans, B. A.; Shields, C. W.; Gutiérrez, R. A.; Carroll, N. J.; Yellen, B. B.; López, G. P. Magnetically Responsive Negative Acoustic Contrast Microparticles for Bioanalytical Applications. *ACS Appl. Mater. Interfaces* **2016**, *8* (38), 25030–25035. https://doi.org/10.1021/acsami.6b09591.

(160) Hammarström, B.; Evander, M.; Barbeau, H.; Bruzelius, M.; Larsson, J.; Laurell, T.; Nilsson, J. Non-Contact Acoustic Cell Trapping in Disposable Glass Capillaries. *Lab. Chip* **2010**, *10* (17), 2251–2257. https://doi.org/10.1039/C004504G.

(161) Evander, M.; Gidlöf, O.; Olde, B.; Erlinge, D.; Laurell, T. Non-Contact Acoustic Capture of Microparticles from Small Plasma Volumes. *Lab. Chip* **2015**, *15* (12), 2588–2596. https://doi.org/10.1039/C5LC00290G.

(162) Fornell, A.; Johannesson, C.; Searle, S. S.; Happstadius, A.; Nilsson, J.; Tenje, M. An Acoustofluidic Platform for Non-Contact Trapping of Cell-Laden Hydrogel Droplets Compatible with Optical Microscopy. *Biomicrofluidics* **2019**, *13* (4), 044101. https://doi.org/10.1063/1.5108583.

(163) Cao, Q.; Han, X.; Li, L. Configurations and Control of Magnetic Fields for Manipulating Magnetic Particles in Microfluidic Applications: Magnet Systems and Manipulation Mechanisms. *Lab. Chip* **2014**, *14* (15), 2762–2777. https://doi.org/10.1039/C4LC00367E.

(164) Cushing, K.; Undvall, E.; Ceder, Y.; Lilja, H.; Laurell, T. Reducing WBC Background in Cancer Cell Separation Products by Negative Acoustic Contrast Particle Immuno-Acoustophoresis. *Anal. Chim. Acta* **2018**, *1000*, 256–264. https://doi.org/10.1016/j.aca.2017.11.064.

(165) Liu, Q.; Nian, G.; Yang, C.; Qu, S.; Suo, Z. Bonding Dissimilar Polymer Networks in Various Manufacturing Processes. *Nat. Commun.* **2018**, *9* (1), 846. https://doi.org/10.1038/s41467-018-03269-x.

(166) Farka, Z.; Brandmeier, J. C.; Mickert, M. J.; Pastucha, M.; Lacina, K.; Skládal, P.; Soukka, T.; Gorris, H. H. Nanoparticle-Based Bioaffinity Assays: From the Research Laboratory to the Market. *Adv. Mater. 36* (n/a), 2307653. https://doi.org/10.1002/adma.202307653.

(167) Shields IV, C. W.; Sun, D.; Johnson, K. A.; Duval, K. A.; Rodriguez, A. V.; Gao, L.; Dayton, P. A.; López, G. P. Nucleation and Growth Synthesis of Siloxane Gels to Form Functional, Monodisperse, and Acoustically Programmable Particles. *Angew. Chem. Int. Ed.* **2014**, *53* (31), 8070–8073. https://doi.org/10.1002/anie.201402471.

(168) Ohlsson, P.; Petersson, K.; Augustsson, P.; Laurell, T. Acoustic Impedance Matched Buffers Enable Separation of Bacteria from Blood Cells at High Cell Concentrations. *Sci. Rep.* **2018**, *8* (1), 9156. https://doi.org/10.1038/s41598-018-25551-0.

(169) Wu, M.; Huang, P.-H.; Zhang, R.; Mao, Z.; Chen, C.; Kemeny, G.; Li, P.; Lee, A. V.; Gyanchandani, R.; Armstrong, A. J.; Dao, M.; Suresh, S.; Huang, T. J. Circulating Tumor Cell Phenotyping via High-Throughput Acoustic Separation. *Small Weinh. Bergstr. Ger.* **2018**, *14* (32), e1801131. https://doi.org/10.1002/smll.201801131.

(170) Undvall Anand, E.; Magnusson, C.; Lenshof, A.; Ceder, Y.; Lilja, H.; Laurell, T. Two-Step Acoustophoresis Separation of Live Tumor Cells from Whole Blood. *Anal. Chem.* **2021**, *93* (51), 17076–17085. https://doi.org/10.1021/acs.analchem.1c04050.

(171) Günther, A.; Becker, M.; Göpfert, J.; Joos, T.; Schneiderhan-Marra, N. Comparison of Bead-Based Fluorescence Versus Planar Electrochemiluminescence Multiplex Immunoassays for Measuring Cytokines in Human Plasma. *Front. Immunol.* **2020**, *11*.

(172) Armbruster, D. A.; Pry, T. Limit of Blank, Limit of Detection and Limit of Quantitation. *Clin. Biochem. Rev.* **2008**, *29* (Suppl 1), S49–S52.

(173) Findlay, J. W. A.; Dillard, R. F. Appropriate Calibration Curve Fitting in Ligand Binding Assays. *AAPS J.* **2007**, *9* (2), 29. https://doi.org/10.1208/aapsj0902029.

(174) Instruction Manual: Rabbit OVA IgG (Ovalbumin IgG) ELISA Kit (MBS7606465). https://www.mybiosource.com/rabbit-elisa-kits/ova-igg-ovalbumin-igg/7606465 (accessed 2023-03-04).

(175) Chattopadhyay, P. K.; Hogerkorp, C.-M.; Roederer, M. A Chromatic Explosion: The Development and Future of Multiparameter Flow Cytometry. *Immunology* **2008**, *125* (4), 441–449. https://doi.org/10.1111/j.1365-2567.2008.02989.x.

(176) Gibbs, J.; Vessels, M.; Rothenberg, M.; Kennebunk, M. Selecting the Detection System—Colorimetric, Fluorescent, Luminescent Methods for ELISA Assays.

(177) Myers, J. A.; Curtis, B. S.; Curtis, W. R. Improving Accuracy of Cell and Chromophore Concentration Measurements Using Optical Density. *BMC Biophys.* **2013**, *6* (1), 4. https://doi.org/10.1186/2046-1682-6-4.

(178) Lei, B. U. W.; Prow, T. W. A Review of Microsampling Techniques and Their Social Impact. *Biomed. Microdevices* **2019**, *21* (4), 81. https://doi.org/10.1007/s10544-019-0412-y.

(179) Serafin, A.; Malinowski, M.; Prażmowska-Wilanowska, A. Blood Volume and Pain Perception during Finger Prick Capillary Blood Sampling: Are All Safety Lancets Equal? *Postgrad. Med.* **2020**, *132* (3), 288–295. https://doi.org/10.1080/00325481.2020.1717160.

(180) Brown, L.; Byrne, R. L.; Fraser, A.; Owen, S. I.; Cubas-Atienzar, A. I.; Williams, C. T.; Kay, G. A.; Cuevas, L. E.; Fitchett, J. R. A.; Fletcher, T.; Garrod, G.; Kontogianni, K.; Krishna, S.; Menzies, S.; Planche, T.; Sainter, C.; Staines, H. M.; Turtle, L.; Adams, E. R. Self-Sampling of Capillary Blood for SARS-CoV-2 Serology. *Sci. Rep.* **2021**, *11* (1), 7754. https://doi.org/10.1038/s41598-021-86008-5.

(181) Vainionpää, R.; Waris, M.; Leinikki, P. Diagnostic Techniques: Serological and Molecular Approaches. *Ref. Module Biomed. Sci.* **2015**, B978-0-12-801238-3.02558-7. https://doi.org/10.1016/B978-0-12-801238-3.02558-7.

(182) Gong, F.; Wei, H.; Li, Q.; Liu, L.; Li, B. Evaluation and Comparison of Serological Methods for COVID-19 Diagnosis. *Front. Mol. Biosci.* **2021**, *8*. https://doi.org/10.3389/fmolb.2021.682405.

(183) Rogier, E. W.; Giorgi, E.; Tetteh, K.; Sepúlveda, N. Editorial: Current Research on Serological Analyses of Infectious Diseases. *Front. Med.* **2023**, *10*. https://doi.org/10.3389/fmed.2023.1154584.

(184) Li, T.; Chen, Y.; Chen, Z.; Hao, Y.; Liang, M.; Liu, Y.; Ou, G.; Zhang, H.; Tang, Y.; Hao, Y.; Wageh, S.; Al-Hartomy, O. A.; Kalam, A.; Zhang, B.; Shi, X.; Li, X.; Zhang, H. Early and Sensitive Detection of Pathogens for Public Health and Biosafety: An Example of Surveillance and Genotyping of SARS-CoV-2 in Sewage Water by Cas12a-Facilitated Portable Plasmonic Biosensor. *Research* **2023**, *6*, 0205. https://doi.org/10.34133/research.0205.

(185) Pilevar, M.; Kim, K. T.; Lee, W. H. Recent Advances in Biosensors for Detecting Viruses in Water and Wastewater. *J. Hazard. Mater.* **2021**, *410*, 124656. https://doi.org/10.1016/j.jhazmat.2020.124656.

(186) Carrascal, M.; Sánchez-Jiménez, E.; Fang, J.; Pérez-López, C.; Ginebreda, A.; Barceló, D.; Abian, J. Sewage Protein Information Mining: Discovery of Large Biomolecules as Biomarkers of Population and Industrial Activities. *Environ. Sci. Technol.* **2023**, *57* (30), 10929–10939. https://doi.org/10.1021/acs.est.3c00535.

(187) Gavrilaș, S.; Ursachi, C. Ștefan; Perța-Crișan, S.; Munteanu, F.-D. Recent Trends in Biosensors for Environmental Quality Monitoring. *Sensors* **2022**, *22* (4), 1513. https://doi.org/10.3390/s22041513.

(188) Nichols, Z. E.; Geddes, C. D. Sample Preparation and Diagnostic Methods for a Variety of Settings: A Comprehensive Review. *Molecules* **2021**, *26* (18), 5666. https://doi.org/10.3390/molecules26185666.

(189) Kontou, P. I.; Braliou, G. G.; Dimou, N. L.; Nikolopoulos, G.; Bagos, P. G. Antibody Tests in Detecting SARS-CoV-2 Infection: A Meta-Analysis. *Diagnostics* **2020**, *10* (5), 319. https://doi.org/10.3390/diagnostics10050319.

(190) Fan, Y.; Wang, X.; Ren, J.; Lin, F.; Wu, J. Recent Advances in Acoustofluidic Separation Technology in Biology. *Microsyst. Nanoeng.* **2022**, *8* (1), 1–16. https://doi.org/10.1038/s41378-022-00435-6.

(191) Li, P.; Huang, T. J. Applications of Acoustofluidics in Bioanalytical Chemistry. *Anal. Chem.* **2019**, *91* (1), 757–767. https://doi.org/10.1021/acs.analchem.8b03786.

(192) Geng, W.; Liu, Y.; Yu, N.; Qiao, X.; Ji, M.; Niu, Y.; Niu, L.; Fu, W.; Zhang, H.; Bi, K.; Chou, X. An Ultra-Compact Acoustofluidic Device Based on the Narrow-Path Travelling Surface Acoustic Wave (Np-TSAW) for Label-Free Isolation of Living Circulating Tumor Cells. *Anal. Chim. Acta* **2023**, *1255*, 341138. https://doi.org/10.1016/j.aca.2023.341138.

(193) Li, L.; Wyatt Shields, C.; Huang, J.; Zhang, Y.; A. Ohiri, K.; B. Yellen, B.; Chilkoti, A.; P. López, G. Rapid Capture of Biomolecules from Blood via Stimuli-Responsive Elastomeric Particles for Acoustofluidic Separation. *Analyst* **2020**, *145* (24), 8087–8096. https://doi.org/10.1039/D0AN01164A.

(194) Afzal, M.; Park, J.; Jeon, J. S.; Akmal, M.; Yoon, T.-S.; Sung, H. J. Acoustofluidic Separation of Proteins Using Aptamer-Functionalized Microparticles. *Anal. Chem.* **2021**, *93* (23), 8309–8317. https://doi.org/10.1021/acs.analchem.1c01198.

(195) Naquin, T. D.; Canning, A. J.; Gu, Y.; Chen, J.; Naquin, C. M.; Xia, J.; Lu, B.; Yang, S.; Koroza, A.; Lin, K.; Wang, H.-N.; Jeck, W. R.; Lee, L. P.; Vo-Dinh, T.; Huang, T. J. Acoustic Separation and Concentration of Exosomes for Nucleotide Detection: ASCENDx. *Sci. Adv.* **2024**, *10* (10), eadm8597. https://doi.org/10.1126/sciadv.adm8597.

(196) Thome, C. P.; Fowle, J. P.; McDonnell, P.; Zultak, J.; Jayaram, K.; Neumann, A. K.; López, G. P.; Shields, C. W. Acoustic Pipette and Biofunctional Elastomeric Microparticle System for Rapid Picomolar-Level Biomolecule Detection in Whole Blood. *Sci. Adv.* **2024**, *10* (42), eado9018. https://doi.org/10.1126/sciadv.ado9018.

(197) Laurell, T.; Petersson, F.; Nilsson, A. Chip Integrated Strategies for Acoustic Separation and Manipulation of Cells and Particles. *Chem. Soc. Rev.* **2007**, *36* (3), 492–506. https://doi.org/10.1039/B601326K.

(198) Hammarström, B.; Laurell, T.; Nilsson, J. Seed Particle-Enabled Acoustic Trapping of Bacteria and Nanoparticles in Continuous Flow Systems. *Lab. Chip* **2012**, *12* (21), 4296–4304. https://doi.org/10.1039/C2LC40697G.

(199) Bierbrauer, F.; Kapur, N.; Wilson, M. C. T. Drop Pinch-Off for Discrete Flows from a Capillary. *ESAIM Proc.* **2013**, *40*, 16–33. https://doi.org/10.1051/proc/201340002.

(200) Or, D.; Ghezzehei, T. A. Dripping into Subterranean Cavities from Unsaturated Fractures under Evaporative Conditions. *Water Resour. Res.* **2000**, *36* (2), 381–393. https://doi.org/10.1029/1999WR900311.

(201) Vera, F.; Rivera, R.; Romero-Maltrana, D.; Villanueva, J. Negative Pressures and the First Water Siphon Taller than 10.33 Meters. *PLOS ONE* **2016**, *11* (4), e0153055. https://doi.org/10.1371/journal.pone.0153055.

(202) Mugele, F.; Heikenfeld, J. *Electrowetting: Fundamental Principles and Practical Applications*, 1st ed.; Wiley, 2018. https://doi.org/10.1002/9783527412396.

(203) Reis, N. M.; Needs, S. H.; Jegouic, S. M.; Gill, K. K.; Sirivisoot, S.; Howard, S.; Kempe, J.; Bola, S.; Al-Hakeem, K.; Jones, I. M.; Prommool, T.; Luangaram, P.; Avirutnan, P.; Puttikhunt, C.; Edwards, A. D. Gravity-Driven Microfluidic Siphons: Fluidic Characterization and Application to Quantitative Immunoassays. *ACS Sens.* **2021**, *6* (12), 4338–4348. https://doi.org/10.1021/acssensors.1c01524.

(204) Reis, N. M.; Pivetal, J.; Loo-Zazueta, A. L.; Barros, J. M. S.; Edwards, A. D. Lab on a Stick: Multi-Analyte Cellular Assays in a Microfluidic Dipstick. *Lab. Chip* **2016**, *16* (15), 2891–2899. https://doi.org/10.1039/C6LC00332J.

(205) Barkley, S.; Scarfe, S. J.; Weeks, E. R.; Dalnoki-Veress, K. Predicting the Size of Droplets Produced through Laplace Pressure Induced Snap-Off. *Soft Matter* **2016**, *12* (35), 7398–7404. https://doi.org/10.1039/C6SM00853D.

(206) Wang, S.; Zhang, X.; Ma, C.; Yan, S.; Inglis, D.; Feng, S. A Review of Capillary Pressure Control Valves in Microfluidics. *Biosensors* **2021**, *11* (10), 405. https://doi.org/10.3390/bios11100405.

(207) Akhras, N.; Singh, G.; Gill, K. K.; Bola, S.; Al-Hakeem, K.; Reis, N. M. Numerical Modeling and Experimental Validation of Fluid Flow in Micro- and Meso-Fluidic Siphons. *Front. Chem. Eng.* **2024**, *6*. https://doi.org/10.3389/fceng.2024.1443949.

(208) Liu, H.-C.; Kijanka, P.; Urban, M. W. Fluid Surface Tension Evaluation Using Capillary Wave Measurement with Optical Coherence Tomography. *AIP Adv.* **2020**, *10* (5), 055121. https://doi.org/10.1063/1.5143935.

(209) Dintenfass, L. Internal Viscosity of the Red Cell and a Blood Viscosity Equation. *Nature* **1968**, *219* (5157), 956–958. https://doi.org/10.1038/219956a0.

(210) Gil Rosa, B.; Akingbade, O. E.; Guo, X.; Gonzalez-Macia, L.; Crone, M. A.; Cameron, L. P.; Freemont, P.; Choy, K.-L.; Güder, F.; Yeatman, E.; Sharp, D. J.; Li, B. Multiplexed Immunosensors for Point-of-Care Diagnostic Applications. *Biosens. Bioelectron.* **2022**, *203*, 114050. https://doi.org/10.1016/j.bios.2022.114050.

(211) Harry W Schroeder, J.; Cavacini, L. Structure and Function of Immunoglobulins. *J. Allergy Clin. Immunol.* **2010**, *125* (2 0 2), S41. https://doi.org/10.1016/j.jaci.2009.09.046.

(212) *OVA IgG elisa kit | Rabbit OVA IgG (Ovalbumin IgG) ELISA Kit (MBS7606465)*. https://www.mybiosource.com/rabbit-elisa-kits/ova-igg-ovalbumin-igg/7606465 (accessed 2024-10-18).

(213) *Abcam Mouse IgM ELISA Kit (ab133047)*. https://www.abcam.com/en-us/products/elisa-kits/mouse-igm-elisa-kit-ab133047 (accessed 2024-10-17).

(214) *Mouse IgA ELISA Kit - Invitrogen (EMIGA)*. https://www.thermofisher.com/elisa/product/Mouse-IgA-ELISA-Kit/EMIGA (accessed 2024-10-17).

(215) Jarvey, N.; Henrique, F.; Gupta, A. Asymmetric Rectified Electric and Concentration Fields in Multicomponent Electrolytes with Surface Reactions. *Soft Matter* **2023**, *19* (31), 6032–6045. https://doi.org/10.1039/D3SM00823A.

(216) Bishop, K. J. M.; Biswal, S. L.; Bharti, B. Active Colloids as Models, Materials, and Machines. *Annu. Rev. Chem. Biomol. Eng.* **2023**, *14* (1), annurev-chembioeng-101121-084939. https://doi.org/10.1146/annurev-chembioeng-101121-084939.

(217) Boymelgreen, A.; Yossifon, G.; Park, S.; Miloh, T. Spinning Janus Doublets Driven in Uniform Ac Electric Fields. *Phys. Rev. E* **2014**, *89* (1), 011003. https://doi.org/10.1103/PhysRevE.89.011003.

(218) Ebbens, S.; Jones, R. A. L.; Ryan, A. J.; Golestanian, R.; Howse, J. R. Self-Assembled Autonomous Runners and Tumblers. *Phys. Rev. E* **2010**, *82* (1), 015304. https://doi.org/10.1103/PhysRevE.82.015304.

(219) Pawar, A. B.; Kretzschmar, I. Multifunctional Patchy Particles by Glancing Angle Deposition. *Langmuir* **2009**, *25* (16), 9057–9063. https://doi.org/10.1021/la900809b.

(220) Harraq, A. A.; Choudhury, B. D.; Bharti, B. Field-Induced Assembly and Propulsion of Colloids. *Langmuir* **2022**, *38* (10), 3001–3016. https://doi.org/10.1021/acs.langmuir.1c02581.

(221) Han, K. Electric and Magnetic Field-Driven Dynamic Structuring for Smart Functional Devices. *Micromachines* **2023**, *14* (3), 661. https://doi.org/10.3390/mi14030661.

(222) Diwakar, N. M.; Kunti, G.; Miloh, T.; Yossifon, G.; Velev, O. D. AC Electrohydrodynamic Propulsion and Rotation of Active Particles of Engineered Shape and Asymmetry. *Curr. Opin. Colloid Interface Sci.* **2022**, *59*, 101586. https://doi.org/10.1016/j.cocis.2022.101586.

(223) Peng, C.; Lazo, I.; Shiyanovskii, S. V.; Lavrentovich, O. D. Induced-Charge Electro-Osmosis around Metal and Janus Spheres in Water: Patterns of Flow and Breaking

Symmetries. *Phys. Rev. E* **2014**, *90* (5), 051002. https://doi.org/10.1103/PhysRevE.90.051002.

(224) Gangwal, S.; Cayre, O. J.; Velev, O. D. Dielectrophoretic Assembly of Metallodielectric Janus Particles in AC Electric Fields. *Langmuir* **2008**, *24* (23), 13312–13320. https://doi.org/10.1021/la8015222.

(225) Ma, F.; Yang, X.; Zhao, H.; Wu, N. Inducing Propulsion of Colloidal Dimers by Breaking the Symmetry in Electrohydrodynamic Flow. *Phys. Rev. Lett.* **2015**, *115* (20), 208302. https://doi.org/10.1103/PhysRevLett.115.208302.

(226) Ganguly, A.; Gupta, A. Going in Circles: Slender Body Analysis of a Self-Propelling Bent Rod. *Phys. Rev. Fluids* **2023**, *8* (1), 014103. https://doi.org/10.1103/PhysRevFluids.8.014103.

(227) Al Harraq, A.; Bello, M.; Bharti, B. A Guide to Design the Trajectory of Active Particles: From Fundamentals to Applications. *Curr. Opin. Colloid Interface Sci.* **2022**, *61*, 101612. https://doi.org/10.1016/j.cocis.2022.101612.

(228) J. Archer, R.; I. Campbell, A.; J. Ebbens, S. Glancing Angle Metal Evaporation Synthesis of Catalytic Swimming Janus Colloids with Well Defined Angular Velocity. *Soft Matter* **2015**, *11* (34), 6872–6880. https://doi.org/10.1039/C5SM01323B.

(229) Han, K.; Shields, C. W.; Bharti, B.; Arratia, P. E.; Velev, O. D. Active Reversible Swimming of Magnetically Assembled "Microscallops" in Non-Newtonian Fluids. *Langmuir* **2020**, *36* (25), 7148–7154. https://doi.org/10.1021/acs.langmuir.9b03698.

(230) Puce, S.; Sciurti, E.; Rizzi, F.; Spagnolo, B.; Qualtieri, A.; De Vittorio, M.; Staufer, U. 3D-Microfabrication by Two-Photon Polymerization of an Integrated Sacrificial Stencil Mask. *Micro Nano Eng.* **2019**, *2*, 70–75. https://doi.org/10.1016/j.mne.2019.01.004.

(231) Zabow, G. Reflow Transfer for Conformal Three-Dimensional Microprinting. *Science* **2022**, *378* (6622), 894–898. https://doi.org/10.1126/science.add7023.

(232) Al Harraq, A.; Lee, J. G.; Bharti, B. Magnetic Field–Driven Assembly and Reconfiguration of Multicomponent Supraparticles. *Sci. Adv.* **2020**, *6* (19), eaba5337. https://doi.org/10.1126/sciadv.aba5337.

(233) Wang, W.; Mallouk, T. E. A Practical Guide to Analyzing and Reporting the Movement of Nanoscale Swimmers. *ACS Nano* **2021**, *15* (10), 15446–15460. https://doi.org/10.1021/acsnano.1c07503.

(234) Zuk, P. J.; Cichocki, B.; Szymczak, P. GRPY: An Accurate Bead Method for Calculation of Hydrodynamic Properties of Rigid Biomacromolecules. *Biophys. J.* **2018**, *115* (5), 782–800. https://doi.org/10.1016/j.bpj.2018.07.015.

(235) Squires, T. M.; Bazant, M. Z. Induced-Charge Electro-Osmosis. *J. Fluid Mech.* **2004**, *509*, 217–252. https://doi.org/10.1017/S0022112004009309.

(236) Squires, T. M.; Bazant, M. Z. Breaking Symmetries in Induced-Charge Electro-Osmosis and Electrophoresis. *J. Fluid Mech.* **2006**, *560*, 65. https://doi.org/10.1017/S0022112006000371.

(237) Wajnryb, E.; Mizerski, K. A.; Zuk, P. J.; Szymczak, P. Generalization of the Rotne–Prager–Yamakawa Mobility and Shear Disturbance Tensors. *J. Fluid Mech.* **2013**, *731*, R3. https://doi.org/10.1017/jfm.2013.402.

(238) Rotne, J.; Prager, S. Variational Treatment of Hydrodynamic Interaction in Polymers. *J. Chem. Phys.* **1969**, *50* (11), 4831–4837. https://doi.org/10.1063/1.1670977.

(239) Yamakawa, H. Transport Properties of Polymer Chains in Dilute Solution: Hydrodynamic Interaction. *J. Chem. Phys.* **1970**, *53* (1), 436–443. https://doi.org/10.1063/1.1673799.

Appendix A: Magnetically locked Janus particle clusters with orientation-dependent motion in AC electric fields

Previously published as: Gyun Lee, J.*; P. Thome, C.*; A. Cruse, Z.; Ganguly, A.; Gupta, A.; Wyatt Shields, C. Magnetically Locked Janus Particle Clusters with Orientation-Dependent Motion in AC Electric Fields. *Nanoscale* **2023**, *15* (40), 16268–16276. https://doi.org/10.1039/D3NR03744D. All supplementary media may be obtained at the source of publication. *J.G.L. and C.P.T. are co-first authors and contributed equally to this work.

A.1 Abstract

Active particles, or micromotors, locally dissipate energy to drive locomotion at small length scales. The type of trajectory is generally fixed and dictated by the geometry and composition of the particle, which can be challenging to tune using conventional fabrication procedures. Here, we report a simple, bottom-up method to magnetically assemble gold-coated polystyrene Janus particles into "locked" clusters that display diverse trajectories when stimulated by AC electric fields. The orientation of particles within each cluster gives rise to distinct modes of locomotion, including translational, rotational, trochoidal, helical, and orbital. We model this system using a simplified rigid beads model and demonstrate qualitative agreement between the predicted and experimentally observed cluster trajectories. Overall, this system provides a facile means to scalably create micromotors with a range of well-defined motions from discrete building blocks.

A.2 Introduction

Micromotors composed of active colloidal particles have found use in a multitude of applications, including drug delivery,[23–26] cell manipulation,[27–29] flexible electronics,[30–32] and cargo transport.[33–37] Such micromotors can be propelled by various energy sources, including magnetic,[38–43] acoustic,[24,44–46] and electric fields,[33,47–50] as well as catalytic reactions.[51–55] As a category of electrical stimulation, induced-charge electrophoresis (ICEP) is a useful method to drive the motion of metallodielectric particles (e.g., dielectric particles with metal patches) in alternating current (AC) electric fields due to the highly tunable interactions between the particles and applied field.[33,47,84,98,215] In the case of a metallodielectric particle undergoing ICEP, the patch geometry is a major determinant of particle locomotion;[86–88,216] however, the ability to control patch morphology, and thus particle trajectory, is limited.

Previous work has studied the locomotion of dimeric Janus particle clusters,[217,218] which have the capacity to exhibit non-linear trajectories. However, this approach has only been shown to produce two regimes of locomotion (i.e., linear and orbital). By assembling Janus particles (i.e., spherical particles with two distinct hemispheres) into multiparticle clusters with complex relative orientations, we hypothesized that it is feasible to replicate the motion of singular Janus particles and access new regimes of motion not otherwise attainable using traditional Janus particles.

Here, we utilize a high-throughput approach to show the first demonstration of magnetically “locked” assemblies of metallodielectric Janus particles that exhibit five distinct regimes of locomotion when driven by ICEP (i.e., translational, rotational, trochoidal, helical, and orbital). Four of these regimes are accessible by clusters comprising only two Janus particles. By assembling Janus particles into larger clusters, such as trimers, or assembling particles with non-hemispherical patches (i.e., patchy particles)[96,219,220], we observe a broader diversity of motions

within a single experiment (e.g., orbital motions of patchy-Janus particle clusters and helical motions of trimeric Janus particle clusters). To examine the relationship between particle orientations within a cluster and the resultant cluster motions, we show that a force-torque model can qualitatively predict the trajectory of assembled clusters in AC electric fields. This system provides a simple, high-throughput avenue for the study and future design of micromotors with distinct trajectories and functions, such as those that must navigate complex 3D environments to deliver cargo.

A.3 Results and Discussion

In the case of metallodielectric particles, ICEP originates from asymmetric electroosmotic flows over the regions of differing polarizabilities. When a uniform AC field in the kHz frequency range is applied to a metallodielectric Janus particle within a liquid, the particle reorients such that the interface between the hemispheres aligns parallel with the field due to dielectrophoresis (DEP), yielding the greatest possible induced dipole moment.[82,221] After this reorientation, ions in solution accumulate preferentially at the surface of the metallic hemisphere, generating an induced charge cloud. At steady state, due to this induced charge cloud, fluid is drawn to the particle parallel to the field and ejected perpendicular to the field, away from the two hemispheres.[83,222] Importantly, electroosmotic flows dominate over the region of the particle that is more polarizable, resulting in asymmetric fluid flows around the particle and propulsion in the direction of the less polarizable region.[47,82,87,92,96] Thus, to fabricate non-magnetic Janus particles for this study, we used electron-beam (e-beam) evaporation to coat one hemisphere of commercial 5.1 μm fluorescent polystyrene (PS) particles with gold (Au) due to the large mismatch in the polarizability of both materials. To fabricate magnetic Janus particles capable of locking into varied cluster configurations, we

deposited a thin layer of cobalt (Co) – a ferromagnetic material – between the polystyrene and gold layers. For both types of particles, a chromium (Cr) layer was included between the PS and the metal patch to aid adhesion of the patch (Fig. A.1A). After removal from the coating substrate, we transferred the particles to Milli-Q water, as high solution ion content suppresses ICEP, at a concentration of ~2.5x10^6 particles mL^{-1}.[82,88] We then exposed the magnetic Janus particle solution to a permanent magnet (~50 Gauss), ensuring random magnetization of the Co patches of the Janus particles.

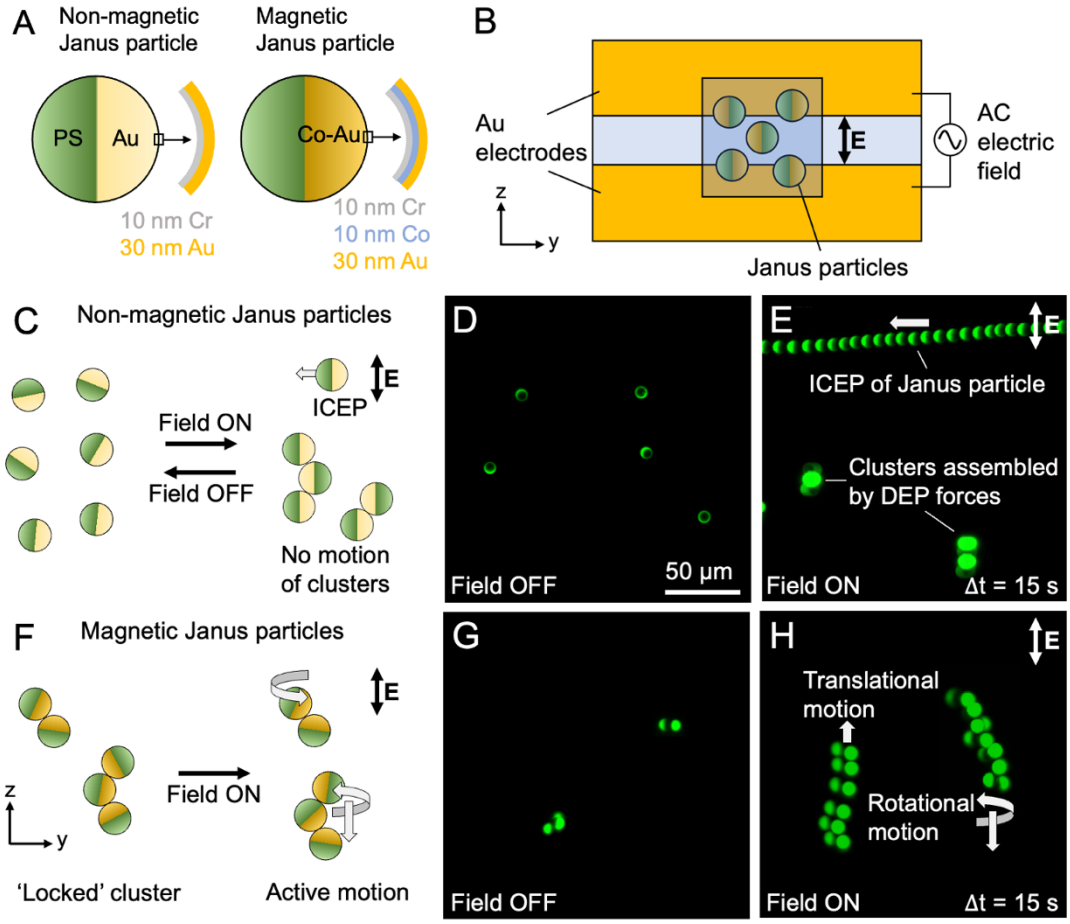

Figure A.1. Fabrication and propulsion of non-magnetic versus magnetically locked Janus particles in AC electric fields. A. Schematic illustration of the preparation of Janus particles.

Polystyrene spheres on a substrate are coated with Cr and Au to prepare non-magnetic Janus particles or Cr, Co, and Au to prepare magnetic Janus particles, all using e-beam evaporation. B. Schematic representation of the coplanar electrode propulsion chamber. The particle dispersion is introduced between two gold electrodes, and a high frequency AC square wave is applied. C. Schematic image showing propulsion and assembly of non-magnetic Janus particles in AC electric fields. Upon removal of the electric field, particles disassemble. D. Fluorescent microscopy image showing dispersed non-magnetic particles before applying an AC electric field. E. Superimposed fluorescent microscopy image of non-magnetic Janus particles in a uniform AC electric field. A single Janus particle propels with a linear trajectory due to ICEP, while particles assembled by dielectrophoretic forces and aligned with the electric field do not exhibit any motion. F. Schematic illustration showing propulsion of a magnetically locked cluster of Janus particles in AC electric fields. G. Fluorescent microscopy image showing pre-assembled magnetic particles before applying AC electric fields. H. Superimposed fluorescent microscopy image showing propulsion of magnetic clusters.

We fabricated coplanar electrokinetic propulsion chambers by depositing 20 nm Cr and 100 nm Au on a glass slide masked with a thin strip of Kapton tape spanning the length of the slide. After metal deposition, the tape was removed to reveal two Au electrodes. We attached copper (Cu) tape to each electrode to act as electrical leads. During experiments, a hydrophobic pen was used to draw a small square outline that overlapped the two electrodes, and two pieces of polytetrafluoroethylene (PTFE) tape were placed perpendicular to the electrodes at the border of the hydrophobic boundary to act as spacers. After this, 10–20 μL of solution containing the particles was pipetted onto the slide within the hydrophobic boundary, and a coverslip was placed on top of the PTFE spacers. A square wave (4 kHz for all experiments) was applied to the chamber to generate the AC electric field (~750 V cm^{-1} for all experiments) within it (Fig. A.1B, Fig. A.5).

We first evaluated chamber operation by loading a solution of non-magnetic Janus particles (i.e., lacking the Co layer) into a chamber situated on a fluorescence microscope equipped with a camera. Without the AC electric field applied, particle orientations were random, though the dense gold hemispheres tended to orient toward the bottom of the chamber, toward the microscope objective, due to gravity (Fig. A.1C, D). Upon applying the electric field, we noted that single

particles displayed linear translation perpendicular to the applied AC electric field, which is characteristic of ICEP of spherical, metallodielectric Janus particles.[82,223] We also observed DEP-mediated clustering of some particles when in close proximity. Such clustering generally led to arrested particle motion due to alignment and coupling of the cluster with the field, which results in DEP forces dominating over ICEP forces (Fig. A.1E).[224] Upon removal of the applied field, these clusters disassembled as expected.

We then examined pre-magnetically locked Janus particles in the chamber. In the absence of an applied AC electric field, we saw a diverse population of Janus particle clusters, including many dimers and trimers (Fig. A.1F-H). Upon application of the field, we observed a range of motions, including translational, rotational, trochoidal, helical, and nil (arrested) motions (Fig. A.1H, A6, A7). Notably, unlike the clusters of non-magnetic Janus particles that dispersed when the applied field was removed, clusters of magnetic Janus particles retained their configurations after removal of the AC electric field, confirming their assembly is mediated by the magnetic Co layer and not by DEP forces.

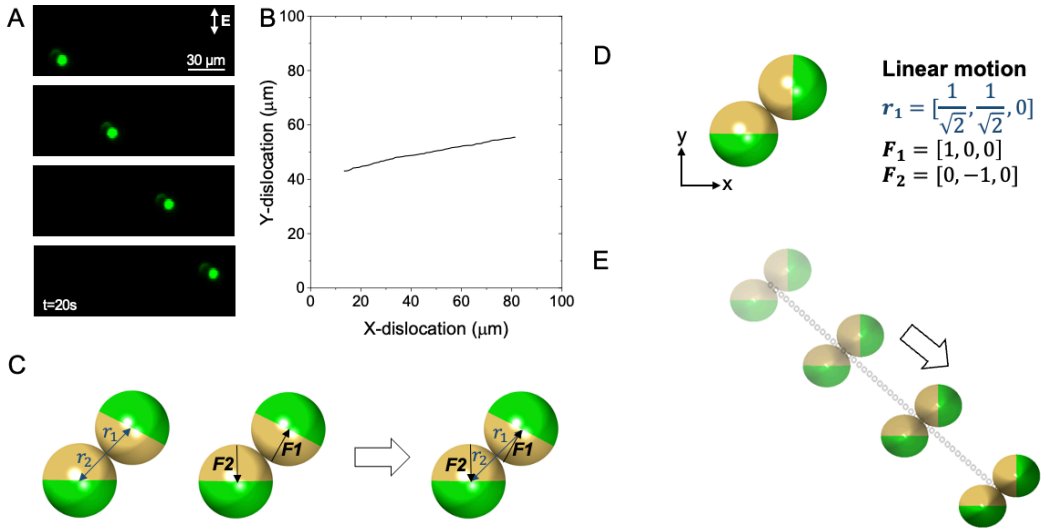

Figure A.2. Janus particle dimer exhibiting linear translational motion. A. Time-lapse image of an experimentally observed Janus particle dimer displaying linear translation, captured via fluorescence microscopy. B. Cluster trajectory, extracted from the tracking video used to create the time-lapse image in (A). C. Schematic illustration detailing the approach for defining relative particle orientations in an assembled cluster. D. Schematic illustration of the configuration of the dimer from (A) and the extracted approximate vectors that define the configuration. E. Trajectory of the cluster in (D) as simulated using a rigid beads model.

To begin exploring the nature of the diverse cluster motions we observed, we analyzed a dimer configuration that exhibited linear translation without rotation. As seen in both the time-lapse images (Fig. A.2A; Movie S1) and particle trajectory plot (Fig. A.2B), the particle cluster moves linearly; however, the direction of motion differs from that of a single Janus particle undergoing ICEP in that neither of the PS hemispheres directly face the direction of motion. We hypothesized that this cluster motion was a direct result of the relative orientation of the individual Janus particles. To explore this more rigorously, we defined the orientation of the two particles using a common origin (i.e., the point of contact between the two particles), two position vectors, $\boldsymbol{r_1}$ and $\boldsymbol{r_2}$, and two force vectors, $\boldsymbol{F}_1$ and $\boldsymbol{F}_2$, that point from the center of the patch of each particle to its PS center (Fig. A.2C, Fig. A.8). After video analysis, we determined the position vectors of the particles in the cluster to be directed along the position vectors $\boldsymbol{r_1} = [1/\sqrt{2}, 1/\sqrt{2}, 0]$ and $\boldsymbol{r_2} = [-1/\sqrt{2}, -1/\sqrt{2}, 0]$ with the point of contact designated as the origin. Notably, as $\boldsymbol{r_2}$ is always the negative of $\boldsymbol{r_1}$, we report only $\boldsymbol{r_1}$ for convenience in the remainder of this discussion. The force vectors, representing the relative orientation of the metallic patches in the assembly are given by $\boldsymbol{F}_1 = [1,0,0]$ and $\boldsymbol{F}_2 = [0,-1,0]$ (Fig. A.2D). We then modeled these particles by a rigid beads model where the complex forces due to asymmetric electroosmotic flow over the particles are instead modeled as a single net effective force acting normal to the center of each magnetic patch (additional information available in the "Janus assembly propulsion modeling" section and

the Supplementary Materials). Using this model, we generated theoretical trajectories of this dimer configuration and found qualitative agreement between theory and experiments (Fig. A.2E), wherein the dimer cluster experienced linear translation toward the PS hemispheres.

To further evaluate the distinct types of motions exhibited in this system and further verify predictions by our model, we isolated and captured videos of dimeric clusters that exhibited rotational (Fig. A.3A; Movie S2), trochoidal (Fig. A.3B; Fig. A.9; Movie S3), and helical motions (Fig. A.3C; Fig. A.10; Movie S4). We define rotational motion as the spinning of clusters about their common origin (i.e., close to or in line with their point of contact) and helical motion as the orbit of clusters around a central point outside of the dimer while undergoing translation. Last, we define trochoidal motion as concurrent rotational and translational motion. The tracked experimental trajectories of clusters exhibiting rotational, trochoidal, and helical motions are shown in Fig. A.3D, E, and F, respectively. We analyzed videos to determine the approximate relative orientations of particles within a cluster; following this, we generated theoretical trajectories for each of these clusters using the previously described rigid beads model (Fig. A.3G, H, and I). Again, we found strong qualitative agreement between the character of the trajectories predicted by the model and those observed experimentally. It may be expected that the proximity of particles in a dimer or other cluster configuration would lead to disruption of the electroosmotic flows over the particles, therefore impacting particle trajectories;[217] however, this was noted and addressed by Wu et al., where these perturbations were modeled through a first-order method of reflections.[225] In essence, each constituent bead moves due to the external electric field along with the entrained electrohydrodynamic flow of the other bead as a first-order correction. While qualitatively similar to the beads modeling technique applied in our analysis, our methodology captures corrections beyond the first order and is hydrodynamically more precise for a pair of

touching spheres than Wu et al. In contrast, the force calculations in our model are only accurate up to the leading order, where the net forces and torques are the sum of the electric forces independently acting on each particle. Hence, we do not capture the perturbation in force on a particle due to the presence of the other. This perturbation being a higher-order effect is not necessary to qualitatively predict the motion of our clusters,[226] as seen in Figs. A.2E, and A.3G-I. Indeed, the qualitative agreement between the four distinct observed and predicted motions (i.e., translational, rotational, trochoidal, and helical) suggests that the simplified effective net forces normal to the patch hemispheres are sufficient for model-based, qualitative prediction of the character of complex motions arising from slight changes to the relative orientations of Janus particles in a dimeric cluster.

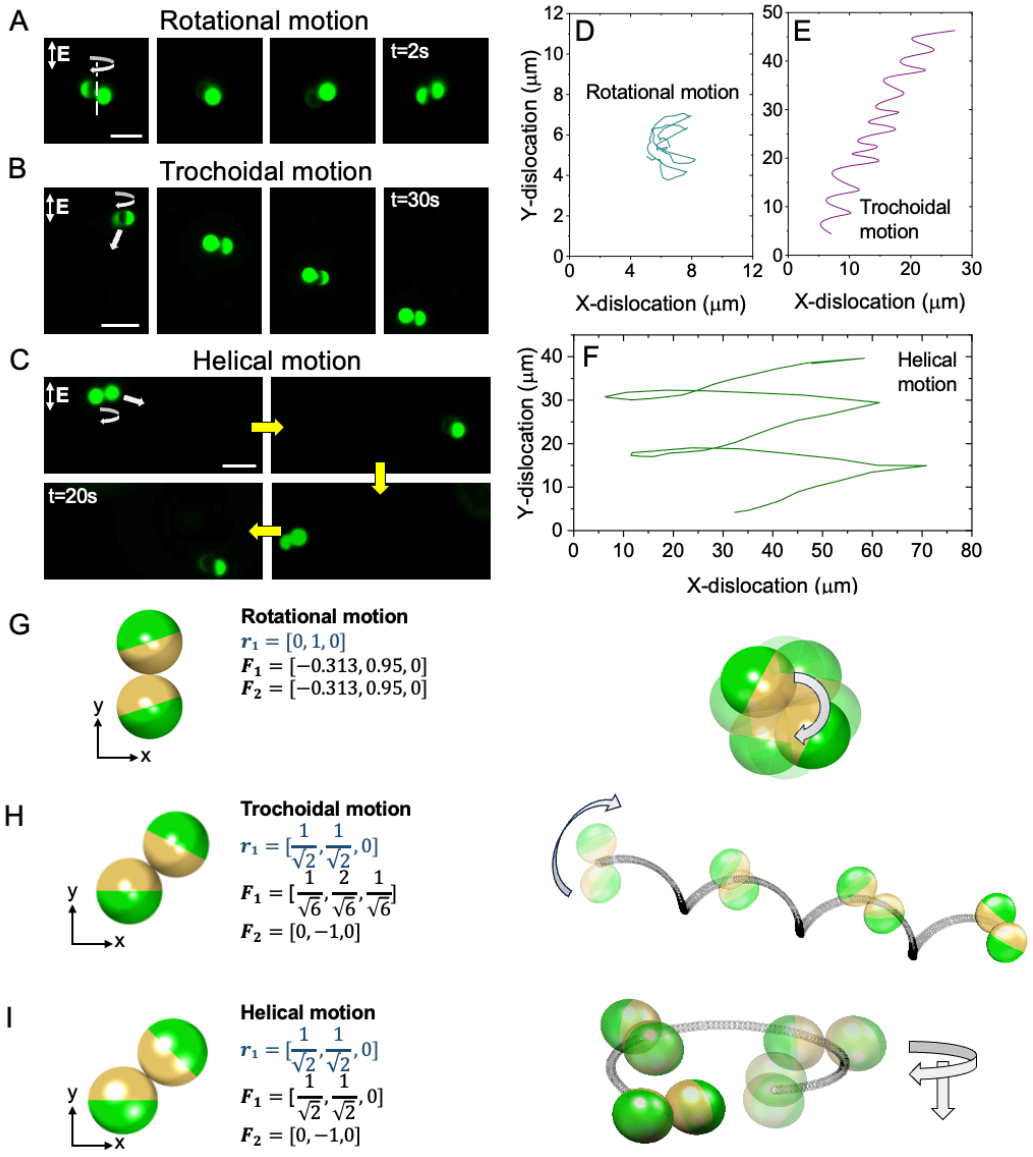

Figure A.3. Janus particle dimers exhibiting rotational, trochoidal, and helical motions. A-C. Time-lapse images of experimentally observed dimers exhibiting (A) rotational, (B) trochoidal, and (C) helical motions, captured via fluorescence microscopy. D-F. Plotted particle trajectory for (D) rotational, (E) trochoidal, and (F) helical motions extracted from the particle tracking videos used to generate the time-lapse images in (A), (B), and (C), respectively. G-I. Schematic illustrations of the approximate configurations of the dimers and position vectors as well as trajectories of the clusters in (A), (B), and (C), respectively, as simulated using a rigid beads model. Scale bars in (A), (B), and (C) = 10 μm.

In addition to dimers, this system spontaneously generates more complex clusters, including trimers, tetramers, etc., each displaying unique motions. To continue exploring the richness of this system, we examined the motion of dimers consisting of both patchy and Janus particles as well as trimeric clusters. To fabricate patchy particles, we used glancing angle deposition of the metallic layers described earlier to form non-hemispherical patches (Fig. A.11). Using these particles, we first examined a dimer cluster consisting of a Janus particle and a patchy particle with a triangular patch. Compared the propulsion of a dimer formed from two Janus particles, which rotates about an axis found within the cluster (Fig. A.3A, A.4A), we observed that a dimer formed from Janus particle and a patchy particle rotates about an axis that is outside of the cluster (Fig. A.4B, C; Movie S5). This orbital motion may be attributed to a combination of the orbital component of the motion of the patchy particle, which is known to be a three-dimensional helix[87,227], and the linear translational motion of the Janus particle. When combined, the translational motion of the Janus particle of the dimer counteracts the translational motion of the patchy particle along the Z-direction, thus preventing helical motion along the Z-direction.

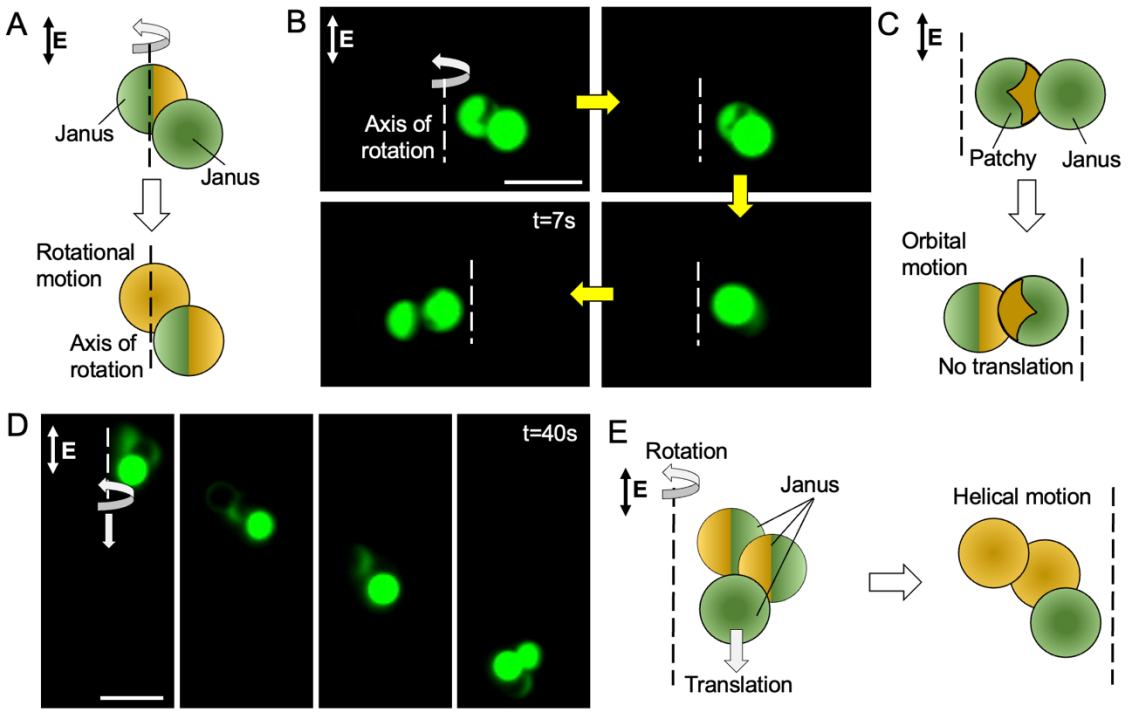

Figure A.4. Patchy particle dimers and Janus particle trimers exhibiting orbital and complex helical motions. A. Schematic illustration showing rotational motion of a Janus-Janus particle cluster (Fig. A.3A). B. Time-lapse images of an experimentally observed Janus patchy particle cluster exhibiting an orbital motion, captured via fluorescence microscopy. C. Schematic illustration showing orbital motion of a patchy-Janus particle cluster. D. Time-lapse images of an experimentally observed a trimeric cluster exhibiting helical motion, captured via fluorescence microscopy. E. Schematic illustration showing helical motion of a trimeric cluster. Scale bars in (A) and (D) = 10 μm.

As previously described, we observed several trimeric clusters with numerous configurations. A rigorous study of these more complex clusters is reserved for future work; however, we studied one trimer configuration that exhibited helical motion (Fig. A.4D; Movie S5). Upon extracting the geometric orientation of the particles, we observed that the effective forces on the patches of individual spherical particles in the assembly appear to be the primary contributors to the experimentally observed direction of orbit along the helical path (Fig. A.4E). This example highlights the ability to access various regimes of motion with multiparticle micromotor clusters,

which may be useful for the development of micromotors capable of performing complex tasks such as transporting and manipulating high-value cargo.

A.4 Conclusions

We show a simple system that leverages magnetic locking of metallodielectric particles into clusters of varied configurations to experimentally explore a range of particle trajectories in a single experiment. We further demonstrate that a rigid beads model qualitatively aligns with the experimentally observed, complex motions of various configurations of dimeric clusters. This suggests that electrohydrodynamic interactions between particles does not play a substantial role in cluster motion, but the summed forces due to ICEP normal to the metallic patch of each particle dominate in the case of the dimers studied.

The presented system could enable the future design of electrokinetic micromotors. By predicting the trajectories of specific cluster configurations, it becomes possible to design particle assemblies to accomplish specific tasks. In this system, the assembly of particles into distinct dimeric and trimeric clusters through magnetic locking is predominantly random. However, by leveraging techniques such as glancing angle deposition of the magnetic patch[87,219,228], templating magnetic patches onto micromotors,[229–231] or dynamic assembly of magnetic clusters after application of the electric field, researchers can create particles that predictably assemble and self-limit to a desired cluster configuration to access a prescribed regime of motion and accomplish a specific task. For example, by depositing magnetic patches much smaller than one hemisphere of the Janus particle, therefore reducing the number of possible cluster configurations, particles could be programmed to form consistent clusters to reliably exhibit one or more of the trajectories revealed in this study. If combined with other technologies, such as the ability to carry other

particles, cells, or molecules, these programmed clusters could be used to deliver rare or high-value cargo through complex 3D environments.

A.5 Experimental Section

A.5.1 Janus particle preparation

Janus particles were prepared by e-beam evaporation of Cr, Co, and Au onto a submonolayer of 5.1 μm green or red fluorescent PS particles (Magsphere). To prepare the submonolayers, a convective assembly-inspired approach was used.[97] Specifically, two borosilicate glass slides were cleaned and dried with acetone (Millipore Sigma). The substrate slide was attached horizontally to the immobile end of a GenieTouch syringe pump (Kent Scientific), while the deposition slide was attached to the mobile syringe holder connected to the driveshaft. The deposition slide was brought into contact with the substrate slide at a ~45˚ angle. The particles were washed three to four times into milli-Q water (MQW) to remove surfactants and the solution was concentrated to 10 wt.%. After briefly sonicating, 10 μL of the particle solution was pipetted onto the substrate slide at the point of contact with the deposition slide, forming a thin, uniform line of particle solution across the contact line between the slides. The syringe pump was calibrated to a 30 mL Becton Dickinson syringe and set to the full position. Then, the pump was engaged, and the deposition slide was pushed across the substrate slide at a rate of 2.5 mL min^{-1} until the deposited particle solution was exhausted. This occurred approximately halfway across the deposition slide when the pump indicated an ejected volume of ~13 mL. The deposition slide was then cleaned to prevent particle buildup, and the slides were once again brought into contact slightly past where the previous particle deposition ended. This procedure was repeated to fill the slide. To fabricate non-magnetic Janus particles, slides with

submonolayers were then coated with 10 nm Cr for enhanced metal patch adhesion and 30 nm Au using an electron-beam evaporator (Edwards Auto 306 Cryo). To fabricate magnetic Janus particles, slides with submonolayers were instead coated with 10 nm Cr, 10 nm Co, and 30 nm Au. Coated particles were removed from the slides by gently scraping with a metal spatula, resuspended in MQW, and transferred to a microcentrifuge tube for storage. The particles were then sonicated for ~30 sec to separate aggregates.

A.5.2 Patchy particle preparation

For fabrication of particles with triangular patches (i.e., patchy particles), the same PS particles were deposited on a glass slide via a Langmuir-Blodgett trough (NIMA). Briefly, 1 mL of a 5 wt.% solution of PS spheres dispersed in a 50 vol.% aqueous ethanol solution was carefully sprayed at the air-water interface of a trough filled with MQW using a pipette. The particles were deposited on a substrate at a surface pressure of 22 mN m^{-1} to form a closed-pack monolayer of a colloidal crystal (Fig. A.11). The triangular metal patch was introduced on the PS particles by glancing angle deposition (angle between the substrate and the incident metal vapor = 10°), and the substrate was transferred to an e-beam deposition chamber.[96,219,232] The metal deposition on the particles was performed identically to that described for the preparation of magnetic Janus particles.

A.5.3 Coplanar propulsion chamber fabrication

To fabricate coplanar propulsion chambers, borosilicate glass slides were masked with a ~2 mm adhesive Kapton tape mask that covered the length of the slides. Then 20 nm Cr and 100 nm Au were deposited on the masked slides by e-beam evaporation. After removal of the mask,

the roughly 2 mm uncoated gap in the center of the slide (along its length) remained, with two electrodes on either side. Two strips of Cu tape were adhered to the top of the Au electrodes to form connection points for electrical leads. Additional details on the fabrication and use of the propulsion chamber are available in the Supplementary Materials.

A.5.4 ICEP propulsion experiments

The coplanar propulsion chambers were washed thoroughly with acetone before each experiment. A hydrophobic barrier pen (IHC World) was used to draw a roughly 1.25 cm x 1.25 cm square outline that overlapped with both electrodes. Two pieces of PTFE tape (RS Crum & Company) were placed flat and perpendicular to the electrodes at the boarder of the hydrophobic boundary. Then 10–20 μL of Janus particle cluster samples were pipetted onto the small space left between the PTFE tape spacers and the Au electrodes, and a coverslip was placed over the spacers. Then the entire chamber was placed on a Zeiss AxioVert A1 TL/RL inverted fluorescence microscope equipped with a Axiocam 305 mono camera (Zeiss, Germany). An Agilent 33210A waveform generator (Agilent) was attached to a Tegam 2340 high voltage amplifier (Tegam), and electrical leads from the amplifier were attached to the Cu tape on the propulsion chamber. A 4 kHz square wave signal was generated, amplified, and applied to the propulsion chamber, forming an electric field with magnitudes of ~750 V cm^{-1}. Resultant cluster motion was observed and recorded using the microscope camera, typically in fluorescence mode, using a 120 W mercury lamp (Excelitas) and a 545/25 nm excitation filter and a 605/70 nm emission filter or a 470/40 nm excitation filter and a 525/50 nm emission filter (Zeiss).

A.5.5 Video processing

Videos of clusters undergoing ICEP captured during experiments were analyzed using ImageJ software.[233] Videos were exported as AVI files while maintaining the native micron/pixel ratio and relative time information. All color correction, cropping, and time-lapse image overlay generation was completed using standard ImageJ functions. To track particles and extract position information, the "analyze particles" feature was used.

A.5.6 Janus assembly propulsion modeling

To model the presented Janus assemblies, we used a rigid beads model driven by an effective force on the particle.[234] The rigid beads model is able to capture hydrodynamic interactions in multiparticle assemblies comprising two or more particles. In this model, the effective force acting on each individual particle has not been mechanistically derived. A detailed derivation can be found elsewhere in literature.[226,235,236]

As stated previously in ICEP literature,[83,235,236] the inward electroosmotic flow around the particle is enhanced on the side of the more polarizable surface. Our model qualitatively captures this effect by considering an outward, constant force directed symmetrically through the centroid of the metallic patch of each individual spherical particle in the assembly. The magnitude of the force is estimated from scaling estimates from the results of Squires and Bazant.[236] For spherical Janus particles with hemispherical caps, the translation velocity is $U_{ICEP} \sim 3R\epsilon E^2/32\eta$. Assuming that only the hydrodynamic drag and the force due to the induced charge asymmetry are acting on the body. Hence, the effective force on the sphere is $F_{ICEP} = 18\pi R^2\epsilon E^2/32$. Utilizing U_{ICEP} and F_{ICEP} to scale the velocity and force in our calculations, we consider a non-dimensional force of magnitude one acting through the centroid of the patch.

Additional information on obtaining the particle velocity and trajectory for a general dimeric configuration is available in the Supplementary Materials.

A.6 Author Contributions

This manuscript was written through contributions of all authors, and all authors have given final approval to the final version of the manuscript. C.P.T. and J.G.L. led experimental setup and investigation, data analysis, and manuscript drafting. A.Ganguly., Z.A.C., and A.Gupta. led model creation and use.

A.7 Acknowledgments

The authors thank to Prof. Daniel Schwartz (CU Boulder) for the use of the Langmuir-Blodgett trough.

A.8 Supplementary Materials

A.8.7 Coplanar electrode propulsion chamber.

The propulsion chamber utilized in this study is shown in Fig. A.5. To operate the chamber, a sample of particle clusters was placed between the two gold electrodes within a drawn hydrophobic boundary and two PTFE tape spacers. After placing a coverslip on top of the PTFE spacers, the particle sample spread to the boarders of the hydrophobic boundary. An electric field was generated by applying an AC square wave from a function generator attached to the device by leads and copper tape.

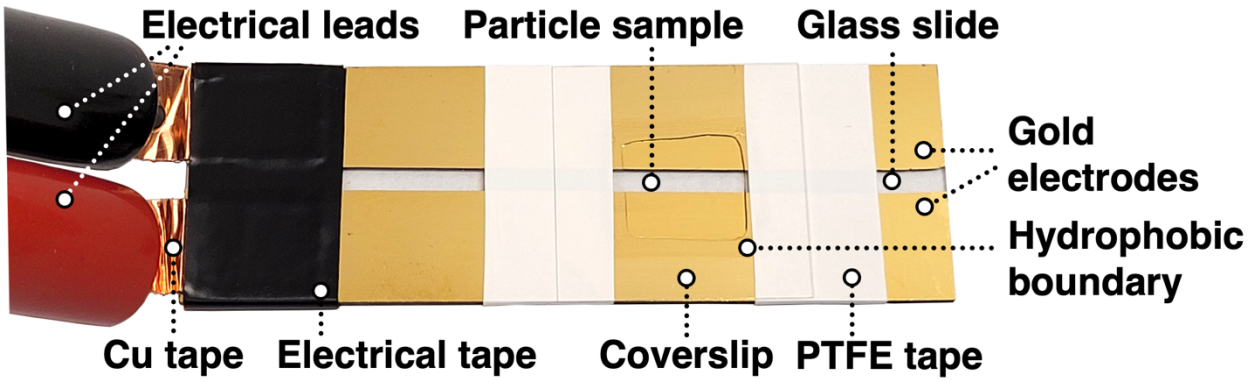

Figure A.5. Image of the coplanar electrode propulsion chamber used to apply the AC electric field to particle samples.

A.8.8 Alignment of Janus clusters and assembly of Janus particles upon applying the AC electric field.

As shown in Fig. A.1C-E of the main text, non-magnetic Janus particle clusters can cluster and be aligned by the applied field due to DEP, resulting in arrested motion. Notably, this phenomenon can also occur, though infrequently, for magnetic Janus particle clusters (Fig. A.6).

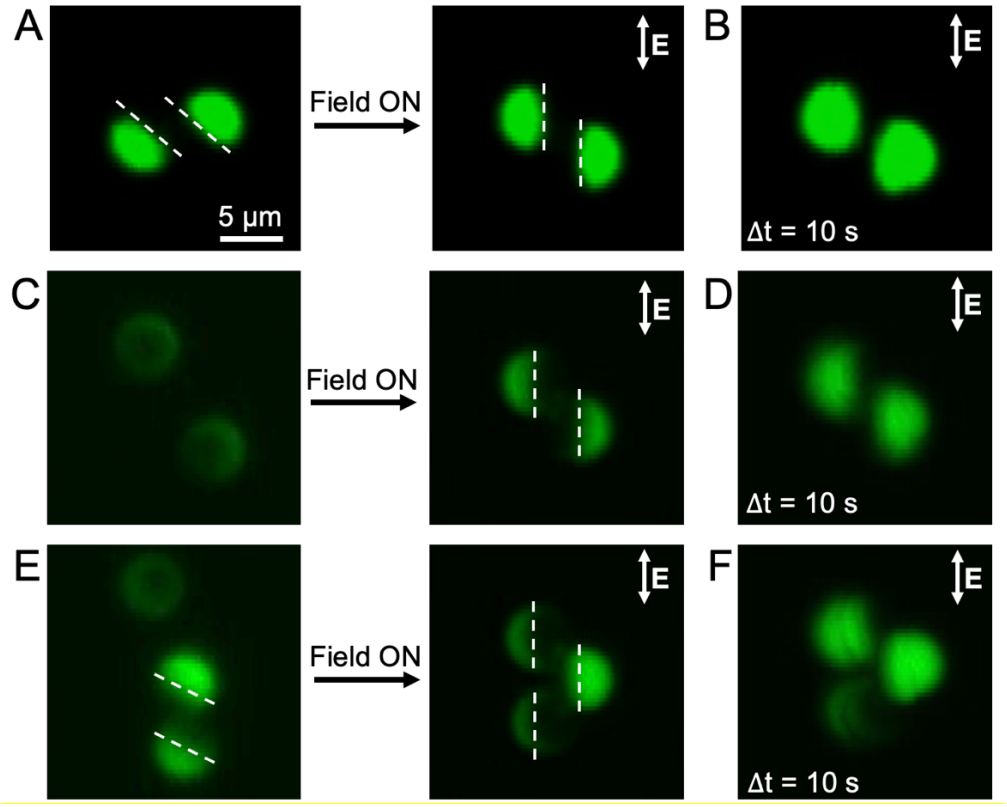

Figure A.6. Fluorescent microscope images of magnetic Janus particles of staggered chains exhibiting no motion in an AC electric field. A. Images showing the alignment of a pre-assemble magnetic Janus particle dimer upon the application of the electric field. B. Superimposed microscope images showing a Janus particle dimer in (A) with no motion in an electric field. C. Images showing the assembly of Janus particles into a staggered chain upon the application of the electric field. D. Superimposed microscope images showing a Janus particle dimer in (C) with no motion in an electric field. E. Images showing the assembly of a Janus particle and a Janus dimer into a staggered chain upon the application of the electric field. F. Superimposed microscope images showing a Janus trimer in (E) with no motion in an electric field.

A.8.9 Inhibited motion of a Janus particle dimer.

Among the regimes of motions found in the presented system, several clusters resulted in inhibited (nil) motion (Fig. A.7).

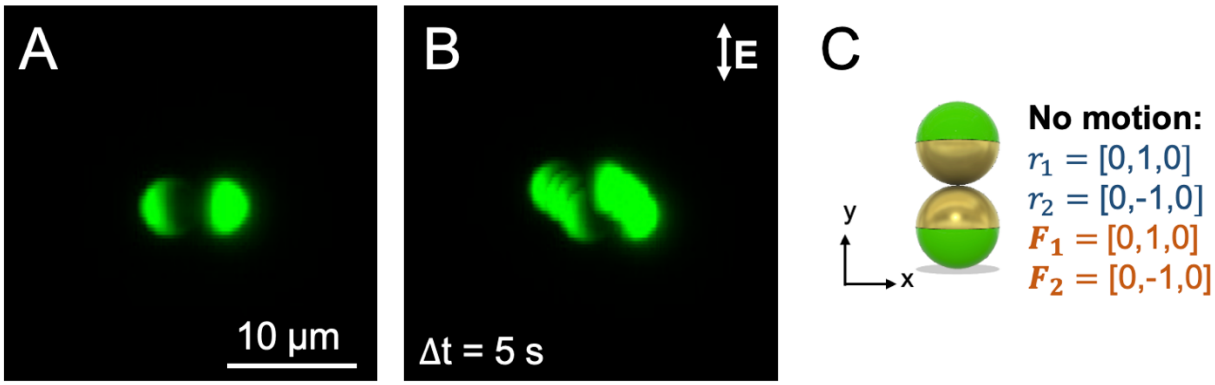

Figure A.7. Janus particle cluster exhibiting no motion in an AC electric field. A. Fluorescent microscope image of two Janus particles facing each other in a dimeric cluster. B. Superimposed fluorescent microscope images showing a Janus particle dimer in (A) with no motion in an AC electric field. The slight motion of the dimer is attributed to bulk fluid flow in the propulsion chamber. C. Schematic illustration of the configuration of the dimer showing no motion and the extracted approximate vectors using a rigid bead model showing no motion.

A.8.10 Theoretical framework.

To gain a mechanistic understanding of the experimentally realized particle motion, we examined the motion of dimers using a mobility formulation. The dimer configurations were seen to depend on two geometric parameters: (i) the position of the point-of-contact between the two spheres; and (ii) the relative positions of the metallic patches on the particles (Fig. A.8).

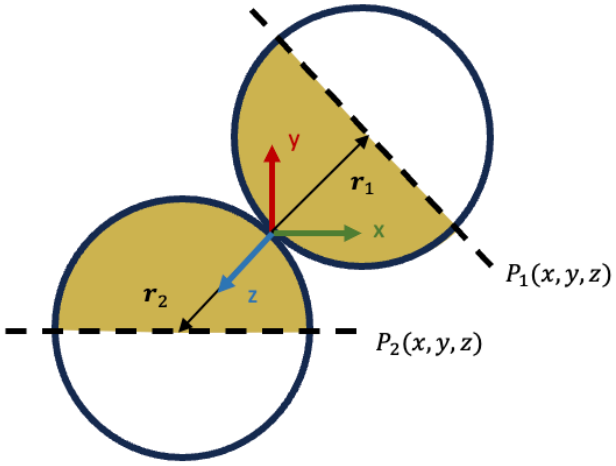

Figure A.8. Schematic illustration of the geometry of a general dimer configuration. The point-of-contact between the particles is the origin of the local coordinate system. The position vectors of the centers of the two spherical particles are $\boldsymbol{r_1}$ and $\boldsymbol{r_2}$, respectively. The metallic patches are specified using 3D planar functions $p_1(x,y,z)$ and $p_2(x,y,z)$ such that the metallic surfaces are always in contact with each other.

The configurations of particles within the dimers are obtained by different combinations of $\boldsymbol{r_1}$, $\boldsymbol{r_2}$, $p_1(x,y,z)$, $p_2(x,y,z)$, described in Fig. A.7 and the corresponding caption. The hydrodynamic properties of these rigid dimer configurations are obtained by implementation of the Generalized Rotne-Prager-Yamakawa method on these dimeric systems.[234] The length scale of these dimers is small, and it is appropriate to describe the flow around these particles using Stokes and continuity equations,

$$\eta \nabla^2 \boldsymbol{v} - \nabla p = 0, \tag{A.1}$$

and

$$\boldsymbol{\nabla} \cdot \boldsymbol{v} = 0, \tag{A.2}$$

where $\boldsymbol{v}$ is the fluid velocity, p is the pressure, and η is the fluid viscosity. The force and velocity moments on the dimer can be represented in terms of their velocity moments due to the linearity of Eqs. (A.1) and (A.2)

$$\begin{bmatrix} \boldsymbol{F} \\ \boldsymbol{T} \end{bmatrix} = -\begin{bmatrix} \zeta^{tt} & \zeta^{tr} \\ \zeta^{rt} & \zeta^{rr} \end{bmatrix} \begin{bmatrix} \boldsymbol{U} \\ \boldsymbol{\Omega} \end{bmatrix}. \tag{A.3}$$

The force $\boldsymbol{F} = [\boldsymbol{F_1}\ \boldsymbol{F_2}]$ and torque $\boldsymbol{T} = [\boldsymbol{T_1}\ \boldsymbol{T_2}]$ are 6-dimensional vectors, where $\boldsymbol{F_1}$, $\boldsymbol{T_1}$, $\boldsymbol{F_2}$, $\boldsymbol{T_2}$ are the force and torque on each of the two particles, respectively. The direction of $\boldsymbol{F}_1$ and $\boldsymbol{F}_2$ depends on both the position vectors $\boldsymbol{r}_1$and $\boldsymbol{r}_2$ and the orientation of the patches $p_1$and p_2. There are no external torques acting on the particle, $\boldsymbol{T}_1 = \boldsymbol{T}_2 = 0$. The translation and rotation velocities, $\boldsymbol{U}$ and $\boldsymbol{\Omega}$, are similarly written. An inversion in Eq. $\begin{bmatrix} \boldsymbol{F} \\ \boldsymbol{T} \end{bmatrix} = -\begin{bmatrix} \zeta^{tt} & \zeta^{tr} \\ \zeta^{rt} & \zeta^{rr} \end{bmatrix} \begin{bmatrix} \boldsymbol{U} \\ \boldsymbol{\Omega} \end{bmatrix}$.

(A.3) gives us the mobility expression,

$$\begin{bmatrix} \boldsymbol{U} \\ \boldsymbol{\Omega} \end{bmatrix} = \begin{bmatrix} \mu^{tt} & \mu^{tr} \\ \mu^{rt} & \mu^{rr} \end{bmatrix} \cdot \begin{bmatrix} \boldsymbol{F} \\ \boldsymbol{T} \end{bmatrix}, \tag{A.4}$$

by which $\boldsymbol{U}$ and $\boldsymbol{\Omega}$ are obtained for a given $\boldsymbol{F}$ and $\boldsymbol{T}$. In the absence of a magnetic field, when the particle is being propelled by an AC electric field, the dimers rotate as a rigid body. This allows us to rewrite the grand mobility expression in Eq. (A.4) to a mobility expression where the force, torque, and velocities are defined with respect to the center of mass of the particle,

$$\begin{bmatrix} \boldsymbol{U_c} \\ \boldsymbol{\Omega_c} \end{bmatrix} = \begin{bmatrix} m^{tt} & m^{tr} \\ m^{rt} & m^{rr} \end{bmatrix} \cdot \begin{bmatrix} \boldsymbol{F_c} \\ \boldsymbol{T_c} \end{bmatrix}. \quad \text{(A.5)}$$

The force and torque acting on the particle center of mass are obtained by addition of the individual $\boldsymbol{F_i}$ and $\boldsymbol{T_i}$ acting on the i^{th} particle, $\boldsymbol{F_c} = \sum_i \boldsymbol{F_i}$ and $\boldsymbol{T_c} = \sum_i (\boldsymbol{T_i} + \boldsymbol{r_i} \times \boldsymbol{F_i})$. The detailed derivation of the mobility coefficients is given by a generalized version of the Roten-Prager-Yamakawa mobility expression and can be found in Wajnryb et al. [4].[237–239] Equation (A.5) conveniently provides $\boldsymbol{U_c}$ and $\boldsymbol{\Omega_c}$ for specific $\boldsymbol{F_c}$ and $\boldsymbol{T_c}$ through the mobility matrix $\boldsymbol{m}$, which depends on the geometric configuration of the dimer. In the next sub-section, we provide a short outline of particle kinematics.

Particle kinematics

We consider that the driving force on the dimer is constant at a body frame of reference $(\boldsymbol{e_x}, \boldsymbol{e_y}, \boldsymbol{e_z})$. Consequently, the rotation and translation velocity, $\boldsymbol{U_c}$ and $\boldsymbol{\Omega_c}$, are also in this body frame. To obtain the laboratory frame motion of the particle, the body frame unit vectors are evolved with time according to

$$\frac{d\boldsymbol{e_i}}{dt} = \boldsymbol{\Omega_c} \times \boldsymbol{e}_i, \quad i = x, y, z$$
$$\frac{d\boldsymbol{R_c}}{dt} = \boldsymbol{U_c} \quad \text{(A.6)}$$

where the unit vectors $\boldsymbol{e_i}$, and the center-of-mass position are expressed in the laboratory reference frame. The expressions in Equation (A.6) can be written as a linear system of equations to obtain the body frame of reference and center of mass position with time

$$\boldsymbol{e_i}(t+dt) = \boldsymbol{e}_i(t) + \frac{d\boldsymbol{e}_i}{dt}\delta t$$
$$\begin{bmatrix} \boldsymbol{e}_x(t+dt) \\ \boldsymbol{e}_y(t+dt) \\ \boldsymbol{e}_z(t+dt) \end{bmatrix} = \boldsymbol{R} \begin{bmatrix} \boldsymbol{e}_x \\ \boldsymbol{e}_y \\ \boldsymbol{e}_z \end{bmatrix}. \quad (A.7)$$

This resulting rotation matrix, $\boldsymbol{R}$, allows for the center-of-mass position to be rotated and translated to follow a path of motion within the body frame of reference. The respective particle and patch positions are further updated using the rotation matrix to adjust their position within the same reference frame.

$$r_{COM}(t+dt) = r_{COM}(t) + \boldsymbol{U} \cdot \boldsymbol{R}\, dt \quad (A.8)$$

A.8.11 Extended characterization of trochoidal and helical motions of Janus dimers in an AC electric field.

To further examine the trochoidal and helical motions shown in Fig. A.3B and C of the main text and evaluated spatially in Fig. A.3E and F, we evaluated the trochoidal and helical cluster movement using time as a third dimension (Fig. A.9 and A.10). The oscillating behaviors in the X-direction of each trajectory over time are signatures of trochoidal and helical motions.

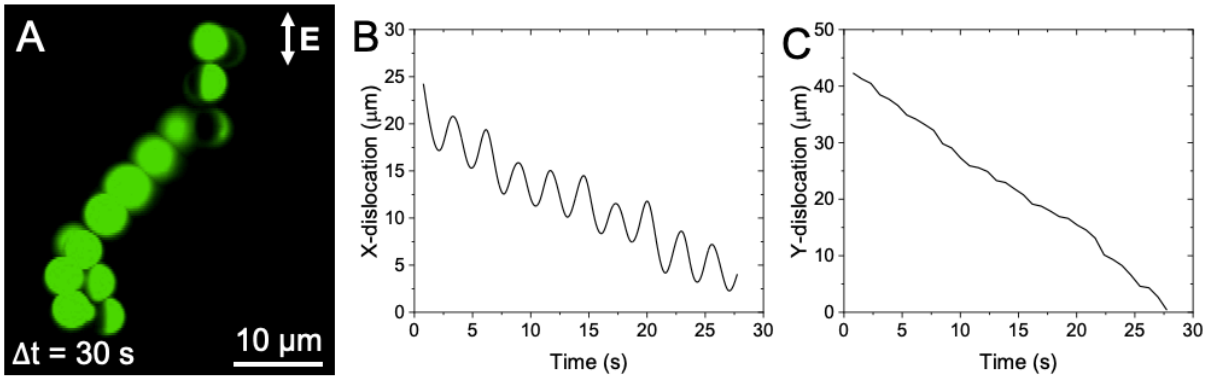

Figure A.9. Characterization of trochoidal motion of Janus dimer in an AC electric field. A. Superimposed fluorescent image of a Janus dimer self-propelling within trochoidal motion in an AC electric field. B-C. Displacement of a Janus dimer with trochoidal motion in X- and Y-directions over time.

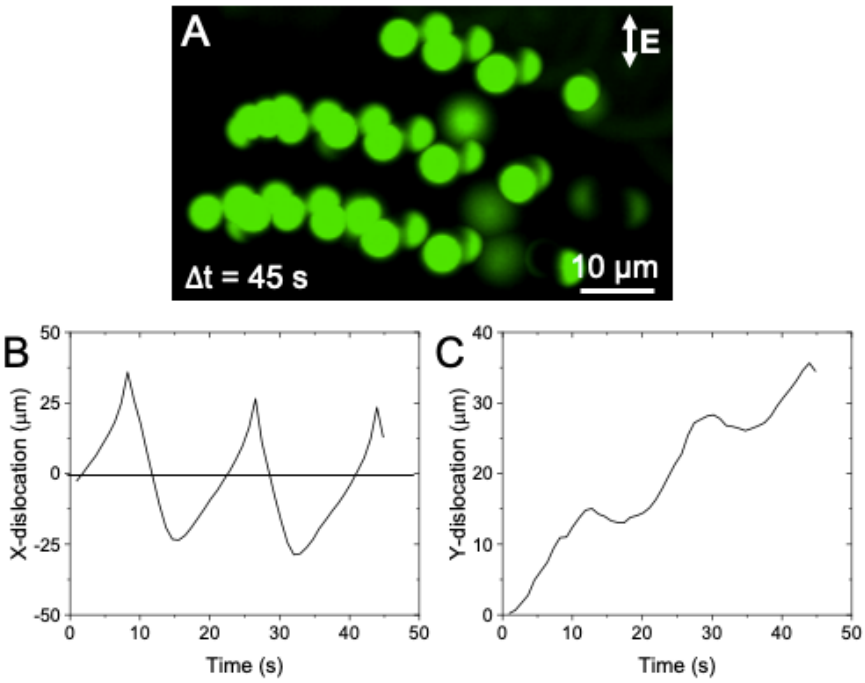

Figure A.10. Characterization of helical motion of Janus dimer in an AC electric field. Superimposed fluorescent image of a Janus dimer self-propelling within helical motion in an AC electric field. B-C. Displacement of a Janus dimer with helical motion in X- and Y- directions over time.

A.8.12 Additional patchy particle fabrication details.

Patchy particles were fabricated by glancing angle deposition of Cr, Co, and Au during electron-beam evaporation (Fig. A.11).

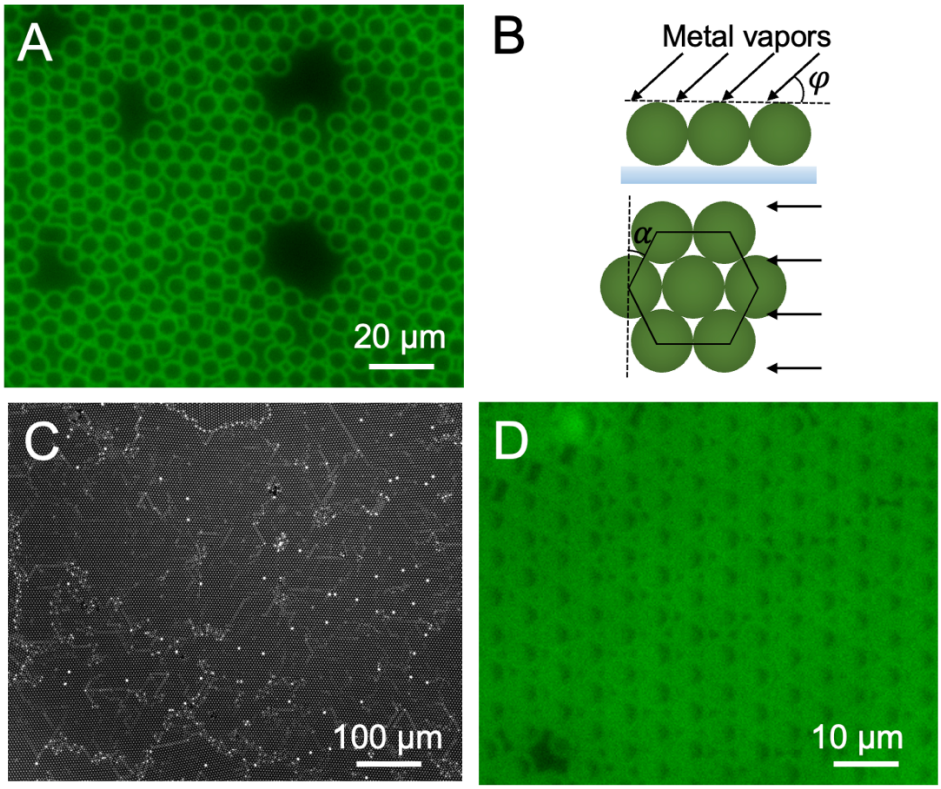

Figure A.11. Fabrication of patchy particles. A. Fluorescent microscope image showing polystyrene (PS) spheres in a submonolayer (diameter = 5.1 µm) assembled using a convective assembly method. B. Schematic illustration of glancing angle deposition of metal onto PS spheres. φ = angle of incident vapor beam, α = monolayer orientation angle. C. Bright-field microscope image showing a closed-pack monolayer of PS spheres assembled by Langmuir-Blodgett deposition. D. Fluorescent microscope image showing PS spheres with triangular patches on their surfaces ($\varphi = 10°$).

Appendix B: Supplementary Materials for Chapter 2

B.1 Supplementary Figures

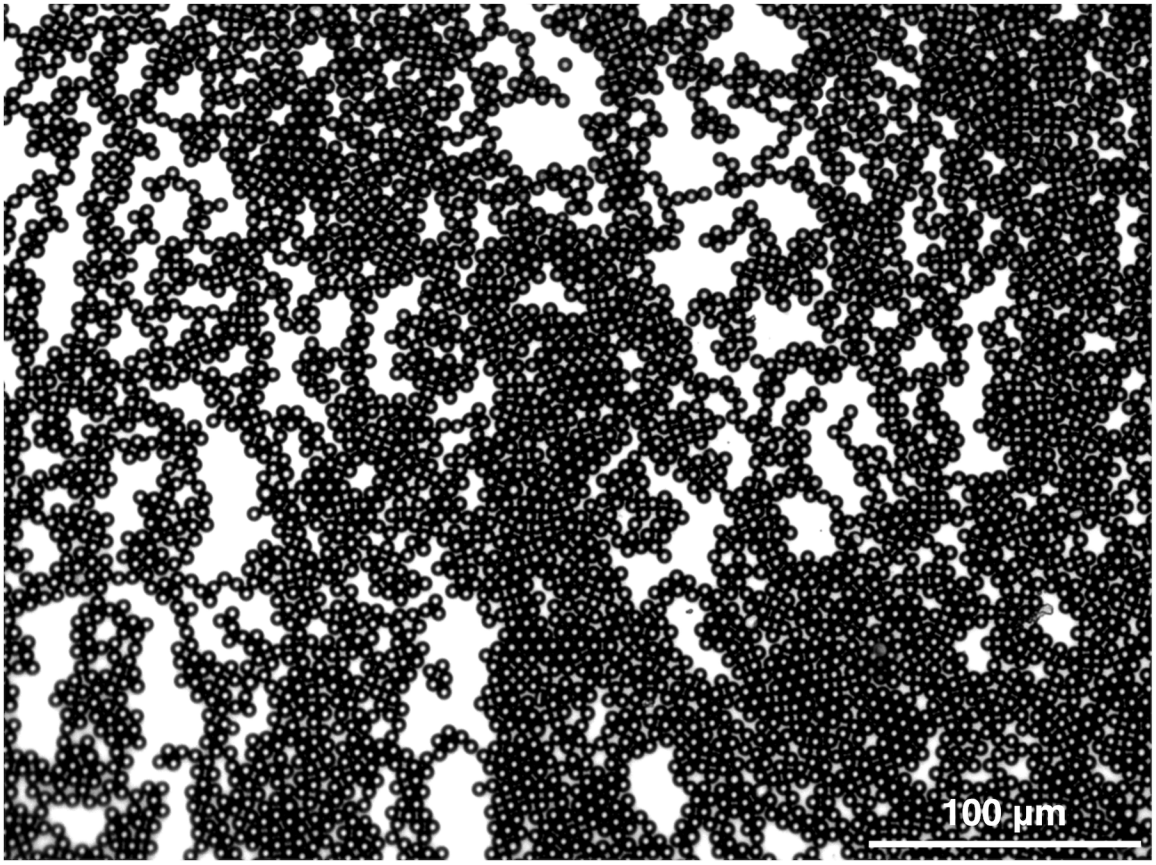

Figure B.1. Representative brightfield image of a submonolayer of PS particles on a glass slide after deposition via the modified convective assembly method.

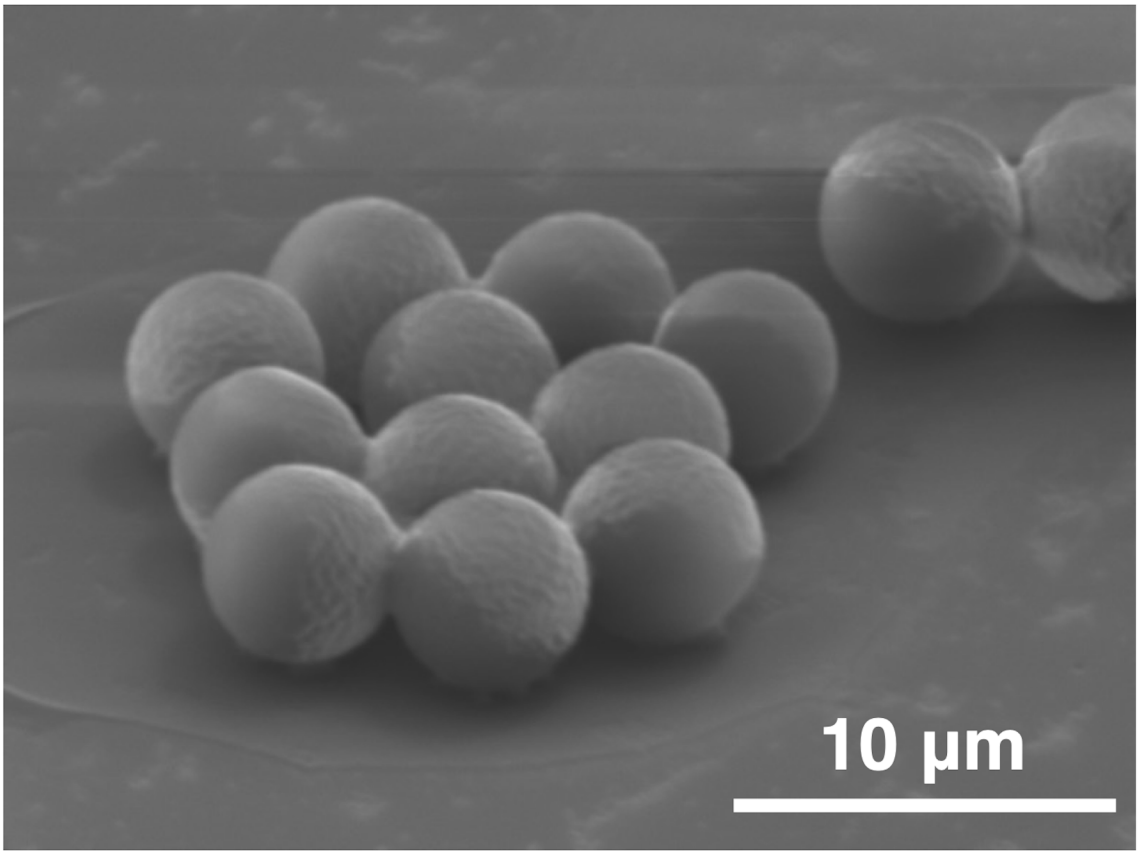

Figure B.2. Unmodified scanning electron microscopy image of Janus particles. Au patches exhibit a rough appearance with light gray color on the dark PS surface. The image was taken using a Hitachi SU3500 SEM in a secondary electron imaging mode at an acceleration voltage of 15 kV.

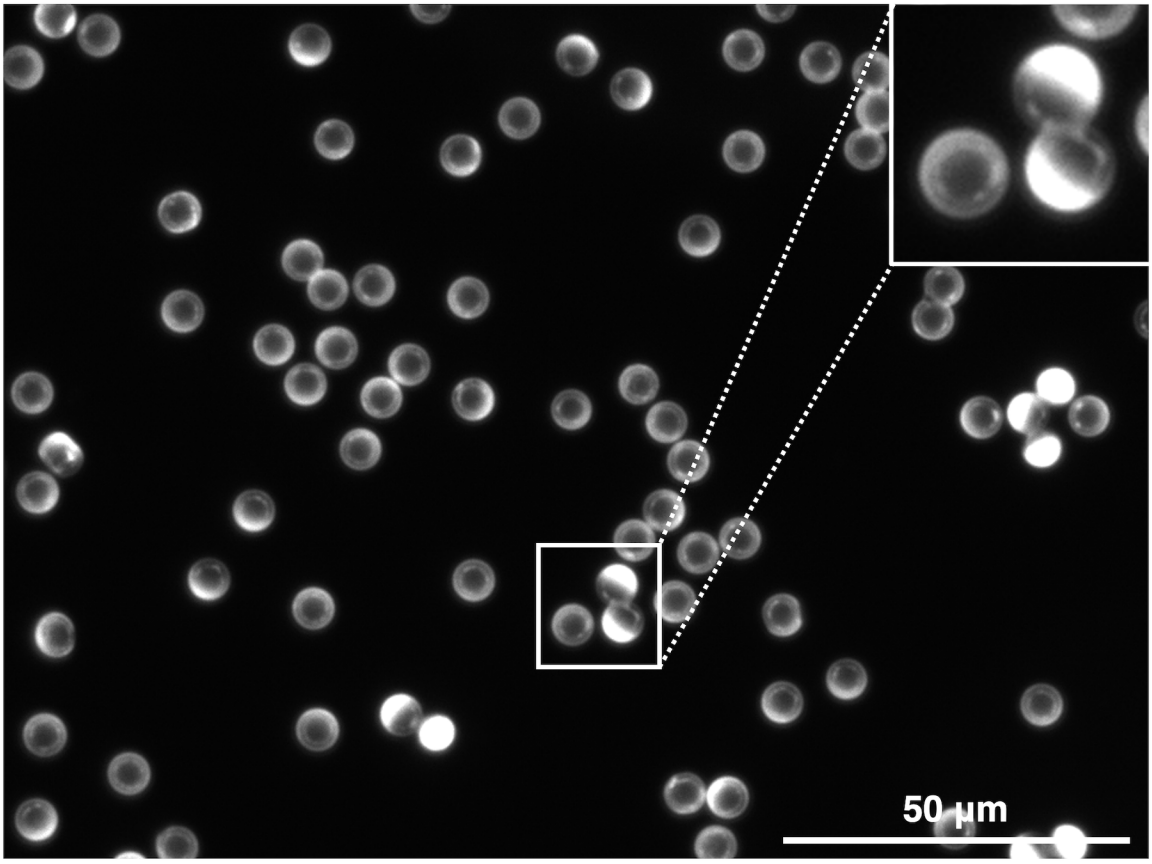

Figure B.3. Representative fluorescence image of Janus particles in MQW. Light and dark regions of the particles are PS and gold, respectively. Due to the density of the gold patch, particles typically settle with the gold hemisphere facing downward (i.e., toward the microscope objectives) in the absence of an applied field. Insert shows an enhanced detail of particles with the two distinct hemispheres clearly visible.

Appendix C: Supplementary Materials for Chapter 3

C.1 Additional Methods, Results, and Discussion.

C.1.1 Additional ICEP tracking data

The complete particle tracks and total displacements of the six Janus particle types studied in the manuscript are shown in Figures C.1 and C.2, respectively.

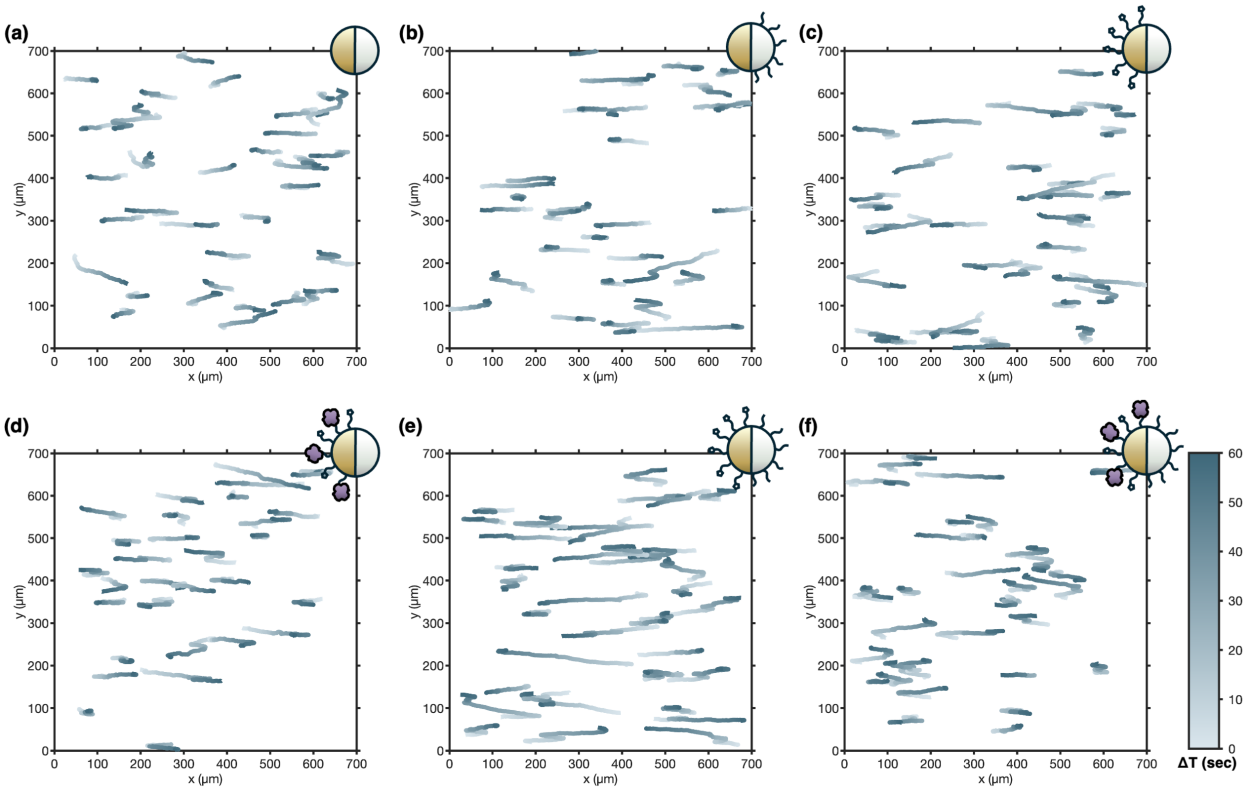

Figure C.1. Combined particle tracks of tracked Janus particles over 60 sec. Particle types include: (a) JP (b) JP-PEG (c) JP-BPT (d) JP-BPT-SA (e) ICEM (d) ICEM-SA.

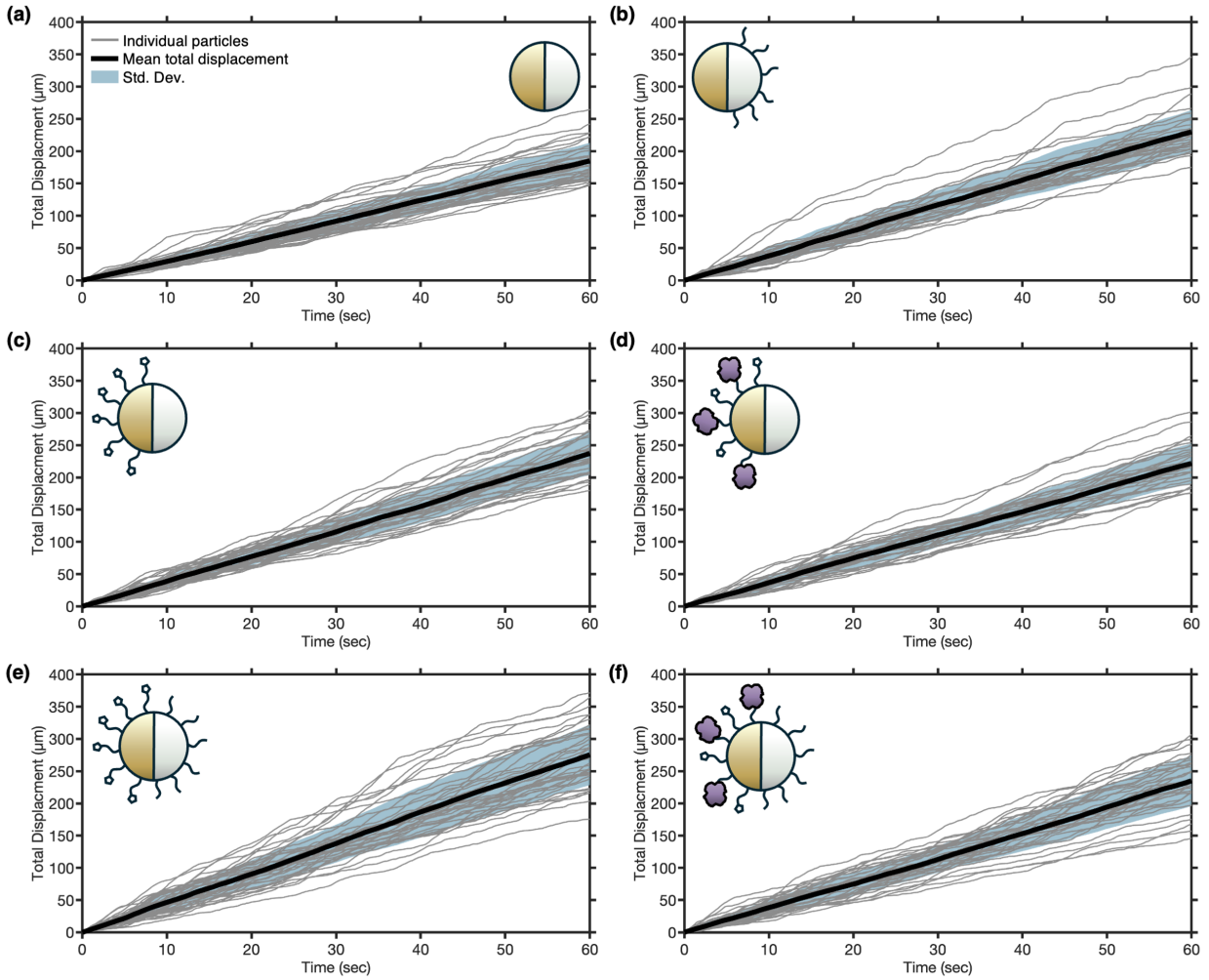

Figure C.2. Total displacement and average total displacement of tracked Janus particles over 60 sec. Particle types include: (a) JP (b) JP-PEG (c) JP-BPT (d) JP-BPT-SA (e) ICEM (d) ICEM-SA.

C.1.2 Si-PEG probe particle functionalization characterization

To confirm functionalization of silica (Si) probe particles with polyethylene glycol (PEG), we prepared Si-PEG and Si probe particles as described in the main text. We additionally produced Si-biotin PEG particles by modifying the surfaces of Si particles with 1 kDa biotin-PEG-silane (Laysan Bio) using the same methods followed for modification of Si particles with PEG. We then incubated the Si, Si-PEG, and Si-biotin PEG probe particles with Alexa Fluor 594-conjugated

streptavidin (SA). As the Si-biotin PEG particles can specifically capture SA due to the presence of biotin molecules, these particles were included as a positive control. We measured the fluorescence intensity of these three particle types, as well as Si particles not incubated with SA (negative control), using flow cytometry (BDFACS Celesta). We noted that Si particles incubated with the fluorescent SA exhibited high fluorescence near that of the positive control particles, indicating significant nonspecific adsorption of SA to the bare Si surface (Fig. C.3). However, Si particles modified with PEG exhibited a fluorescence intensity distribution approximately 2 orders of magnitude less than that of the unmodified Si particles incubated with SA. As PEG brushes are known to decrease the extent of nonspecific adsorption of proteins to modified surfaces, this result indirectly confirms the presence of surface-bound PEG on the surface of Si-PEG probe particles.

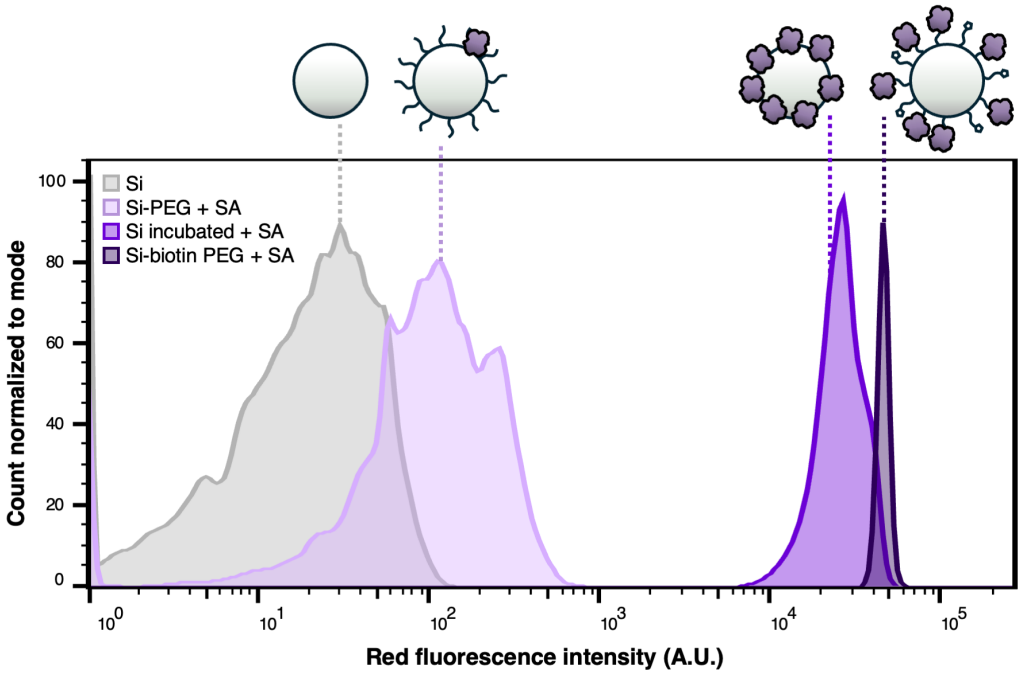

Figure C.3. Representative fluorescence intensity histograms of modified Si probe particles. Fluorescence intensity distributions of Si probe particles (negative control), Si-PEG probe particles incubated with fluorescent SA, Si probe particles incubated with fluorescent SA, and Si-biotin-PEG particles incubated with fluorescent SA (positive control).

C.1.3 DEP trapping and recording

The setup described in the "DEP trapping and recording" section of the manuscript was designed in Autodesk Fusion and 3D printed with a Original Prusa i3 MK3S+ 3D printer (Fig. C.4). This 3D printed holder reduces movement of the electrode chamber during video recordings.

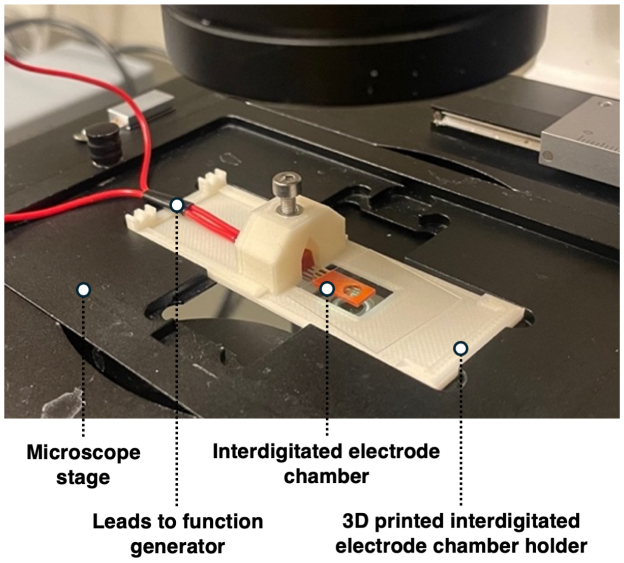

Figure C.4. IDE trapping chamber setup. IDE device prepped with silicone trapping chamber fastened to a custom 3D printed device holder and fixed to the microscope stage. Soldered wires were connected to leads attached to a function generator.

C.1.4 Complete data for f_{CM} fitting

The entirety of the f_{CM} values obtained by DPM and used to generate fits in Fig. 3.5b of the manuscript are displayed in Fig. C.5.

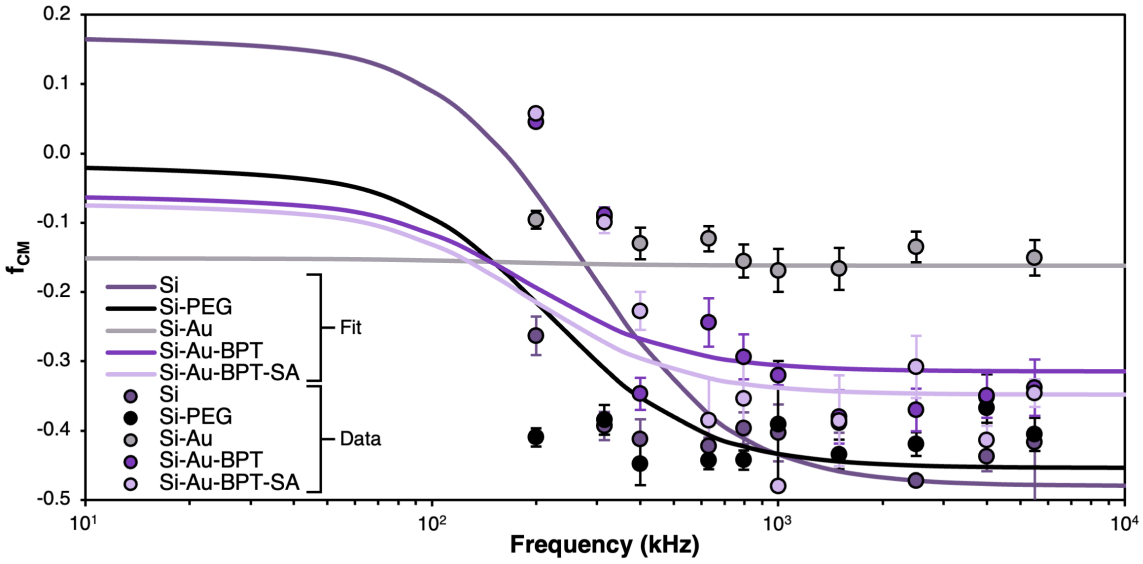

Figure C.5. f_{CM} experimental and fit results. f_{CM} experimental data points for all five probe particle types analyzed in the study, in addition to the f_{CM} fits detailed in Fig. 3.5b of the manuscript. N = 2-12, error bars indicate STE.

C.1.5 Experimental ICEP speed results

Silica-based Janus particles were modified and propelled by ICEP in a 4 kHz, 750 V cm^{-1} electric field and the average speed of at least 30 particles and standard error (STE) for each condition are reported in Table C.1. Particle speed was determined by simple linear regression of all particle displacement over time to extract the slope.

Table C.1. Experimental ICEP results.

	Average Particle Speed (μm/s)	STE
JP	3.12	0.0098
JP-BPT	3.96	0.0114
JP-PEG	3.87	0.0134
JP-BPT-SA	3.69	0.0118
ICEM	4.64	0.0168
ICEM+SA	3.91	0.0136

C.1.6 Supplementary equations for DPM analysis.

Equations that were not included in the main text but are essential for DPM analysis can be found in Table C.2. The equations and additional theory can be found in the corresponding references found in the manuscript.

Table C.2. Relevant equations for DPM analysis.

Mechanical Equilibrium Height	$h_m = \lambda \ln\left(\frac{64\pi\varepsilon_m a\left(\frac{kT}{z_v e}\right)^2 \tanh\left(\frac{z_v e\Psi_p}{4kT}\right)\tanh\left(\frac{z_v e\Psi_w}{4kT}\right)}{\lambda\frac{4}{3}\pi a^3(\rho_p-\rho_m)g}\right)$
Normalized Electric Field	$E^*(x,z) = \left[\frac{\left(2+1.268\frac{d_g}{d_e}\right)}{\pi\left(1.250+0.634\frac{d_g}{d_e}\right)}\right]\left[\left(0.25+\left(\frac{z}{d_g}\right)^2-\left(\frac{x}{d_g}\right)^2\right)^2+\left(\frac{2xz}{{d_g}^2}\right)^2\right]^{-1/4}$
The Real Component of the Clausius-Mossotti Factor	$f_{CM} = \frac{\omega^2(\varepsilon_p-\varepsilon_m)(\varepsilon_p+2\varepsilon_m)+(\sigma_p-\sigma_m)(\sigma_p+2\sigma_m)}{\omega^2(\varepsilon_p+2\varepsilon_m)^2+(\sigma_p+2\sigma_m)^2}$
Dielectric Particle Conductivity	$\sigma_p = \sigma_{bulk}+\frac{2}{a}\left[4(1+\left[\frac{2\varepsilon_m}{\eta D}\left(\frac{kT}{ze}\right)^2\right])\lambda\sinh^2\left(\frac{ze\zeta}{4kT}\right)+2\left[\frac{2\varepsilon_m}{\eta D}\left(\frac{kT}{ze}\right)^2\right]\beta^{-1}\sinh^2\left(\frac{ze\zeta}{2kT}\right)\right]\sigma_m$

Real Component of Effective Complex Permittivity	$Re\left[\tilde{\varepsilon}_{p\,eff}\right] = [2R_{N-1}^6\varepsilon_N(\omega^2(\varepsilon_{N-1}-\varepsilon_N)^2+(\sigma_{N-1}-\sigma_N)^2)$ $+ 3R_{N-1}^3R_N^3(\varepsilon_N(\omega^2(\varepsilon_{N-1}-\varepsilon_N)(\varepsilon_{N-1}+2\varepsilon_N)+\sigma_{N-1}^2)$ $+ (\varepsilon_{N-1}-2\varepsilon_N)\sigma_N^2) + R_N^6\varepsilon_N(\omega^2(\varepsilon_{N-1}+2\varepsilon_N)^2+(\sigma_{N-1}+2\sigma_N)^2)]$ $/\left[R_{N-1}^6(\omega^2(\varepsilon_{N-1}-\varepsilon_N)^2+(\sigma_{N-1}-\sigma_N)^2)\right.$ $+ 2R_{N-1}^3R_N^3\left(\omega^2(\varepsilon_{N-1}-\varepsilon_N)(\varepsilon_{N-1}+2\varepsilon_N)+(\sigma_{N-1}-\sigma_N)(\sigma_{N-1}+2\sigma_N)\right)$ $\left.+ R_N^6(\omega^2(\varepsilon_{N-1}+2\varepsilon_N)^2+(\sigma_{N-1}+2\sigma_N)^2)\right]$

C.1.7 f_{CM} results for each probe particle type

The first step in DPM is to assess the frequency dependent response of the studied particle through determination of the f_{CM}. Analysis of the DEP equilibrium motion of each probe particle type yielded experimentally determined f_{CM} values at each frequency studied within the range of 200 kHz – 5.5 MHz. Comprehensive results for the frequency-dependent f_{CM} and standard error of each probe particle are included in Table C.3, and corresponding values are also plotted in Figure C.5.

Table C.3. Experimentally determined f_{CM} values and STE.

	Si		Si-PEG		Si-Au		Si-Au-BPT		Si-Au-BPT-SA	
Frequency (kHz)	f_{CM}	STE	f_{CM}	STE	f_{CM}	STE	f_{CM}	STE	f_{CM}	STE
200	-0.26	0.028	-0.41	0.013	-0.10	0.013	0.05	0.006	0.06	0.002
315	-0.39	0.020	-0.38	0.021	-0.09	0.010	-0.09	0.010	-0.10	0.015
400	-0.41	0.029	-0.45	0.030	-0.13	0.023	-0.35	0.023	-0.23	0.027
630	-0.42	0.013	-0.44	0.013	-0.12	0.018	-0.24	0.035	-0.39	0.061
795	-0.40	0.023	-0.44	0.014	-0.16	0.024	-0.29	0.033	-0.35	0.054
1000	-0.40	0.041	-0.39	0.092	-0.17	0.031	-0.32	0.014	-0.48	0.005
1500	-0.39	0.014	-0.43	0.021	-0.17	0.030	-0.38	0.039	-0.39	0.066
2500	-0.47	0.005	-0.42	0.017	-0.13	0.022	-0.37	0.031	-0.31	0.045
4000	-0.44	0.021	-0.37	0.049	-0.35	0.037	-0.35	0.032	-0.41	0.021
5500	-0.42	0.090	-0.41	0.024	-0.15	0.026	-0.34	0.040	-0.35	0.020

C.1.8 Results from assessment of ICEO flows in selected model system

As described in the main text, we predicted changes to ICEO flows associated with ICEP of Janus particles due to surface modifications using individual permittivity contributions determined from DPM. Using DPM results and the model discussed in the manuscript, the ICEO flows on each Janus particle hemisphere, as well as the resultant speed, were calculated for each Janus particle and results are included in Table C.4.

Table C.4. Predicted Janus particle speeds from theoretical model.

	$\frac{1}{(1+K_1)}$	$\frac{1}{(1+K_2)}$	**U** (μm/s)
JP	0.9927	0.0124	0.9803
JP-BPT	0.9060	0.0124	0.8936
JP-PEG	0.9927	0.0124	0.9803
ICEM	0.9060	0.0124	0.8937
ICEM+SA	0.8645	0.0124	0.8521

C.1.9 Comparison of experimentally measured ICEP speed and theoretically predicted speed

Results corresponding to Fig. 3.6 of the main text are included in Table C.5 and Table C.6. Experimental and theoretical changes of ICEP due to the addition of polymers were evaluated by comparison of JP-BPT and JP-PEG speed relative to unmodified JP speed (Table C.5). Experimental and theoretical changes of ICEP speed due to capture of protein were evaluated by comparison of ICEM-SA speed relative to ICEM speed (Table C.6).

Table C.5. Experimental and theoretical ICEP speed of Janus particles modified by polymers relative to unmodified Janus particles.

	Average Normalized Particle Speed (μm/s)	$\mathbf{U}_i/\mathbf{U}_{JP}$
JP	1.00	1.00
JP-BPT	1.27	0.91
JP-PEG	1.24	1.00

Table C.6. Experimental and theoretical ICEP speed of Janus particles with captured SA relative to control ICEMs.

	Average Normalized Particle Speed (μm/s)	$\mathbf{U}_i/\mathbf{U}_{ICEM}$
ICEM	1.00	1.00
ICEM+SA	0.84	0.95

Appendix D: Supplementary Materials for Chapter 4

D.1 Additional Methods, Results, and Discussion.

D.1.1 Optimization of the acoustic waveform.

Before use in experiments, frequency sweeps from 730–770 kHz were conducted on individual trapping channels to determine the proper operating frequency, which was estimated based on the extent of heating and the magnitude of the voltage across the transducer at a given frequency, with minimal heating and maximum voltage being targeted. Transducers were also assessed for heating during operation at 5–40 V_{pp}, and 30 V_{pp} was selected as the standard applied voltage as transducer temperatures did not exceed 37˚C with continuous operation (i.e., >10 min) at this voltage.

D.1.2 NACPs of reduced polydispersity for fNACP-based assays.

As described in the main text, a low polydispersity fraction of NACPs was isolated from the polydisperse bulk of NACPs produced by homogenization. The reasoning for this was twofold: first, polydisperse NACPs, such as those filtered without vortexing to remove NACPs larger than ~50 μm, appear as a large population on forward scatter (FSC) versus side scatter (SSC) flow cytometry plots (Fig. D.1A). This population overlaps with the typical location of blood components on the same plot, preventing the ability to differentiate NACPs from blood components based on FSC and SSC alone, as can be done with the NACPs that were vortexed while filtering to reduce retention of NACPs smaller than the filter size (Fig. D.1B). Second, due to the wide distribution of particle sizes in the NACPs filtered without agitation, the fluorescence

intensity distribution of the NACP population is sufficiently broad to reduce confidence for anti-OVA detection assays (Fig. D.1C). After filtration with vortexing, the fluorescence intensity distribution of the NACPs is significantly narrower (Fig. D.1D).

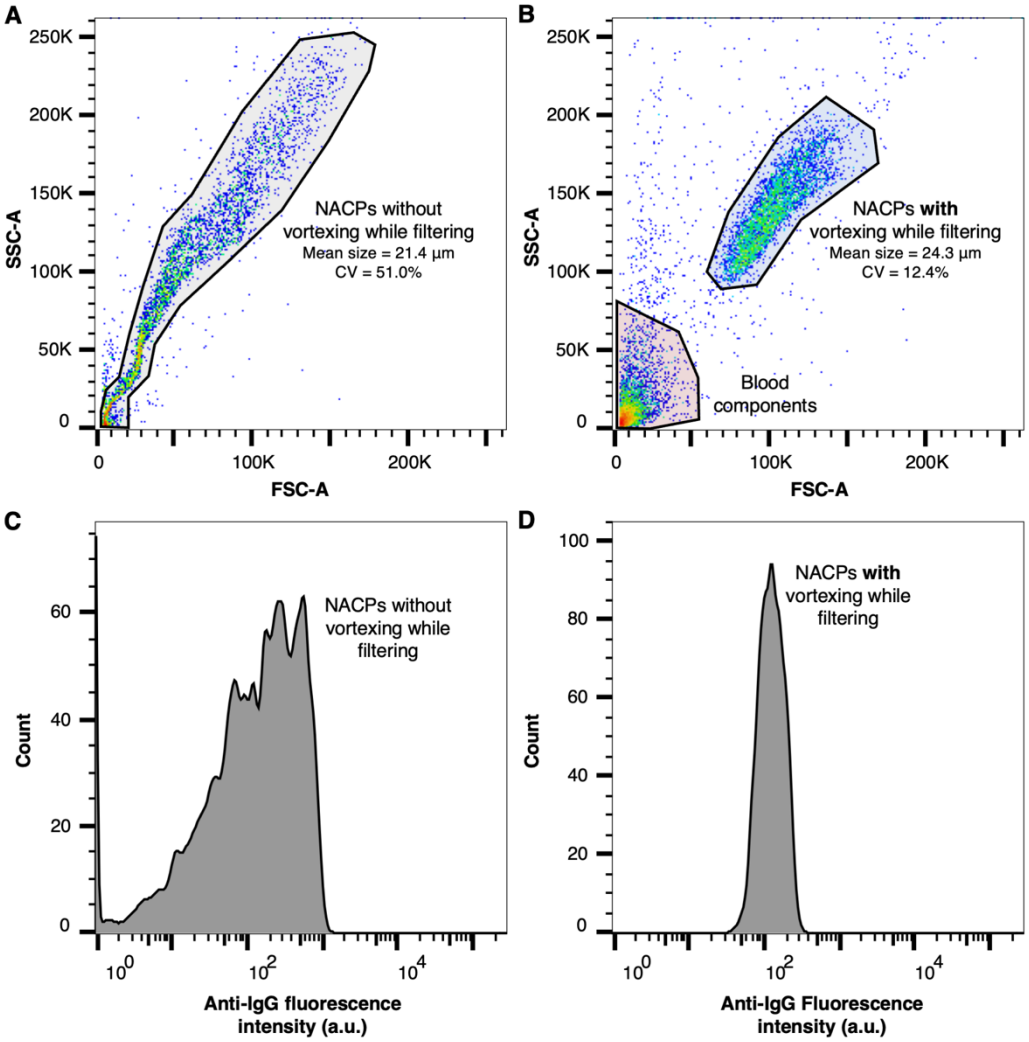

Figure D.1. Flow cytometry of unfiltered and filtered NACPs. (A) Representative FSC vs. SSC plot of NACPs that were filtered without vortexing. **(B)** Representative FSC vs. SSC plot of NACPs filtered as described in the main text and mixed with whole blood. **(C)** Anti-IgG fluorescence intensity of the NACPs from (A) not incubated with fluorescent anti-IgG. **(D)** Anti-IgG fluorescence intensity of the filtered NACPs from (B) not incubated with fluorescent anti-IgG.

D.1.3 Flow cytometry gating for NACP trapping evaluation.

During analysis of separated waste and purified samples, as described in the text, blood components and NACPs were gated based on FSC and SSC (Fig. D.2A,D). Within the blood component gate, WBCs were readily identified based on a comparison of two fluorescence channels, 450 nm emission with a bandwidth of ±40 nm and 535 nm emission with a bandwidth of ±50 nm, both with excitation by a 405 nm laser (Fig. D.2B). By gating in this manner, NACPs and WBCs could be isolated from RBCs and other debris (Fig. D.2C).

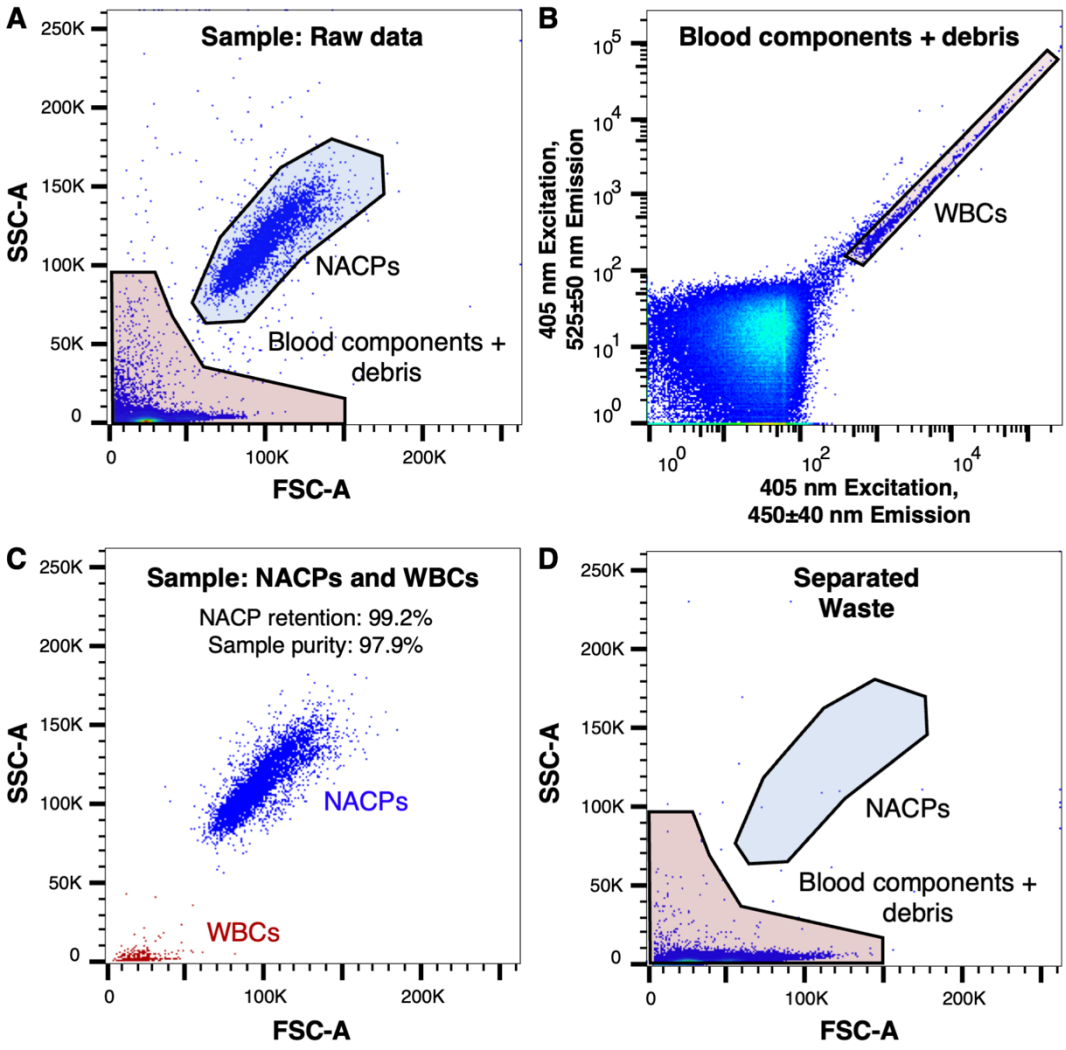

Figure D.2. Representative plots of flow cytometry gating for NACP trapping evaluation. **(A)** Representative FSC vs. SSC plot of a raw data from a purified sample from trapping experiments with gates showing the NACPs and the blood components. **(B)** Representative plot showing the gating of WBCs in the purified sample stained by NucBlue. **(C)** Representative FSC vs. SSC plot of NACPs and WBCs gated in (A) and (B), including calculated NACP retention and sample purity. **(D)** Representative FSC vs. SSC plot of the waste from trapping experiments with gates showing the NACPs and the blood components. Measurements in (D) are used to calculate NACP retention and sample purity in (C).

D.1.4 Extended manual trapping operation data.

Individual results for NACP retention and sample purity from the manual trapping study, shown in cumulative form in Fig. 4.3G of the main text, are shown in Fig. D.3. NACP retention and sample purity did not differ significantly between any of the operators.

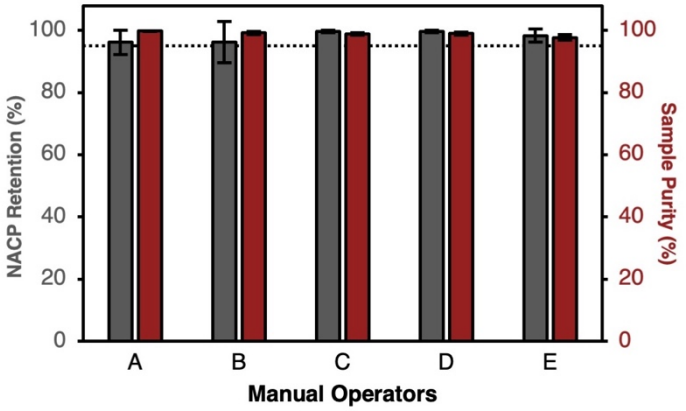

Figure D.3. Individual operator results from manual trapping study. Data is presented as mean ± standard deviation, N = 5 (A-D) or 4 (E). Dotted line shows 95% target NACP retention and sample purity.

D.1.5 Flow cytometry gating for fNACP-based assay.

Control NACPs and capture fNACPs were gated by FSC and SSC (Fig. D.4A). Within this population, control NACPs were differentiated by increased fluorescence from FSA that was exclusively used on control NACPs (Fig. D.4B). Both populations were also analyzed for anti-IgG fluorescence, with the median anti-IgG fluorescence intensity of the fNACP population being correlated to anti-OVA concentration (Fig. D.4C).

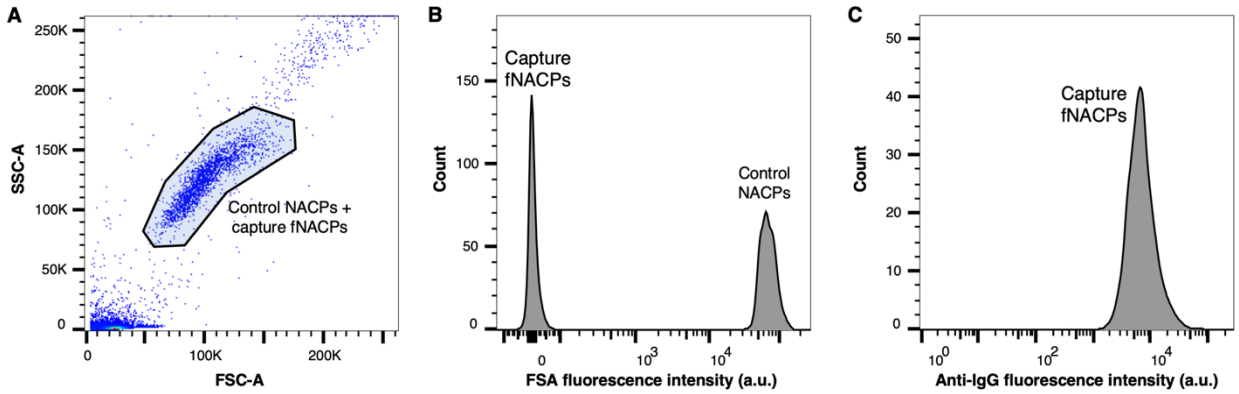

Figure D.4. Representative plots of flow cytometry gating for fNACP-based assay. (A) Representative FSC vs. SSC plot of a purified sample from the acoustic pipette with gates showing the NACPs and blood components. **(B)** Representative plot of FSA fluorescence intensity of the gated control NACPs and capture fNACPs from (A). **(C)** Representative plot of anti-IgG fluorescence on the capture fNACPs identified from (B).

D.1.6 fNACP-based detection specificity.

To assess fNACP specificity, we incubated the fNACPs in buffer with no anti-OVA or 0.1 nM anti-OVA for 30 min, followed by incubation with fluorescent anti-IgG for 30 min. We found that the median anti-IgG fluorescence of control fNACPs and fNACPs incubated with only fluorescent anti-IgG were not statistically different, while the fNACPs incubated with fluorescent anti-IgG after anti-OVA showed dramatically increased fluorescence (Fig. D.5). These results provided two key insights: first, labeling of fNACPs by the secondary antibody is specific, and thus, the system has a high signal-to-noise ratio, which is crucial for achieving high sensitivity assays. Second, because nonspecific adsorption of the secondary antibody was negligible for the group lacking anti-OVA, the results provide further evidence that fNACPs are resistant to nonspecific adsorption.

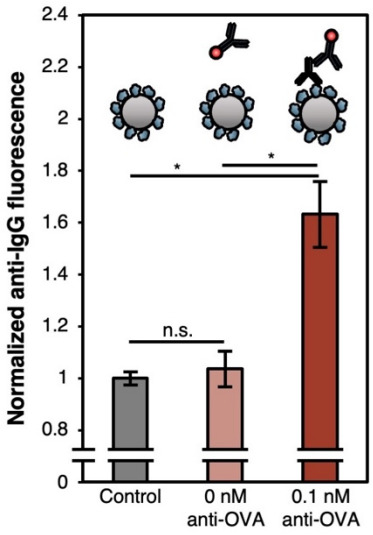

Figure D.5. fNACP detection specificity. fNACP fluorescence intensity of blank fNACPs, fNACPs incubated with only fluorescent anti-IgG, and fNACPs incubated with fluorescent anti-IgG after incubation with 0.1 nM anti-OVA. Data is presented as mean MFI ± standard deviation. N = 3, *P<0.05. Significance between conditions was evaluated using a one-tailed Student's t-test.

D.1.7 Additional pipette details.

The printed and assembled acoustic pipette, shown predominantly in schematic form in Fig. 4.6 of the main text, are shown in Fig. D.6.

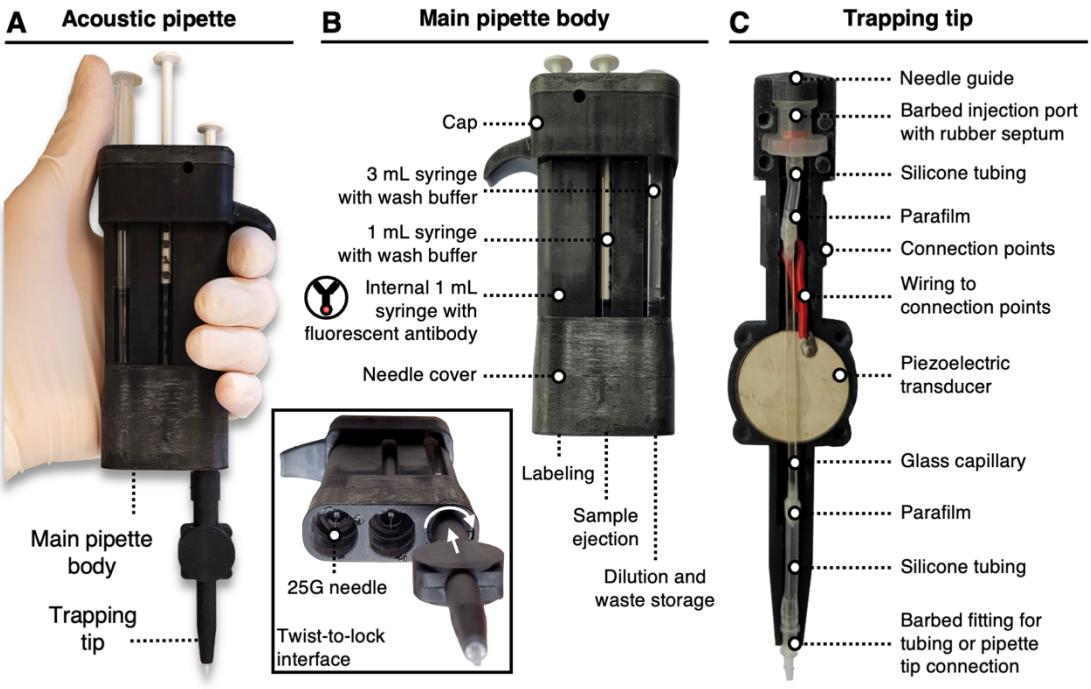

Figure D.6. Additional acoustic pipette overview. (A) Image of acoustic pipette. Inset image shows mechanism for movement and locking of trapping tip, as well as internal needles used to access the trapping channel. **(B)** Image and details of the main pipette body. **(C)** Image and details of the trapping tip.

To enable others to reproduce and utilize the acoustic pipette design, we have included stereolithography (STL) files for each of the 3D printed components of the acoustic pipette (Fig. D.7). Using these files, readers may print necessary components using personal 3D printers. Notably, due to differences in printer performance, material, and plating approaches, some minor post-printing modifications may be necessary to enable proper pipette function.

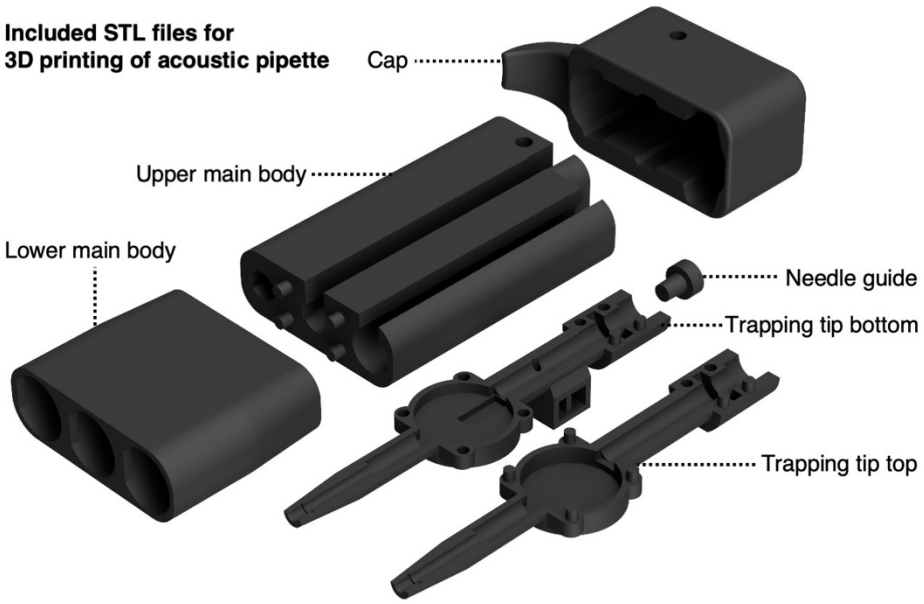

Figure D.7. Acoustic pipette STL files included for 3D printing. 3D renders of STL files for printing of main pipette components.

D.1.8 Additional pipette assembly.

Necessary materials, both 3D printed and non-printed, for assembly of the acoustic pipette are detailed in Fig. D.8. In addition to the listed components of the pipette (Fig. D.8A), assembly requires cyanoacrylate glue, solder, a soldering iron, and wire cutters. To assemble the main body, the upper main body and lower main body are fit together by a pressure fit (Fig. D.8B and C). If needed, cyanoacrylate glue can be added to the interface between the two parts to ensure a strong bond. After attaching needles to the 3 mL and 1 mL syringes, the syringes can be inserted into the main body. The cap is then placed over the main body; if needed, a small rod can be inserted through the hold in the cap and upper main body to ensure the cap remains in place. To assemble the trapping channel, a wire should be soldered to each side of the piezoelectric transducer, both slightly off center to allow space for the capillary (Fig. D.8D). Then, the glass capillary should be glued to the transducer using a thin layer of cyanoacrylate glue. The capillary should lay flat

against the transducer. The silicone tubing can then be attached to each end of the capillary. If needed, the connection can be sealed with cyanoacrylate glue and parafilm. The silicone tube on the side of the transducer with wires can be connected to a barbed luer lock, into which the rubber septum and needle guide can be inserted. The other silicone tubing can be attached to a barbed tubing connector. With that, the trapping channel components can be placed in the trapping tip bottom, with the wires being routed through the holes to the connection points (Fig. D.8E). Finally, the trapping tip top can be pressure fit to the trapping tip bottom to contain the trapping channel components (Fig. D.8F).

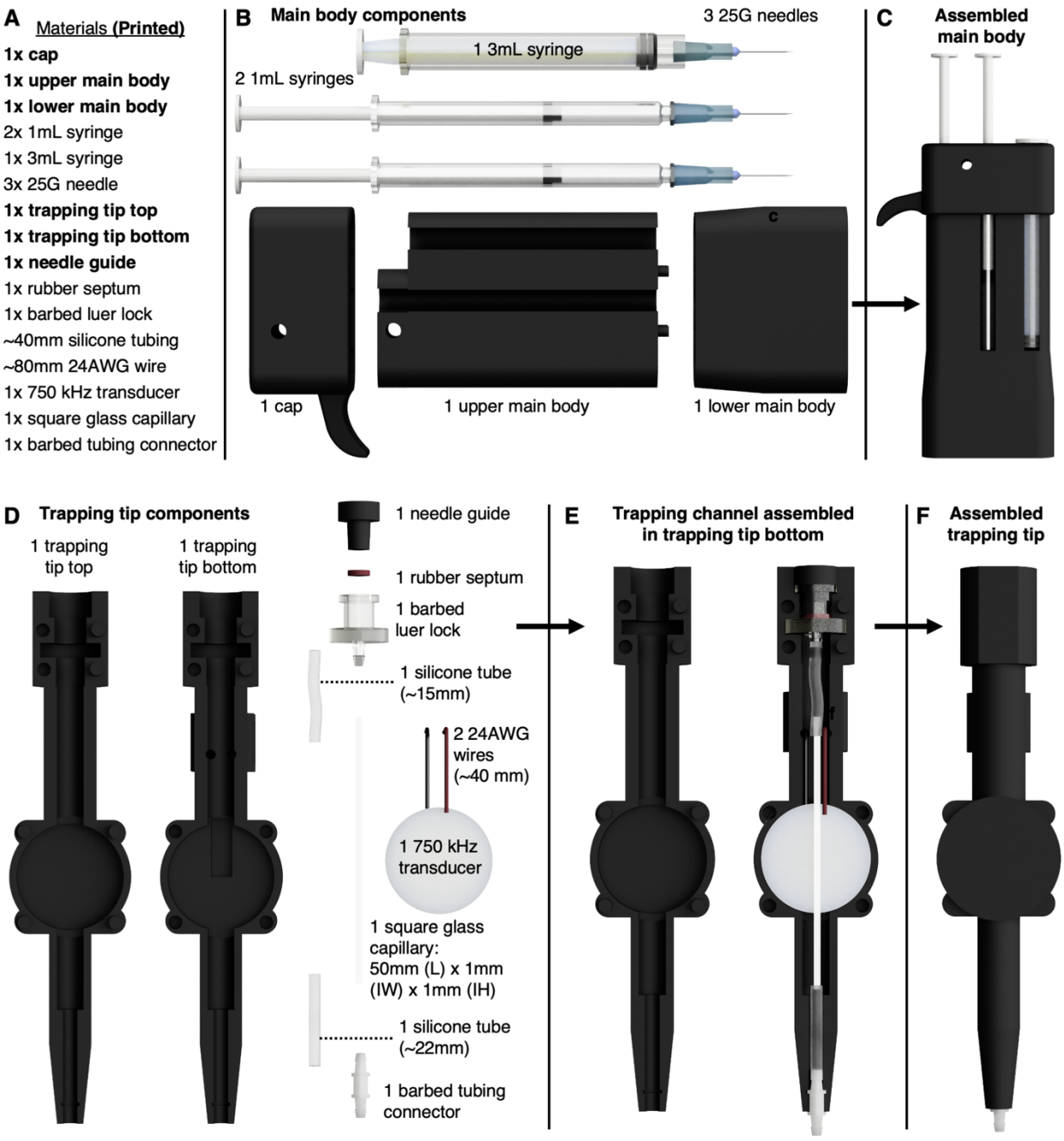

Figure D.8. Materials for acoustic pipette assembly. (A) List of pipette components needed for acoustic pipette assembly, with 3D printed components denoted in bold text. (B) Render of disassembled main body components. (C) Render of assembled main pipette body. (D) Render of disassembled trapping tip components. (E) Render of assembled trapping channel in trapping tip bottom. (F) Render of assembled trapping tip.

D.1.9 Main fluorimeter housing fabrication and assembly.

The fluorimeter structural housing consisted of five 3D-printed structural components and multiple commercially available components (Fig. D.9). The five 3D-printed structural components (STLs available in Supplementary Materials) include the main fluorimeter housing, the pipette docking cap, a SP filter holder, a LP filter holder, and a photodiode holder. These components are modified versions of the commercially available Thorlabs CVH100/M (cuvette holder with fiber adapter assembly), CVH100-CV (light-tight cover for cuvette holder), CVH100-FH (mounted filter holder), CP35_M (30 mm Cage Plate with Ø1" Double Bore M4 Tap), and CP33_M (SM1-Threaded 30 mm Cage Plate 0.35" Thick 2 Retaining Rings M4 Tap), respectively. All five structural components were designed using Fusion 360 and printed on a Bambu P1S printer with matte black PLA and a 0.2 mm layer height. The main fluorimeter housing (Fluorimeter main housing.STL) provided structural support for holding the 100 uL cuvette (Thorlabs, CV10Q1FE), pipette docking cap, filters, photodiode, and fiber adapter lens assemblies. One-inch ports with 30 mm rectangularly patterned M2 compatible holes were located on all four sides of the housing, which accepted the LP filter holder and photodiode holder cage plates (Fluorimeter LP holder.STL and Fluorimeter photodiode holder.STL respectively). A Thorlabs SMA905 threaded fiber adapter with 20 mm focal length lens press fit into the front of the housing. Light was provided through a compatible SMA fiber optic cable. The SP filter holder (Fluorimeter SP holder.STL) housed a Thorlabs FESH0600 600 nm SP filter directly in front of the fiber adapter lens. The filter was held in the mount with an M3 4.0 mm setscrew inserted at a 45-degree angle from the mount side. The sample cuvette was lowered onto the cuvette pedestal inside the main housing through a square access port in the top of the housing. Once in place, the pipette docking cap (Fluorimeter pipette docking cap.STL) was pressed onto the top of the housing. An Edmund

#15-457 590 nm 1-inch LP filter was placed into the LP filter holder and locked with an M4 4 mm set screw. A Thorlabs SM1PD1B large area mounted silicon photodiode with 350-1100 nm sensitivity and a grounded anode self-tapped into the photodiode holder. Electrical connectivity to the photodiode amplifier was achieved with a compatible BNC coaxial cable. Ninety degrees relative to the fiber adapter lens, Thorlabs ER1-P4 cage assembly rods were screwed into the main housing using the cage plates for alignment. The cage plates were ordered such that the filter assembly mates to the housing and the photodiode mates to the filter assembly. The cage plates were pressed firmly towards the main housing to block external light and fixed in place on the cage assembly rods with four M4 4 mm set screws per cage plate. A light seal was created by snapping Thorlabs SM1CP2 externally threaded end caps into side ports opposite the photodiode and fiber adapter ports.

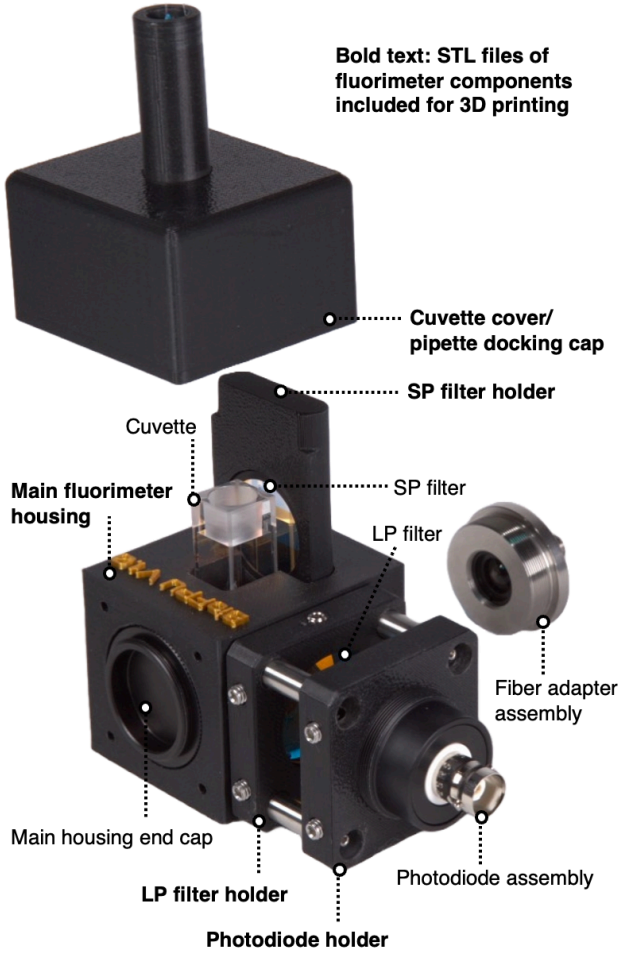

Figure D.9. Exploded view of the main fluorimeter housing and associated components. STL files of all items shown in bold text (the main fluorimeter housing, the pipette docking cap, the SP filter holder, the LP filter holder, and photodiode holder) are available as Supplementary Materials.

D.1.10 Additional fluorimeter cuvette housing details.

The cuvette housing accepts one cuvette per experiment. The cuvette used in this work was a 100 uL synthetic quartz cuvette with four polished sides. The sample sat in the bottom of the rectangular channel of the cuvette. Light entered the cuvette housing through the threaded fiber adapter and was focused by the integrated lens before passing through the 600 nm SP filter. This filter removed band light below 610 nm, preventing the majority of the source light from reaching

the photodiode, which would otherwise result in an elevated baseline photocurrent. Filtered light passed through the channel illuminating the sample. The bottom of the cuvette sat 4.0 mm off the housing floor on a pedestal to align the sample channel with the center of the incoming light source, providing maximum illumination of the sample. Light that passed through the cuvette channel terminated on the housing cap opposite to the fiber adapter. To reduce baseline photocurrent, it was important to use non-reflective materials for the end caps to maximize incident light absorption. Light striking the sample causes the fluorophore on fNACP samples to fluoresce, emitting photons with max emission at ~617 nm in all directions. Photons emitted at a right angle to the incoming light first passed through a 590 nm LP filter before striking the silicon photodiode mounted to the housing wall. The LP filter passed light above 610 nm, further attenuating light within the housing that was not generated from the fluorophore while passing the photons from sample fluorescence to the photodiode detector. The large area of the silicon photodiode provided a large target for integrating many photons, which helped to compensate for the moderate photodiode responsivity of ~.35 A/W at 617 nm. Other photodiode technologies like avalanche photodiodes could be used to significantly increase the detector sensitivity, allowing for a lower minimum threshold of detection and reduced demand on the photodiode amplifier performance.

D.1.11 LED and driver.

The fluorometer light source was generated by a Thorlabs M565F3 565 nm with 105 nm BW fiber coupled LED, which can be driven with a maximum of 700 mA at a typical forward voltage drop of 2.9 V. Typical emitted light power is 13.5 mW for 1995 mW of electrical power when used with a 400 μm diameter multimode fiber. A threaded optical SMA connector mounted on the LED housing allowed for the mating of an SMA multimode fiber optic cable for light

transmission to the main fluorimeter fiber adapter. For this system, a 1 m long and 400 um diameter SMA-SMA multimode fiber patch cable (Thorlabs, M28L01) was used. The LED was driven with a 1.2 A at 8.0 V (maximum) programmable constant current source (Thorlabs, UPLED) connected by an included Thorlabs M8 x 1 compatible circular connector cable. The LED driver was powered using a Thorlabs DS12 12V AC to DC power supply and connected to a software control GUI (Thorlabs, upSERIES) via a standard data micro-USB cable. The GUI was used to enable and disable power to the LED as well as set the LED drive current. During data collection, the LED was powered for ~30 min at 700 mA to let the device stabilize thermally and optically before any measurements were taken.

D.1.12 Photodiode amplifier and photodiode.

A Thorlabs SM1PD1B large area mounted silicon photodiode with a grounded anode served as the fluorimeter detector. The photodiode was capable of detecting 350−1100 nm light and had a peak responsivity of .725 A/W at 970 nm, a maximum dark current of 600 nA, and a junction capacitance of 375 pF measured at 5.0 V. The photodiode had a male BNC connector to electrically interface the diode anode to the cable shield and the cathode to the inner conductor. A generic BNC to BNC cable was used to connect the photodiode to a benchtop photodiode amplifier (Thorlabs, PDA200C). The photodiode amplifier had a full-scale current measurement range from 100 nA to 10 mA with a bandwidth of 1-500 kHz, respectively, with RMS noise of 0.02% of the full-scale range. In all experiments, the amplifier was set to a 100 nA range, which corresponds to a bandwidth of 1 KHz, a resolution of 10 pA, and an analog output conversion coefficient of 10^8 V/A, limited between 0−10 V. Both the amplifier input connected to the photodiode and the output connected to the data acquisition unit accepted a standard BNC connection. Before collecting data,

the photodiode amplifier was left running for one hour to allow it to reach thermal equilibrium. To reduce background signal before experiments, the LED was turned off, the current range was set to 100 nA, and the offset calibration potentiometer was adjusted until a minimum signal output from the photodiode amplifier was recorded on the attached oscilloscope (typically 1.6 mV baseline).

D.1.13 Data acquisition and computer.

The analog voltage output of the photodiode amplifier was interfaced to a USB data acquisition unit (Digilent, Analog Discovery 2) with a generic BNC to BNC coaxial cable. The data acquisition unit was connected to a PC using a micro-USB cable. Control software (Digilent, Waveforms) was used to set the scope horizontal and vertical axis to 5 sec/div and 20 mV/div, respectively, with a sampling rate of 100 Hz. For each experiment, the photodiode amplifier voltage was measured for ~50 seconds and the sampled data was recorded to a CSV file for post processing.

D.1.14 5PL fit parameters and validation.

Fit parameters for the fits in Figs. 4.5B and 4.7B are found in Table D.1.

Table D.1. 5PL fit parameter values.

Parameter	Fig. 4.5B	Fig. 4.7B
a	27.2056	59.733
d	79632	7536.4
c	580.6031	2404600
b	0.765	0.7353
g	0.177	649.9033

After fitting the data in Figs. 4.5B and 4.7B, we validated the fits by calculating the average percent relative error (%RE) of experimentally measured values relative to values predicted by the 5PL fits at each anti-OVA concentration investigated. %RE is given by:

$$\%RE = 100\% \times \frac{P - E}{E} \qquad (D.1)$$

where P is the predicted MFI and E is the experimentally measured MFI. All values of %RE fell below 25%, and all but one point fell below 13%, suggesting an acceptable fit for both sets of data (Fig. D.10).

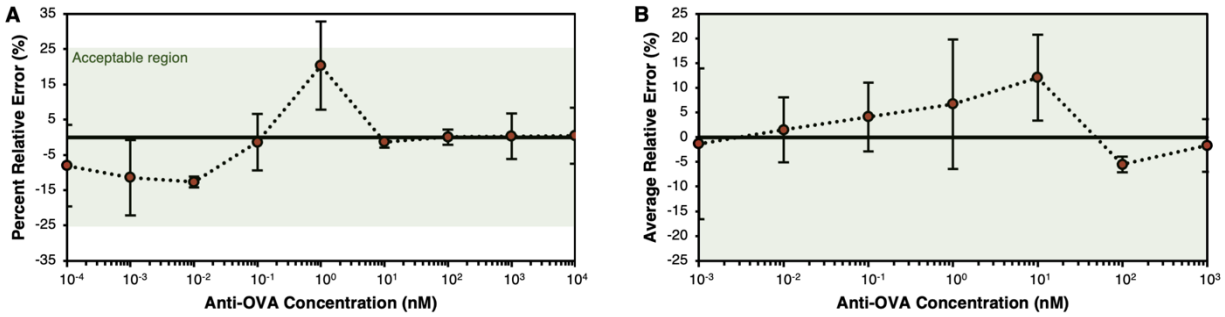

Figure D.10. %RE for 5PL fits. (A) %RE for 5PL fit in Fig. 4.5B of the main text**. (B)** %RE for 5PL fit in Fig. 4.7B of the main text**.**

D.1.15 Raw data.

The following tables provide raw data used to create plots in the manuscript with N < 20.

Table D.2. Raw data for Fig. 4.3D.

Condition	Retention	Purity
Lysed	0.9467	0.9944
Lysed	0.9907	0.9829
Lysed	0.9973	0.9678
Lysed	0.9946	0.9535
Lysed	0.9983	0.9674
Unlysed	0.9934	0.9300
Unlysed	0.9976	0.9935
Unlysed	0.9948	0.9804
Unlysed	0.9919	0.9785

Table D.3. Raw data for Fig. 4.3E, F, and G.

Flow rate (mL/min)	Retention	Purity
0.5	0.9925	0.9643
0.5	0.9937	0.9757
0.5	1.0000	0.9873
0.5	0.9921	0.9735
0.5	1.0000	0.9938
1	0.9926	0.9655
1	0.9950	0.9759
1	1.0000	0.9090
1	1.0000	0.9779
1	1.0000	0.9881
1.5	1.0000	0.9954
1.5	0.9929	0.9772
1.5	1.0000	0.9878
1.5	0.9964	0.9930
1.5	0.9956	0.9993
2	0.9679	0.9979
2	1.0000	0.9956
2	0.9751	0.9959
2	1.0000	0.9880
2	0.9769	0.9918
3	0.9865	0.9964
3	1.0000	0.9953
3	0.9944	0.9966
3	0.9965	0.9954
3	0.9898	0.9924
5	0.9767	0.9963
5	0.9443	0.9975
5	0.9708	0.9976
5	0.9945	0.9949
5	0.9423	0.9982
6	0.9068	0.9740
6	0.9469	0.9538
6	0.8332	0.9798
6	0.8629	0.9734

Table D.4. Raw data for Fig. 4.3G and D.3.

Operator	Retention	Purity
A	0.9025	0.9986
A	1.0000	0.9985
A	0.9800	0.9952
A	0.9799	0.9986
A	0.9451	0.9972
B	0.9903	0.9951
B	0.8441	0.9988
B	0.9985	0.9914
B	0.9976	0.9844
B	0.9818	0.9889
C	1.0000	0.9846
C	0.9906	0.9944
C	0.9923	0.9925
C	1.0000	0.9842
C	1.0000	0.9874
D	0.9973	0.9892
D	1.0000	0.9837
D	0.9890	0.9950
D	1.0000	0.9915
D	0.9976	0.9886
E	0.9975	0.9655
E	0.9526	0.9867
E	0.9850	0.9790
E	0.9974	0.9766

Table D.5. Raw data for Fig. 4.4D.

Condition	NACP FSA
Without separation	17746
Without separation	17692
Without separation	17692
Without separation	18019
Without separation	17855
With separation	17057
With separation	18295
With separation	18129
With separation	18240
With separation	18520

Table D.6. Raw data for Fig. 4.5B.

Anti-OVA Concentration (nM)	Control NACPs Median Anti-IgG Fluorescence (A.U.)	Capture fNACPs Median Anti-IgG Fluorescence (A.U.)
10000	451	28892
10000	373	25891
10000	337	24735
1000	69	11238
1000	80	12771
1000	76	12053
100	42	3146
100	40	3283
100	52	3233
10	34	641
10	41	661
10	34	649
1	34	114
1	31	101
1	35	124
0.1	30	43
0.1	32	48
0.1	34	49
0.01	36	36
0.01	35	35
0.01	35	34
0.001	31	29
0.001	32	29
0.001	38	36
0.0001	38	35
0.0001	32	29
0.0001	29	27
0	33	32
0	32	29
0	31	28
	31	28

Table D.7. Raw data for Fig. 4.7B.

Anti-OVA Concentration (nM)	Control NACPs Median Anti-IgG Fluorescence (A.U.)	Capture fNACPs Median Anti-IgG Fluorescence (A.U.)
1000	258	7203
1000	305	6554
1000	254	6534
100	83	2612
100	101	2581
100	97	2669
10	97	474
10	101	529
10	94	549
1	80	130
1	121	164
1	100	154
0.1	95	80
0.1	84	70
0.1	82	75
0.01	89	67
0.01	78	61
0.01	80	59
0.001	110	77
0.001	103	57
0.001	94	54
0	258	67
0	300	66
0	256	68
0	176	62
0	224	64
0	236	67

Table D.8. Raw data for Fig. 4.7F.

Anti-OVA Concentration (nM)	Capture fNACPs Anti-IgG Fluorescence (A.U.)
1000	1.2215
1000	1.2320
1000	1.2270
100	1.0746
100	1.1171
100	1.0993
10	1.1088
10	1.0510
10	1.0267
0	1.0150
0	1.0332
0	0.9957

Table D.9. Raw data for Fig. D.5.

Condition	Capture fNACPs Median Anti-IgG Fluorescence (A.U.)
No Secondary	29.3
No Secondary	28.6
No Secondary	27.8
No Primary	31.8
No Primary	29.0
No Primary	28.0
Primary and Secondary	42.5
Primary and Secondary	48.2
Primary and Secondary	49.2

Appendix E: Supplementary Materials for Chapter 5

E.1 Additional Methods, Results, and Discussion.

E.1.1 Additional device component details

The separator consists of 5 main printed parts: the upper siphon chamber array, a trapping channel array holder, a left and right side, and an electrical port cover. Two 3D printed transducer clips hold the transducer in place on the trapping channel array holder. The components were designed to accommodate the trapping array and electrical ports and to be assembled by nuts and screws (Fig. E.1).

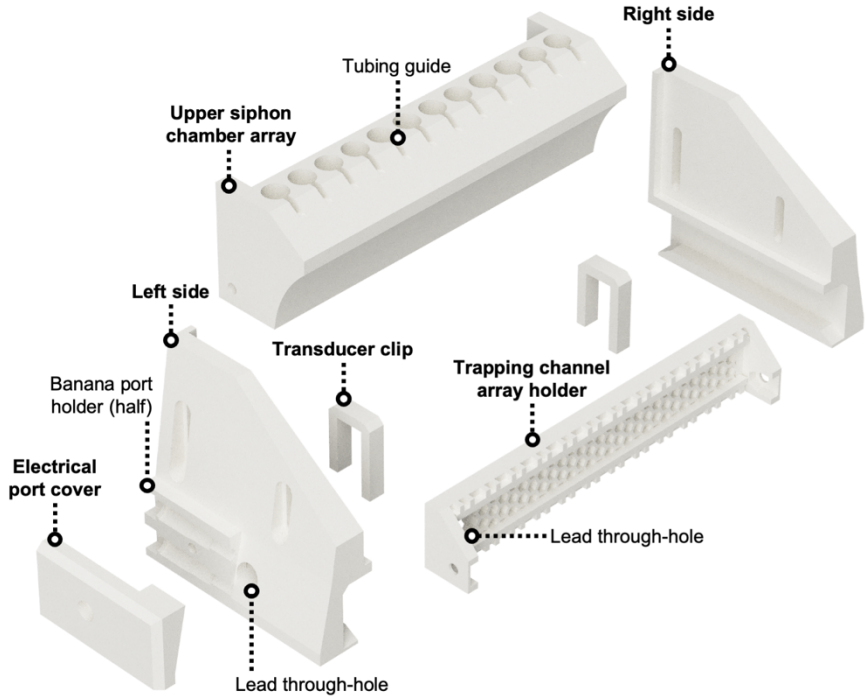

Figure E.1. Exploded view of 3D printed multichannel acoustic pipette components. All components were printed via MSLA printing.

E.1.2 Additional device characterization details.

To analyze washing of blood from the device channels, we measured absorbance of fluids collected after sequential washes, as described in the main text. To specifically measure presence of blood, we conducted an absorbance scan of diluted porcine whole blood and identified absorbance peaks specific to porcine blood. We selected 542 nm as the wavelength for subsequent absorbance measurements (Fig. E.2).

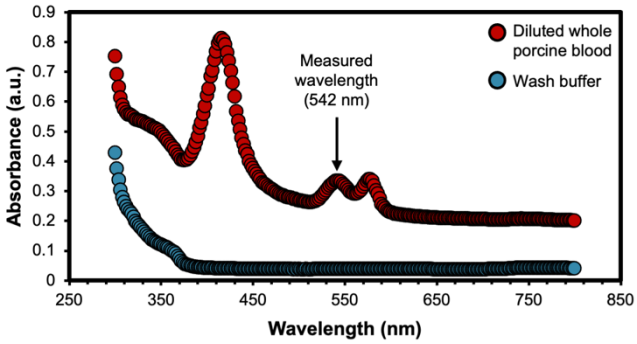

Figure E.2. Absorbance scan of blood and wash buffer. Absorbance of blood and wash buffer over the range of 300-800 nm.

As described in the main text, washing of blue-dyed water from the device required 2 wash cycles, as characterized by measurement of the absorbance of fluids collected after sequential washing of the device (Fig. E.3). The absorbance of fluid collected after the 3rd wash was only 2.09 ± 0.14% of the absorbance of the initial wash, whereas the absorbance of undyed water controls was 1.45 ± 0.04% of the absorbance of the initial wash.

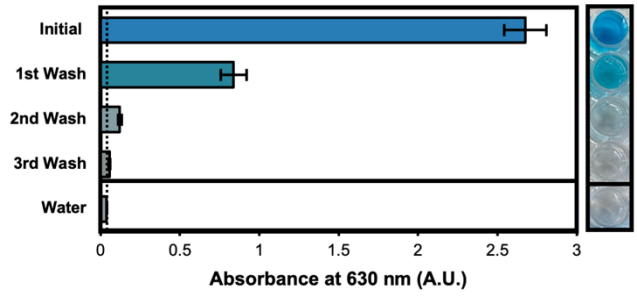

Figure E.3. Device washing characterization. Absorbance readings of samples collected after washing blue-dyed water with undyed water.

E.1.3 Additional 5PL fitting data

The values of the parameters used to generate the 5PL fits shown in Fig. 5.4 and 5.5 of the main text are provided in Table E.1.

Table E.1. Values of parameters for all 5PL fits presented in the main text.

Parameter	Anti-OVA	IgM	IgA	IgA in blood
a	152.67	148	96.4	69.9
b	177990.2948	384062.031	1079091.31	635791.961
g	0.17457423	0.00923409	0.00374808	0.00512338
c	69.50141509	0.0821905	0.096631	1.93524368
d	0.864236918	1.38773508	1.27691857	1.00398194